

## CHAPTER 3

# Descriptions of the Four Machines at 500 GeV c.m.

### 3.1 TESLA

#### 3.1.1 Overview

##### 3.1.1.1 Introduction

The design work and technical R&D for a next generation linear collider based on superconducting technology began in 1992 and is performed by a broad international collaboration, with DESY in Hamburg being the coordinating laboratory. At present, the TESLA collaboration has more than 40 member institutes from 10 countries. The complete layout of the TESLA facility is described in a technical report published in 2001 [1], which includes an update of the earlier design study [2], an estimate of the cost and construction schedule, and a description of the proposed TESLA site next to the DESY laboratory.

TESLA uses 9-cell niobium cavities (Figure 3.1) cooled by superfluid Helium to  $T = 2$  K and operating at L-band frequency (1.3 GHz). The design gradient at  $E_{cm} = 500$  GeV is  $E_{acc} = 23.8$  MV/m and the quality factor  $Q_0 = 10^{10}$ . Because the power dissipation in the cavity walls is extremely small, the accelerating field can be produced with long, low peak power rf pulses; this results in a high rf to beam power transfer efficiency, allowing a high average beam power while keeping the electrical power consumption within acceptable limits ( $\sim 100$  MW).

The relatively low frequency of the TESLA linac is beneficial for accelerating and *conserving* ultra-small emittance beams. As a result, the emittance dilution can be reduced to acceptable levels in TESLA using relatively relaxed alignment tolerances for the linac components (see Section 3.1.3).

The choice of superconducting rf also permits to use a long rf pulse (1 ms) and a relatively large bunch spacing (337 ns at  $E_{cm}=500$  GeV). Three benefits result directly from this long bunch train:

## DESCRIPTIONS OF THE FOUR MACHINES AT 500 GEV C.M.

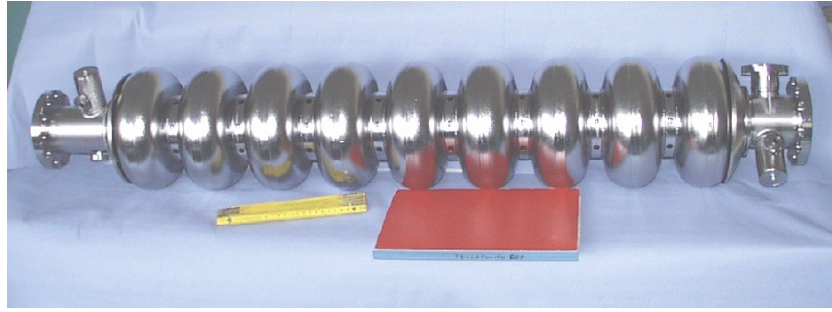


FIGURE 3.1. The 9-cell niobium cavity for TESLA.

- A fast (MHz) bunch-to-bunch feedback can be used to correct the orbit within one beam pulse. Such a feedback system will maintain the beams in collision at the IP, making TESLA relatively insensitive to mechanical vibrations which could otherwise lead to serious luminosity reduction.
- A head-on (zero crossing-angle) collision scheme can be used, with large-aperture superconducting quadrupoles in the interaction region.
- In the event of an emergency, a fast safety system can “turn off” the beam within a fraction of a pulse.

The potential benefits of superconducting rf summarized previously have been acknowledged since the beginning of linear collider R&D. However, in the early 1990s when the R&D program was launched at the TESLA Test Facility (TTF), the projected costs based on existing superconducting rf installations were considered too high. The main challenge for TESLA, therefore, was a reduction in the cost per unit accelerating voltage by a large factor. The approach adopted to reduce the cost was to:

- Increase the achievable gradients available at that time (5–8 MV/m) by about a factor of 4
- Reduce the cost per unit length of the superconducting structures by a similar factor

The achievements during the first phase of the TTF program are summarized in Section 3.1.2. To date, more than seventy 9-cell cavities have been processed and tested. The results show that a gradient of about 25 MV/m is feasible with a reliability sufficient for large scale industrial production. Furthermore, the integrated system test performed in the TTF linac demonstrated beam acceleration with parameters close to the TESLA-500 design goal.

Further progress on the cavity performance has recently been obtained by applying electropolishing to the niobium surface. Test results with single-cell resonators repeatedly show gradients above 30 MV/m. The best single-cell performance obtained to date is  $E_{acc}=42$  MV/m. First results for 9-cell electropolished cavities also show gradients well

above 30 MV/m. We are therefore confident that the cavities in the TESLA linac will be able to operate at a gradient above 30 MV/m, allowing a significant increase in the achievable center-of-mass energy.

On the basis of industrial studies, a cost estimate for the superconducting linac and all other main subsystems of the collider has been worked out and published in March 2001 as part of the Technical Design Report. The total investment cost amounts to 3,136 million Euro, out of which 1,131 million Euro are for the superconducting accelerator modules. This latter figure is well in accord with the original cost goal of US\$2,000 per MV of accelerating voltage.

### 3.1.1.2 General Layout and Parameters

A sketch of the overall layout of the TESLA linear collider is shown in Figure 3.2. The figure also indicates schematically the X-ray Free Electron Laser Facility, which is an integral part of the proposed TESLA facility. Since the impact of the FEL integration on the collider design and performance is, if any, very small and the FEL itself is not of concern for this report, it will not be considered further in the following.

The baseline design for the TESLA linear collider has a single interaction region with head-on collisions (Section 3.1.5). As indicated in Figure 3.2 an optional second IR with crossing angle is foreseen. The crossing angle permits using this IR for photon-photon collisions, as described in Appendix 1, part-VI of the TDR. The beam switchyard for the second IR is included in the baseline layout for the delivery system.

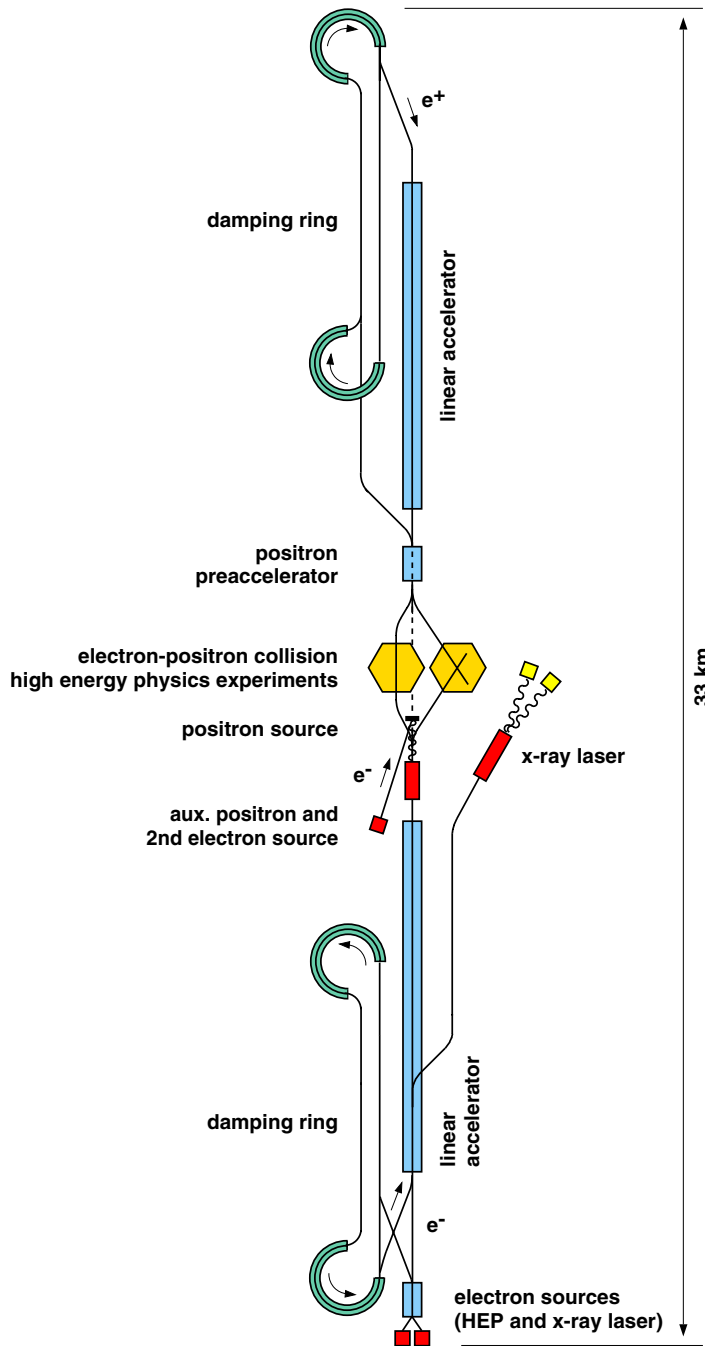
The positron source makes use of an elegant scheme originally proposed at Novosibirsk. Positrons are produced from  $\gamma$ -conversion in a thin target (Section 3.1.4), after which they are preaccelerated in a conventional 200 MeV L-band linac, followed by a 5 GeV superconducting accelerator. The photons are generated by passing the high-energy electron beam through an undulator placed after the main linac, before transporting the beam to the IP.

The electron beam is generated in a polarized laser-driven gun (Section 3.1.4). After a short section of conventional linac, the beam is accelerated to 5 GeV in superconducting structures identical to the ones used for the main linac. The baseline design assumes that the electrons are stored in a damping ring very similar to the one required for the positron beam. The possibility of replacing the electron ring by a flat-beam low emittance electron gun is presently under study.

The positron beam is injected into the damping ring at an energy of 5 GeV. The bunch train is stored in the ring in a compressed mode, with the bunch spacing reduced by about a factor of 16; even with this compression, a large ring circumference of about 17 km is still required. To avoid building an additional large ring tunnel, a so-called “dog-bone” design is used (Section 3.1.4). The layout has two 8 km straight sections placed entirely in the main linac tunnel; additional tunnels are only required for the 1 km circumference loops at either end.

The two main linear accelerators (Section 3.1.3) are each constructed from roughly ten-thousand one-meter long superconducting cavities. Groups of twelve cavities are installed in a common cryostat (cryomodule); the current design is based on that used in the TTF, modified to be slightly more compact. The cryomodules also contain

DESCRIPTIONS OF THE FOUR MACHINES AT 500 GEV C.M.



H.Weise 3/2000

FIGURE 3.2. Sketch of the overall layout of TESLA.

superconducting magnets for beam focusing and steering, beam position monitors, and higher-order mode absorbers.

The rf power is generated by some 300 klystrons per linac, each feeding 36 9-cell cavities. The required  $\sim 10$  MW peak power per klystron includes a 10% overhead for correcting phase errors during the beam pulse which arise from Lorentz force detuning and microphonics. The high-voltage pulses for the klystrons are provided by conventional modulators.

The cryogenic system for the TESLA linac is comparable in size and complexity to the one currently under construction for the LHC at CERN. Seven cryogenic plants are foreseen, each one serving a  $\sim 5$  km long linac subsection. The cooling capacity of the first section of the electron linac is increased to accommodate the higher load from the additional FEL beam pulses.

The beam delivery system between the linac and the IP (Section 3.1.5) consists of collimation, beam diagnostics and correction, and final focus sections. The design of the final focus system is essentially the same as the Final Focus Test Beam (FFTB) system successfully tested at SLAC. Beam size demagnification and chromatic corrections for the TESLA design parameters are no more ambitious than at the FFTB. The beams can be kept in collision at the IP to a high precision by using a fast bunch-to-bunch feedback, which measures and corrects the beam-beam offset and crossing angle on a time scale small compared to the beam pulse length. The design of the beam delivery system is optimized for a single head-on interaction point. The complete system of  $\sim 3.3$  km will fit into a straight tunnel between the linacs. All the magnet systems and beamline geometry are designed to allow an upgrade to a beam energy of 400 GeV. As previously mentioned, a second IR with a 34 mrad crossing angle is also foreseen, which could be used for  $\gamma\gamma$  or  $e^- \gamma$  collisions. On the electron linac side, care has been taken to place the positron source (undulator) upstream of the beam switchyard, so as not to exclude the possibility of  $e^+e^-$  collisions at the second IR.

The two linear accelerators as well as the beam delivery system will be installed in an underground tunnel of 5 m diameter (see Figure 3.3). A 2000 m<sup>2</sup> experimental hall is foreseen to house the detector; the hall can be extended to house a second detector should the second IR be constructed. Seven additional surface halls are required for the cryogenic plants, spaced at intervals of about 5 km along the linacs, and are connected to the underground tunnel by access shafts. The halls will also contain the modulators which generate the HV pulses for the klystrons. The pulse transformers are placed in the tunnel close to the klystrons; the long cables required to connect the modulators to the transformers contribute a few percent to the total power losses, but it is an advantage to allow access to the modulators for maintenance during machine operation. Exchange of klystrons, however, will require an interruption of the machine operation: with an energy overhead of 2% foreseen in the design, and assuming an average klystron lifetime of 40,000 hr, maintenance breaks of one day every few weeks will be necessary.

Within the TESLA collaboration there is broad agreement that the facility should be constructed at an existing High Energy Physics laboratory to reduce project costs and construction time. Both DESY and FNAL have been considered as possible sites. DESY as the coordinating laboratory in the collaboration has taken over the task of working out a detailed plan for the TESLA site North-West of the DESY laboratory. In this scenario, the

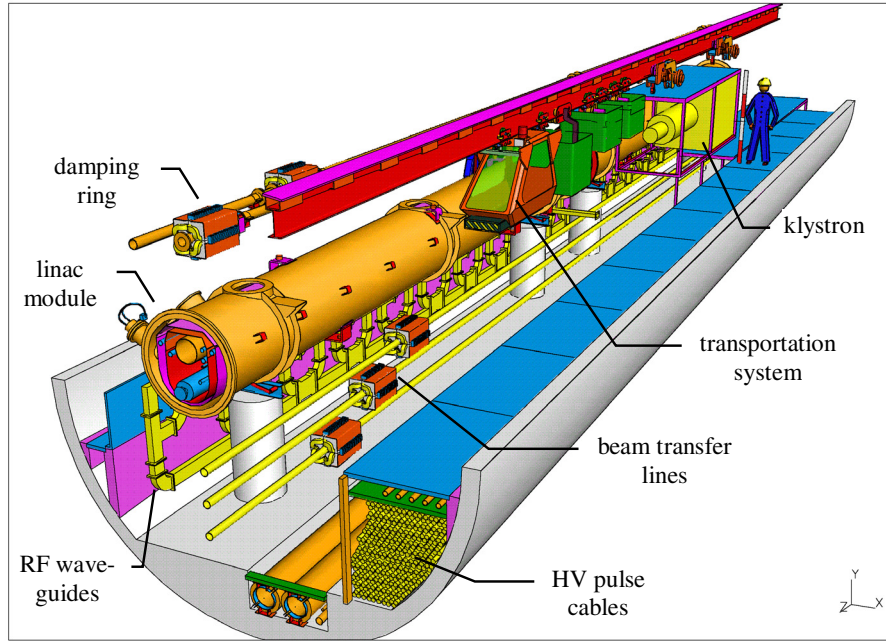


FIGURE 3.3. Sketch of the 5 m diameter TESLA linac tunnel.

linac tunnel starts at the DESY site in a direction tangential to the west straight section of HERA, so as not to exclude an electron-proton linac-ring collider option. The central area is situated about 16 km from the DESY site in a rural part of the North German state (Bundesland) of Schleswig-Holstein, and accommodates both the collider detector hall for Particle Physics and the FEL radiation user facility.

### 3.1.1.3 Parameters for 500 GeV

Besides the center-of-mass energy of the colliding beams, the second key parameter for a linear collider is the luminosity  $L$ , given by

$$L = \frac{n_b N_e^2 f_{rep}}{4\pi\sigma_x^* \sigma_y^*} \times H_D$$

where	$n_b$	number of bunches per pulse
	$N_e$	number of electrons (positrons) per bunch
	$f_{rep}$	pulse repetition frequency
	$\sigma_{x,y}^*$	horizontal (vertical) beam size at interaction point
	$H_D$	disruption enhancement factor (typically $H_D \sim 2$ )

An important constraint on the choice of IP parameters is the effect of beamstrahlung: the particles emit hard synchrotron radiation in the strong electromagnetic space-charge field of

the opposing bunch. Beamstrahlung causes a reduction and a spread of the collision energy and can lead to background in the detector. The energy loss  $\delta_E$  is therefore typically limited to a few percent. By choosing a large aspect ratio  $R = \sigma_x^*/\sigma_y^* \gg 1$ ,  $\delta_E$  becomes independent of the vertical beam size and the luminosity can be increased by making  $\sigma_y^*$  as small as possible. The TESLA parameter set (Table 3.1) reflects these considerations: it demonstrates the potential for high luminosity, while maintaining a low level of beamstrahlung.

TABLE 3.1

TESLA parameters for the  $E_{cm}=500$  GeV baseline design. The machine length includes a 2% overhead for energy management.

TESLA-500		
Accelerating gradient	$E_{acc}$ [MV/m]	23.8 <sup>a</sup>
RF frequency	$f_{rf}$ [GHz]	1.3
Total site length	$L_{tot}$ [km]	33
Active length	[km]	21.8
Repetition rate	$f_{rep}$ [Hz]	5
Beam pulse length	$T_P$ [ $\mu$ s]	950
Number of bunches per pulse	$n_b$	2820
Bunch spacing	$\Delta t_b$ [ns]	337
Charge per bunch	$N_e$ [ $10^{10}$ ]	2
Emittance at IP	$\gamma\varepsilon_{x,y}$ [ $10^{-6}$ m·rad]	10, 0.03
Beta at IP	$\beta_{x,y}^*$ [mm]	15, 0.4
Beam size at IP	$\sigma_{x,y}^*$ [nm]	553, 5
Bunch length at IP	$\sigma_z$ [mm]	0.3
Beamstrahlung	$\delta_E$ [%]	3.2
Luminosity	$L_{e^+e^-}$ [ $10^{34}$ cm <sup>-2</sup> s <sup>-1</sup> ]	3.4
Power per beam	$P_b/2$ [MW]	11.3
Two-linac primary electric power (main linac rf and cryogenic systems)	$P_{AC}$ [MW]	97
$e^-e^-$ collision mode:		
Beamstrahlung	$\delta_{E,e-e^-}$ [%]	2.0
Luminosity	$L_{e-e^-}$ [ $10^{34}$ cm <sup>-2</sup> s <sup>-1</sup> ]	0.47

<sup>a</sup> With the present site layout for TESLA, 23.4 MV/m was the required energy gain per meter of accelerator structure. A detailed analysis by the ILC-TRC revealed that the gradient has to be increased to 23.8 MV/m when rf phasing, especially for BNS damping, is taken into account.

### 3.1.1.4 Operation at Lower Energies

Operating the linac at reduced accelerating gradient for lower center-of-mass energy is an obvious possibility. In principle, an optimum match of the rf system to the beam impedance can be done by changing the external load, thus allowing for an increase in beam current and pulse length. On the other hand, at lower gradient the emittance growth in the linac increases. In order to obtain an approximate scaling of the luminosity at reduced energy, we disregard both the possibility of higher beam intensity and enhanced emittance dilution. In this case, the luminosity scales simply as  $L \propto E_{cm}$  as a result of reduced adiabatic damping of the emittances. Simultaneously, the beamstrahlung goes down approximately as  $\delta_B \propto E_{cm}^2$ . It has been checked that the acceptance of the beam delivery system is sufficient to accommodate the larger absolute beam emittance down to an energy of about 50 GeV (Z-pole).

A serious complication for low energy operation arises from the positron source. The source is laid out for an overhead factor of 2 (number of positrons within the damping ring acceptance per electron in the high energy drive beam) at an electron energy of 250 GeV. This overhead reduces to 20% at 175 GeV beam energy. Since a certain amount of overhead in the source intensity is likely to be necessary to achieve full positron intensity in routine operation, we consider 175 GeV beam energy ( $E_{cm}=350$  GeV) as the lowest energy for which the positron linac can operate at full design beam current. For beam energies of 175–100 GeV, the positron intensity drops approximately linearly with energy and the luminosity goes down as  $\propto E_{cm}^2$ . There is a possibility, though, to retain full intensity even for operation at the Z-pole. This can be accomplished by splitting up the electron linac into a section which accelerates the colliding beam and a section which produces the drive beam for the positron source. This would require an additional electron source and a bypass line for the colliding (50 GeV) beam. The details of such a layout have not yet been worked out. The luminosity as a function of energy resulting from these assumptions is shown in Table 3.2.

TABLE 3.2  
Estimated luminosity at lower energies (see text).

c.m. Energy [GeV]	Luminosity [ $10^{34}$ cm $^{-2}$ s $^{-1}$ ]
350	2.38
200	0.78
100	0.6 (with bypass)

### 3.1.1.5 Electron-Electron and $\gamma\gamma$ Collisions

The head-on  $e^+e^-$  interaction region can also be operated in  $e^-e^-$  mode. The disadvantage here is that the luminosity enhancement arising from self-focusing for oppositely charged bunches turns into a de-focusing effect for like charges, with  $H_D < 1$ . Assuming identical beam parameters, we find a luminosity seven times smaller than for the  $e^+e^-$  mode (see Table 3.1).

The photon collider option, where the electrons are converted into high energy photons by interaction with a laser beam just upstream of the IP, requires construction of the second interaction region with the large crossing angle. Unlike the  $e^+e^-$  case, the beamstrahlung constraint is not present for  $\gamma\gamma$  collisions, and the horizontal beam size at the IP can be reduced still further. Table 3.3 lists a possible  $\gamma\gamma$  parameter set which reflects the lack of the beamstrahlung constraint: the horizontal emittance is at the limit achievable with the present damping ring design, while the IP beta-functions are compatible with a final focus system design similar to the  $e^+e^-$  collider version (except, of course, for the crossing angle). Additional improvements are conceivable, but require further design studies of these subsystems. Crab-crossing is assumed to avoid a luminosity reduction caused by the crossing angle. The actual usable  $\gamma\gamma$  luminosity is smaller than the geometric value by an order of magnitude, since not all the electrons are converted by Compton scattering, and only part of the luminosity spectrum is within a few percent of the peak collision energy.

TABLE 3.3

Beam parameters for the  $\gamma\gamma$  option. The effective luminosity takes into account only the high energy peak of the luminosity spectrum ( $E_{cm,\gamma\gamma} \sim 400$  GeV).

TESLA-500, $\gamma\gamma$		
Repetition rate	$f_{rep}$ [Hz]	5
Beam pulse length	$T_P$ [ $\mu$ s]	950
Number of bunches per pulse	$n_b$	2820
Bunch spacing	$\Delta t_b$ [ns]	337
Charge per bunch	$N_e$ [ $10^{10}$ ]	2
Emittance at IP	$\gamma\varepsilon_{x,y}$ [ $10^{-6}$ m·rad]	3, 0.03
Beta at IP	$\beta_{x,y}^*$ [mm]	4, 0.4
Beam size at IP	$\sigma_{x,y}^*$ [nm]	157, 5
Bunch length at IP	$\sigma_z$ [mm]	0.3
Geometric luminosity	$L_{geom}$ [ $10^{34}$ cm $^{-2}$ s $^{-1}$ ]	5.8
Effective $\gamma\gamma$ luminosity	$L_{\gamma\gamma}$ [ $10^{34}$ cm $^{-2}$ s $^{-1}$ ]	0.6

## 3.1.2 Results of Superconducting Accelerator Development

### 3.1.2.1 Superconducting Cavities

The TESLA cavity is a 9-cell standing wave structure of about 1 m length whose fundamental TM mode has a frequency of 1300 MHz. The cavity is made from solid niobium and is bath-cooled by superfluid helium at 2 K. Each cavity is equipped with: a helium tank; a tuning system driven by a stepping motor; a coaxial rf power coupler; a pickup probe; and two higher-order mode (HOM) couplers. A side view of the TTF cavity with the beam tube sections and the coupler ports is shown in Figure 3.4. The important cavity parameters are listed in Table 3.4.

DESCRIPTIONS OF THE FOUR MACHINES AT 500 GEV C.M.

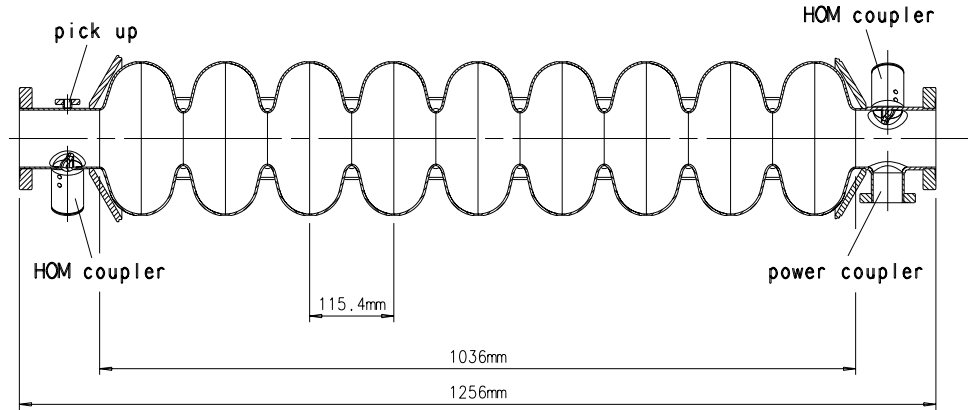


FIGURE 3.4. Side view of the 9-cell cavity with the main power coupler port and two higher-order mode couplers.

TABLE 3.4

Parameters of the 9-cell cavity (note that we adopt here the definition of shunt impedance by the relation  $R = V^2/P$ , where  $P$  is the dissipated power and  $V$  the peak voltage in the equivalent parallel LCR circuit).

Type of accelerator structure	standing wave
Accelerating mode	TM <sub>010</sub> , $\pi$ -mode
Fundamental frequency	1300 MHz
Nominal gradient $E_{acc}$ for TESLA-500	23.8 MV/m
Quality factor $Q_0$	$> 10^{10}$
Active length $L$	1.038 m
Cell-to-cell coupling $k_{cc}$	1.87%
Iris diameter	70 mm
$R/Q$	1036 $\Omega$
$E_{peak}/E_{acc}$	2.0
$B_{peak}/E_{acc}$	4.26 mT/(MV/m)
Tuning range	$\pm 300$ kHz
$\Delta f/\Delta L$	315 kHz/mm
Lorentz force detuning constant $K_{Lor}$	$\sim 1$ Hz/(MV/m) <sup>2</sup>
$Q_{ext}$ of input coupler	$2.5 \times 10^6$
Cavity bandwidth at $Q_{ext}=2.5 \times 10^6$	520 Hz
Fill time	420 $\mu$ s
Number of HOM couplers	2

The superconducting resonators are fabricated from bulk niobium by electron-beam (EB) welding of deep-drawn half cells. The tubes for the beam pipes and the coupler ports are made by back extrusion and are joined to the cavity by EB welds. Stiffening rings are welded between cells to reduce the Lorentz force detuning by a factor of 2 to about 400 Hz at 23.8 MV/m. A tuning mechanism is used to adjust the cavity resonance frequency. By inserting a piezo element into the tuning system, the dynamic Lorentz force detuning during the rf pulse can be completely compensated, as was successfully demonstrated with tests at the TTF. This would reduce the 10% overhead in rf power for gradient stabilization, which is presently still included in the rf system design parameters.

The TESLA cavities are similar in layout to the 5-cell 1.5 GHz cavities of the electron accelerator CEBAF, which were developed at Cornell University and fabricated by industry. At that time the cavities considerably exceeded the design gradient of 5 MV/m: hence they were considered to have a significant potential for further improvement, and the CEBAF cavity manufacturing methods were adopted for TESLA. Improved quality control of the superconducting material and of the fabrication methods were made, and important new steps were introduced into the cavity preparation:

- Chemical removal of a thicker layer from the inner cavity surface
- Eddy current scanning to identify bulk inclusions of macroscopic impurities (*e.g.*, Tantalum) in the Niobium sheets prior to cavity fabrication
- A 1400°C annealing with a titanium getter to improve the niobium heat conductivity and to homogenize the material
- Rinsing with ultra-pure water at high pressure (100 bar) to remove surface contaminants
- Destruction of field emitters using High Power Processing

Application of these techniques—combined with an extremely careful handling of the cavities in a clean-room environment—has led to accelerating fields which exceed the TESLA-500 design goal of 23.8 MV/m. Figure 3.5 shows the excitation curves (quality factor  $Q_0$  versus gradient  $E_{acc}$ ) for nine cavities from the third industrial production series. These measurements are done in a vertical cryostat with CW rf excitation. About half of the more than 70 cavities tested so far were also measured in pulsed operation (at full design pulse length and repetition rate), fully equipped with rf input and HOM couplers and mounted in a horizontal cryostat. No degradation in performance with respect to the vertical tests was observed: the average gradient of 31 cavities was 24.5 MV/m in the vertical test and 25.5 MV/m in pulsed operation.

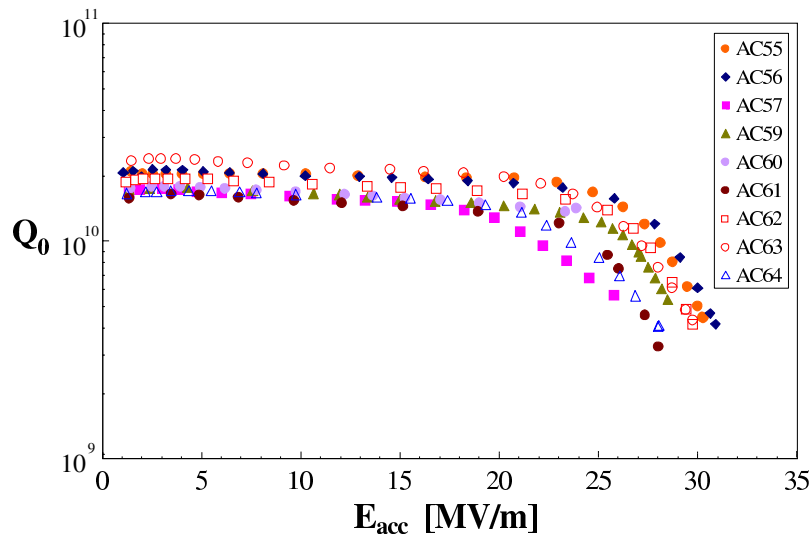


FIGURE 3.5. Excitation curves of cavities of the third production series.

### 3.1.2.2 Developments Toward Higher Gradients

At present, three main obstacles might prevent us from approaching the superconductor limit of  $\sim 50$  MV/m in multicell niobium cavities:

- Foreign material contamination in the niobium
- Insufficient quality and cleanliness of the inner rf surface
- Quality of the welds

Niobium for microwave resonators has to be of extreme purity for two reasons: dissolved gases like hydrogen, oxygen and nitrogen impair the heat conductivity at liquid helium temperature; and contamination by normal-conducting or weakly superconducting clusters close to the rf surface may cause a premature breakdown of the superconducting state. The niobium for the TTF cavities was processed in industry with plants which are in addition used for other metals. For the large series production of cavities needed for the TESLA collider, it would be economical to install dedicated facilities for the niobium refinery and the forging and sheet rolling operations. A substantial improvement in material quality can be expected from specialized installations which are designed for the highest cleanliness, and which are free of contamination by other metals. The same applies for the electron-beam welding machines which must conform to Ultra High Vacuum standards: such a high-quality EB welding machine will be used at DESY in the cavity R&D program.

The recent TTF cavities have been made from eddy-current-checked niobium with gas contents in the few ppm range and an  $RRR$  of 300. Ten 9-cell cavities have been tested before and after the  $1400^\circ\text{C}$  heat treatment which raises the  $RRR$  to more than 500. The average gain in gradient was 4 MV/m. The result implies that, with the present surface preparation by chemical etching, the heat treatment is an indispensable step in achieving

the TESLA-500 goal. From tests at KEK there is some evidence that the tedious and costly 1400°C heat treatment may not be needed in cavities prepared by electropolishing.

The Buffered Chemical Polishing (BCP) used at TTF to remove a 100–200  $\mu\text{m}$  thick damage layer produces a rough niobium surface with strong grain boundary etching. An alternative method is “electropolishing” (EP) in which the material is removed in an acid mixture under current flow. Sharp edges and burrs are smoothed out and a very glossy surface can be obtained.

Since 1995, gradients above 35 MV/m have been routinely obtained at KEK in several electropolished L-band single-cell niobium cavities. Most of these cavities were made from *RRR* 200 material and not subjected to a high temperature heat treatment for post-purification. A KEK-Saclay collaboration demonstrated that EP raised the accelerating field of a 1-cell cavity by more than 7 MV/m with respect to BCP. When the electropolished surface was subjected to a subsequent BCP, the cavity suffered a clear degradation in rf performance which could be recovered by a new EP. Thus there is strong evidence that EP is the superior surface treatment method.

CERN, DESY, KEK and Saclay started a joint R&D program with EP of half cells and 1-cell cavities in August 1998. Gradients between 35 and 42 MV/m are now routinely being achieved (see Figure 3.6). The current program focuses on cavities made from niobium with *RRR*=300. An important goal is to determine whether or not the high gradients so far achieved can be obtained without the time-consuming 1400°C heat treatment.

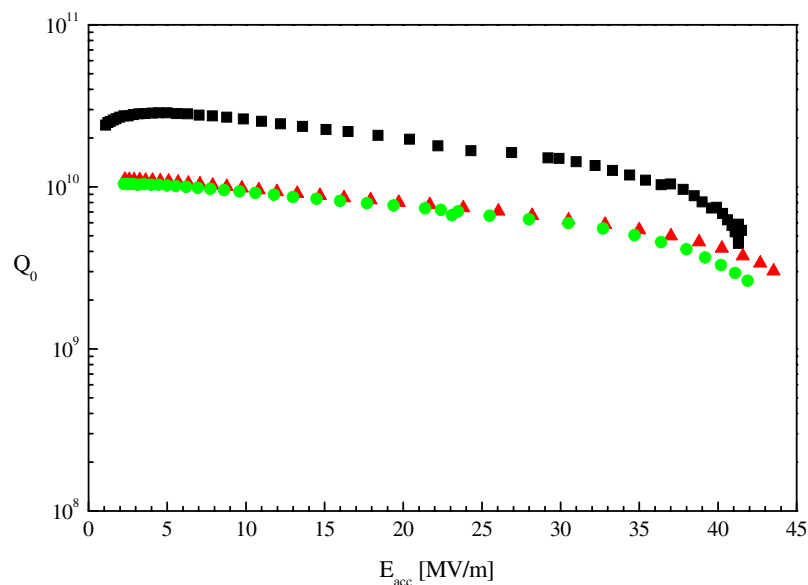


FIGURE 3.6. Excitation curves of three electropolished single-cell cavities without heat treatment at 1400°C. The tests have been performed in different cryostats and under slightly different conditions (magnetic shielding, helium temperature).

Recently it has been found that an *in-situ* baking of the evacuated cavity at 100–150°C (following the EP and clean water rinsing) is an essential step in reaching higher gradients

## DESCRIPTIONS OF THE FOUR MACHINES AT 500 GEV C.M.

without a strong degradation in quality factor. The underlying mechanism is not yet understood. The baking was applied to all single-cell cavities.

The transfer of the EP technique to multicell cavities requires considerable investment. In a first test a 9-cell TESLA resonator has been electropolished by a Japanese company, improving its performance from 22 to 32 MV/m (Figure 3.7). An EP facility for 9-cell cavities is under construction at DESY. Given the results obtained so far, it is likely that EP will form an essential part of producing cavities capable of achieving the 35 MV/m operating gradient needed for TESLA-800.

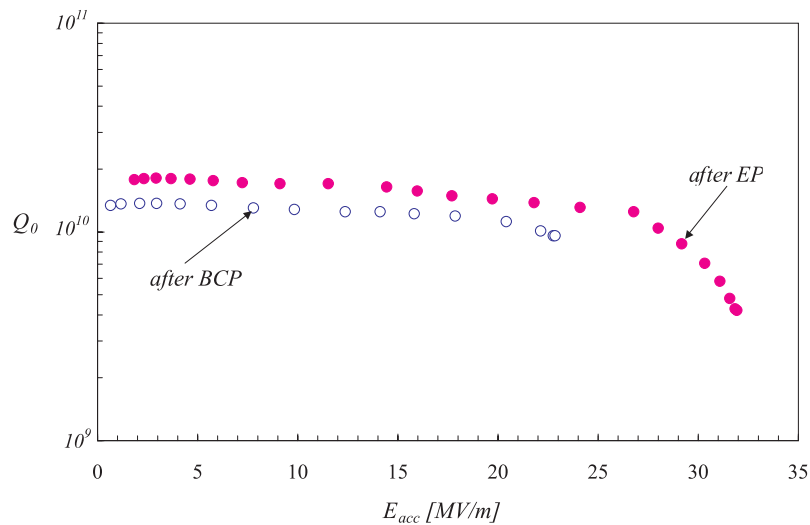


FIGURE 3.7. Excitation curve of a TESLA 9-cell cavity after buffered chemical polishing (BCP) and electropolishing (EP), but before application of the baking procedure.

### 3.1.2.3 The Superstructure Concept

A fundamental design goal for a linear collider is to maximize the active acceleration length in the machine and to reduce the cost of the radio frequency system. Hence it is desirable to use accelerator structures with as many cells as possible both to increase the filling factor and to reduce the number of power couplers and waveguide components. However, the number of cells per cavity ( $N$ ) is limited by the conditions of field homogeneity and the presence of trapped modes. The sensitivity of the field pattern to small perturbations grows quadratically with the number of cells. The probability of trapping higher-order modes within a structure also increases with  $N$ ; such modes with a small field amplitude in the end cells are difficult to extract by the HOM couplers.

The limitations on the number of cells per cavity can be circumvented by joining several multicell cavities to form a so-called superstructure. Short tubes of sufficient diameter (114 mm) enable power flow from one cavity to the next. Two types of superstructures have been investigated in detail: Superstructure I consisting of four 7-cell resonators; and, more

recently, Superstructure II consisting of two 9-cell resonators. The chain of cavities is powered by a single input coupler mounted at one end. HOM couplers are located at the interconnections and at the ends. All cavities are equipped with their own tuners. The cell-to-cell coupling is  $k_{cc}=1.9\%$ , while the coupling between two adjacent cavities in a superstructure is two orders of magnitude smaller at  $k_{ss} \sim 3 \times 10^{-4}$ : due to this comparatively weak inter-cavity coupling the issues of field homogeneity and HOM damping are much less of a problem than in a single long cavity with  $N = 28$  or 18 cells. The shape of the center cells is identical to those in the 9-cell TTF structures while the end cells have been redesigned to accommodate the larger aperture of the beam tube. The gain in filling factor with the (preferred) version II is 6% and the number of power couplers is reduced by a factor of 2 compared to the baseline design of the TESLA linac. With an accelerating gradient of 35 MV/m the energy reach of TESLA is 800 GeV when built with these superstructures. Whether to go from the baseline design to the superstructure concept will be decided after the tests with beam in the TTF linac, which are scheduled for 2002.

### 3.1.2.4 Integrated System Test

In order to demonstrate the feasibility of the TESLA technology in a fully integrated system test with beam, a test linac was set up at the TTF. In this linac, accelerator modules containing eight 9-cell cavities each, together with focusing and steering magnets and beam instrumentation are installed. The beam is generated in a low-emittance photocathode rf gun. Additional sections in the beam line are a bunch compressor, collimation section, undulator section for the Free Electron Laser and high energy electron and photon beam analysis area.

So far three accelerator modules have been tested, two of which have been continuously in operation over the past two years, accumulating about 10,000 hr of beam time. A substantial fraction of the beam time was allocated to the FEL studies, which yielded first lasing at 100 nm wavelength in February 2000 and saturation of the FEL radiation in September 2001. The FEL studies were done at reduced beam energy with accelerating gradients between about 12 and 17 MV/m.

The studies performed with the accelerator modules include measurements of maximum beam acceleration, determination of the static and dynamic cryogenic load, active stabilization of the energy gain over the length of the bunch train and excitation of Higher Order Modes.

The static load is in accord with the design values at 4.5 K and 70 K and slightly exceeds the design value at 2 K due to additional diagnostic equipment which will not be present in the TESLA linac.

The average accelerating gradients measured with beam for modules 1, 2, and 3 are 14, 19, and 22 MV/m, respectively. The measured cryogenic load was in accord with the design value for the unloaded quality factor of  $Q_0 = 10^{10}$ . This confirmed that no significant degradation in cavity performance had happened from the vertical test stand to operation in the module.

Acceleration of a bunch train with the full TTF design specifications (0.8 ms pulse length, 8 mA pulse current) was demonstrated and the rms bunch-to-bunch energy spread was measured to be below  $10^{-3}$  (see Figure 3.8).

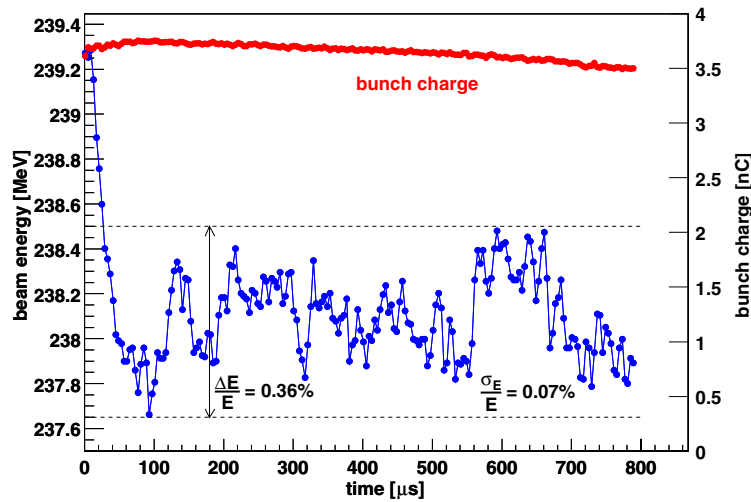


FIGURE 3.8. Acceleration of long macro pulses. The beam energy and the bunch charge within one single macro pulse are shown. The rf control system was operated with the feedback loop active for beam loading compensation. The bunch spacing was 444 ns.

### 3.1.3 Main Linac

#### 3.1.3.1 Layout and Parameters

The main linac is built with accelerator modules which are conceptually very similar to the ones at TTF. The main difference is a slight improvement in filling factor, by reducing the inter-cavity spacing from 0.34 m to 0.28 m and by accommodating twelve instead of eight 9-cell cavities in a length of about 17 m instead of 12 m, thus saving on the number of module inter-connections. In the first half of the linac every second and in the second half every third module includes a quadrupole, steering coils and BPMs. This step in the otherwise constant-beta lattice is merely introduced to save space and components, the impact on the beam dynamics is small. An overview of the main linac components and parameters is given in Table 3.5.

The rf power is provided by 10 MW multibeam klystrons, each driving three accelerator modules (36 cavities total). The power requirement takes into account a 10% regulation reserve for accelerating field stabilization and 6% losses in the waveguide system. An overview of power consumption and efficiencies is given in Table 3.6. The klystrons are powered by 12 kV modulators with solid state IGBT switches, followed by a 1:12 step up pulse transformer. The modulators are installed in external halls (accessible for maintenance and repair during machine operation) and are connected to the pulse transformers installed next to the klystrons in the tunnel by 12 kV pulse cables.

TABLE 3.5

Overview of components in each of the two main linacs. A 2% overhead for energy management is included.

Injection energy [GeV]	5
Energy gain at $E_{acc}=23.8$ MV/m [GeV]	245
Total length [km]	14.4
Active length [km]	10.7
Number of cavities per module	12
Number of modules	858
Module length (with quad) [m]	15.9 (16.8)
Number of quadrupoles	350
Number of klystrons	286
Number of cavities per klystron	36
Peak power per klystron [MW]	9.7
RF power to beam per cavity [kW]	231
RF pulse/beam pulse length [ms]	1.37/0.95

TABLE 3.6

Overview of power consumption and efficiencies for the main linac.

Klystron efficiency [%]	65
Modulator efficiency [%]	85
AC power per modulator/klystron [kW]	120
AC power for auxiliaries per rf station [kW]	14
Total AC power for rf per linac [MW]	37.5
AC to beam efficiency for rf [%]	30.1
AC power cryogenics at 2 K per linac [MW]	4.8
AC power cryogenics at 5–8 K per linac [MW]	2.4
AC power cryogenics at 40–80 K per linac [MW]	2.7
Total AC power per linac [MW]	47.4
Overall AC to beam efficiency [%]	23.3

The cooling power at the different temperature levels required for the modules is provided by three cryogenic plants for each linac, which are installed in external halls spaced by about 5 km along the site<sup>1</sup>. The power requirements for the cryogenics are listed in Table 3.6.

<sup>1</sup>The asymmetry of the cryogenic plant distribution as described in the TDR is due to the cryogenic load from operating part of the electron linac with additional pulses for the FEL facility. This particular detail of the TESLA design is ignored here.

### 3.1.3.2 Beam Dynamics

The focusing lattice is characterized by a  $60^\circ$ -FODO cell length of 65 m and 97 m with maximum  $\beta$ -functions of 127 m and 167 m in the first and second half of the linac, respectively. Vertical steering coils and BPMs are foreseen at every quadrupole, horizontal steering coils at every second (horizontal focusing) quadrupole. The vertical steerers are set to provide an average bending radius of  $6 \times 10^6$  m to follow the curvature of the earth.

The assumed alignment errors and resulting single bunch emittance dilutions are listed in Table 3.7. Alignment of the accelerator modules is done with respect to reference points in the tunnel which are defined by a hydrostatic levelling system with an accuracy of  $20 \mu\text{m}$  over a correlation length of 600 m.

Single bunch dynamics have been studied without and with BNS damping. The latter can be easily implemented for the (almost) constant beta lattice with a correlated energy spread in the first part (5 to 25 GeV) of the linac by operating  $-27^\circ$  off-crest. In the rest of the linac the longitudinal wakefield is compensated by a  $+5^\circ$  off-crest phasing. The beneficial effect of the BNS damping on correlated emittance growth (having a  $y - z$  or  $y' - z$  correlation in phase space) due to orbit jitter is shown in Figure 3.9. The emittance growth due to the transverse wakefield from cavity and module misalignments is well within the available 50% dilution budget from the damping ring extraction to the IP. However, in view of the sensitivity of the luminosity to correlated bunch deformations (see Section 3.1.5) a further reduction of this effect is desirable. It can be provided by empirical optimization with non-dispersive orbit bumps, as shown in Figure 3.10. Since filamentation in the linac is small, intermediate emittance diagnostic stations are not required and the optimization can be done by observing the luminosity signal directly.

For initial linac commissioning a simple one-to-one steering procedure (through the BPM centers) is sufficient, but to reduce dispersive emittance growth the orbit must be smoothed (*i.e.*, the rms orbit kick minimized) by beam based methods, *e.g.*, the shunt method or dispersion free (DF) steering. In effect, after applying beam based alignment, the absolute offsets of the BPMs are replaced by their resolution. It is found that an iterative DF algorithm using sections of 20 FODO cells per step works well and leads to a dispersive emittance growth of about 2% of the design emittance at the IP, more than half of which is related to the initial uncorrelated energy spread. An alternative procedure in which individual quads are switched off and the BPM-to-quad alignment is determined by minimizing the difference orbit downstream (so-called shunt or ballistic method) yields similar results.

The rf kicks, which result from tilted cavities, have originally not been included in the DF steering simulations. They are found to have a significant effect in the first few hundred meters of the linac where the beam energy is relatively low and the uncorrelated energy spread large. For an rms tilt angle of 0.3 mrad the DF steering procedure is perturbed by the presence of the kicks, resulting in a dispersive emittance growth of 50%. This problem can be cured by switching off rf stations in those sections in which the DF steering or ballistic method is applied. After switching the rf back on, the orbit is re-steered to the one obtained by the previous procedure. The residual effect of the structure tilts amounts to about 3.5% emittance growth.

TABLE 3.7

Parameters related to single bunch emittance dilution. Note that the relative emittance dilution is quoted with respect to the design emittance at the IP.

Normalized design emittance $\epsilon_x, \epsilon_y$ [ $10^{-6}$ m·rad]	10, 0.03 (at IP)
Normalized emittance at injection $\epsilon_x, \epsilon_y$ [ $10^{-6}$ m·rad]	8, 0.02
Beam size at injection $\sigma_{x,i}, \sigma_{y,i}$ [ $\mu\text{m}$ ]	320, 16
Beam size at linac exit $\sigma_{x,f}, \sigma_{y,f}$ [ $\mu\text{m}$ ]	60, 3
Initial uncorr. energy spread $\sigma_{E,i}/E$ [%]	2.5
Off-crest rf phase $\Phi_{rf}$ (5 to 25 / 25 to 250 GeV) [°]	-27 / 5
Energy spread $\sigma_{E,f}/E$ at linac exit [ $10^{-4}$ ]	7
Cavity to module axis alignment [mm rms]	0.3
Quad to module axis alignment [mm rms]	0.2
Module alignment [mm rms]	0.2
BPM resolution [ $\mu\text{m}$ rms]	10
Orbit jitter (injection and quad vibration) [ $\sigma_y$ ]	0.7–1
Static dilution $\Delta\epsilon_y/\epsilon_y$ from transverse wake [%]	14
Static dilution $\Delta\epsilon_y/\epsilon_y$ from dispersion with DF steering [%]	2
Correlated dilution $\Delta\epsilon_y/\epsilon_y$ from orbit jitter without/w BNS [%]	2–4 / <0.5
Uncorrelated dilution $\Delta\epsilon_y/\epsilon_y$ from orbit jitter [%]	3–6

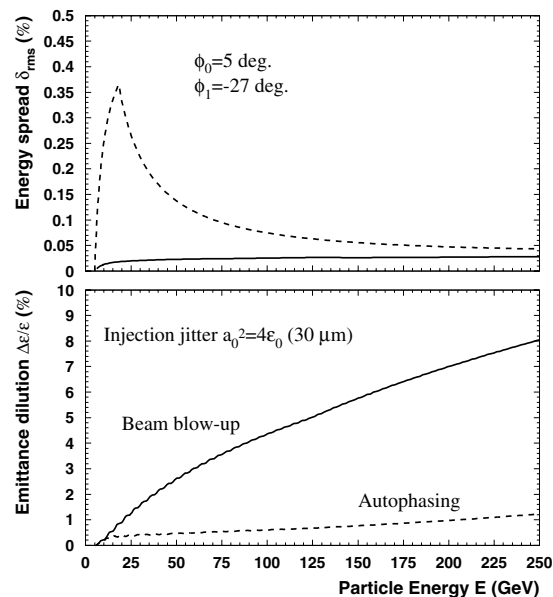


FIGURE 3.9. Illustration of BNS damping in TESLA. The correlated energy spread (dashed curve in upper figure, full curve without BNS) is generated in the 5 to 25 GeV section of the linac and the beneficial effect is shown in the dashed autophasing curve.

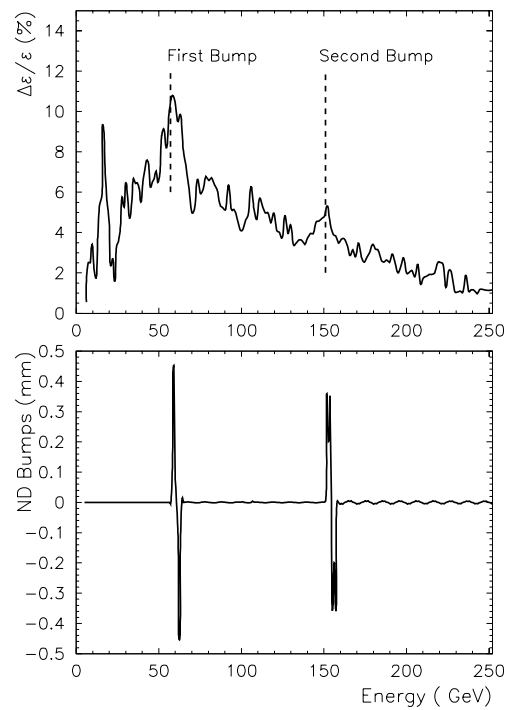


FIGURE 3.10. Example of (non-dispersive) wakefield correction bumps for one particular random seed of misalignments. With two bumps, the emittance growth is reduced by one order of magnitude.

Another detrimental effect of kicks from tilted rf structures occurs in the bunch compressor. Here, the effect is an emittance growth due to the spread of the kick over the length of the bunch. This emittance growth can be tuned out with a dispersion bump applied downstream from the compressor rf section, making use of the almost perfect correlation of the energy deviation with longitudinal position in the bunch. This minimization of emittance dilution is essentially limited by the resolution of the emittance diagnostic section between the compressor and the main linac.

The long range wakefields excited by the beam in the cavities are potentially dangerous, because they can lead to growing bunch oscillation amplitudes over the length of the beam pulse. The higher order modes in the 9-cell cavities have been carefully investigated by numerical calculations, measurements with a network analyzer and resonant excitation with beam in the TTF linac. The HOM couplers are specified such that the quality factors of those modes which couple strongly to the beam are around or below  $10^5$ . The measurements confirmed that the specifications are met, except for one mode at 2.58 GHz in the third dipole passband. The reason for the insufficient damping can be explained by simultaneous weak coupling of one polarization of the mode to both couplers on either end of the cavity. A slight re-arrangement of the couplers is expected to cure this problem.

The beam dynamics calculations with the specified mode properties, including a random mode frequency spread of  $10^{-3}$  from cavity to cavity, show that multibunch beam breakup is not a serious problem. The multibunch emittance growth, averaged over 10 random seeds of cavity misalignments, amounts to 4%. Due to the large bunch spacing, a steady state of HOM excitation is reached after about 100  $\mu\text{s}$ , 10% of the pulse length. A significant bunch-to-bunch orbit variation is only present at the beginning of the train. Even this can be very efficiently corrected: the multibunch orbit pattern is essentially static, *i.e.*, independent of small changes in the beam orbit or the individual bunch charges (see Figure 3.11). By using a fast intra-train orbit correction system, this static part of the bunch-to-bunch orbit variation can be removed. The rms variation of the individual bunch orbits with respect to the average orbit remains below  $0.01\sigma_y$  for injection orbit jitter of  $1\sigma_y$  or random bunch charge fluctuation of 1%.

The orbit stability in the linac has been investigated using the ground and orbit motion measurements performed at HERA. On a long time scale the motion is expected to be diffusion-like, *i.e.*, following the *ATL* rule with a constant  $A=4\times 10^{-6} \mu\text{m}^2\text{m}^{-1}\text{s}^{-1}$  derived from the HERA data. The resulting drift at the end of the linac amounts to  $1\sigma_y$  after 30 s (150 beam pulses). These long term drifts can be corrected with a slow orbit feedback using the steering coils. Concerning jitter on a time scale of a few beam pulses, the ground vibration studies at HERA predict an rms amplitude of 0.5–1  $\sigma_y$  at the linac exit. This causes an uncorrelated emittance growth (from the energy spread at injection) of a few percent and a correlated emittance growth (with BNS damping) of a few tenth of a percent. The resulting jitter in offset and angle of the colliding beams is corrected by the feedback system in the BDS (Section 3.1.5).

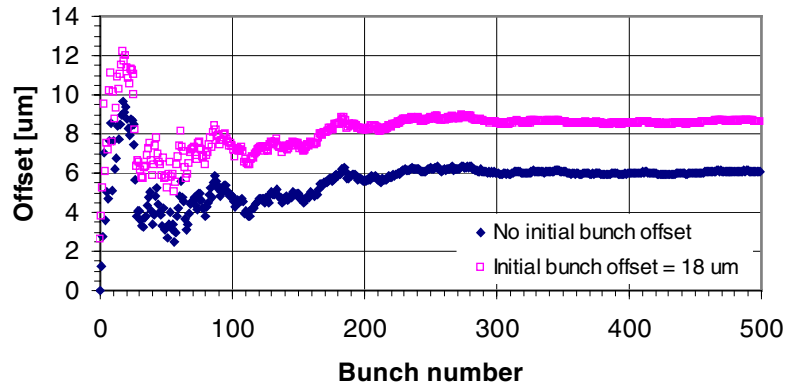


FIGURE 3.11. Orbit offsets in  $\mu\text{m}$  of the first 500 bunches at the end of the linac. The lower curve shows the effects of cavity misalignments only ( $\Delta y_c = 0.5$  mm rms, one seed). The upper curve shows the effects of the same misalignments, but with an additional one  $\sigma_y$  injection error of the beam (coherent betatron oscillation).

### 3.1.4 Injection System and Damping Rings

#### 3.1.4.1 Electron Source

The layout of the polarized electron gun is based on the experience with the polarized source at the SLC and the design for the NLC. The gun uses a GaAs cathode illuminated with 840 nm wavelength light from a Ti:Sapphire laser. It is operated with 1 ms long pulses of 120 kV. The large bunch spacing (337 ns) avoids the potential charge limit problem of the cathode, since it is well above the expected cathode recovery time of 10–100 ns. The initial bunch length of 2 ns (full length) is compressed in a three stage buncher system operating at 108 MHz, 433 MHz and 1.3 GHz, respectively. The final bunch length is  $\sigma_z = 3.4$  mm at a beam energy of 12 MeV. The normalized beam emittance obtained from computer simulations is  $42 \mu\text{m}\cdot\text{rad}$  for a bunch charge of 3.7 nC, 15% higher than the design bunch charge in the main linac. The buncher section is followed by a normal conducting 1.3 GHz accelerator section (two 5-cell cavities powered by one 10 MW klystron) and two standard main linac superconducting accelerator modules, which together increase the beam energy to 500 MeV.

In addition to the polarized source, an unpolarized source is foreseen, the layout of which is very similar to the existing setup at the TTF. This source is thought to be used for commissioning, machine study and unpolarized luminosity operation purposes. The beam lines of the two sources are merged by means of a switching magnet prior to injection into the 0.5 to 5 GeV electron pre-accelerator. This 4.5 GeV linac consists of 18 standard main linac cryomodules operating at a gradient of 21 MV/m and powered by six 10 MW klystrons.

### 3.1.4.2 Positron Source

The positron injection system has to provide a total charge of about  $5 \times 10^{13} e^+$  per beam pulse, which is not realistically feasible with a conventional (electron on thick target) source. Instead, a scheme, originally proposed at Novosibirsk, is used where photons are generated by the high energy electron beam in an undulator and converted into  $e^+e^-$  pairs in a thin target (Figure 3.12). This leads to a comparatively low heat load on the target and better capture efficiency behind the target due to the smaller transverse momentum spread of the particles emerging from the target. The particles are captured in a strong, tapered solenoidal field (adiabatic matching device) and pre-accelerated to 250 MeV in a normal conducting 1.3 GHz linac. The linac requires seven 10 MW rf stations of the TESLA main linac type. The beam is transferred in a 2 km long beam line to the positron linac tunnel on the opposite side of the interaction region. Part of this beam line (500 m) is installed in a separate tunnel to bypass the experimental hall. Acceleration to 5 GeV takes place in a superconducting linac of the standard TESLA type, except for an enhanced focusing (reduced quadrupole spacing) in the first accelerator modules.

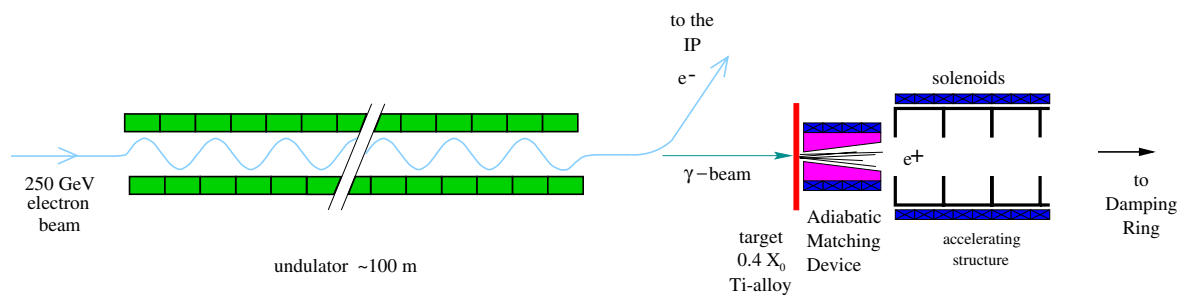


FIGURE 3.12. Sketch of the positron source layout.

The main parameters of the positron source are shown in Table 3.8.

Passage through the undulator, placed between the end of the 250 GeV linac and the beam delivery system, causes the energy spread in the electron beam to increase from  $0.5 \times 10^{-3}$  to  $1.5 \times 10^{-3}$ , with an average energy loss of 1.2%, both of which appear tolerable. The emittance growth is small in both planes (0.1%) with field strength and alignment tolerances of 1% and 1 mrad, respectively, per period of the planar undulator. The undulator-based positron source requires an electron beam energy greater than 150 GeV for full design positron beam intensity. At center-of-mass energies below 300 GeV the luminosity is reduced due to a lower positron beam current. If lower energy running at maximum luminosity becomes important, then additional electron beam pulses and bypass-beamlines are foreseen to drive the positron source independently from the (lower-energy) beam used for physics.

When the planar undulator is replaced by a superconducting helical undulator, polarized positrons can be produced. The polarized positron option is technically more ambitious and is considered a potential upgrade at a later stage of operation. The achievable polarization ranges from 45% to 60%.

DESCRIPTIONS OF THE FOUR MACHINES AT 500 GEV C.M.

TABLE 3.8  
Overview of the positron source main parameters.

<b>Undulator</b>	
Peak field	0.75 T
Length	100 m
Period length	14.2 mm
Gap height	5 mm
$\gamma$ -spot size on target	0.7 mm
Photon beam power	135 kW
<b>Target</b>	
Material	Ti-alloy
Thickness	1.42 cm ( $0.4X_0$ )
Pulse temperature rise	420 K
Average power deposition	5 kW
<b>Adiabatic Matching Device</b>	
Initial field	6 T
Taper parameter	$30 \text{ m}^{-1}$
End field	0.16 T
Capture cavity iris radius	23 mm
<b>General</b>	
Capture efficiency	16%
Number of positrons per electron	2
Normalized $e^+$ -beam rms emittance	0.01 m
Beam energy at pre acc. exit	250 MeV
Total energy width	$\pm 30 \text{ MeV}$
Total phase spread at 1.3 GHz	$\pm 7.5^\circ$
Required D.R. normalized acceptance	0.048 m

In addition to the main undulator-based source, a low-intensity auxiliary  $e^+$  source will be installed for commissioning and machine study purposes. The auxiliary source should be capable of generating a bunch train of a few percent of the design intensity.

### 3.1.4.3 Damping Rings

The positron (electron) beam is injected into the damping ring at an energy of 5 GeV. The bunch train is stored in the ring in a compressed mode, with the bunch spacing reduced by a factor of about 17; even with this compression, a large ring circumference of about 17 km is still required. To avoid building an additional large ring tunnel, a so-called “dog-bone” design is used (Figure 3.13). The layout has two 7.5 km straight sections placed entirely in the main linac tunnel; additional tunnels are only required for the 1 km circumference loops at either end. About 400 m of wiggler sections are needed to achieve sufficient damping. Fast kickers with  $<20$  ns rise and fall time are required for compression and decompression of the bunch train at injection and extraction respectively.

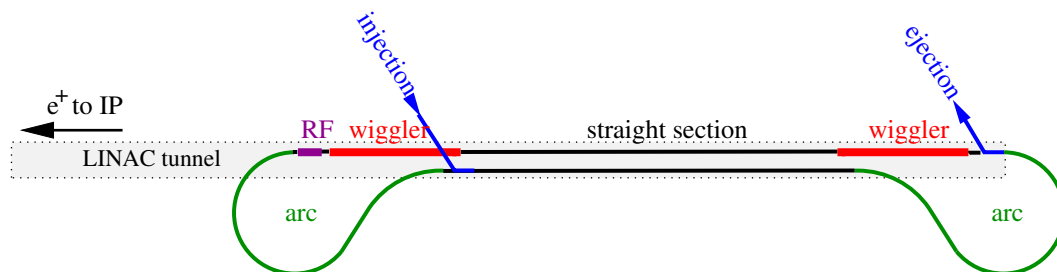


FIGURE 3.13. Conceptual layout of the positron damping ring. The electron ring is similar with the exception that the injection point is located close to the indicated ejection position at the beginning of the linac.

An overview of the damping ring parameters is given in Table 3.9.

Despite its unconventional shape, the damping ring does not exhibit any unusual beam dynamics. The only exception, related to the large ratio of circumference to beam energy, is a large incoherent space charge tune shift. The effect can be significantly reduced, however, by artificially increasing the beam cross-section in the long straight sections.

The ring arcs use a TME-type lattice with 15.2 m cell length (50 cells per arc). The field strength of the dipole magnets is relatively weak (0.2 T) and consequently the arcs contribute only about 5% to the damping. The emittance contribution from the arcs amounts to  $\epsilon_{x,arc}=2\times 10^{-6}$  m. The cells are tunable for smaller emittance, at the expense of reduced dynamic aperture, a feature which can be made use of for the photon collider option of TESLA. The lattice in the long straight sections is a simple FODO structure with 100 m cell length and  $45^\circ$  phase advance.

The permanent magnet wigglers have a peak field of 1.67 T with 25 mm gap height and 40 cm period length. There are in total 90 wiggler modules of 4.8 m length each, installed in a FODO lattice with 12 m cell length. The emittance contribution from the wigglers can be adjusted in a range  $\epsilon_{x,wiggler}=2.5$  to  $8\times 10^{-6}$  m-rad by varying the horizontal beta function.

DESCRIPTIONS OF THE FOUR MACHINES AT 500 GEV C.M.

TABLE 3.9

Parameters for the TESLA positron damping ring. Where different, values for the electron damping ring are given in parentheses.

Energy $E$	5 GeV
Circumference $C$	17 km
Horizontal extracted emittance $\gamma\varepsilon_x$	$8 \times 10^{-6}$ m·rad
Vertical extracted emittance $\gamma\varepsilon_y$	$2 \times 10^{-8}$ m·rad
Injected emittance $\gamma\varepsilon_{x(y)}$	0.01 m·rad ( $10^{-5}$ m·rad)
Number of damping times $n_\tau$	7.2 (4.0)
Cycle time $T_c$	0.2 s
Damping time $\tau_d$	28 ms (44 ms)
Number of bunches $n_b$	2820
Bunch spacing $\Delta\tau_b$	20 ns
Number of particles per bunch $N_e$	$2.0 \times 10^{10}$
Current	160 mA
Energy loss/turn	21 MeV (14 MeV)
Total radiated power	3.2 MW (2.1 MW)
Tunes $Q_x, Q_y$	72.28, 44.18
Chromaticities $\xi_x, \xi_y$	-125, -68
Momentum compaction $\alpha_c$	$1.2 \times 10^{-4}$
Equilibrium bunch length $\sigma_z$	6 mm
Equilibrium momentum spread $\sigma_p/P_0$	0.13%
Transverse normalized acceptance $A_{x y}$	0.05 m
Momentum spread acceptance $A_p$	$\pm 1\%$

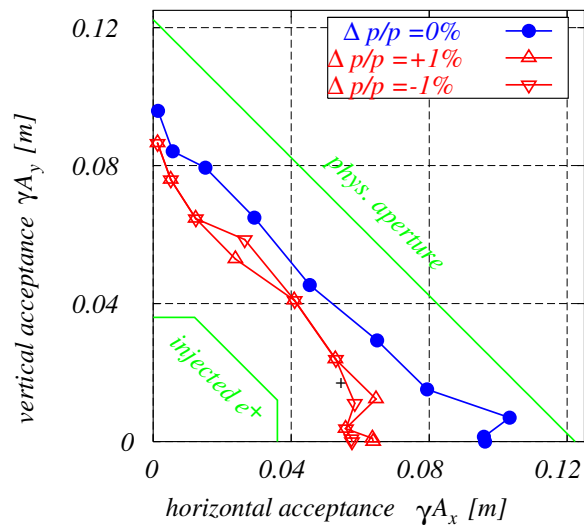


FIGURE 3.14. Dynamic acceptance of the damping ring. The simulations include quadrupole and sextupole alignment errors which result in an average emittance coupling of 1%, and the real physical aperture as the maximum amplitude limit. The phase space volume of the incoming beam as defined by acceptance of the positron pre-accelerator is also shown.

The single particle beam dynamics have been investigated assuming 0.1 mm rms position errors and 0.2 m-rad rms roll angles for the magnets and 10  $\mu\text{m}$  resolution for the beam position monitors. The dynamic acceptance obtained from tracking simulations is larger than the required 0.05 m (normalized) over the  $\pm 1\%$  range of momentum deviation (Figure 3.14). The small emittance ratio  $\epsilon_y/\epsilon_x=0.2\%$  requires minimization of betatron coupling and spurious vertical dispersion in addition to the usual standard orbit correction. Correction of the coupling can be done with a set of skew quadrupoles, whereas the dispersion correction can be done systematically by measuring difference orbits with shifted rf frequency or empirically by tuning dispersion bumps. Once a “golden orbit” is established, it must be maintained at a level of 10  $\mu\text{m}$  BPM resolution. From the expected diffusive ground motion, this requires orbit correction to be applied once every few minutes, which is not problematic. A possibly harmful effect on the orbit and emittance stability could also arise from magnetic stray fields in the tunnel varying with time. At present such effects are not quantitatively sufficiently well known. Possible counter-measures would be magnetic shielding of the vacuum pipe and/or a faster orbit correction feedback.

The unusually large circumference to energy ratio together with the small beam emittance causes the incoherent space charge tune shift to reach a value ( $\Delta Q_y=0.23$ ) uncommon for high energy electron storage rings. In a collider ring like LEP the total beam-beam tune shift has a similar value and the ring has operated routinely with an emittance ratio of 0.5%. The situation in the damping ring is different in two respects: first, the space charge effect is spread over the entire length of the ring instead of localized in a few positions (collision points). This practically eliminates the resonances which are present in the collider case. Second, in the damping ring the tune shift is modulated at twice the synchrotron frequency, because the charge density and thus the tune shift depends on the

longitudinal position of a particle in the bunch. Depending on the choice of tunes, this can lead to a crossing of low order resonances (in particular  $Q_x = Q_y$ ) and to an increase of the vertical betatron amplitude. This effect has been observed in simulations in which the space charge effect was included. In order to reduce the tune shift, a closed betatron coupling bump is inserted over the length of the two long straight sections, which transforms the flat beam into a round one. Inside this insertion, the particle motion is characterized by a rotating mode in 4D phase space. The closure of the bump is insensitive to phase errors such as arising from the lattice chromaticity, as long as they are equal in  $x$  and  $y$ . The space charge tune shift is reduced by almost one order of magnitude and simulations including the coupling transformation show that there is no vertical blow-up, for the nominal design parameters and even for a case with the horizontal emittance reduced by factor of 4.

The rf system has to provide a circumferential voltage of 54 MV and deliver an average power of 3.2 MW to the beam. A system of 12 single cell 500 MHz superconducting cavities very similar to the ones in operation at CESR is used. The strong higher order mode damping in this approach avoids problems with HOM driven multibunch instabilities. Therefore only a low bandwidth feedback system which cures the unstable mode driven by the resistive wall impedance is required. Regarding single bunch instabilities, the design bunch charge is safely below the limits for turbulent bunch lengthening or transverse mode coupling.

The fast beam-ion instability has been investigated with simulations. With a  $N_2$  equivalent vacuum pressure of  $10^{-9}$  mbar, the electron bunch train is found to remain stable.<sup>2</sup> A detailed investigation of the electron cloud instability for the positron beam has not yet been done.

### 3.1.4.4 Bunch Compressor

The bunch compressor provides a reduction of the bunch length by a factor of 20 (from 6 to 0.3 mm) prior to injection of the beam into the main linac. It consists of three standard accelerator modules operating at a gradient of 23.8 MV/m and with a phase of  $113^\circ$  relative to the bunch center, and a 90 m long wiggler-type lattice with a momentum compaction of  $R_{56}=0.215$  m. Incoherent and coherent synchrotron radiation effects have been investigated, the resulting growth of the horizontal emittance is less than 1%. The final energy spread at the exit of the compressor is 2.7% rms. The compressor section is followed by a beam diagnostics and coupling correction section. It is thought that this section together with the compressor lattice can be used for pre-linac beam collimation. A detailed study of this collimation system has not yet been performed.

Between the damping ring extraction and the compressor a spin rotator section is inserted. It uses a pair of solenoids interleaved with an  $8^\circ$  bending magnet and is capable of adjusting the spin polarization vector in any direction of solid angle<sup>3</sup>. The betatron coupling effect of the solenoids is cancelled by means of a  $-I$  transformation between the solenoids. The residual emittance growth due to chromaticity is 1% at maximum solenoid strength.

<sup>2</sup>The simulations were performed for a beam at equilibrium emittances and without the coupling bump in the straight sections. A refined analysis done during the ILC-TRC process showed that a vacuum pressure of  $10^{-10}$  mbar is necessary in the straight sections.

<sup>3</sup>Note that for longitudinal polarization at the IP the spin at injection into the linac must have a vertical component, because, due to the curvature of the earth, it is rotated in the main linac.

### 3.1.5 Beam Delivery System

#### 3.1.5.1 Basic Layout and Optics

The TESLA BDS for the primary  $e^+e^-$  IR is about 3.3 km in length (linac to linac). The IR itself sits slightly off-center, with the  $e^-$  and  $e^+$  delivery systems being 1759 m and 1677 m in length respectively. The slight asymmetry is due to the undulator-based  $e^+$  source at the exit of the  $e^-$  linac. From the first bend magnet in the switchyard both lattices are identical. The system is laid out for a maximum beam energy of 400 GeV.

Figure 3.15 plots  $\sqrt{\beta_{x,y}}$  and the dispersion function ( $D_x$ ) for the BDS ( $e^-$ ). Figure 3.16 shows the geometry of the electron BDS, including the Fast Emergency Extraction Line (FEXL), and an indication of the location of the positron source system. The IP has a transverse offset with respect to the linac of 1.82 m, and the net bending angle is zero. The various modules which separate out the functionality of the BDS are:

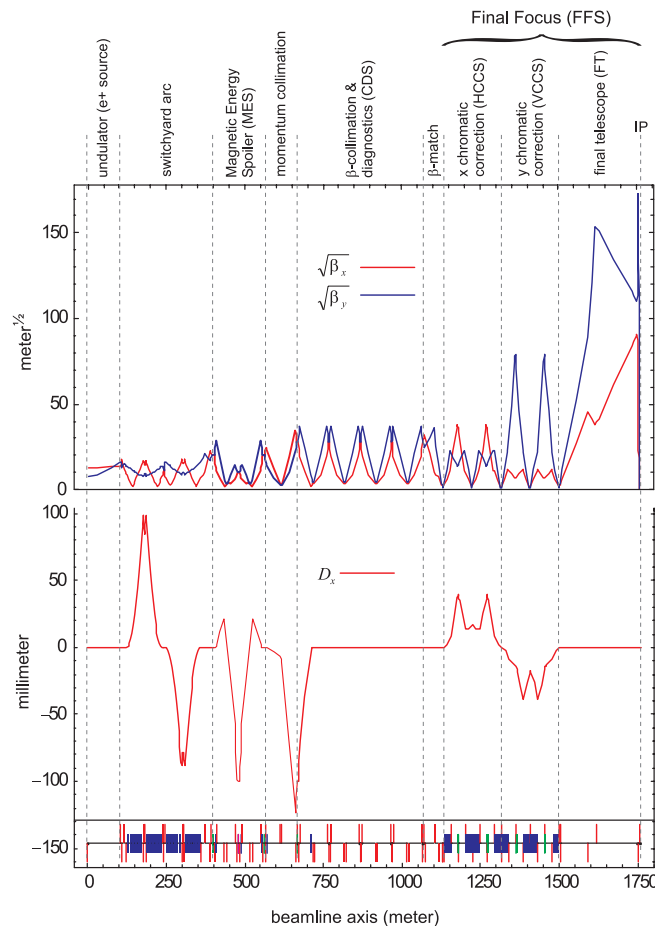


FIGURE 3.15. Optics functions for the TESLA BDS ( $e^-$ ).

## DESCRIPTIONS OF THE FOUR MACHINES AT 500 GEV C.M.

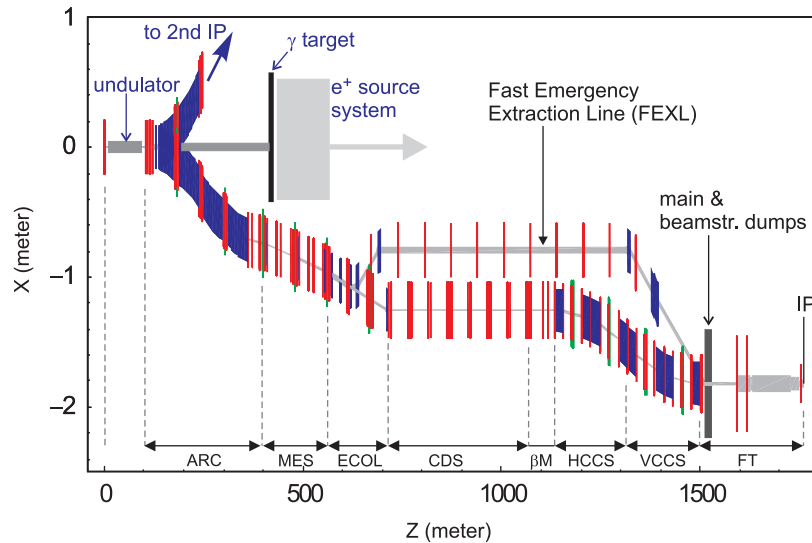


FIGURE 3.16. Geometry of the primary  $e^-$  BDS from linac to IP.

**$e^+$  Source Undulator:** Contains space for the  $e^+$  source undulator (Section 3.1.4).

**Switchyard Arc:** A double bend achromat arc which acts as a switch to a second IR and allows enough clearance for the  $e^+$  source photon target (Section 3.1.4). The emittance growth due to synchrotron radiation is negligible at 250 GeV beam energy, but it adds  $\Delta\epsilon_x = 1.1 \times 10^{-6}$  m to the normalized horizontal emittance at 400 GeV.

**Magnetic Energy Spoiler (MES):** A dispersive section containing non-linear elements which “blow up” the beam at the downstream energy collimator in the event of a large energy error. It works in the following way: an octupole positioned at a high linear dispersion point generates a  $3^{rd}$  order dispersion which causes the off-energy beam to pass off-axis through a downstream skew sextupole. The sextupole then generates horizontal to vertical coupling which increases the vertical beam size on the collimator. The beam size magnification is a factor of 6 for an energy deviation of  $-2\%$ , which protects the collimator from damage when hit by several bunches in the train—this gives sufficient time to trigger the fast emergency dump kickers which send the rest of the beam onto the beam dump through the extraction line (see below).

**Momentum Collimation:** A point of high dispersion where the primary energy collimator will be placed.

**Collimation and Diagnostics Section (CDS):** A repetitive lattice where a series of spoilers and absorbers are used to collimate the beam halo. This section provides relatively high beta ( $\sim 1000$  m) points  $45^\circ$  apart in phase advance and also supports the emittance measurement station. The required transverse collimation depth is defined by the apertures in the interaction region and amounts to  $12\sigma_x$  and  $74\sigma_y$ , energy collimation is set at  $\pm 1.5\%$ .

**$\beta$ -Match:** Matching from the CDS to the entrance (image point) of the Final Focus System.

**Final Focus System (FFS):** A second-order achromatic telescope system which focuses the beam at the IP. The optics uses two pairs of non-interleaved sextupoles, very similar to the design of the FFTB successfully tested at SLAC. The final transformer, which provides the necessary beam size demagnification at the IP, has been increased in length in order to allow a clear extraction path for the beamstrahlung to the main beam dump hall, about 250 m from the IP. The momentum bandwidth of the system is  $\pm 0.4\%$ , sufficient for the incoming beam energy spread ( $1.6 \times 10^{-3}$  rms for electrons and  $0.6 \times 10^{-3}$  rms for positrons, respectively).

**Fast Emergency Extraction Line (FEXL):** This beam line is primarily intended to extract the remainder of the bunch train safely to the beam dump in the event of a machine protection trip. The latter can be triggered by, for example, large orbit offsets at high dispersion or large beta points, enhanced loss rates at collimators or failure of components (especially power supplies) during the beam pulse. Emergency extraction of the beam is provided by a 200  $\mu\text{rad}$  fast kicker followed by a 6 mrad septum magnet, with a delay of no more than a few bunches. In the initial machine commissioning phase and possibly later for dedicated machine studies a DC magnet can be used in order to permanently direct the beam to the dump instead of passing it through the final focus and interaction region.

### 3.1.5.2 Interaction Region

The layout of the IR is shown in Figure 3.17. The most important components are:

- The cryostat housing the final superconducting quadrupole doublet
- One stripline and two cavity beam position monitors (BPM), which are primarily used by the inter-bunch fast feedback system
- A laser interferometer for single beam profile measurement at 0.8 m from the IP
- The instrumented mask constructed from high  $Z$  material to absorb most of the  $e^+e^-$  pairs and their secondaries
- One luminosity monitor (pair counter) on each side of the IP located at the lowest aperture radius of 1.2 cm on the inner mask

In the beam direction, the aperture limitations are set by the forward cylindrical mask of 24 mm diameter housing the pair luminosity monitor, and by the superconducting quadrupole doublet itself, consisting of a 1.7 m and a 1.0 m long quadrupole ( $dB_y/dx=250$  T/m), with an inner diameter of 48 mm.

The beam-beam interaction can be characterized by the disruption parameter  $D_y$  and the beamstrahlung parameter  $\Upsilon$ . The former is defined as the ratio of bunch length to focal length of the beam-beam space charge force, which tends to decrease the beam size during bunch collision and therefore enhances the luminosity by a factor  $H_D$  with respect to the nominal geometric luminosity. For TESLA the disruption effect is strong ( $D_y \sim 25$ ), which

## DESCRIPTIONS OF THE FOUR MACHINES AT 500 GEV C.M.

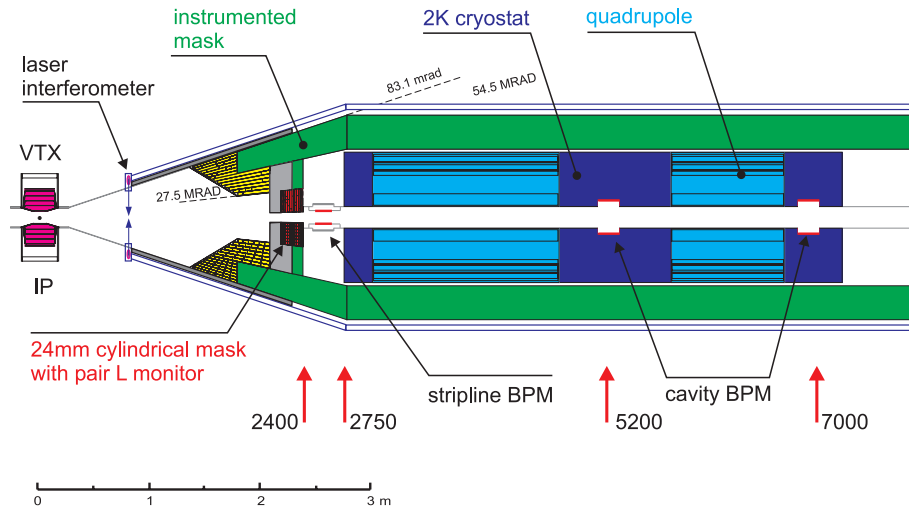


FIGURE 3.17. Interaction region layout.

has consequences for luminosity stabilization, as discussed in Section 3.1.5.4. The enhancement factor can be optimized by shifting the waist position to  $0.8\sigma_z$  before the position of the IP: in this case  $H_D=2.1$ .

The beamstrahlung parameter relates the beamstrahlung photon energy to the beam energy, the small value  $\Upsilon=0.06$  (0.09) at 500 (800) GeV indicates that beamstrahlung is essentially in the classical regime. The average number of photons radiated per electron (positron) is 1.6 and the typical photon energy a few GeV. The associated luminosity spectrum  $d\mathcal{L}/d\sqrt{s}$  is characterized by a peak close to the nominal center of mass energy and a low-energy tail (see Figure 3.18). The fractional luminosity in the 99.5–100%  $E_{cm}$  energy bin amounts to 58%.

A small fraction of the beamstrahlung photons creates  $e^+e^-$  pairs (about  $10^5$  particles per bunch crossing with typical energy of a few GeV). The Tungsten mask shown in Figure 3.17 shields the detector from background radiation generated by the pairs. The inner part of the cylindrical mask is equipped with a counter which can be used as a fast luminosity detector. With this monitor a complete scan of relative luminosity with a resolution of about 1% can be performed within a single beam pulse. The parameters scanned can be, for example, relative beam position and angle at the IP, waist position or spurious dispersion.

### 3.1.5.3 Beam Extraction and Dump

The head-on colliding beams are separated outside the IR by a 20 m long electrostatic deflector. A magnetic field is superimposed on the electric field such as to zero the deflection for the incoming beam. The total deflection angle for the outgoing beam is 0.8 mrad in the vertical plane (downward). The angle is further increased to a total of 15 mrad by subsequent septum and dipole magnets. At the position of the main beam dump (250 m from the IP) the outgoing beam has reached a vertical separation of about 2 m from the incoming beam. Furthermore, the downward deflection reduces the muon

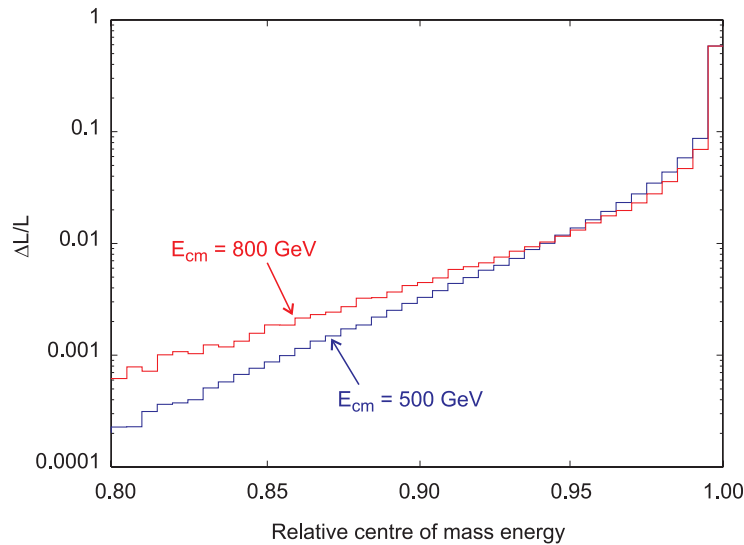


FIGURE 3.18. Luminosity spectra for 500 GeV and 800 GeV center of mass energy.

radiation at the surface to a safely acceptable level. The beam extraction line is equipped with protective collimators in front of some of the magnets to shield them from losses of particles in the low energy tail of the spent beam. The total losses between the IP and the dump amount to 0.1% of the beam power. The optics of the extraction line is designed to provide a minimum beam cross section of  $0.4 \text{ mm}^2$  in the worst case of a non-colliding beam. This together with a slow beam sweeping system guarantees to keep the temperature rise in the water dump below  $40^\circ\text{C}$  and the particle density on the dump entrance window an order of magnitude below the long-term failure limit. The beam dump system requires a sophisticated water preparation plant in order to handle the chemical and radiological effects in the water in the absorber vessel. In addition, the dump hall is shielded by 4 m of heavy concrete to avoid neutron activation of the surrounding soil and ground water.

The beamstrahlung is transported to the main dump hall essentially without losses (less than 50 W out of 360 kW total power). About 90% of the power is absorbed in the beamstrahlung dump at 250 m, roughly 40 kW of power escape through the hole in the absorber required for passage of the incoming beam. This remaining power is absorbed after the beamstrahlung photons are separated from the incoming beam by the dipole magnets of the FFS.

### 3.1.5.4 Luminosity Stabilization

Maintaining the luminosity stable at the design value has essentially two aspects regarding the BDS: first, the beams must be kept in collision at the IP and second, spot size dilution must be avoided. Both issues are much more severe in the vertical plane than in the horizontal plane, and the latter will be ignored in the following.

The tolerances for relative offset and angle at the IP are tight as a result of the high disruption parameter, which gives rise to the so-called single bunch kink instability, a

special version of the two-stream type of collective instabilities. The effect of this instability is that initial relative displacements of the bunches or deformations (such as the “banana” shape resulting from wakefields in the linac) are amplified during collision. In linear approximation the growth in oscillation amplitude can be shown to be exponential with a rate proportional to  $\sqrt{D_y}$ . The sensitivity of the luminosity to offsets and angles has been studied with beam-beam simulations. It turns out that in order to limit the luminosity reduction to less than 10% the orbit at the IP must be stabilized within one tenth of a sigma in both offset and angle (without the instability one would naively expect this tolerance to be about half a sigma).

The expected orbit jitter amplitude, generated by quadrupole vibration in the BDS, has been derived from a ground motion model based on measurements at HERA. The HERA ring is built about 15 m underground in the North-West region of the city of Hamburg. Several main roads with usually heavy traffic pass nearby or even over the ring tunnel. One may therefore consider the HERA data as a worst case (upper limit) scenario for the orbit stability predictions in TESLA.

The rms amplitude of ground motion measured in the HERA tunnel amounts to about 70 nm at frequencies above 1 Hz (*i.e.*, integrated over the spectrum) and to about 20 nm above 5 Hz. In order to accurately determine the effect on the orbit, the spatial correlations of the ground motion must also be known. Measurements of the coherence of the ground motion as a function of distance have been performed with a pair of seismometers. From these the relative motion of two points at distance  $s$  can be derived. The result of the analysis for the case of frequencies at and above 5 Hz are shown in Figure 3.19 as an example. From these data a relative ( $\pi$ -mode) vibration amplitude of the two final doublets (with a separation of  $\sim 8$  m) of about 10 nm can be concluded, which alone yields a pulse-to-pulse relative orbit jitter of  $2\sigma_y$  at the IP. Taking into account the other quadrupoles in the BDS it is estimated that the orbit jitter which must be handled by the fast orbit feedback amounts to about  $10\text{--}30\sigma$  in offset and  $2\sigma$  in angle at the IP. The fast angle feedback uses a BPM installed at a high beta point in the FFS and a kicker magnet at appropriate phase upstream from the FFS. The specified BPM resolution is  $1\ \mu\text{m}$  for the required  $0.1\sigma$  stabilization in angle at the IP. The angle jitter produced by quadrupoles downstream from the BPM is negligible. The offset feedback makes use of the strong beam-beam deflection which bunches colliding with an offset receive (about  $5\ \mu\text{rad}$  for  $0.1\sigma_y$  offset). This orbit kick is measured by BPM's on either side of the IP. The specified BPM resolution is  $5\ \mu\text{m}$  and the time resolution must be  $<15\ \text{ns}$  to separate incoming from outgoing bunches.

Orbit variations due to quadrupole vibrations are also a source of beam size dilution, caused by dispersive and  $xy$  coupling effects. It is found that with an uncorrelated quadrupole motion of 70 nm rms the reduction in luminosity amounts to 12% of the design value. This effect can be reduced by an order of magnitude by actively stabilizing the few most sensitive quadrupoles. An actively stabilized magnet support was tested and reduced the rms vibration amplitude to 20 nm at frequencies above about 1 Hz. On a longer time scale, diffusion-like ground motion becomes important. The so-called *ATL*-rule states that the mean square relative motion of two points is proportional to time and the distance between the points. From long-term orbit drift measurements in HERA a constant  $A=4\times 10^{-6}\ \mu\text{m}^2\text{m}^{-1}\text{s}^{-1}$  has been derived. Using this model, simulations for the BDS show that with a BPM resolution of  $1\ \mu\text{m}$  a simple one-to-one orbit correction applied once

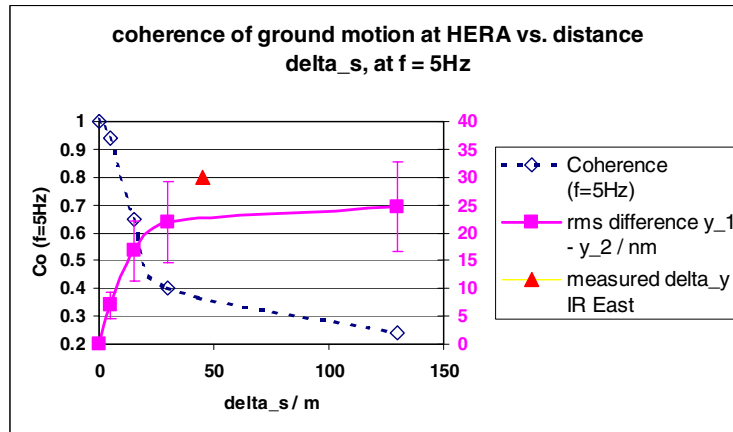


FIGURE 3.19. Relative rms vibration amplitude ( $f \geq 5$  Hz) in the HERA tunnel as a function of distance between the points where the seismometers were placed (squares, right hand scale) and the measured coherence (diamonds, left hand scale). These data were taken in 1995. A more recent (2000) result for the difference amplitude across the interaction region East is also shown (triangle).

every 5 s (25 linac pulses) limits the luminosity reduction to about 2%. On a time scale of days an additional dispersion tuning must be applied.

As mentioned previously, correlated emittance growth, *i.e.*,  $z - y$  and  $z - y'$  correlations in the bunches have a stronger effect on the luminosity than uncorrelated growth because of the kink instability. This effect and its detailed dependence on various parameters is being studied in great detail in collaboration with the CLIC and NLC groups. Some of the beam-beam simulation results obtained for TESLA are discussed in what follows.

Calculations of the luminosity were performed assuming uncorrelated vertical emittances of  $2.4 \times 10^{-8}$  m-rad and  $2.2 \times 10^{-8}$  m-rad at the IP for electrons and positrons, respectively (electrons have a larger energy spread after passing through the  $e^+$  source wiggler and will therefore experience more dispersive dilution in the BDS). To the uncorrelated phase space distribution  $z - y$  and  $z - y'$  correlations are added which reflect the functional form of the transverse and longitudinal wakefields in the linac. The two contributions are assumed to have equal amplitude, but independent random phase in  $y, y'$  space for both of the colliding bunches. The beam-beam simulation is repeated for many random seeds of the phases. The resulting average luminosity as a function of correlated emittance growth is shown in Figure 3.20. One notices that the luminosity reduction for 1% correlated emittance dilution is as large as 15%, in contrast to a 0.5% reduction expected for an uncorrelated dilution of equal magnitude. For larger relative dilution, this difference becomes smaller but remains significant.

The simulations reveal that even though the initial charge distributions of the two colliding bunches have zero average offset, there is often (depending on the phases of the correlated distortions) a net deflection angle for the bunches present after collision. This will in practice be interpreted by the IP feedback as a “real” offset, and appropriate re-steering of the orbit will be generated. Taking this into account the simulation yields a systematically

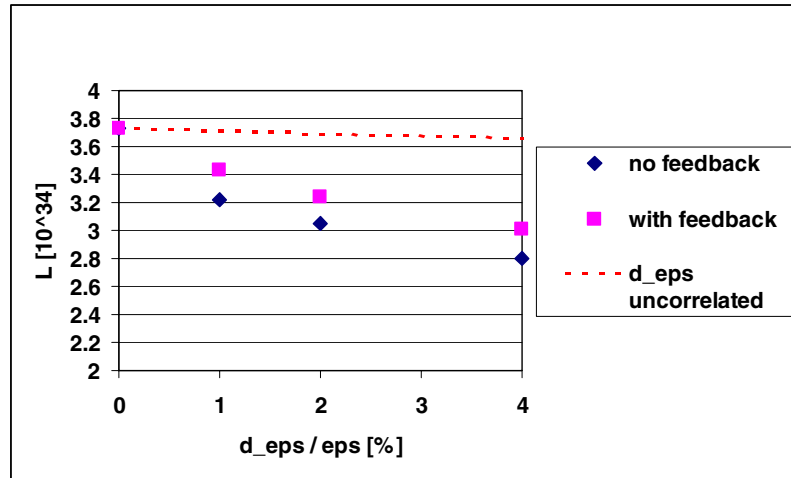


FIGURE 3.20. Luminosity as a function of correlated emittance growth obtained from beam-beam simulations (see text). The diamonds are the results without feedback, the squares with IP steering feedback “on.” The dashed line denotes the expected luminosity if the emittance growth was uncorrelated.

higher luminosity, but only a fraction of the luminosity loss is recovered (see Figure 3.20). When empirically re-steering the bunches in both offset and angle, most of the luminosity can be recovered.

In order to achieve the design luminosity, the correlated emittance growth has to be kept at the level of 1%. Since the static part of emittance dilution in the linac can be tuned out, using the luminosity as the sensitive parameter to optimize, this tight requirement applies only to the bunch-to-bunch and pulse-to-pulse variations of the wakefield effects. According to the main linac studies, a 1% limit for the dynamic part of correlated emittance dilution is achievable, although marginally.

One possibility to reduce the sensitivity of the luminosity to correlated emittance growth is a reduction of the disruption parameter by shortening the bunches. An alternative parameter set with  $\sigma_z$  reduced by a factor of 2 to 0.15 mm,  $\beta_x$  increased from 15 to 20 mm and  $\beta_y$  decreased from 0.4 to 0.3 mm has been investigated. The beam-beam simulations show clearly (Figure 3.21) a more stable luminosity than for the reference parameters. This also applies to the required accuracy for IP steering, where the tolerance could be relaxed from  $0.1\sigma$  to  $0.3\sigma$  in offset and angle. The price to pay for such a modification is a higher beamstrahlung ( $\delta_B$  increases from 3.2% to 3.9%) and a second stage bunch compressor. In view of the relatively limited uncertainty in the achievable luminosity due to the kink instability effect, which is not more than about 10 to 15% for the reference parameters, the need for such a design modification may be considered questionable.

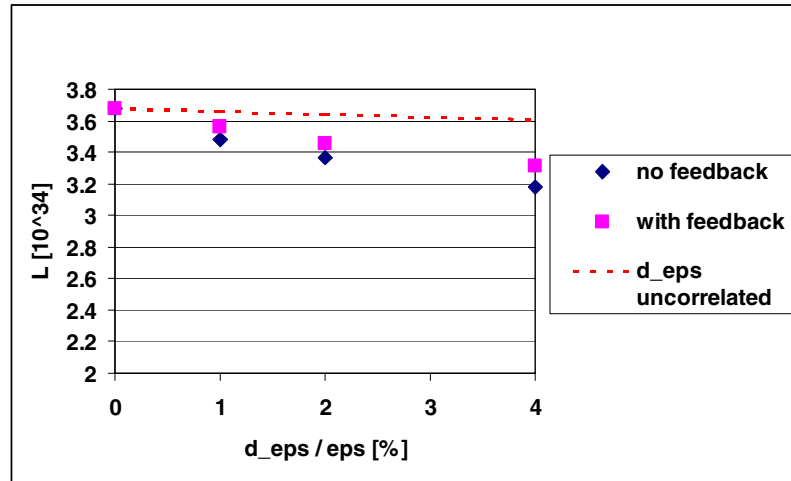


FIGURE 3.21. Same as Figure 3.20, but for a modified parameter set with reduced disruption parameter (see text).

## 3.2 JLC-C

### 3.2.1 Introduction

JLC-C is a version of an electron-positron linear collider based on normal-conducting, C-band rf technology at 5.712 GHz. The development of the JLC started in 1986 for a TeV-range collider project with X-band (11.424 GHz) as the most probable Main Linac frequency. Since around 1991, C-band has also been studied as an alternative main linac frequency, putting more emphasis on the lower end of the energy range desired for the linear collider,  $E_{CM} \leq 500$  GeV, and on the possibility of earlier construction [3].

Obviously, higher frequencies are more advantageous for attaining higher accelerating gradients and hence higher beam energies within a given site length. However, there is no intrinsic advantage, with respect to the luminosity, of going to higher frequencies at a given maximum wall-plug power. On the other hand the technical issues, such as the high current density in the klystrons and the tolerances related to the accelerator structure, become more serious as the frequency goes higher. The choice of C-band is a trade-off between the gradient requirement and the technical problems. Thus the motivation for the C-band collider is technical conservativeness. In the design process we did not pursue extremely high luminosity but instead tried to keep every parameter within a safe region. For instance the beam voltage of the klystron has been chosen to be as low as 350 kV, giving relatively low power efficiency ( $\sim 50\%$ ), which is one of the reasons why the luminosity per unit wall-plug power is lower than in the X-band design. We expect, however, that the actual integrated luminosity, taking into account the possible machine tuning and down time, will not be lower.

We have so far studied the rf system of the C-band collider. Studies of other parts such as injectors and the beam delivery specific to the C-band linacs have not yet been done mainly due to manpower but also because we do not foresee major difficulties in these parts compared with X-band. Therefore, we only describe the C-band rf system here.

### 3.2.2 Parameters

The overall C-band designs so far published have emphasized the lower end of the energy range desired for the linear collider, 500 GeV c.m., and have not described the upgrade path to higher energies in detail. It has been assumed that a double-power klystron can be developed and that the site can be lengthened by factor  $\sqrt{2}$  to reach 1 TeV. However, the feasibility of the double-power klystron is not obvious. In addition, the progress of the X-band technology has shown that an X-band collider will be possible within a few years.

Thus, our strategy for C-band is that a C-band collider should be built as early as possible and later, when the X-band technology has matured, an X-band extension should be added to reach 1 TeV. In keeping with this scenario we have chosen a parameter set compatible with the later addition of an X-band extension. In fact the beam parameters are basically identical to those in the X-band design. The adaptation to the X-band beam parameters does not actually reduce the luminosity of the C-band collider. In this respect the key parameter is the beam train length. Normally, the optimum train length is longer in lower frequency linacs. However, it is even shorter in the old designs of the C-band than in the X-band collider, basically because a short train length is preferred for the C-band rf pulse compressor. Thus, we do not lose luminosity by adopting the X-band beam parameters.

The important parameters of the C-band collider are summarized in Table 3.10 and Table 3.11. Although the center-of-mass energy in the megatable is 500 GeV, here we present the parameter set for 400 GeV c.m. because that energy seems to be enough for the first stage experiments on Higgs and top quark physics, and because the shorter length of the C-band linacs is preferred when they are to be extended later with X-band for higher energy within a limited site length. This choice is obviously tentative. It may change if the physics situation changes.

In this table the DLDS pulse compression system is assumed for the X-band section in the energy upgrade stage. We can replace it with the SLED-II system but at least several years are expected from the first to the second stage so that the DLDS technology is expected to be mature.

Since the study of compatibility with an X-band extension has started only recently, the parameters that appear in the following sections are not completely consistent with those in Table 3.10 and Table 3.11. In particular, the rf pulse length and the beam train length in Table 3.10 are longer by up to 4/3 compared to (for example) the klystron pulse length in the following sections. We believe the differences will not cause serious changes to the hardware already developed.

TABLE 3.10  
C-band and C-X hybrid parameters.

	C Alone	Hybrid C	Hybrid X	Units
Center-of-mass energy ( $E_{CM}$ )	400		1000	GeV
<b>Beam Property</b>				
Initial beam energy ( $E_i$ )	8	8	200	GeV
Final beam energy ( $E_f$ )	200	200	500	GeV
Number of particles per bunch (N)	0.75		0.75	$\times 10^{10}$
Number of bunches per pulse ( $n_b$ )	192		192	
Number of particles per pulse ( $n_b N$ )	144		144	$\times 10^{10}$
Bunch spacing ( $t_b$ )	1.4		1.4	ns
Beam pulse length ( $n_b t_b$ )	268.8		268.8	ns
Repetition frequency ( $f_{rep}$ )	100		100	Hz
Normalized emittance (DR exit) ( $\gamma\epsilon_x$ )	$3 \times 10^{-6}$		$3 \times 10^{-6}$	m-rad
( $\gamma\epsilon_y$ )	$2 \times 10^{-8}$		$2 \times 10^{-8}$	m-rad
R.m.s. bunch length ( $\sigma_z$ )	200		110	$\mu\text{m}$
<b>Main Linac</b>				
Unloaded gradient ( $G_0$ )	41.8	41.8	70	MV/m
Loaded gradient <sup>a</sup> ( $G$ )	31.1	31.1	53.8	MV/m
Active length (each linac) ( $L_{act}$ )		6.11	6.16	km
Wall plug power ( $P_{AC}$ )	140	140	122	MW
AC to rf efficiency ( $\eta_{AC \rightarrow RF}$ )	24.12	24.12	37.4	%
RF to beam efficiency ( $\eta_{RF \rightarrow B}$ )	25.9	25.9	26.7	%
<b>Modulator</b>				
Efficiency ( $\eta_{mod}$ )		67	80	%
Number of modulators (/beam)		1696	285	
<b>Klystron</b>				
Peak power		50.12	75	MW
Pulse length		2.762	1.60	$\mu\text{s}$
Efficiency ( $\eta_{kly}$ )		50	60	%
Number of klystrons (/beam)		1696	2280	
<b>Pulse Compressor</b>				
Type		Diskloaded	SLED-II	
Time compression factor		1/5		
Efficiency ( $\eta_{cmpr}$ )		80		%
Waveguide loss		10		%

*Continued in Table 3.11.*

<sup>a</sup> Includes single/multibunch loading and  $\cos \phi_{RF}$ .

## DESCRIPTIONS OF THE FOUR MACHINES AT 500 GEV C.M.

 TABLE 3.11  
 C-band and C-X hybrid parameters (continued).

	C Alone	Hybrid C	Hybrid X	Units
Center-of-mass energy ( $E_{CM}$ )	400		1000	GeV
<i>Continued from Table 3.10.</i>				
<b>Accelerator Structure</b>				
Structure type	CG choke-mode $3\pi/4$		RDDS $5\pi/6$	
Structure length	1.8		0.9	m
Iris radius ( $a/\lambda$ )	0.171–0.126		0.210–0.148	
(average) ( $\langle a/\lambda \rangle$ )	0.148		0.18	
Group velocity ( $v_g/c$ )	3.60–1.14		5.1–1.1	%
(average) ( $\langle v_g \rangle / c$ )	2.12		2.5	%
Filling time ( $T_f$ )	285		120	ns
Attenuation parameter ( $\tau$ )	0.524		0.511	
Average $Q$ -factor ( $Q$ )	9772		8574	
Shunt impedance ( $r_s$ )	53.7		81.2	M $\Omega$ /m
Number of structures (/beam)	3392		6840	
Peak power into a structure	90.2		85	MW
<b>Interaction Point</b>				
Number of particles per bunch ( $N^*$ )	0.75		0.75	$\times 10^{10}$
Normalized emittance ( $\gamma\epsilon_x$ )	$3.6 \times 10^{-6}$		$3.6 \times 10^{-6}$	m·rad
( $\gamma\epsilon_y$ )	$4.0 \times 10^{-8}$		$4.0 \times 10^{-8}$	m·rad
Crossing angle ( $\phi_{cross}$ )	7		7	mrad
Beta function ( $\beta_x$ )	8		13	mm
( $\beta_y$ )	0.2		0.11	mm
RMS beam size ( $\sigma_x$ )	271		219	nm
( $\sigma_y$ )	4.52		2.3	nm
Disruption parameter ( $D_x/D_y$ )	0.289/17.3		0.08/10.0	
Number of beamstr. photons ( $n_\gamma$ )	1.30		1.3	
Energy loss by bremsstrahlung ( $\delta_{BS}$ )	2.72		8.9	%
Average Upsilon parameter ( $\langle \Upsilon \rangle$ )	0.057		0.29	
Nominal luminosity	7.01		15.7	$10^{33} \text{ cm}^{-2} \text{ s}^{-1}$
Luminosity <sup>b</sup> ( $\mathcal{L}$ )	10.1		25	$10^{33} \text{ cm}^{-2} \text{ s}^{-1}$
Luminosity / 100 MW AC ( $\mathcal{L}/P_{AC}$ )	7.24		9.54	$10^{33}$

<sup>b</sup> Includes pinch effect but does not include the crossing angle.

### 3.2.3 Main Linacs

The C-band rf unit is shown schematically in Figure 3.22. Two 50-MW klystrons, each driven by a separate modulator, are combined in a 3-dB hybrid and compressed to 350 MW by a pulse compressor with disk-loaded coupled cavities to feed four 1.8-m-long accelerator structures.

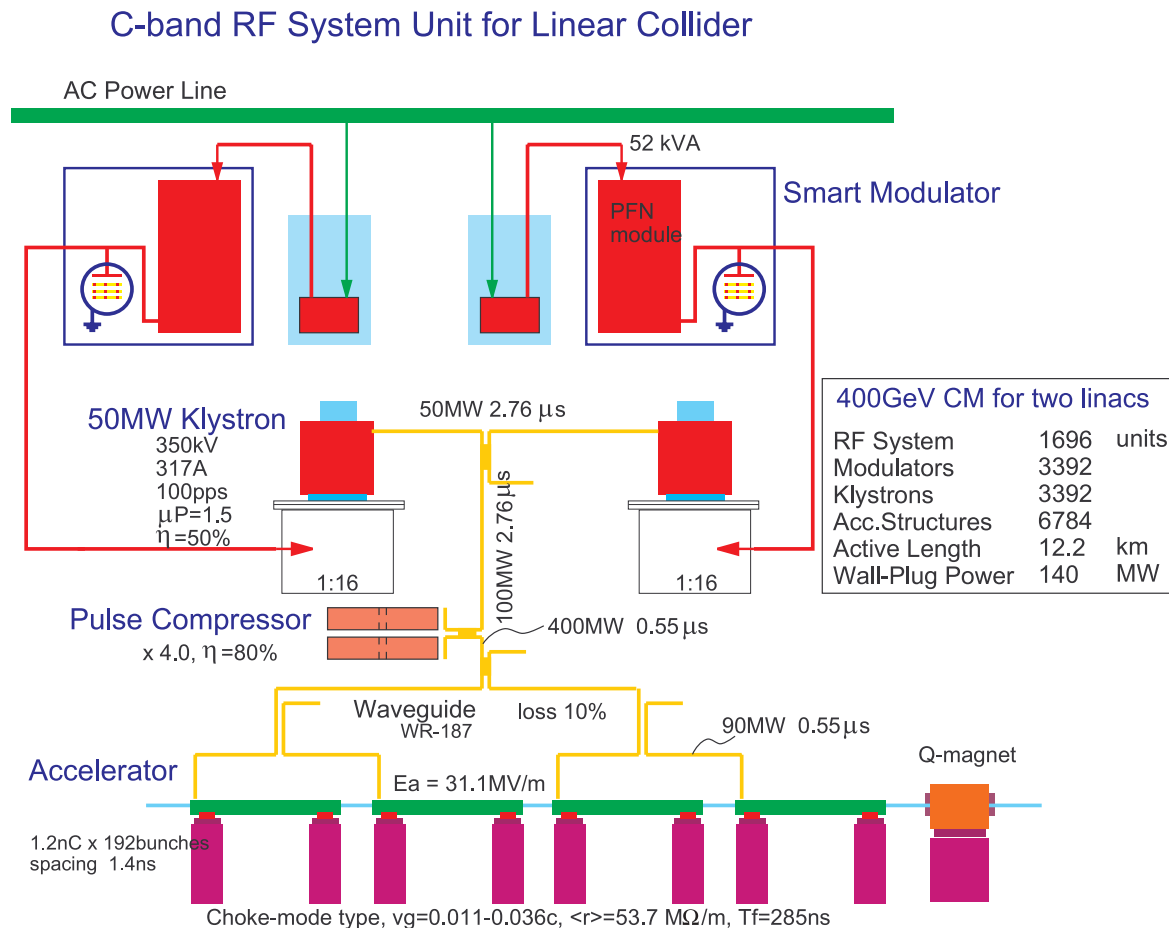


FIGURE 3.22. Schematic diagram of the C-band rf unit.

#### 3.2.3.1 Modulators

In conventional modulator systems the thyatron switch is one of the most troublesome components. Its lifetime is short ( $\sim 3 \times 10^9$  shots) and varies from tube to tube. The protection circuits, consisting of a number of diodes, snubber capacitors, and resistors, occupy a lot of space. Conventional modulator tanks are massive, expensive, and require oil for insulation.

Our modulator for the C-band system is different from conventional ones. The charging power supply is a constant current source using an inverter power supply. The short-circuit

## DESCRIPTIONS OF THE FOUR MACHINES AT 500 GEV C.M.

current is limited below a few amperes by the inverter power supply. The PFN charging starts after a long delay controlled by a master trigger generator, which will provide fault-free operation of the thyatron.

Figure 3.23 is a simplified circuit diagram. The PFN is an 18-stage Guillemin *E*-type *LC* network. We do not need a de-*Q*'ing system to regulate the PFN voltage. There is no bulky thyrite to present the low inverse voltage required for thyatron deionization in the EOLC circuit, owing to the command-charging scheme of the inverter power supply.

Figure 3.24 shows the waveform with the klystron load. The leading edge of the pulse is clean due to the low noise. The peak voltage at the flat top is 350 kV, which is measured with a capacitive voltage divider mounted inside the pulse tank. The pulse width at 75% of the peak voltage is 4.35  $\mu$ s. The rise time (10% to 90%) is 0.96  $\mu$ s. The ripple at the flat top is less than  $\pm 0.5\%$  and the pulse-to-pulse voltage stability is as low as 0.35% owing to the regulation precision of the inverter power supply. The inverse voltage is less than 35 kV which is small enough to guarantee reliable operation of the active components such as the inverter power supply, the thyatron, and the klystron tube. The measured time jitter of the klystron beam pulses at the 350-kV pulse voltage is 1.2 ns.

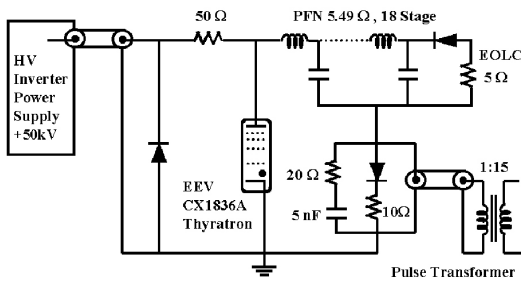


FIGURE 3.23. Schematic diagram of the C-band modulator circuit.

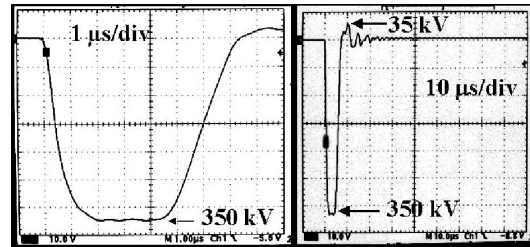


FIGURE 3.24. Output waveform of the modulator.

The efficiency of the present modulator system is 47.9% (85% charging efficiency and 56.4% pulsing efficiency). A relaxation of the ripple requirement, which can be achieved by using a pulse compressor and phase-amplitude modulation, will allow a larger ripple up to 2–3%. We expect to obtain efficiency as high as 67%.

### 3.2.3.2 Klystrons

We have developed and tested 50-MW C-band klystrons (the E3746 series). Figure 3.25 shows a cross-sectional view of the klystron. We constructed two tubes with different output cavities: one with a single gap and the other with a three-cell traveling-wave cavity. The second tube was designed to reduce the electric field gradient at the output cavity and to raise the power efficiency by smoother deceleration of the electron beam.

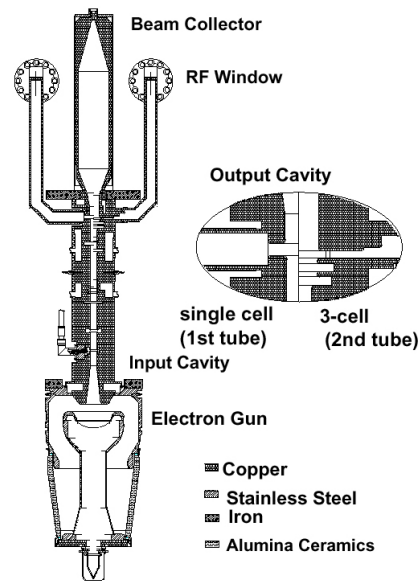


FIGURE 3.25. Cross-sectional view of the E3746 C-band klystron.

The second klystron achieved 54 MW of output power at the 369-kV beam voltage, 2.5- $\mu$ s pulse width and 50-Hz repetition rate in the test performed in 1998. The test results and design parameters are summarized in Table 3.12. Figure 3.26 shows the output waveform from the second tube. Figure 3.27 compares the measured output power and efficiency with the computer simulation using the FCI code. The agreement is extremely good—within 1%.

TABLE 3.12  
Design parameters and test results for the E3746 klystron.

	Design	Test
Output power [MW]	49	53.9
Beam voltage [kV]	350	368.7
Beam current [A]	317	333.0
Drive power [W]	300	323
Power efficiency [%]	44	43.9
RF pulse width [ $\mu$ s]	2.5	2.5
Beam perveance [ $\mu$ A/V <sup>3/2</sup> ]	1.53	1.49
Repetition rate [Hz]	50	50
Solenoid coil power [kW]		4.55

The power consumption of the C-band klystron's solenoid magnet ( $\sim$ 5 kW) is not large compared to the total power consumption. However, by replacing the solenoid magnet with a permanent magnet one can eliminate the DC power supply, the water cooling system and its interlock. This will make the klystron system much simpler.

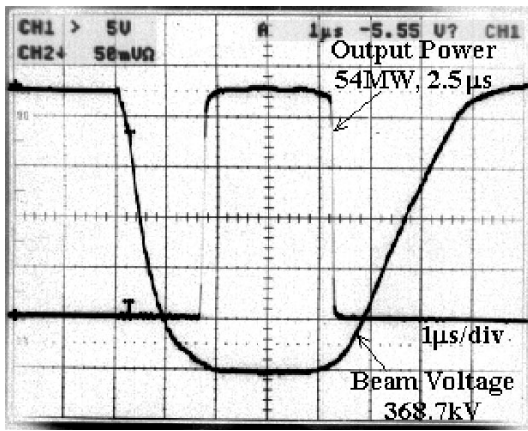


FIGURE 3.26. Output waveform of the klystron.

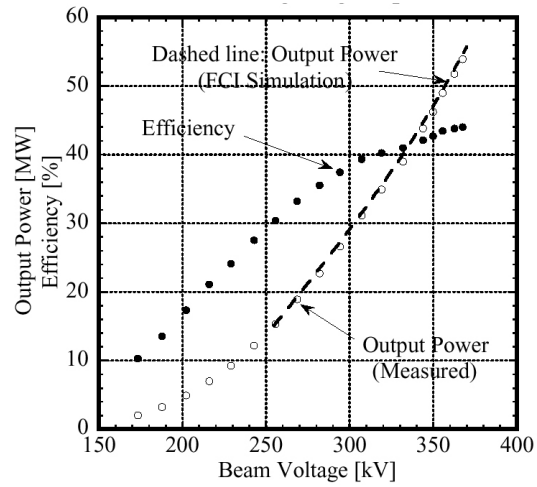


FIGURE 3.27. Output power and efficiency of E3746 klystron. The dashed line is a result of computer simulation using FCI and the circles represent the measured results.

In order to minimize the required R&D for the first C-band PPM klystron, we adopted the same design as the third solenoid-focused E3746 tube, except for the drift tube region. The cutaway view is shown in Figure 3.28 and the specification is summarized in Table 3.13. We chose magnetic stainless steel (Mag-SUS) for the pole-piece material instead of pure iron and neodymium ( $\text{Nd}_2\text{Fe}_{14}\text{B}$ ) as the magnet material. Simply stacking disks alternately of Mag-SUS and OFC, and processing in an HIP vessel filled with pressurized Ar gas at  $1200 \text{ kgf/cm}^2$  and temperature  $800^\circ\text{C}$  for 2 hours, we bonded them in one block by diffusion bonding. No brazing-alloys were used in this process. After machining the rf cavities and beam drift tube on the bonded PPM stack, they were assembled together by conventional brazing.

TABLE 3.13  
Target parameters of C-band PPM klystron.

Output power [MW]	50	Permanent magnet	Neodymium N40A
RF pulse width [ $\mu\text{s}$ ]	2.5	Residual induction, $B_r$ [Tesla]	1.2
Beam voltage [kV]	350	Coercive force, $H_c$ [kOe]	11
Beam current [A]	317	Peak field (on axis, upstream) [kG]	2.0
Power efficiency [%]	48	PPM pitch [mm]	30
Perveance ( $10^{-6}$ ) [ $\text{A/V}^{3/2}$ ]	1.53	Pole-piece	Mag-SUS
Drift tube radius (upstream) [mm]	7.5		Fe+14%Cr+C(20ppm)
(downstream) [mm]	9.0		
Beam radius (upstream) [mm]	5.0		

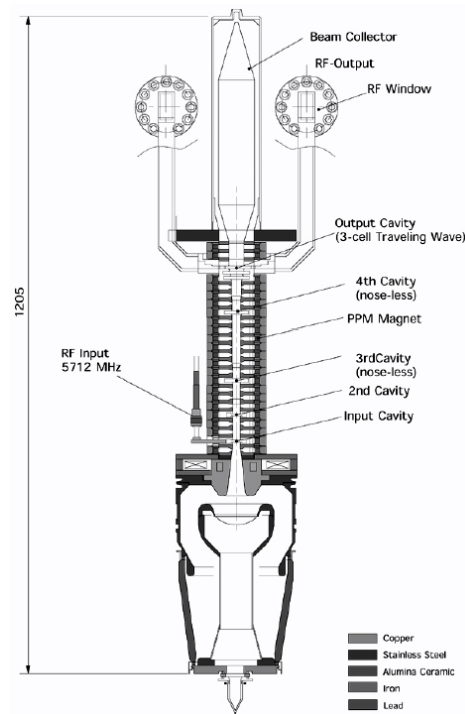


FIGURE 3.28. Cut-away view of the first C-band PPM klystron, TOSHIBA-E3747.

Figure 3.29 shows the waveform of the output power together with the beam voltage and the input drive power. The first C-band PPM klystron generated 37 MW at the 350-kV beam voltage,  $2.5\text{-}\mu\text{s}$  pulse width, and 50-Hz repetition rate. The measured beam loss was less than 1%. Figure 3.30 shows the measured output power as a function of the beam voltage.

A parasitic oscillation was found when the gun voltage exceeded 320 kV. Its frequency was around 5726 MHz, which is in the gain-bandwidth. We believe the oscillation is due to back-streaming electrons from the beam collector, which causes a positive feedback of an rf signal from the output cavity to the input cavity. The second PPM klystron is being designed to avoid this problem.

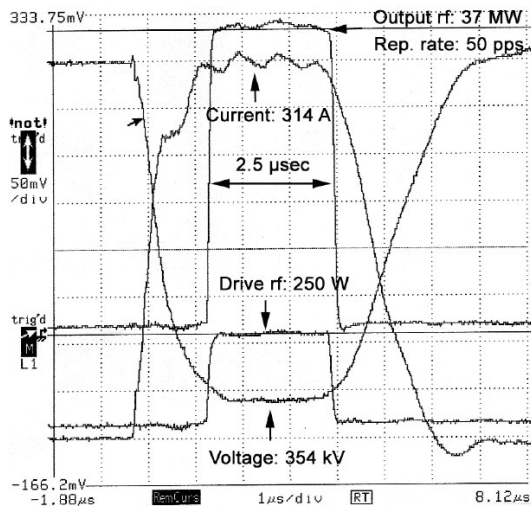


FIGURE 3.29. Output waveform of C-band PPM klystron.

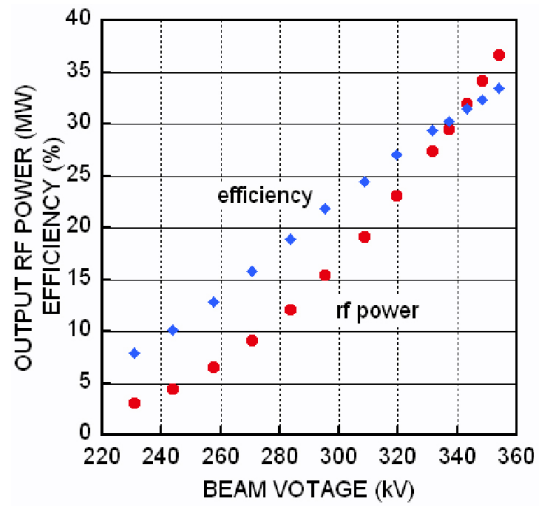


FIGURE 3.30. Output power and efficiency of C-band PPM klystron.

### 3.2.3.3 Pulse Compressor

We use a three-cell coupled-cavity pulse compressor instead of a delay-line type compressor like SLED-II. The cavity is very compact, having a length of 800 mm and a diameter of 160 mm. It is very easy to fabricate at low cost. To compensate for the ringing response associated with the multicell structure, the amplitude modulation is applied to the input power. A cold-test model of this type of pulse compression succeeded in generating a flat pulse in 1997.

In order to obtain higher efficiency we introduced a new scheme of phase modulation. It makes use of the power that otherwise would be wasted during the rise time of the modulator pulse. The system is depicted schematically in Figure 3.31. It consists of a fast phase modulator, a vector rf voltage detector, a solid-state driver amplifier, and a feedback control computer. In this system the voltage detector monitors the power flow at several points: the klystron output, the pulse compressor output, and the output coupler of the accelerator structure. Software computes the deviations from the target values and stores the phase modulation pattern in the memory of the fast phase modulator. The feedback loop is applied to successive pulses to maintain a constant energy gain. The feedback is automatically controlled to compensate for various situations: system failure, temperature change, timing drift, *etc.* In the two-klystron system shown in Figure 3.31 the phase-to-amplitude conversion is performed to flip the input voltage of the rf pulse compressor.

A cold test was performed with the pulse compressor, the modulator (flat-top pulse length 2.0  $\mu$ s) and the E3746 klystron. The resulting power gain is plotted in Figure 3.32. We observed an enhancement of 1.25 due to the phase modulation and obtained a power gain of 3.5. It should be noted that a 2.5- $\mu$ s flat pulse would have been needed to reach this power gain if the phase modulation were not applied.

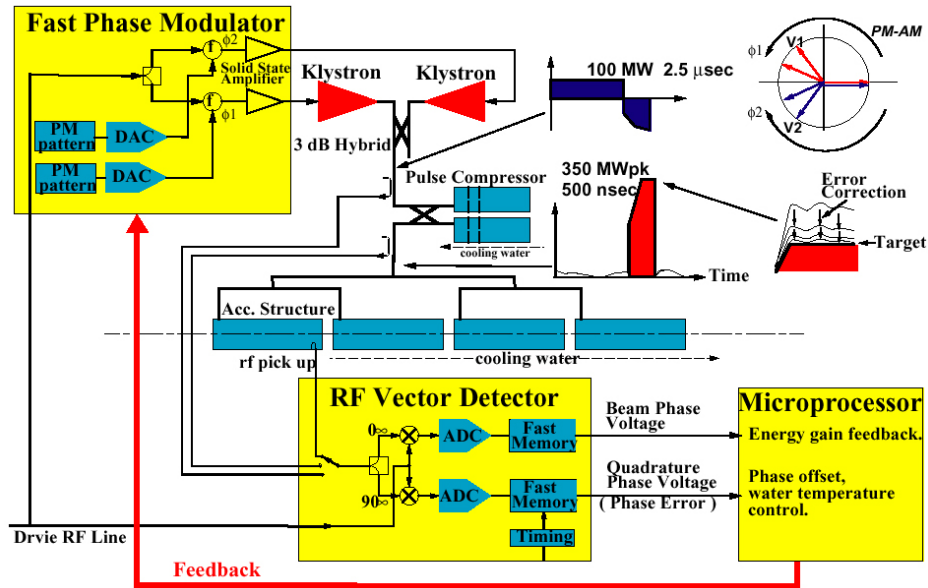


FIGURE 3.31. Schematic diagram of the phase modulation system.

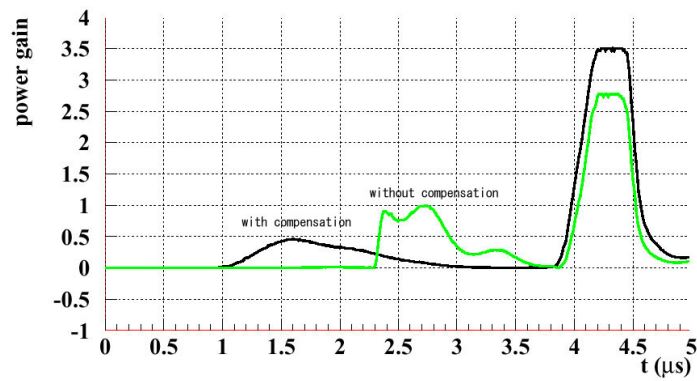


FIGURE 3.32. The power gain of the rf pulse compressor with and without phase compensation.

## DESCRIPTIONS OF THE FOUR MACHINES AT 500 GEV C.M.

The pulse compressor requires the highest  $Q$  value of all the normal-conducting cavities used in linear colliders. In the three-cell design the first and third cavities resonate in  $TE_{01,15}$  and the second cavity resonates in  $TE_{01,5}$ . The theoretical  $Q$  values for OFC are 185,400 and 82,600. The power gain is sensitive to the properties of the third cavity since the microwave energy is stored mainly in that cavity. In particular the shift of the resonance frequency is 10.8 kHz and 6.6 kHz under 1- $\mu\text{m}$  changes of the length and diameter, respectively. In order to limit the decrease of the power gain within 1%, the change of the frequency must be less than 25 kHz, corresponding to a length change of 2.3  $\mu\text{m}$ . If copper is used, then the temperature must be controlled within 0.3°C.

In order to relax the temperature stability requirement we are developing a compressor made of copper-plated super-invar, whose thermal expansion coefficient is smaller than copper by 1/40. A single cell in the  $TE_{01,15}$  mode was constructed using super-invar material made by casting for lower cost. It was low-power tested in 2001. The change of the resonance frequency with temperature was measured. The result was better than that for the copper cavity by a factor of 1/4 but was not fully satisfactory. This is possibly due to the thermal expansion of the copper endplate which was electron-beam welded to the super-invar body. (Copper was chosen because of a thermal conductivity problem.) High power tests will be done soon.

### 3.2.3.4 Accelerator Structure

In the linacs for linear colliders it is an essential requirement to damp the long-range transverse deflecting wave generated by the beam. In 1992, the so-called choke-mode cavity was proposed which is an axisymmetric open cavity. The beam-induced wave is strongly damped by the electromagnetic radiation through a radial line into open space (and is absorbed by an absorbing material) while the accelerating rf wave is trapped inside the cavity by a choke filter. The concept was confirmed in the experimental test performed at ATF-KEK in 1994, where a bunched electron beam was successfully accelerated in a prototype choke-mode cavity designed for S-band up to a gradient of  $\sim 50$  MV/m.

Figure 3.33 shows the C-band model. The whole structure is constructed by stacking axially symmetric cells. The cell body, the annulus of the choke, and the space for the HOM absorber are machined on a copper disk by turning on a lathe. The vacuum seal and mechanical structure are maintained by stacking the cells and plating a copper layer from outside. The SiC ceramic ring is the HOM absorber, and it is mounted in the disk with a metal spring insert (MC Multilum-contact). Since all parts are axially symmetric and can be turned on a lathe, the choke-mode approach has a big advantage for manufacturing compared to other ideas for wakefield damping.

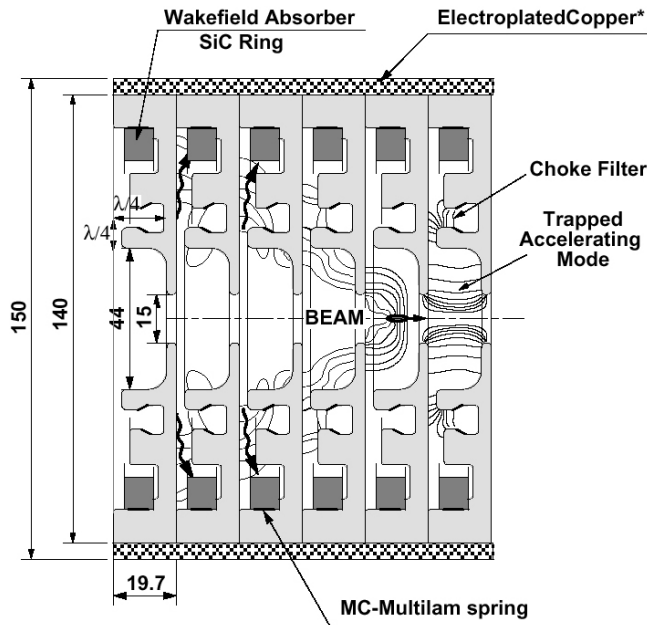


FIGURE 3.33. Cut-away view of the C-band choke-mode structure.

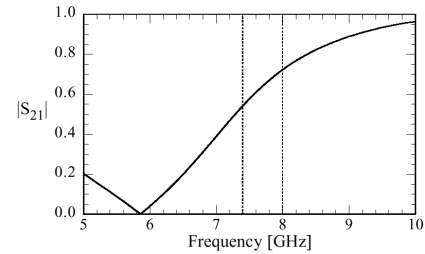


FIGURE 3.34. Dipole transmission of the choke.

The choke-mode concept has solved the multibunch problem but there is still the short-range wakefield problem, which causes tight fabrication and alignment tolerances for high-frequency cavities. The choice of C-band will be reasonable, considering the technical difficulties of tolerances at higher frequencies. The straightness tolerance is  $\pm 50 \mu\text{m}$  (maximum bow) for a 1.8-m structure and the cavity-to-cavity random misalignment tolerance is  $\sim 30 \mu\text{m}$  for an emittance increase of 25%. (These numbers are based on old studies.) However, the effect of the decrease of the charge per bunch from old designs ( $1.1 \times 10^{10}$  to  $0.75 \times 10^{10}$ ) more than compensates the effect of the decrease of the target vertical emittance ( $3 \times 10^{-8} \text{m}\cdot\text{rad}$  to  $2 \times 10^{-8}$ ) so that the tolerance will be even looser.

The frequency of the HOMs is not constant along the structure since we adopt a semi-constant gradient structure. The dimensions of cells, the choke filters, and the absorbers are designed in the following manner.

First, let us describe the optimization of individual cells. A part of the wakefield is reflected at the choke even though the radial line effectively extracts the wakefield. This can be a serious problem if the frequency of the main wakefield component is near the dipole stop-band frequency of the choke. In our case the main contribution to the transverse wakefield comes from  $\text{TM}_{110}$  whose frequency ranges from 7.4 to 8 GHz depending on the iris aperture ( $2a$ ). Figure 3.34 shows the transmission coefficient of the choke. The dominant  $\text{TM}_{110}$  mode is in the region between the two dashed lines. One finds that only 1/3 to 1/2 of the  $\text{TM}_{110}$  power is transmitted to the absorber. Because of this effect a simple matched (no reflection) absorber at the outer end of the radial line does not provide sufficient damping. This problem can be solved by deliberately introducing some reflection to the absorber.

## DESCRIPTIONS OF THE FOUR MACHINES AT 500 GEV C.M.

As shown in Figure 3.33, the absorber is a ring of SiC ceramics of rectangular cross section. This simple shape was adopted for three reasons: (a) it is easy to fabricate, (b) the reflection coefficient of the  $TM_{110}$  mode can be controlled by the width, and (c) the reflection coefficient above  $TM_{110}$  is relatively low. The width of the SiC ring is chosen to optimize the amplitude of the optimum reflection coefficient at the  $TM_{110}$  frequency. Although the reflection coefficient is optimized at the dominant  $TM_{110}$  frequency, absorption of all the field energy is sufficient for smaller peaks at higher frequencies. By the optimization of the absorber one can get faster damping by a factor of 2–3.

Next, consider the whole structure. The iris diameter  $2a$  changes linearly with the cell number from 17.4 mm to 12.54 mm. This variation of the cell dimension introduces detuning of the HOMs and additional damping by spectral broadening. All the choke dimensions including the radial position are the same for the whole structure. The absorber dimension optimized by the procedure changes slightly from entrance to exit. The radial position changes from 46.5 mm to 44.5 mm but the width is fixed to 10 mm since the optimized reflection coefficient is almost the same over the whole structure.

A test structure was fabricated at KEK and installed in ASSET at SLAC in 1998 for wakefield tests. It was confirmed that the wakefield is damped as expected (the solid line in Figure 3.35) up to 1.6 ns (0.5 m) from about 15 to 1 V/pC/m/mm. This means that the basic concept of the choke-mode structure is confirmed. However, after this point, the measured wakefield showed a high frequency oscillation with amplitude of 0.8–1.0 V/pC/m/mm. This would cause a marginal emittance dilution of about 25%. This oscillation has spectral components at 20 and 23 GHz. It was realized with computer simulations that under certain conditions a mode can be trapped at a very high frequency whose field pattern has a node at the slot location, thus causing no power to leak out to the absorber. It turned out that a shift of the  $z$ -location of the damping slot by 2 mm can eliminate the trapped modes.

In the context of the wake function one constraint comes from the requirement of compatibility with the future X-band extension to the C-band linac. We adopted the bunch spacing of 1.4 ns for C-band collider as well as for the future X-band extension. It is possible to adopt 2.8 ns for the C-band collider but 1.4 ns is absolutely needed for the second stage. In Figure 3.35, the wake at 1.4 ns is still sizeable even when the trapped modes are eliminated. The value of the wake is marginal (possibly fatal) for the acceptable emittance increase. However, one can fine-adjust the cavity dimension without changing the major properties so that a node of the wake is located at 1.4 ns. If the wake has to be smaller for example by a factor of 5 (actually this is more than enough), then the phase of the wake must be less than 0.2 radian after about ten oscillations. This only requires the fabrication accuracy of 1/300, which is actually not a constraint.

In the test cavity a set of three rf-BPMs was installed in some cells (upstream, center, and downstream) as shown in Figure 3.36. The design of the rf BPM is depicted in Figure 3.37. The rf signal from the two rf BPM's, the wakefield monitor and the reference cavity are processed with the band-pass filters (7854 MHz, 3% bandwidth), down-converted to 310 MHz, and finally sampled with a four-channel digital scope. The reference signal is used to find the beam timing and the beam phase. The wakefield signal from the two pickup

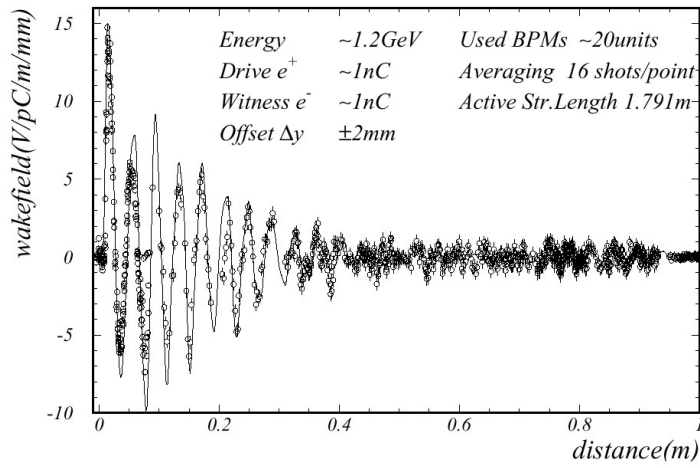


FIGURE 3.35. Measured (circles) and expected (solid line) wakefield.

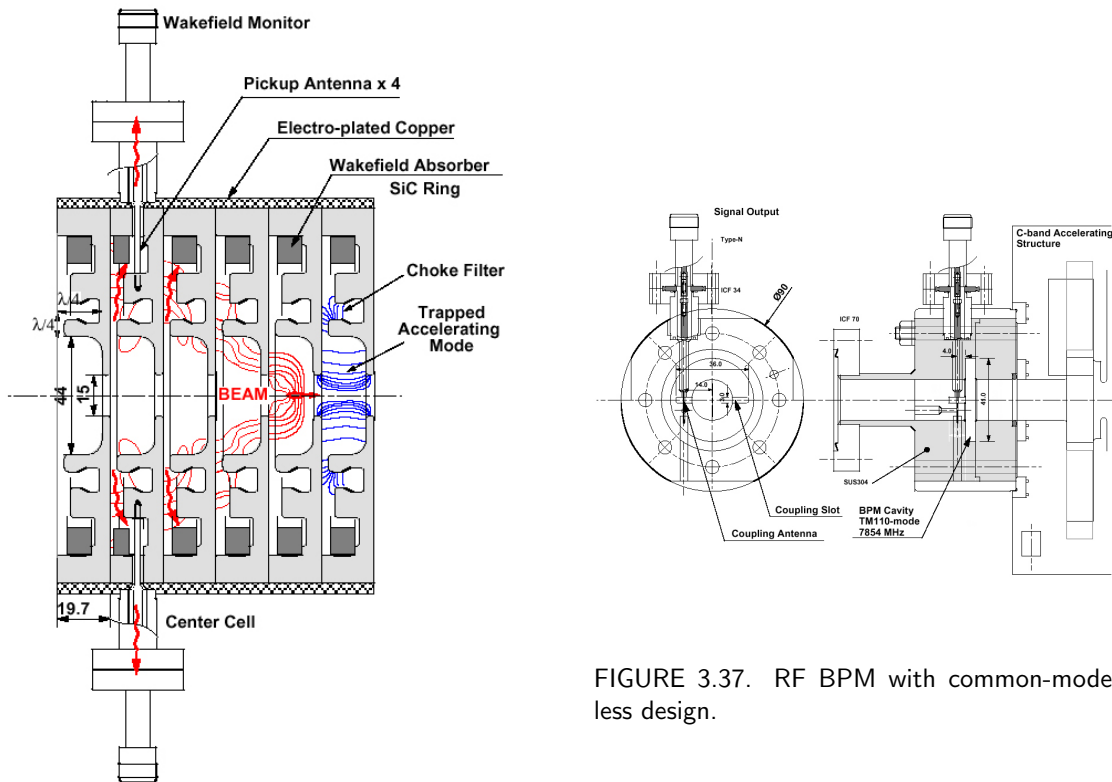


FIGURE 3.37. RF BPM with common-mode-less design.

FIGURE 3.36. Choke-mode structure with rf-BPM.

antennas at the center BPM are combined in a 180-degree hybrid to eliminate the common-mode power. The data analysis showed that the center BPM had an offset of  $63 \mu\text{m}$  with respect to the mean center of the upstream and downstream BPMs. By taking into account the calibration data, the straightness of the structure was found to be  $49 \mu\text{m}$ , which is just at the border of the design tolerance. The observed spatial resolution was about  $8 \mu\text{m}$  (limited by high digital noise in the sampling scope).

High power tests of the C-band choke-mode cavities have not yet been done. However, the same model is adopted in the SCCS (SPring-8 Compact SASE Source) project which will be constructed shortly. We do not foresee the breakdown problem found in X-band structures since the surface field is lower and the group velocity is low (in the range 3.6% to 1.1% of  $c$ ).

### 3.3 JLC-X/NLC

#### 3.3.1 Introduction

The JLC-X/NLC is a linear collider designed to provide luminosity at center-of-mass (c.m.) energies between 90 GeV and 1.3 TeV. It is based on normal conducting X-band rf technology. This technology was chosen for four reasons. First, at the higher rf frequency, the X-band technology is a reasonable extrapolation from the well understood S-band technology and it permits much higher accelerator gradients. Although the gradients achieved so far have not proved to be as high as initially thought, they are still much higher than possible at lower rf frequencies. Second, although the higher rf frequency demands tighter tolerances than S-band or lower frequencies, these tolerances have either been achieved in test facilities or are a small extrapolation (a factor of 2–3) from what has been attained. Third, the normal conducting design allows the linear collider subsystem designs to be based on other operating accelerators or accelerator subsystems. This is very important because, while the rf systems can be demonstrated in relatively inexpensive test facilities, it would be difficult and expensive to verify the other subsystems which are essential for the luminosity performance of the collider. Finally, all technologies which have presently been considered for reaching the multi-TeV region will have challenges similar to those that have been addressed in the X-band design but more difficult. Thus, the normal-conducting design provides an essential link to still higher collision energies.

The JLC and NLC have been presented in detail in the *1997 JLC Design Study* (JDS) [3] and the *1996 Zeroth-Order Design Report* (ZDR) [4]. During the last five years, the two designs have converged on a common parameter set while the linear collider R&D programs have led to substantial improvements over the original proposals. In addition, over the last five years, the physics program for a linear collider has evolved significantly, and as a consequence, the JLC-X/NLC has been modified to provide greater flexibility and higher luminosity. Further details on the design can be found in the *2000 International Study Group Report* [5] and the *2001 Report on the Next Linear Collider* [6].

The X-band linear collider is based on extensive experience from the first linear collider, the Stanford Linear Collider (SLC), as well as other modern accelerators and numerous test facilities including ASSET, the Final Focus Test Beam (FFTB) and the NLC Test Accelerator (NLCTA) at SLAC, and the Accelerator Test Facility (ATF) at KEK. In particular, the polarized electron source and the positron production system are modest

extensions of the SLC sources. The damping rings are similar to third-generation synchrotron light sources and are required to produce an equilibrium emittance that is only a factor of 2 below what has been achieved at the Advanced Light Source (ALS) in Berkeley or the ATF at KEK. The bunch compressor is based on experience from the SLC bunch compressor and is similar to, although not as difficult, as the bunch compressors for the new SASE-based short wavelength FEL drivers. Finally, a prototype X-band rf system has been operated successfully at the NLCTA since 1997. In principle, this system could be used today to build a 500-GeV c.m. collider, but there is active R&D on a next generation of components that are more efficient and less expensive to build and operate.

To preserve the small beam emittance during acceleration, the X-band structures must be designed to minimize wakefields, and both the structures and the focusing quadrupoles must be aligned to very tight tolerances. Structures fabricated in Japan and the United States already meet construction tolerances tighter than those required for JLC-X/NLC. The wakefield properties of these prototype structures have been measured precisely in the ASSET test facility and agree well with the calculations. The required alignment accuracy has also been demonstrated in ASSET. Beam-based alignment techniques developed for the SLC and FFTB quadrupoles have achieved close to the necessary accuracy, and extensive simulations indicate that these techniques are capable of preserving the emittance through a 14-km linac using diagnostics and correction hardware which needs to be only a factor of 2–3 better than that used at the FFTB. The FFTB also demonstrated the validity of the final-focus optics and achieved a demagnification of the beam size greater than required for JLC-X/NLC. All of these results have led to improvements in the design and increased confidence in its capabilities.

The JLC-X/NLC will be described in the following sections. It should be noted that although the JLC and NLC have the same rf system designs and the same beam parameters, small differences still exist between the two designs. The JLC would likely operate at a repetition rate that is a multiple of the 50 Hz line frequency while the NLC would operate at 120 Hz—this leads to different luminosities for the same beam parameters and requires slightly different damping rings. Finally, many of the detailed optical designs differ, partly because the NLC designs have continued to be refined while many of the JLC designs have not been revisited since the 1997 JDS. To address this problem, this chapter will present only the optics of the current NLC design but will note the differences where they exist. Finally, the optical decks contain detailed information on the placement of the diagnostic and control equipment which is essential for operating the collider, but these systems will not be discussed because of space limitations.

### 3.3.2 Parameters and Layout

The JLC-X/NLC collider parameters and layout have evolved over the last five years. These changes have been motivated by a desire to provide additional physics opportunities and to reduce the capital costs of the facility. The facility is designed for optimal performance at a c.m. energy of 1 TeV, but with flexibility to begin operation at 500 GeV and be upgraded to match the needs of physics as they evolve. Key areas and systems are designed for energies above 1 TeV. In particular, by reducing the beam current, the presently envisioned linac that would deliver beam for 1 TeV collisions, would still be able to deliver substantial luminosity at a c.m. energy of 1.3 TeV.

## DESCRIPTIONS OF THE FOUR MACHINES AT 500 GEV C.M.

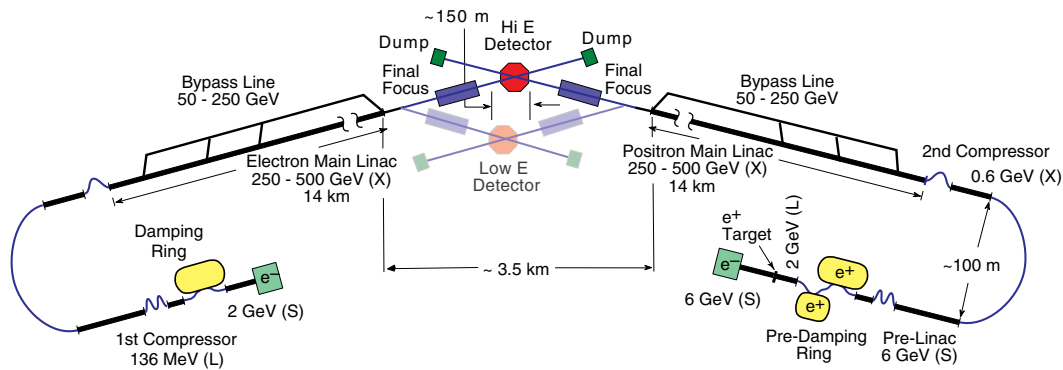


FIGURE 3.38. Schematic of the JLC-X/NLC.

The collider configuration is shown schematically in Figure 3.38. The 1 TeV collider is roughly 30 km in length. The main linac rf systems are capable of generating 250 GeV beams (500 GeV c.m. collisions) in one half of the two 14-km long linac tunnels that are part of the initial configuration. The upgrade to 1 TeV c.m. energy can be achieved by completing the main linacs with replicas of the rf components used in the initial construction, or, more likely, with improved versions of those components. Bypass lines along the main linac allow beams of various energies to be transported to the experiments, fully covering the energy range from 90 GeV to 1.3 TeV. The beam sources and damping rings that make up the injectors for the main linacs are designed to meet specifications for 1.5 TeV collisions.

To accommodate the physics demands for energy flexibility, the design includes two interaction regions. One is optimized for high energy, 250 GeV to 1.5 TeV, and is configured so that it is ultimately upgradable to multi-TeV. The other is designed for precision measurements at lower energy, 90 to 500 GeV, although it could be upgraded to operate at  $\sim 1$  TeV as well. The final focus can actually accommodate beams of up to 2.5 TeV in a length of about 800 meters. To capitalize on the multi-TeV potential of the new design, it was also necessary to eliminate other bending between the linac and the high energy IP. In the NLC design, a 20 mrad crossing angle at the IP is used to avoid parasitic interactions of one bunch with the later bunches in the opposing train and to ease the extraction line design. The linacs are not collinear but are oriented with a shallow 20 mrad angle between them to produce the desired crossing angle at the high-energy IR without additional bending. The beams to the second IR are bent by about 25 mrad, which is acceptable for energies up to  $\sim 1$  TeV. The low-energy IR has a larger 30 mrad crossing angle for compatibility with a possible  $\gamma/\gamma$  option. Finally, in the JLC design, the primary IP has a crossing angle of 7 or 8 mrad and the non-collinear linac layout has not been planned. However, the crossing angle of the second IP is 30 mrad as in the NLC design.

The primary  $e^+/e^-$  parameters for the JLC-X/NLC are listed in Table 3.14. The beams consist of bunch trains with 192 bunches separated by 1.4 ns. The repetition rate would be 150 Hz for Stage I and 100 Hz at Stage II in Japan while, in the US, the repetition rate would remain 120 Hz at both stages. Although not listed, the collider is also designed to operate with 96 bunches of  $1.5 \times 10^{10}$  particles and a 2.8 ns bunch spacing—this later

TABLE 3.14  
Parameters for Stage I and Stage II of the JLC-X/NLC.

Center-of-mass energy [GeV]	Stage I		Stage II	
	500		1000	
Site	Japan	US	Japan	US
Luminosity [ $10^{33}$ ] incl. dilutions	25	20	25	30
Repetition rate [Hz]	150	120	100	120
Luminosity within 1% of $E_{c.m.}$ [%]	64		58	
Bunch charge [ $10^{10}$ ]	0.75		0.75	
Bunches/rf pulse	192		192	
Bunch separation [ns]	1.4		1.4	
Lum. dilution for tuning and jitter [%]	5		5	
Injected $\gamma\epsilon_x / \gamma\epsilon_y$ [ $10^{-8}$ m·rad]	300 / 2		300 / 2	
$\gamma\epsilon_x / \gamma\epsilon_y$ at IP [ $10^{-8}$ m·rad]	360 / 4		360 / 4	
$\beta_x / \beta_y$ at IP [mm]	8 / 0.11		13 / 0.11	
$\sigma_x / \sigma_y$ at IP [nm]	243 / 3.0		219 / 2.1	
$\sigma_z$ at IP [ $\mu\text{m}$ ]	110		110	
Upsilon average	0.13		0.28	
Pinch enhancement	1.49		1.42	
Beamstrahlung $\delta_B$ [%]	4.6		7.5	
Photons per $e^+/e^-$	1.3		1.3	
Loaded gradient [MV/m]	50		50	
Linac length [km]	6.9		13.8	

DESCRIPTIONS OF THE FOUR MACHINES AT 500 GEV C.M.

option might be preferred for  $\gamma\text{-}\gamma$  collisions but also provides higher  $e^+/e^-$  luminosity while increasing the beamstrahlung and emittance dilution. During the initial stage, the center-of-mass energy is assumed to be 500 GeV with a luminosity of  $2.5 \times 10^{34} \text{ cm}^{-2}\text{s}^{-1}$  ( $2.0 \times 10^{34} \text{ cm}^{-2}\text{s}^{-1}$ ) at the repetition rate of 150 Hz (120 Hz), although the collider might be started with a lower initial energy depending on the physics interest. The second stage assumes the installation of the full rf system to reach a center-of-mass energy of 1 TeV with a luminosity of  $2.5 \times 10^{34} \text{ cm}^{-2}\text{s}^{-1}$  ( $3.0 \times 10^{34} \text{ cm}^{-2}\text{s}^{-1}$ ) at a repetition rate of 100 Hz (120 Hz). In addition, sets of nominal parameters for operation of the low-energy IR are listed in Table 3.15.

TABLE 3.15  
Low energy operation parameters for the NLC.

Center-of-mass energy [GeV]	92	250	350
Luminosity [ $10^{33}$ ]	3.5	9.4	13.2
Luminosity within 1% of $E_{c.m.}$ [%]	92	75	65
Repetition rate [Hz]	120	120	120
Bunch charge [ $10^{10}$ ]	0.75	0.75	0.75
$\sigma_x / \sigma_y$ at IP [nm]	630 / 6.2	380 / 3.8	320 / 3.2
Beamstrahlung $\delta_B$ [%]	0.18	1.1	2
Photons per $e^+/e^-$	0.49	0.79	0.92
Polarization loss [%]	0.08	0.21	0.34

It should be noted that the JLC-X/NLC traveling wave accelerator structures are tested to the full unloaded gradient of 65 MV/m; this differs from the testing of the standing-wave superconducting structures which are only tested to the maximum *loaded* gradient of 23 to 35 MV/m. Because the cavities are tested to the full unloaded gradient, the JLC-X/NLC collider could operate at an energy roughly 25% higher than nominal with 30% of the nominal luminosity by reducing the average beam current. Thus, without modification to the rf system, the Stage II JLC (NLC) could deliver a luminosity of  $7 \times 10^{33} \text{ cm}^{-2}\text{s}^{-1}$  ( $9 \times 10^{33} \text{ cm}^{-2}\text{s}^{-1}$ ) at a c.m. energy of 1.25 TeV. A plot of the luminosity versus energy for the Stage II NLC is plotted in Figure 3.39; using the bypass lines and the two interaction regions, the collider is designed to fully cover the energy region between 90 GeV and 1.3 TeV.

The beam parameters listed in Table 3.14 and Table 3.15 have been chosen to balance total luminosity against the fraction of luminosity close to the center-of-mass energy and the bremsstrahlung-related backgrounds. The luminosity spectrum can be described by two parameters, the number of beamstrahlung photons radiated per incident electron  $n_\gamma$  and the average energy lost to the beamstrahlung  $\delta_B$ . These parameters can be traded against each other to optimize the total luminosity and the luminosity spectrum for any given experiment. The parameters presented in Table 3.14 and Table 3.15 are only an illustrative set.

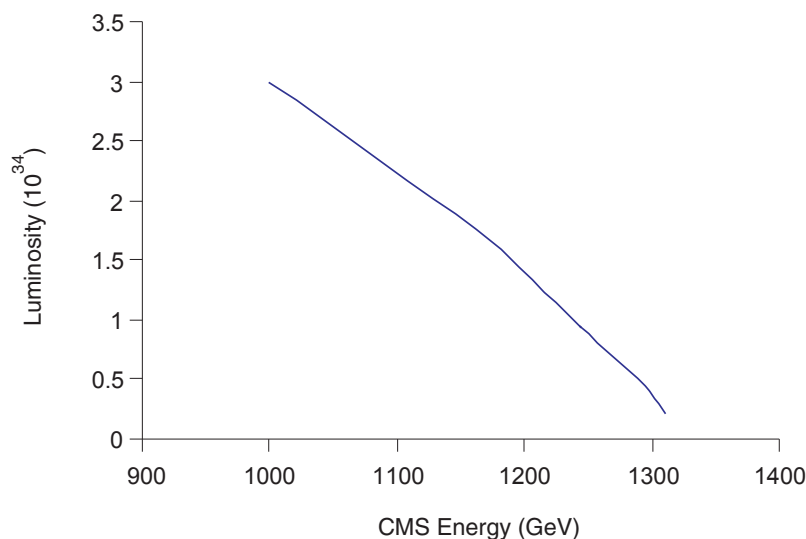


FIGURE 3.39. Energy versus luminosity for Stage II NLC rf system.

Detailed emittance and beam-jitter budgets are shown in Table 3.16; these are discussed in Section 3.3.6 along with the beam-based alignment and jitter-stabilization techniques. The design luminosities, listed in Table 3.14, include 5% luminosity degradation beyond the explicit emittance dilutions to account for beam jitter and beam tuning. It is important to emphasize that the JLC-X/NLC has been designed with generous margins throughout to facilitate attaining the design luminosity rapidly.

It should also be noted that the ultimate luminosity of the collider is roughly a factor of 2 higher than the design. This higher luminosity might be attained if the beam-based alignment techniques can be pushed to even higher precision and the beam-beam limitations due to the high disruption parameter that impact the TESLA design can be overcome; the disruption parameter for these high luminosity parameters is roughly 20 which is still less than the TESLA values of 25–28. The ultimate luminosity, referred to as the “intrinsic luminosity,” is determined by physical limitations such as the finite damping time of the damping rings and synchrotron-radiation emission in the bunch compressors and final focus. These intrinsic beam emittances and luminosity are listed in Table 3.17 for comparison with the design values.

Next, possible parameters for operation as a  $\gamma/\gamma$  collider are listed in Table 3.18. These parameters are based on the JLC-X/NLC beam with a 2.8 ns spacing and 96 bunches as noted earlier. The  $\gamma/\gamma$  interaction region would be located in the “Low Energy IR” (LEIR) which has a large crossing angle of 30 mrad to facilitate extracting the disrupted  $e^-$  beams. To take full advantage of the photon interaction, the horizontal and vertical beta functions have been reduced at the IP which has been verified with tracking simulations.

Finally, as described, the JLC-X/NLC is designed to operate with center-of-mass energies up to  $\sim 1.5$  TeV. The next logical step for electron-positron facilities would then be a linear collider that operates in the 3-TeV to 5-TeV center-of-mass range with a luminosity of  $10^{35}$  or more, using a design such as CLIC. The history of accelerator laboratories makes one

DESCRIPTIONS OF THE FOUR MACHINES AT 500 GEV C.M.

TABLE 3.16  
NLC Design Emittance and Jitter budgets for 500 GeV c.m. parameters.

Region	$\gamma\epsilon_x$ [ $\mu\text{m}\cdot\text{rad}$ ]	$\gamma\epsilon_y$ [ $\mu\text{m}\cdot\text{rad}$ ]	X jitter [ $\sigma_x$ ]	Y jitter [ $\sigma_y$ ]
Damping ring	3.0	0.020	0.1	0.1
Injector (8 GeV)	0.2	0.002	0.1	0.1
Main linac	0.1	0.010	0.1	0.3
Beam delivery	0.3	0.008	0.1	0.3
Final doublet			0.1	0.25
Total at IP	3.6	0.04	0.22	0.51

TABLE 3.17  
Intrinsic versus design emittances and luminosity for JLC-X/NLC at 1 TeV.

	Intrinsic	Design
Damping rings $\gamma\epsilon_x / \gamma\epsilon_y$ [ $10^{-8}$ m·rad]	300 / 1	300 / 2
Main linac $\gamma\epsilon_x / \gamma\epsilon_y$ [ $10^{-8}$ m·rad]	315 / 1	330 / 3
Beam delivery $\gamma\epsilon_x / \gamma\epsilon_y$ [ $10^{-8}$ m·rad]	330 / 1	360 / 4
Luminosity [ $10^{33}$ ]	63	30

TABLE 3.18  
Parameters for  $\gamma/\gamma$  collisions at the JLC-X/NLC.

Beam energy	250 GeV
Luminosity including dilutions	$3.2 \times 10^{33}$
Repetition rate	120 Hz
Bunches/rf pulse $\times$ bunch separation	$96 \times 2.8$ ns
Bunch charge	$1.5 \times 10^{10}$
$\gamma\epsilon_x / \gamma\epsilon_y$ at IP	360 / $7.1 \times 10^{-8}$ m·rad
$\beta_x / \beta_y$ at IP	4 / 0.065 mm
$\sigma_x / \sigma_y$ at IP	172 / 3.1 nm
$\sigma_z$ at IP	156 $\mu\text{m}$
Conversion point $\rightarrow$ IP	2 mm

point clear: the investment in the infrastructure of the accelerators, including the beamline housings, is significant and therefore the infrastructure should be used and reused for as long as possible. This has led to the use of existing synchrotrons as injectors for new synchrotrons, and in some cases to the decommissioning of existing accelerators so that the tunnels or components can be recycled for use in new accelerators. It is this history that has shaped the decision to make the design as compatible as possible with future energy upgrades.

While it is too early to determine the technologies that will be used at a multi-TeV linear collider, a general review of the issues discussed previously reveals many of the requirements of such a facility. The JLC-X/NLC configuration has been developed with these requirements in mind. For example, the multi-TeV linear collider will require a site with low levels of ground motion, a crossing angle of at least 20 mrad, beam delivery systems with weak bend magnets, and in all probability a main-linac tunnel that can accommodate a second beamline for the “drive beam.” All of these features are included in the design. In many cases, the requirements are identical to those of a future facility. In other cases, configuring the design to accommodate a future linear collider did not cause additional financial or technical penalties. This permits the injectors, beam delivery systems, and main-linac housings to be used in a multi-TeV collider, although the main-linac accelerator structures and rf power sources would need to be replaced and some upgrades of the damping rings, bunch compressors, and final-focus beamlines would be required.

### 3.3.3 Main Linacs and RF Systems

The main JLC-X/NLC linac tunnels are each 13.8 km long and contain the necessary rf system as well as three diagnostic regions and three extraction sections that feed the bypass line (see Figure 3.40). The tunnels are designed to be long enough to hold the full complement of accelerator structures to reach 1 TeV in the center-of-mass at the design luminosity, although, in the first stage of the project, only the first half of the tunnels would be filled with structures. The installation would start from the low-energy end of the tunnel to allow maximum flexibility in choosing the appropriate energy upgrade steps to match physics interests and funding profiles.

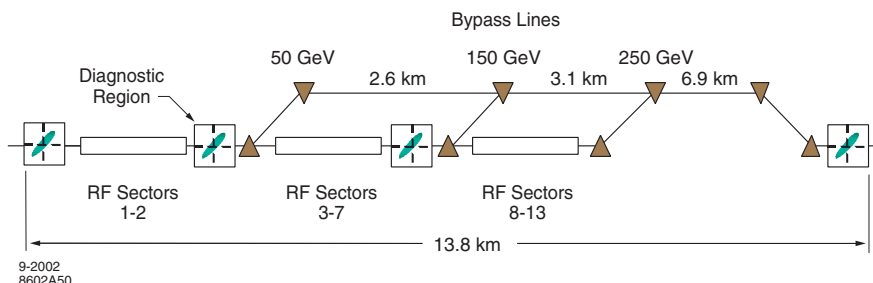


FIGURE 3.40. Schematic of the JLC-X/NLC linac layout; each sector contains 20 rf units in a length of 520 meters.

## DESCRIPTIONS OF THE FOUR MACHINES AT 500 GEV C.M.

The JLC-X/NLC linac would contain 254 rf units at Stage I (500 GeV c.m.). Each rf unit contains one solid-state induction modulator driving eight 75-MW 1.6- $\mu$ s klystrons arranged in pairs. Each of the four klystron pairs powers a dual-mode SLED-II pulse compression system which feeds an rf girder with six 0.9-m accelerator structures. The linac beam-line enclosure would contain the accelerator structures while the modulators and klystrons will be installed in a separate utility enclosure. This simplifies access and maintenance which is essential to ensure the desired reliability and collider availability. The SLED-II lines could be placed in either the main linac tunnel or in the utility tunnel—both options have advantages: the main linac tunnel has better temperature control however the utility tunnel allows easy access for upgrades and maintenance of the SLED-II systems.

Because of the transverse wakefields of the accelerator structures, it is undesirable to transport the beam through a large number of unpowered structures. In order to maximize luminosity at lower energy, a non-accelerating “bypass” line is provided to bring the low-energy beams to the end of the linac. The bypass line will share the main-linac tunnel, and will be installed at the same elevation as the main beamline. The design includes three transfer points where the beam can be diverted into the bypass line at 50, 150 and 250 GeV, and a return at the end of the linac to bring the beam back into the collimation section. These are sufficient to support a continuous variation of beam energy over the whole range.

The linac transport optics were chosen to minimize the dispersive and wakefield-related beam emittance growth. In the NLC design, quadrupole magnets, in a FODO configuration, are located after every (one, two, or three) rf girders at the (beginning, middle, or end) of each linac. The quadrupoles in the rf regions will have 12.7-mm-diameter apertures and vary in length from 0.32 m to 0.96 m. The rf girders and quadrupoles will be supported on movers that will be remotely adjusted during beam operation based on signals from the structure manifolds and beam position monitors (BPMs) in the quadrupole magnets.

As will be discussed in Section 3.3.6, extensive effort has been made to ensure that the beam emittance can be preserved along the linac. The signals from the structure manifolds will be used to directly align the accelerator structures to the beam; as discussed in Section 3.3.3.5 measurements using the manifolds in prototype structures have already shown the required precision. The BPMs located at the quadrupole magnets will be used to align the quadrupoles. Although the required quadrupole alignment is roughly 25 times smaller than that achieved in the SLC and about 3 times smaller than in FFTB, the BPMs are specified to have resolutions of 0.3  $\mu$ m which has been demonstrated in prototype rf BPMs and is 50 times smaller than that in the SLC linac and 3 times smaller than that in the FFTB. Because the expected alignment precision scales with the diagnostic resolution, using the quad-shunting beam-based alignment technique utilized at the FFTB with the improved BPM resolution should attain the desired alignment.

Simulations indicate that the desired alignment precision will be attained. However, to provide additional safety margin, provision has been made to utilize two other beam-based alignment techniques pioneered at the SLC: dispersion-free steering and emittance correction bumps. These techniques are relatively sensitive to details of the energy profile along the linac and the beam optics. To monitor the beam energy, energy spread, and emittance, there will be four diagnostic regions along the length of the linac where these parameters can be measured parasitically. In addition to being needed for the beam-based alignment and emittance correction techniques, continuous, non-invasive monitoring was

found to be essential during the SLC operation because it facilitates rapid diagnosis of faults and makes it possible to correlate disparate effects.

In the following sections, the rf system will be described in greater detail and then, in Section 3.3.6, the emittance preservation and luminosity performance issues will be discussed.

### 3.3.3.1 RF Systems

Outstanding progress has been made in applying and extending the science and engineering of microwave power and acceleration systems from S-band, the enabling technology for the SLAC linac, to X-band, which can provide the significant performance improvements and cost reductions needed for a high-energy linear collider. New modulators, klystrons, microwave power distribution systems, and accelerator structures that can meet the challenging demands of a linear collider are in the final stages of development. The R&D on these components has been pursued as a joint effort between SLAC and KEK as part of the International Study Group (ISG) developing designs for an X-band linear collider.

The 11.424-GHz rf systems are similar in character to those in the SLAC linac. Electrical energy is transformed in several stages: the induction modulators convert AC power to high-voltage pulsed DC; the klystrons transform the pulsed DC to high-power rf; the SLED-II pulse compression system combines the power from two klystrons with pulse lengths of  $1.6 \mu\text{s}$  and, by storing the power, compresses it into pulse lengths of 400 ns and sends it to sets of six accelerator structures; and finally, the six structures on each rf girder accelerate the beam. The baseline JLC-X/NLC rf system is illustrated in Figure 3.41.

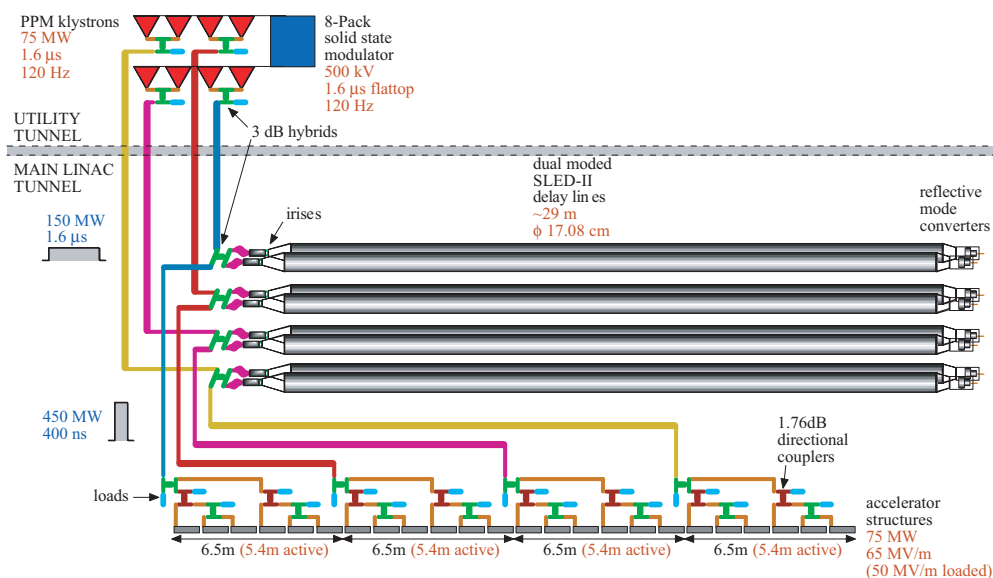


FIGURE 3.41. Schematic of a JLC-X/NLC linac rf unit (one of 254 per linac); the SLED-II delay lines could be located in either the linac or utility tunnels.

Because the AC power required to drive the accelerator is high, especially at a c.m. energy of 1 TeV, much effort has been focused on maximizing the efficiency of the conversion and transfer of energy at every stage of the rf system. Both the JLC and NLC design teams have been investigating alternate pulse compression systems with higher efficiency than the SLED-II rf system. In particular, the Delay Line Distribution System (DLDS) will be pursued as a possible high efficiency option to the SLED-II pulse compression system. However, because of the simpler topology of the SLED-II system, it will be faster to demonstrate a SLED-II pulse compression system at the full JLC-X/NLC power specifications than it will be to test a full DLDS system. In addition, the JLC-X/NLC SLED-II pulse compression system is based on the SLED-II systems that have operated at the NLCTA for over five years, providing confidence in the design. We believe that, by first pursuing the SLED-II-based baseline rf design and then moving toward a higher efficiency system, we will be able to demonstrate the feasibility of the X-band rf system while still working to improve the system efficiency.

The parameters of the JLC-X/NLC major rf subsystems (klystrons, modulators, rf distribution, and accelerator structures) are listed in Table 3.19. The unloaded gradient ( $G_U$ ) of 65 MV/m is close to optimal in the tradeoff between energy-related costs (*e.g.*, modulators and klystrons), which scale roughly as  $G_U$ , and length-related costs (*e.g.*, structures and beam-line tunnel), which scale roughly as  $1/G_U$ . However, the overall linac cost has a fairly weak dependence on unloaded gradient in the range of interest for the JLC-X/NLC (50 to 100 MV/m). The beam parameters were chosen as a tradeoff between increasing rf-to-beam efficiency and easing tolerances related to both short-range and long-range transverse wakefields effects.

A brief description, including design choices and R&D progress, of each major rf subsystem follows.

### 3.3.3.2 Modulators

The 75-MW PPM klystrons require pulses of roughly 500 kV and 260 A. Initially, conventional line-type modulators like those used in the SLAC linac were considered for this purpose. These modulators contain pulse-forming networks that are slowly charged and then rapidly discharged, via a thyatron, through a step-up transformer to generate the high-voltage pulse. These modulators have several drawbacks including low efficiency and the use of thyatrons, which have relatively short lifetimes (10,000–20,000 hr) and require periodic adjustments. As an alternative, the idea of a solid-state induction-type modulator was explored, based on recent advances in high-power, solid-state switches (Insulated Gate Bipolar Transistors or IGBTs). The concept is to sum many low-voltage sources (2–4 kV) inductively to yield the desired klystron voltage. This has been implemented by having each source drive a toroidal-shaped transformer made with Metglass or Finemet cores. The cores are stacked so secondary windings, which sum the output voltages, can be threaded through them. Each source is essentially a capacitor that is slowly charged and then partially discharged through an IGBT switch to generate the pulse.

The solid state NLC modulator is designed to power eight klystrons. It is constructed from 42 Metglass cores, each driven by two 6.5 kV IGBTs operating at 4 kV and 3 kA. These drive a 3-turn secondary winding for an output pulse of 500 kV, 2160 Amps that is 1.6  $\mu$ s long. The modulator is roughly 2 meters high and consists of two stacks of 21 cores.

TABLE 3.19  
JLC-X and NLC rf system parameters.

	JLC-X	NLC
RF units per linac (500 GeV c.m.)	254	
AC power for modulators per linac	65.9 MW	
AC power for other rf + cooling rf system per linac	9.6 MW	
Total AC power related to rf per linac	75.5 MW	
Beam power per linac	6.9 MW	
AC-to-beam power efficiency	8.8%	
Modulator type	1:1 linear induction	1:3 induction
Modulator efficiency	80%	80%
Number of rf modulators per rf unit	1	1
Klystron type	PPM	
Beam voltage/current	490 MV / 260 A	
Output power	75 MW	
Klystron pulse length	1590 ns	
Klystron efficiency	55%	
Number of klystrons per rf unit	8	
Type	SLED-II	
Modes	TE <sub>01</sub> & TE <sub>02</sub>	
Power gain = number of feeds per rf unit	4	
Switching time	8 ns	
RF pulse length per feed	396 ns	
Compression efficiency	75%	
RF phase advance per cell	150 degrees	
Structure input group velocity	5.1% c	
Structure length	0.90 m	
Field attenuation factor ( $\tau$ )	0.510	
Number of structures per rf feed	6	
Fill time	120 ns	
Average acceleration shunt impedance	81.2 Mohm/m	
Loading shunt impedance	82.4 Mohm/m	
Peak rf power into structure	75.0 MW	
Unloaded accelerator gradient ( $G_u$ )	64.8 MV/m	
Beam loading	23%	
Multibunch loading	14.7 MV/m	
Single bunch loading	0.30 MV/m	
Loaded accelerating gradient	49.8 MV/m	
Average rf phase	11.0 degrees	
RF overhead (3% BNS + 3% failed + 2% FB)	8%	
Length of powered linac	6.6 km	
Length of unpowered linac (for upgrade to 1 TeV c.m.)	6.6 km	
Total length of diagnostic and bypass regions	0.6 km	
Total length of each linac tunnel	13.8 km	

## DESCRIPTIONS OF THE FOUR MACHINES AT 500 GEV C.M.



FIGURE 3.42. Photograph of the NLC induction modulator with three of the SLAC 5045 klystrons that are used as a load.

A full-scale prototype based on 4.5 kV IGBTs is shown in Figure 3.42. The JLC modulator, referred to as the Linear Induction Modulator, is similar except that it uses a single-turn secondary to produce 500 kV and 2 kAmps to eliminate the production and installation of the secondary windings. The design has three times the number of cores although, on average, cores are smaller.

For fast pulse performance, the IGBT drivers must be operated in a regime where they are not well modelled. The drivers are designed for locomotive traction, requiring continuous high power operation at a few kV and 600–800 A. The pulsed-power requirements of the modulator are very high  $dI/dt$ , peak currents that nearly saturate the bipolar switch, high voltage lasting only for a few microseconds, and inductive connections through the drivers to capacitive loads (klystrons). After each pulse, the core has to be reset, and stored energy recovered. This must be done without producing transients on the gate of the IGBT sufficient to exceed its ratings and destroy the transistor. Several key technical challenges encountered in bringing the designs from concept to working prototype include:

- IGBTs have a known susceptibility to neutron radiation induced from cosmic rays, or accelerators, which can cause a Single Event Upset (SEU) that latches and destroys the bipolar transistor. Shielding solves this problem in the JLC-X/NLC applications.
- Many studies have been conducted to develop circuits that will protect the IGBTs under conditions of a short circuit to the load and of core saturation. Some wiring layout changes have been made in the transistor itself to minimize unwanted transients.
- To protect the stack if one IGBT fails, a circuit was developed that assures that, on failure, the device is shorted and disconnects its drive voltage from the cell primary single turn. Therefore, the stack suffers an incremental drop in voltage due to the loss of the one cell, which could be compensated by either slightly raising the supply

voltage on each cell or by turning on spare “hot” IGBT cards which will be installed in each modulator. This fail-soft feature will enable longer periods of continuous operation without interruptions for maintenance.

- Two approaches are being adopted to limit the energy delivered if one of the klystrons arcs. Passive inductance from the stack to each tube, and between tubes, is used to slow the transfer of charge to the faulting tube. In addition, the entire stack is designed to sense the fault and shut off in about 400 ns, drawing most of the load’s stored charge and shunting it to ground. Klystron faults have been studied on pairs of X-Band klystrons in NLCTA at SLAC, so far with no apparent degradation.
- Recently, current and voltage distribution in the two commercial IGBT hybrid packages currently being used have been modelled on a 3D simulator. The commercial hybrid circuits consist of between 9 and 16 bonded dies, each with multiple IGBTs, on a single substrate mounted on a heat sink. The cause of observed failures in one of the layouts has been traced to the highly non-uniform distribution of high  $dI/dT$  current densities as a function of chip location on the die, due to unsymmetrical placement with respect to buses, and uneven wire bonding. During the fast rise time transient currents in different bond wires and single chips vary by more than 10:1. A new symmetrical geometry has been modelled which eliminates this effect entirely. Also some simple bond wire changes with the present layout will improve distribution by a factor of 2–3. While the IGBTs now in hand are totally sufficient to support the present program, development of a more robust device for fast pulse applications is being pursued with manufacturers.

At SLAC, a full-scale prototype induction modulator has been built using 3.3 kV IGBTs and a stack of 76 ferrite cores. Testing began in October 2001 (Figure 3.42) and proceeded to full voltage at low power using a water load. The modulator was then tested to near full power, but less than full voltage, using three 5045 S-band klystrons operating as diodes. These klystrons are the only loads available that permit testing close to the full power. To study the modulator in extreme conditions, the voltage was further raised to deliberately arc the 5045 klystrons. During the arc testing, damage occurred to the IGBTs. This problem was solved by adding “snubber” circuits to damp the high frequency reflections and upgrading the IGBTs to 4.5 kV models. This prototype modulator has now been moved to the NLCTA to power the SLED-II pulse compression system and demonstrate the JLC-X/NLC baseline X-band rf system. Another 8-pack modulator using 6.5 kV IGBTs is under construction at the Lawrence Livermore Laboratory and should be completed in 2003. At KEK, the design for the Linear Induction Modulator, shown in Figure 3.43, is nearing completion and a full prototype should be operating in 2003.

### 3.3.3.3 Klystrons

The X-band power required for the JLC-X/NLC has driven the development of klystrons much further than those available commercially. The designs first considered were similar in concept to the solenoid-focused S-band klystrons used in the SLAC linac. The general design goal was to achieve the highest peak power and the longest pulses possible while minimizing the overall klystron cost. As a first step, the XL4 klystron was designed in the early 1990s and achieved its target power of 50 MW. Thirteen of these XL4s have been

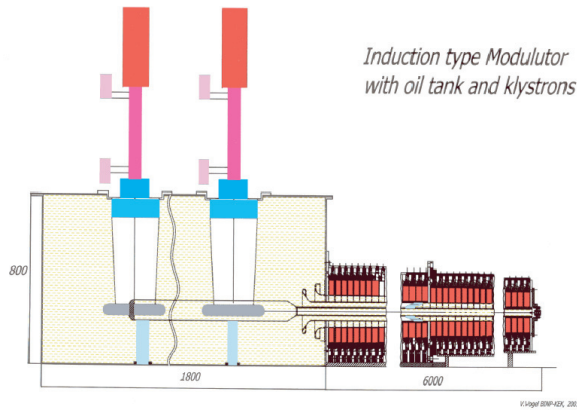


FIGURE 3.43. Schematic of the JLC Linear Induction Modulator design.

built. They are used as X-band rf sources for R&D at the SLAC Klystron Test Laboratory and the Next Linear Collider Test Accelerator (NLCTA). They reliably generate 1.5- $\mu$ s, 50-MW pulses with a 43% beam-to-rf efficiency. In a test, one XL4 klystron was run at 120 Hz with 75-MW, 1.5- $\mu$ s pulses which were produced with 48% efficiency. An XL4 has also been operated at 2.4  $\mu$ s and 50 MW without difficulty. At KEK, two similar klystrons (XB72K-9 and XB72K-10) also operate with 1.5- $\mu$ s pulses at 50 MW. The integrated running time of the XL4/XB72K klystrons is around 40,000 hours, during which there have been no major failures (the JLC-X/NLC lifetime goal is 20,000 hours).

With the success of these solenoid focused klystrons, attention turned to developing a permanent magnet focusing system which would consume no power. In the Periodic Permanent Magnet (PPM) design, many magnet rings with alternating polarities are interleaved with iron pole pieces to generate a periodic axial field between the gun anode and beam collector. The resulting focusing strength is about 2 kG, which is smaller than the 5-kG field in the solenoid-focused klystrons. The weaker PPM field has led to a klystron design with a higher voltage-to-current ratio, which reduces the space charge defocusing and increases the klystron efficiency; the micropervance of the 75 MW PPM klystrons is between 0.70 and 0.80 and the klystrons operate at roughly 500 kV and 250 A.

The first PPM klystron was built at SLAC in 1996 to generate 50-MW pulses, like the XL4s. It worked well, producing 1.5- $\mu$ s, 50-MW pulses with an efficiency of 55%, close to the predicted performance. The next klystron, referred to as the XP1, then was designed for 75 MW. After modification, the klystron delivered over 90 MW in a 0.7- $\mu$ s pulse length and 79 MW at 2.8  $\mu$ s with 60% efficiency. The repetition rate was limited to 1-Hz due to heating of the uncooled magnet stack. The most recent klystron at SLAC, the XP3, has been designed to operate at a 60 Hz repetition rate at 75 MW and a 3.2  $\mu$ s pulse length; the 3.2  $\mu$ s pulse length, which is twice the rf system requirement, was chosen to increase the energy output from each klystron and thereby reduce the required number of klystrons by a factor of 2. Two of these klystrons have been built however neither reached the desired output power due to fabrication errors; a third is being constructed.

At KEK, three PPM klystrons have been designed and built by industry. The first, PPM-1, was completed in 2000 and produced 56 MW with pulse lengths of 1.5  $\mu$ s and roughly 50%

efficiency. The second, PPM-2, was completed in 2001 and produced 70 MW in a pulse length of 1.5  $\mu$ s with a 55% efficiency before a modulator problem halted testing. This klystron was operated at 25 Hz. The most recent klystron, PPM-3, is being tested. It has operated at 68 MW with a 1.5- $\mu$ s pulse length and 53% efficiency. The repetition rate is limited by the modulator to 50 Hz, however, thermal measurements show that the tube could safely operate at 100 Hz without additional cooling. With further testing it is expected that the klystron will produce the desired 75-MW power with an efficiency of about 55%.

Finally, next-generation klystrons are being designed at SLAC and KEK. At KEK, the PPM-4 is a version of the PPM-3 optimized for mass production and should be delivered in February 2003. At SLAC, the XP4 is being designed for completion in 2003. The goal of both programs is to produce a number of klystrons to be lifetime tested.

### 3.3.3.4 RF Pulse Compression

Using the klystron output power to drive the accelerator structures is complicated by the different pulse-length and peak power requirements. While long, relatively low power klystron pulses are optimal from a klystron cost perspective, shorter pulses are needed to power the structures to minimize overall cost. An rf pulse compression system is used to match these conditions.

The goal in compressing the pulse (and increasing the peak power) is to make the transition efficiently with as little waveguide as possible. The Delay Line Distribution System (DLDS), proposed at KEK, is a very efficient system. Other options include the Binary Pulse Compression system, which has comparable efficiency, and the SLED-II system, which is less efficient but requires less waveguide. All of these rf distribution systems are characterized by the ratio of the klystron to structure pulse length or the compression ratio. In the JLC-X/NLC design, a compression ratio of four is needed. The rf system is based on a dual-moded SLED-II compression system which was chosen for two reasons. First, while other pulse compression systems are more efficient, they are more complicated and, unfortunately, this will delay the demonstration of the system. Second, the NLC Test Accelerator group has a lot of operational experience with SLED-II pulse compression whose technology has been established for years. The only challenge is that the full power JLC-X/NLC version must produce 400 ns pulses of 450 MW—the SLED-II systems at the NLC Test Accelerator and the Klystron Test Laboratory have generated 240 ns pulses of 270 MW and 150 ns pulses of 480 MW. The new over-moded components that have been developed are expected to have no trouble operating at the higher field levels. Finally, the routing of the rf power is controlled with the klystron phases. An 8-ns period is allotted for each phase shift, making the total klystron pulse length needed to accelerate the JLC-X/NLC bunch train equal to 1.59- $\mu$ s.

To fully demonstrate the SLED-II system, the prototype NLC solid state modulator has been moved to the NLC Test Accelerator. Four 50-MW klystrons will be used to power a dual-moded SLED-II system as illustrated in Figure 3.44. With four times pulse compression, the SLED-II system will be able to produce 600-MW in a 400 ns pulse; this is 33% higher power than required in the JLC-X/NLC, giving confidence in the SLED-II design. The system could also be operated with a 2.4- $\mu$ s input pulse and six times compression to deliver over 800 MW. The high power tests will be complete by mid-2003 at

## DESCRIPTIONS OF THE FOUR MACHINES AT 500 GEV C.M.

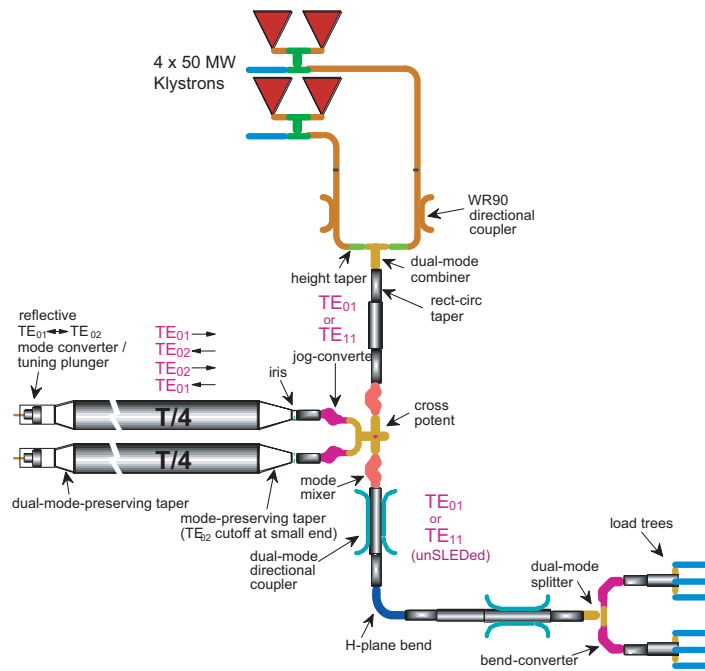


FIGURE 3.44. Schematic of the dual-moded SLED-II demonstration at the NLCTA.

which point the rf power will be directed into the NLCTA enclosure to power one rf girder of accelerator structures.

To prevent significant attenuation while transmitting the power through the long waveguides, the rf power is transported in low-loss circular modes. A low-power transmission test of the three circular modes in a 55-m delay line was performed at KEK to verify the expected power attenuation per unit length of the modes. The results of the test confirm the viability of any of the  $TE_{01}$ ,  $TE_{02}$ , or  $TE_{12}$  modes for a pulse compression system. At the present time, the JLC-X/NLC SLED-II delay lines use two circular modes, the  $TE_{01}$  and  $TE_{02}$ .

Finally, two tunnel configurations have been considered: a Cut and Cover construction, where the klystron galleries can be much shorter than the linac tunnel, and a dual tunnel construction, where the klystrons and modulators are placed in the parallel tunnel. These layouts have an impact on the pulse compression scheme. In the SLED-II pulse compression scheme, the rf units can be configured in either a distributed or localized manner, although, if the rf units are localized, additional waveguide is needed to direct the power to the respective rf girders which will reduce the efficiency of the system.

### 3.3.3.5 Structures

The JLC-X/NLC linacs will each contain about 5 km of X-band accelerator structures to increase the beam energy from the 8 GeV at injection to 250 GeV for collisions at the IP. There are three basic requirements on the structure design: it must transfer the rf energy to the beam efficiently to keep the machine cost low; it must be optimized to reduce the

short-range wakefields which depend on the average iris radius; and it must suppress the long-range transverse wakefields to prevent multibunch beam breakup.

As part of the JLC-X/NLC development, many X-band accelerator structures have been constructed ranging in length from 20 cm to 1.8 meters. Originally, the focus of the structure R&D was on controlling the long-range wakefields. The acceleration gradient was not a major concern—short structures had quickly reached gradients much higher than needed in the JLC-X/NLC design and the longer structures were not tested because there was insufficient rf power available.

The long-range wakefield suppression was challenging because the wakefields must be reduced by two orders-of-magnitude within an inter-bunch spacing of 1.4 ns. The solution is to use a combination of detuning and damping. The detuning is generated by choosing the frequencies of the lowest (and strongest) band of dipole modes so that the modes excited by an off-axis bunch do not add constructively. This detuning produces an approximately Gaussian falloff in the net wakefield generated by each bunch. Detuning works well to suppress the wakefield for about the first 30 ns, after which the amplitude increases due to a partial recoherence of the mode excitations. To offset this rise, weak mode damping was introduced. The damping is achieved by coupling each cell through a longitudinal slot to four TE<sub>11</sub> circular waveguides that run parallel to the structure. Two of the circular waveguide manifolds are in the horizontal plane and couple to the vertically deflecting dipole modes while two are in the vertical plane and couple to the horizontally deflecting modes. At the ends of the structures, the circular manifold waveguide makes a transition to rectangular waveguide, which transports the power out of the structure to processing electronics so the signals can be used for beam position monitoring.

Until recently, the JLC-X/NLC design choice was a traveling-wave 1.8-m Rounded Damped Detuned Structure (RDDS) with 206-cells. The rf group velocity varies from 12%  $c$  at the upstream end to 3%  $c$  at the downstream end to achieve a nearly constant gradient along the structure. The basic parameters were defined primarily by the choice of average cell iris size, which determines the strength of the short-range (intra-bunch) transverse wakefield. The phase advance was chosen to be 120 degrees per cell, the same as in the SLAC S-band structure. This value gives a high shunt impedance per unit length for good efficiency. An average iris radius equal to 18% of the rf wavelength was chosen to limit the wakefield-related bunch emittance growth in the JLC-X/NLC linacs.

To build a structure, disks and cells are first rough-machined using regular lathes and milling machines. At this stage, more than 40  $\mu\text{m}$  of extra copper are left on all surfaces except the coupling slots and manifolds. Final machining is done to micron accuracy and 50 nm surface finish using single crystal diamond turning. The cells are carefully cleaned and rinsed with ozonized water, and then stacked in the V-block of a special fixture. The whole stack is pre-diffusion bonded at 180°C and final-diffusion bonded at 890°C. The final assembly including flanges, vacuum ports, WR90 waveguides for the fundamental mode, and WR62 waveguides for the dipole modes are brazed in a hydrogen furnace at 1020°C. The brazed section is then installed on a strongback for final mechanical measurement and straightening in a CMM (Coordinate Measuring Machine). Straightness at the  $\pm 20 \mu\text{m}$  level has been achieved over the length for some of the 1.8-m structures; this exceeds the JLC-X/NLC requirements.

## DESCRIPTIONS OF THE FOUR MACHINES AT 500 GEV C.M.

During the assembly process, microwave quality control is used to evaluate the cell and structure properties at several steps. This is particularly important since the cells are not designed to be tuned. As the cells are fabricated, the fundamental and dipole modes are measured to look for significant cell-to-cell deviations. Stacks of cells are also measured to verify that the phase advance is correct at 11.424 GHz. If the net phase error deviates by more than several degrees, then the dimensions of subsequent cells are modified to compensate the phase shift. After the structure is assembled, a semi-automated bead pull system is used to measure the field phase and amplitude along the structure.

To determine if the long-range wakefield of the structure is as predicted, the wakefield is measured in the Accelerator Structure SETup (ASSET) facility in the SLAC Linac. The positron beam passes first through the structure and induces a wakefield the effects of which are then observed with a trailing electron bunch. A comparison of the measurements and prediction is shown in Figure 3.45 for the RDDS1 structure. Although the agreement is excellent, the wakefield is larger than originally designed and is not acceptable for JLC-X/NLC. This is due to a defect in the final assembly procedure. Several cells of the structure were distorted by a support ring during the final braze of the vacuum manifolds onto the outside of the structure. This changed their frequency by about 30 MHz. To estimate the effect of this error, the phase advance of the fundamental mode was measured after assembly. A corresponding change in the dipole frequencies was then included in the wakefield prediction. Despite this localized defect, the random dipole frequency error of the rest of the cells is less than 1 MHz, which is demonstrated by the fact the wakefield dips to the 0.1 V/pC/m/mm level at about 25 ns. In earlier structures (DDS1 and DDS3), smaller wakefields were achieved.

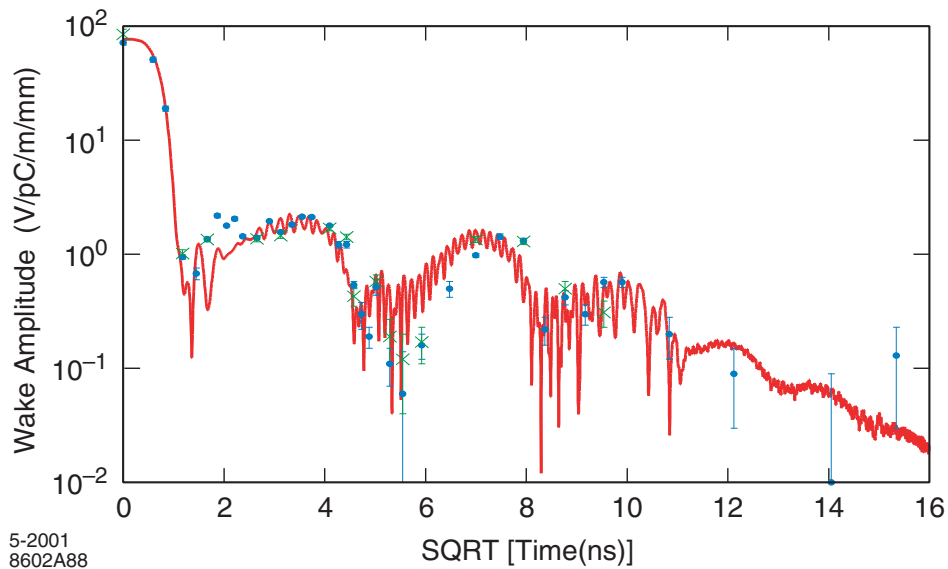


FIGURE 3.45. Comparison of measured and predicted wakefield for the RDDS1 structure.

Centering tests were also performed in ASSET using the dipole signals from the manifolds. The measured positions along the structure from the manifolds were compared with the results of mechanical measurements of the relative cell misalignments. The agreement was excellent at the 1–2  $\mu\text{m}$  level. In another test, two dipole readings were used as a guide to position the positron beam; this models the beam-based alignment technique proposed for the JLC-X/NLC. Measurements of the resulting short-range wakefield ( $< 300$  ps) indicated that the beam had been centered to less than 12  $\mu\text{m}$  rms in the structure. This measurement incorporates both the precision of the dipole mode measurement (estimated to be 1–2  $\mu\text{m}$  rms) and the internal structure misalignments. The resulting precision is close to the requirement for JLC-X/NLC operation.

The original design for the NLC Test Accelerator only delivered  $\sim 100$  MW to each 1.8-m accelerator structure to produce a gradient of roughly 50 MV/m—this was essentially the design described in the 1996 NLC ZDR. Four of the 1.8-m long structures that had been developed for the wakefield suppression studies were installed in the NLCTA and processed up to the desired 50-MV/m gradients.

The gradient limitations in the JLC-X/NLC prototype structures were only seen in 1999 when higher-power X-band sources were installed with the goal of generating gradients in excess of 70 MV/m. During this period, a 1.3-m JLC structure was also tested at the Klystron Test Laboratory at SLAC and it achieved gradients up to 85 MV/m with 150-ns pulses. However, the phase profiles from before and after processing of the JLC structure showed that the net phase shift through the structure had changed by 25 degrees, indicating significant changes to the cell dimensions. This shift occurred only in the upstream two-thirds of the structure with most of it at the upstream end. A visual inspection showed pitting along the irises of these upstream cells.

A similar pattern of damage was also observed when processing one of the 1.8 m damped, detuned structures to 70 MV/m with 240-ns pulses in the NLCTA. During about 1,000 hours of operation at high gradient, the net phase shift increased by 90 degrees. Once this degradation was seen, bead-pull measurements were made on the remaining three 1.8-m structures. All of these had about 500 hours of operation at gradients less than 55 MV/m. Although the phase shifts were much smaller, the same pattern of damage was observed.

Based on these results, it was hypothesized that the damage causing the phase shifts was related to the higher group velocity at the upstream end of the structures. To study the factors contributing to the damage, a series of six structures were built (called the T-Series) with different lengths (20, 53 and 105 cm) and lower group velocities (5%  $c$  and 3%  $c$  at the upstream ends). In addition, various improvements were made to the structure cleaning, handling and processing procedures to determine their impact on high-gradient performance.

The rf processing of the T-Series structures started at higher gradients (55–65 MV/m) than that (35–45 MV/m) for the 1.8 m structures. In addition, much less damage was observed in these structures at gradients above 70 MV/m than in the 1.8 m structures at gradients of 50–65 MV/m. After processing to 80–85 MV/m, the breakdown rate at 70 MV/m was dominated by events in the input and output couplers. The breakdown rates in the body of the structures (*i.e.*, excluding the couplers) at 70 MV/m were close to acceptable for the JLC-X/NLC at the design pulse width of 400 ns. For the three 53 cm, 3%  $c$  initial group

## DESCRIPTIONS OF THE FOUR MACHINES AT 500 GEV C.M.

velocity structures that were tested, the breakdown rates were  $< 0.1$ ,  $0.2$  and  $0.3$  per hour, respectively, while the goal is  $< 0.1$  per hour.

An autopsy of the input coupler on one of the structures revealed melting along the edges of the waveguide openings to the cell, and extensive pitting near these edges and on the coupler iris. The waveguide edges see large rf currents that are a strong function of their sharpness, and the associated pulse heating can be significant. By design, the edges in the T-Series structures were sharper ( $76\text{-}\mu\text{m}$  radius) than those in the 1.8-m structures ( $500\text{-}\mu\text{m}$  radius). Recent calculations have shown that the pulse heating for the T-Series structures is in the  $130\text{--}270^\circ\text{C}$  range, well below the copper melting point, but high enough to produce stress-induced cracking, which might enhance the heating.

Based on these observations, a 53 cm, 3% c structure was built with couplers designed to have much lower pulse heating. This structure is currently being tested and has performed very well, with no obvious enhancement of the coupler breakdown rates relative to the other cells. For the full structure, breakdown rates of about 1 per 25 hours at 73 MV/m and 1 per hour at 92 MV/m have been measured with 400 ns pulses. All future structures will be made with couplers similar those used in this test.

Although the results from the T-Series structures are very encouraging, their average cell iris radii are too small to meet JLC-X/NLC short-range wakefield requirements. To increase the iris size while maintaining a low group velocity, a structure design with thicker irises and a higher phase advance per cell ( $150^\circ$  instead of  $120^\circ$ ) design has been adopted. Two such structures (H-Series) have been built, one 60 cm long with an initial group velocity of 3% c, and the other 90 cm long with an initial group velocity of 5% c. Both are detuned for wakefield suppression, but do include manifolds for wakefield damping.

Unfortunately, these structures have the earlier, T-Series type couplers since they were built before the coupler pulse heating problem was discovered. Making the problem worse, the H-Series structures have lower shunt impedance than the T-Series structures, so the pulse heating is relatively high. During their processing at NLCTA, the coupler breakdowns have indeed limited the gradient to values lower than that achieved with the T-Series structures. In addition, at short pulse lengths where the coupler events did not dominate, the processing rate was much slower than that for the T-Series structures. The larger iris thicknesses of the H-Series structures are certainly a contributing factor, but they do not explain the full difference.

The best results to date in an H-series structure have been achieved with the 60 cm, 3% c structure, which has been processed to 72 MV/m with 400 ns pulses. At 65 MV/m, the current JLC-X/NLC design gradient, the breakdown rate in the body of this structure meets the goal of  $< 1$  per 10 hours. The program until Summer 2003 is to test several H-Series structures with improved couplers, culminating in one that is fully damped and detuned for wakefield suppression. Later, 5.4 m of such structures will be powered with the SLED-II rf source to demonstrate full system integration and to improve performance statistics.

### 3.3.4 Injectors

The NLC Injector System is designed to produce low emittance, 8 GeV electron and positron beams at 120 Hz for injection into the main linacs. Each beam consists of a train of 192 bunches of  $0.75 \times 10^{10}$  particles spaced by 1.4 ns. The horizontal and vertical

emittances are specified to be  $\gamma\epsilon_x=3.2 \mu\text{m}\cdot\text{rad}$  and  $\gamma\epsilon_y = 0.022 \mu\text{m}\cdot\text{rad}$  at injection into the main linacs, and the bunch length is in the range of 90 to 150  $\mu\text{m}$ . Electron polarization of greater than 80% is required. Electron and positron beams are generated in separate accelerator complexes, each of which contains the source, damping ring systems, L-band, S-band, and X-band linacs, bunch length compressors, and collimation regions.

The need for low technical risk, reliable injector subsystems has been a major consideration in the design effort. Technologies chosen for the design of the injector systems are solidly based on experience with previously built and operated high energy colliders and with third-generation synchrotron light sources. Polarized electrons are produced using a dc photocathode gun which is very similar to the successful SLC polarized source. Unpolarized positrons are generated using multiplexed target systems which will be run in parallel; the peak energy deposition in each target assembly is designed to be identical to that of the SLC positron system, which ran for more than 5 years without incident. The parameters of the two main damping rings are similar to the present generation of synchrotron light sources and the B-Factory colliders in that they must store high-current beams ( $\sim 1 \text{ A}$ ) while attaining small normalized emittances. The acceleration gradient in the injector S-band linacs is only modestly higher than the gradient in the SLC linac and the S-band klystrons are based on the 65 MW SLAC 5045 klystrons. Injector L-band linacs have been designed with low gradients to avoid problems associated with high fields in the structures or ancillary rf distribution systems. The X-band rf for the bunch length compressors is adapted from the main linac rf development.

There are two separate injector complexes to produce the low-emittance trains of electron and positron bunches for injection into the main linac. The electron injector includes a polarized photocathode gun, a bunching system and an S-band booster linac to deliver a 1.98 GeV beam to the damping ring. For the positron injector, an unpolarized electron gun and bunching system followed by a 6 GeV (10 GeV) drive linac provides the electron beam needed to produce positrons in the NLC (JLC) design. Multiple positron targets are required to keep the energy deposited in each target below the threshold for material damage. The electrons are split by an rf separator and directed onto 3 out of 4 multiplexed targets and positron capture sections. The bunches are then recombined into the desired bunch train format and accelerated in a 1.98 GeV L-band (S-band) linac to the positron pre-damping ring in the NLC (JLC) design. Because of the large emittance of the captured positrons, large-aperture L-band rf is used for acceleration and a pre-damping ring is required to reduce the emittance of the positrons before injection into the main damping ring. Two identical rings are used to damp the positron and electron bunch trains from the injectors to a normalized emittance of 3  $\mu\text{m}\cdot\text{rad}$  in the horizontal and 0.02  $\mu\text{m}\cdot\text{rad}$  in the vertical for the nominal 1.4 ns bunch spacing.

After extraction from the damping rings, the beam passes through a spin rotator system that can be used to orient the electron spin in an arbitrary direction to ensure longitudinal polarization of the beams at the IP. In the baseline design, the spin rotating solenoids are only installed in the electron beamline. However, the positron beamline is identical so that additional solenoids can easily be installed later for operation with either polarized positrons or with polarized electrons.

After the spin rotators, the bunch length must be compressed from 4 mm to 110  $\mu\text{m}$  before injection into the main X-band linacs. This is accomplished in a 2-stage bunch compressor that is identical for the two beams. The first stage uses an L-band rf section followed by a

wiggler to compress the bunch to a length of about 0.5 mm. This is followed by a 6 GeV S-band pre-linac and the second-stage bunch compressor with a  $180^\circ$  arc, an X-band rf section and a chicane. The second stage can produce a bunch length between 90 and  $150 \mu\text{m}$ . In the present layout, the electron booster and pre-linac are housed in the same tunnel to minimize infrastructure costs. The positron drive linac, booster and pre-linacs also share a common tunnel and support buildings.

Descriptions of the choice of injector layouts, the polarized electron source, the positron system, damping ring systems, and bunch length compression systems follow.

### 3.3.4.1 Polarized Electron Source

The electron injector source system creates polarized electron beams of the required energy and emittance for injection into the electron damping ring system. The polarized electron beams are produced with a DC photocathode electron gun, bunched in a 714 MHz subharmonic rf system and accelerated in an S-band linac to 1.98 GeV, the energy of the damping ring. Each beam consists of a bunch train of 192 bunches with  $0.8 \times 10^{10}$  particles per bunch that are spaced by 1.4 ns. The electrons at the end of the source booster linac are predicted to have an rms emittance of  $50 \mu\text{m}\cdot\text{rad}$  from PARMELA simulations. To ensure reliable operation, the system is required to produce beams with rms emittances that are less than twice the simulated value, *i.e.*,  $100 \mu\text{m}\cdot\text{rad}$ . In addition, the transverse jitter is specified to be less than the rms beam size and the energy jitter less than 1%. Finally, the spin polarization is specified to be 80%. All of these requirements are similar to those attained during operation of the SLC. A summary of the design parameters is given in Table 3.20.

The polarized electron source consists of a polarized high-power laser and a high-voltage dc gun with a semiconductor photocathode. Many of the performance requirements for the injector are similar to those in the SLC and the design of the injector is based on the successful SLC injector. The SLC polarized source generated 80% beam polarization. As long as ultra high vacuum conditions were maintained, the cathode lifetimes exceeded thousands of hours, and system availability approached 99%. The most notable differences between the present and the SLC design are the increase in gun high voltage from the SLC value of 120 kV to 175–200 kV and the use of 714 MHz rf for subharmonic bunching. For comparison, a 200 kV polarized electron gun is being developed at Nagoya University.

Improvement of the SLC photocathodes is required for the JLC-X/NLC operation because of the higher pulse charge requirements; the SLC source operated with a single polarized bunch of  $\sim 5 \times 10^{10}$ . Efforts by SLAC and the University of Wisconsin, and at Nagoya University are concentrating on developing cathodes with a highly doped surface layer to permit rapid dissipation of surface charge that builds up as beam is extracted. Recent tests using a strained layer cathode with a 75 Angstrom surface layer are extremely promising. Operating at 120 kV, up to  $8 \times 10^{11}$  electrons have been extracted by illuminating a 1 cm radius spot on the cathode. The polarization of the electrons was measured to be about 78% and no evidence of surface charge limit was observed. The maximum charge extracted was limited by available laser energy in the test laboratory. After being moved to the CID gun in the SLAC linac, the cathode has produced roughly  $10^{13} e^-$  in 300 ns, many times the JLC-X/NLC requirement of  $2 \times 10^{12} e^-$  in 267 ns from the gun. This cathode has been

TABLE 3.20

Beam parameters as delivered by the electron source system to the electron main damping ring system for the 1.4 ns bunch spacing option.

Bunch spacing	1.4 ns
Number of bunches	192
Particles/bunch	$0.8 \times 10^{10}$
Energy	1.98 GeV
Energy adjustability	$\pm 5\%$
Bunch energy variation	1% Full Width
Single bunch energy spread	1% Full Width
Emittance $\gamma\epsilon_{x,y}$ [rms]	100 $\mu\text{m}\cdot\text{rad}$
Bunch length $\sigma_z$	<10 mm
Train population uniformity	1% Full Width
Bunch-to-bunch population uniformity	2% rms
Repetition rate	120 Hz
Horizontal beam jitter $\Delta\gamma J_x$	50 $\mu\text{m}\cdot\text{rad}$
Vertical beam jitter $\Delta\gamma J_y$	50 $\mu\text{m}\cdot\text{rad}$
Polarization	80%
Beam power	58 kW

routinely operating for 6 months during the E-158 physics run. The polarization measured during the E-158 run was about 85%.

An S-band linac is used to accelerate the captured electrons up to the damping ring energy of 1.98 GeV. The loaded gradient of the linac is 17 MeV/m. This linac will use KEK-style SLED systems for rf pulse compression which have been designed and operated at higher field levels than the original SLAC-style SLED systems. Beam emittance growth through the booster linac is not a problem because of the low charge per bunch (in comparison to SLC operation) and because of the relatively large damping ring design acceptance. Standard quadrupole focusing elements are employed together with discrete steering dipoles along the length of the booster linac. Multibunch beam loading in the linac is compensated using the  $\Delta T$  method in which the beam is injected into the accelerator before the rf has fully filled the structures. Fine tuning of the amplitude of the rf in a prescribed fashion after the beam has been injected provides additional control over the energy spread. An energy compression system has been included in the transport line that leads from the end of the linac to the main damping ring to further stabilize the energy and reduce the energy spread of injected bunches by a factor of roughly 2.

To measure the beam emittance, 4-wire parasitic emittance diagnostics are located after the  $e^-$  source (at 80 MeV) and before injection into the main damping ring. In addition, energy, energy spread, and bunch length diagnostics are located in a chicane at the 80 MeV point and in the  $60^\circ$  arc before injection into the main damping ring. To preserve electron helicity, the spin must be rotated into the vertical direction prior to injection into the

damping ring. The  $60^\circ$  arc also rotates the polarization vector from the longitudinal direction into the  $x - y$  plane and a subsequent superconducting solenoid then orients the polarization vertically. To stabilize the trajectory and preserve the emittance, all the quadrupoles have BPMs with  $10 \mu\text{m}$  resolution and horizontal or vertical steering correctors depending on the focusing plane.

### 3.3.4.2 Positron Source

The positron injector source system creates positron beams of the required energy and emittance for injection into the positron damping rings. In the NLC design, positrons are produced by colliding 6.2 GeV electrons into three separate high  $Z$  material targets, capturing the resulting positrons, and accelerating them to the 1.98 GeV energy of the pre-damping ring system. Each beam consists of a bunch train of 192 bunches with  $0.9 \times 10^{10}$  particles that are spaced by 1.4 ns (or 96 bunches with twice the charge that are spaced by 2.8 ns). As required by the pre-damping ring acceptance, the positrons have an edge emittance of 0.03 m-rad and a transverse jitter that is less than 0.015 m-rad; this jitter corresponds to about a 7 mm oscillation at the damping ring entrance. Table 3.21 lists the positron beam parameters required for injection into the pre-damping ring system.

TABLE 3.21

Beam parameters delivered by the positron source system to the positron pre-damping ring system for the 1.4 bunch spacing option.

Bunch spacing	1.4 ns
Number of bunches	192
Particles/bunch	$0.9 \times 10^{10}$
Energy	1.98 GeV
Energy adjustability	$\pm 5\%$
Bunch energy variation	1% Full Width
Single bunch energy spread	2% Full Width
Emittance $\gamma\epsilon_{x,y}$ (edge)	30,000 $\mu\text{m}\cdot\text{rad}$
Bunch length $\sigma_z$	<10 mm
Train population uniformity	1% Full Width
Bunch-to-bunch population uniformity	2% rms
Repetition rate	120 Hz
Horizontal beam jitter $\Delta\gamma J_x$	15,000 $\mu\text{m}\cdot\text{rad}$
Vertical beam jitter $\Delta\gamma J_x$	15,000 $\mu\text{m}\cdot\text{rad}$
Beam power	65 kW

The design of the positron system is based on the system used for the SLC, which demonstrated excellent reliability over many years of operation. The total number of positrons required for the JLC-X/NLC bunch train is almost two orders of magnitude greater than the number of positrons in the single SLC bunch. The design goal is to build a

target system which is expected to survive a 9 month run (120 Hz, 24 hours per day, 7 days per week, with no scheduled outages for maintenance). Targets can be replaced/repared annually in a scheduled 3 month maintenance period.

Positrons are produced by targeting a 6.2 GeV electron beam onto a *WRe* target to create an electro-magnetic shower. The positrons produced in the shower are collected using a 5.8 Tesla magnetic flux concentrator, accelerated to 250 MeV in L-band structures encased in a 0.5 Tesla solenoidal magnetic field, and then injected into an L-band linac and accelerated to 1.98 GeV. The average deposited power is handled by rotating the target and removing the excess heat through water cooling. Of critical concern for target damage is the instantaneous energy deposition per unit volume.

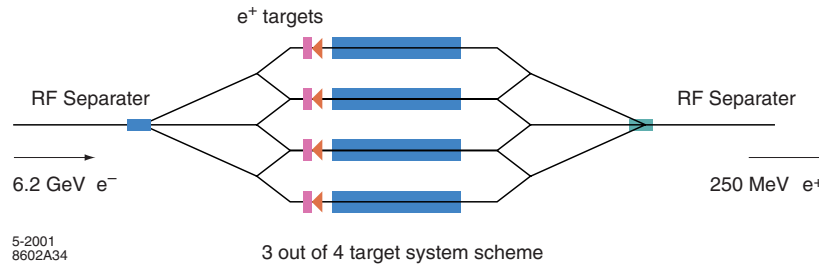
After approximately 1000 days of operation ( $\sim 5$  calendar years), the SLC positron system failed. Upon examination it was found that a water-to-vacuum leak had occurred in one of the target cooling tubes. In addition, cracking and material ejection were found on the exit face of the target.

The peak energy deposition in the SLC target was about 50 J/g under the conditions at which the target failed. This level produces an instantaneous mechanical shock in the *WRe* target material which is about a factor of 2 below the expected ultimate tensile strength of pristine material. However, material hardening of a factor of about 2 from target entrance to target exit was measured along the beam path. The calculated radiation damage to the material is in excess of 3 dislocations per atom (dpa) and the target embrittlement and subsequent loss of material integrity are consistent with the calculated exposure level.

Because of the consistency of the observed damage with expectations from the simulations, it has been decided to limit the shock in the targets to that of the SLC system. In particular, the peak energy deposition and irradiation fluences will be kept by design to less than 50 J/g and 1 dpa. Investigations into the connection between radiation damage due to electrons with that from neutron/proton exposure are continuing. It is useful to tap into the data on material property degradation due to neutron/proton damage since the database of electron induced damage is comparatively limited. Beam tests at SLAC are underway to determine the threshold for material damage and a model of the expected damage is being developed. To date, samples of *Ti*, *Cu*, GlidCop, *Ni*, *Ta*, *W*, and *WRe* have been irradiated in the FFTB area at SLAC. Additional studies will be aimed at developing an optimized target material. Induced damage to candidate target materials will be studied using the E158 beam at SLAC ( $5 \times 10^{11} e^-$ /pulse at 45 GeV, 200–300 ns pulse width, and focusable to small spots).

In order to keep the peak shock stress in the target below the threshold for damage, three  $e^+$  targets operating in parallel are planned to produce the JLC-X/NLC beam. To assure overall system availability, a layout has been adopted where there are 4 target/capture modules, 3 of which are operating at any one time as illustrated in Figure 3.46. The bunches are separated using an rf separator and then directed to the desired targets using dc bending magnets. Access is possible to the fourth target/capture module for maintenance and repair while the other 3 modules are in operation.

The 6.2 GeV electron drive beam, which is used to create the positrons, is based on S-band technology. Because of the need to use three quasi-independent target/capture sections for positron production, the electrons will be generated using a photocathode based source. Fine tuning of the individual electron bunch populations within the drive train is possible


 FIGURE 3.46. Schematic of the conventional  $e^+$  production system.

through bunch-to-bunch intensity adjustments at the source laser. The unpolarized electron source system is essentially identical to the polarized electron source with the exception that shorter laser wavelengths and photocathodes with higher quantum yields will be used.

Positron yield is defined as the number of positrons captured in the pre-damping ring divided by the number of electrons incident on the target. The NLC has adopted the use of L-band (1.4 GHz) for both the initial 250 MeV capture and 1.73 GeV booster linacs. The larger aperture and longer wavelength of the L-band affords a factor of about 30 increase in acceptance over an S-band system. Yield into the pre-damping ring acceptance is calculated based on the initial  $e^+$  distribution, generated using EGS4. The calculated yield is about 1.5, but experience with the SLC shows that this yield can be rapidly degraded by alignment and optical errors in the transport between the  $e^+$  source and the damping rings. It is believed that a 50% margin in the yield should be sufficient. If necessary, the population of the drive  $e^-$  beam can be increased somewhat to produce the desired number of  $e^+$ .

To measure the beam emittance, 4-wire parasitic emittance diagnostics will be located after the 250 MeV point in the  $e^+$  beam line and before injection into the pre-damping ring. In addition, energy, energy spread, and bunch length diagnostics are located in a chicane at the 250 MeV point and in the  $60^\circ$  arc before injection into the pre-damping ring. To stabilize the trajectory and preserve the emittance all of the quadrupoles have BPMs with  $10 \mu\text{m}$  resolution and horizontal or vertical steering correctors depending on the focusing plane.

### 3.3.4.3 Damping Rings

The JLC-X/NLC damping rings are designed to damp the incoming electron and positron beams to the small emittances needed for collisions. The rings have three purposes: (1) damping the incoming emittances in all three planes, (2) damping incoming transients and providing a stable platform for the downstream portion of the accelerator, and (3) delaying the bunches so that feedforward systems can be used to compensate for charge fluctuations. To meet these goals, three damping rings have been designed: two identical main damping rings, one for the electrons and one for the positrons, and a pre-damping ring for the positrons. The pre-damping ring is needed because the emittance of the incoming positrons is much larger than that of the electrons. Each damping ring will store multiple trains of bunches at once. At every machine cycle, a single fully damped bunch train is extracted from the ring while a new bunch train is injected. In this manner, each bunch train can be damped for many machine cycles.

At the SLC, the damping rings were one of the most problematic subsystems. This was because the downstream systems are extremely sensitive to small changes in the injected beams, and because the beams are stored in the rings for a relatively long time, which makes them more sensitive to subtle accelerator physics effects. The parameters of the JLC-X/NLC main damping rings are similar to the present generation of synchrotron light sources and the B-Factory colliders in that they must store high-current beams ( $\sim 1$  A) while attaining small normalized emittances. Table 3.22 compares the damping ring parameters with those of the SLAC B-Factory Low-Energy Ring (PEP-II LER), the Advanced Light Source (ALS) at Lawrence Berkeley National Laboratory, and the Accelerator Test Facility (ATF) damping ring at KEK in Japan. In particular, the stored beam currents are less than half of what the PEP-II LER has achieved, while the emittance, energy, and size of the rings are similar to those of the ALS and the ATF. These other rings have been largely successful in meeting their design parameters, and have been able to test and verify many of the accelerator physics and technology issues that will arise in the damping rings. We believe that this provides confidence that the JLC-X/NLC rings will operate as required.

TABLE 3.22  
Comparison of NLC main damping rings with design parameters of other rings.

	NLC MDR	PEP-II LER	LBNL ALS	KEK ATF
Energy [GeV]	1.98	3.1	1.5	1.54
Circumference [m]	300	2200	197	139
Current [A]	0.8	2.16	0.4	0.6
Equilib. $\gamma\epsilon_x$ [ $\mu\text{m}\cdot\text{rad}$ ]	2.17	400	12	2.8
Equilib. $\gamma\epsilon_y$ [ $\mu\text{m}\cdot\text{rad}$ ]	0.014	12	0.12	0.028

Issues associated with the very small beam emittances, such as intrabeam scattering and ion trapping, continue to be studied in the ALS and ATF. The ATF has achieved emittances of  $\gamma\epsilon_x=2.8 \mu\text{m}\cdot\text{rad}$  and  $\gamma\epsilon_y=0.028 \mu\text{m}\cdot\text{rad}$ , close to those desired in the main damping rings; work continues to improve the performance, which is primarily limited by the diagnostics in that machine. Experiments have also been performed at low energy (1 GeV) in the ALS, where the measured emittances of  $10^9$  particles are  $\gamma\epsilon_x=4 \mu\text{m}\cdot\text{rad}$  and  $\gamma\epsilon_y=0.07 \mu\text{m}\cdot\text{rad}$ . These measurements, combined with theoretical modelling, are designed to improve the understanding of the process of intrabeam scattering in electron storage rings, and to increase confidence in the predictions for the damping rings.

In addition, the PEP-II LER at SLAC, the KEK-B LER at KEK, and the Advanced Photon Source (APS) at Argonne have been used to study the electron-cloud instability and have shown success in controlling and understanding the phenomenon. Simulations based on a simple circular vacuum chamber predict that the growth times of transverse instabilities driven by the electron cloud are greater than  $100 \mu\text{s}$  and can be controlled with a broadband feedback system. The NLC vacuum system design includes an antechamber in which synchrotron radiation is absorbed, significantly reducing the number of photoelectrons in the beam duct and the chamber will likely use a *TiN* or similar coating to reduce the number of secondary electrons.

The similarities with other rings have also simplified the design process, and experience at these other accelerators will continue to be applied to benefit the damping rings designs. For example: the damping ring rf system is based on the higher-order-mode damped cavity designs successfully operating at the SLAC B-Factory and the ATF damping ring, the multibunch feedback systems are based upon the feedback systems successfully verified at the SLAC B-Factory and the ALS, and the vacuum system is similar to that used by the ALS. Furthermore, the design uses “C” quadrupole and sextupole magnets similar to those used at the ALS and the APS, a high-field permanent magnet wiggler similar to those in use at third generation light sources, and a double kicker system for extraction similar to one operational in the ATF. The successful demonstration of these and other systems and components allows a high degree of confidence in achieving the damping ring parameters.

The NLC damping ring complex is designed to operate with the parameters listed in Table 3.23 and the positron damping ring complex is illustrated schematically in Figure 3.47; the JLC design is similar although the repetition rate is slightly different. These design parameters satisfy the requirements of all presently considered NLC upgrades. The rings produce extracted electron and positron beams with emittances  $\gamma\epsilon_x=3 \mu\text{m}\cdot\text{rad}$  and  $\gamma\epsilon_y=0.02 \mu\text{m}\cdot\text{rad}$ , at a repetition rate of 120 Hz. Designs have also been developed which allow repetition rates as high as 180 Hz; in this case, the use of two main damping rings is proposed. The beams in the damping rings consist of multiple trains of 192 bunches with an injected single bunch charge of  $0.8 \times 10^{10}$ . To provide operational flexibility, the rings have been designed to also accommodate trains of 96 bunches spaced by 2.8 ns with maximum single bunch charge of  $1.6 \times 10^{10}$  in the main rings ( $1.8 \times 10^{10}$  in the pre-damping ring), and to operate with a peak current roughly 15% higher than the nominal peak current. In addition, the electron source has been designed to provide additional charge to allow for at least 10% losses during injection into the electron damping ring. Similarly, the positron source has been designed to produce at least 20% additional charge to provide for losses during injection into the pre-damping ring. Finally, the rings have been designed to operate at 1.98 GeV, with an energy range of 5%—1.98 GeV corresponds to a spin tune of 4.5 where depolarizing spin resonances are expected to be small. The energy adjustability will allow the damping rate and/or spin tunes to be shifted, if necessary.

TABLE 3.23  
Requirements for NLC main damping rings.

Repetition rate [Hz]	120
Bunches per train	192
Bunch spacing [ns]	1.4
Bunch population	$0.8 \times 10^{10}$
$\gamma\epsilon_x$ equilib. / $\gamma\epsilon_x$ extract. [ $10^{-6}$ m·rad]	3.0 / 3.0
$\gamma\epsilon_y$ equilib. / $\gamma\epsilon_y$ extract. [ $10^{-8}$ m·rad]	1.4 / 2.0

**3.3.4.3.1 Main Damping Rings** The NLC main damping rings are roughly 300 m in circumference and they measure roughly 60 m by 100 m with a nominal energy of 1.98 GeV. The rings are designed in a racetrack form with two arcs separated by straight

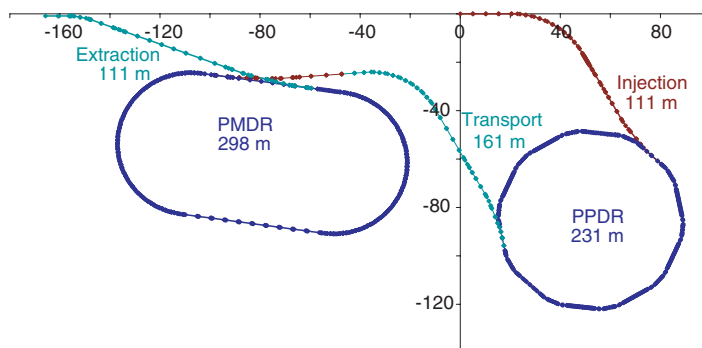


FIGURE 3.47. Schematic of NLC positron damping ring complex.

sections. The main damping rings are designed to damp beams with injected emittances  $\gamma\epsilon_{x,y}=1.5\times 10^{-4}$  m·rad to give extracted beam emittances of  $\gamma\epsilon_x=3\times 10^{-6}$  m·rad and  $\gamma\epsilon_y=2\times 10^{-8}$  m·rad. The rings will operate at 120 Hz. They provide sufficient damping to decrease the injected emittance by four orders of magnitude. The parameters are summarized in Table 3.24 for the main damping rings (MDR), and the positron pre-damping ring (PPDR). The main damping ring lattice is based on detuned Theoretical Minimum Emittance (TME) cells, which were chosen because of efficiency in generating low emittance and eased requirements on the combined-function bending magnets. The chromaticity is corrected with two families of sextupoles and the dynamic aperture is more than sufficient to ensure lossless injection. The damping is performed using both high-field bending magnets and ten 4.6 m sections of damping wiggler.

The dynamic aperture, including effects of errors, is predicted to be in excess of 15 times the injected beam size. Potential limitations due to the contribution from the 46 m of wiggler magnet have been studied. Analytical expressions of arbitrary three-dimensional wiggler fields have been developed, and tracking including the non-linear components of the wiggler field will be used to determine the minimum pole width requirement for the 2.15 T hybrid wiggler magnet. Preliminary analysis indicates that the wiggler with a magnet pole width of 11 cm does not seriously impact the dynamic aperture.

The rings operate with three trains of 192 bunches spaced by 1.4 ns or 96 bunches spaced by 2.8 ns. The bunch trains are injected onto and extracted from the closed orbit using pulsed kickers and DC septa. The bunch trains are separated by 65 ns to allow for the rise and fall times of the injection and extraction kickers. To avoid coupled-bunch instabilities the rf cavities use higher-order-mode damping, based on the PEP-II design, and a transverse bunch-by-bunch feedback system. As stated, the rings are designed to operate with maximum bunch charges of  $1.6\times 10^{10}$  particles; this is roughly 10% more than the maximum needed at the IP with a 2.8 ns bunch spacing.

Finally, because the rings must generate extremely small beam emittances, there are tight jitter and alignment tolerances. Extensive effort has been made to include cancellations and tuning procedures in the design that will ease the tolerances to reasonable levels. Skew quadrupole windings will be incorporated in sextupole magnets to facilitate coupling correction. Quadrupoles and sextupoles will have independent trim control, and magnet movers will be used to facilitate beam-based alignment. BPMs, having a  $1\ \mu\text{m}$  resolution

TABLE 3.24

Parameters for main damping rings and the pre-damping ring.

	MDR	PPDR
Circumference [m]	299.792	230.933
Energy [GeV]	1.98	1.98
Maximum current [A]	0.8	0.75
Maximum repetition rate [Hz]	120	120
Bunch trains $\times$ bunches per train	$3 \times 192$	$2 \times 192$
Train / bunch separation [ns]	65 / 1.4	100 / 1.4
$\nu_x, \nu_y, \nu_s$	27.26, 11.13, 0.0035	11.45, 5.45, 0.0114
$\gamma\epsilon_x$ equilib. [ $\mu\text{m}\cdot\text{rad}$ ]	2.17	60
$\gamma\epsilon_x$ extract., $\gamma\epsilon_y$ extract. [ $\mu\text{m}\cdot\text{rad}$ ]	3.0, 0.02	127, 70
$\sigma_{\Delta E/E}, \sigma_z$	0.09%, 3.6 mm	0.08%, 5.1 mm
$\xi_x$ uncorr., $\xi_y$ uncorr.	-37.12, -28.24	-10.39, -12.23
$\tau_x, \tau_y, \tau_\epsilon$ [ms]	4.76, 5.00, 2.60	5.85, 5.81, 2.90
$U_{sr}$ [kV/turn]	777	525
$\alpha_p$	$2.95 \times 10^{-4}$	$2.00 \times 10^{-3}$
$V_{RF}$	1.1 MV, 714 MHz	1.5 MV, 714 MHz
Lattice	36 TME cells	10 DBA cells

for single turn measurements and  $< 0.3 \mu\text{m}$  resolution for the stored orbit, will be located at every quadrupole. In addition, a synchrotron radiation port will be used for bunch length and initial beam size measurements and, a laser wire, like the system commissioned at the ATF at KEK, will likely be used to measure the damped beam. There will be a 4-wire parasitic emittance measurement as well as energy and energy spread diagnostics located in the extraction line before the spin rotator and first stage bunch compressor. Additional emittance, energy spread and bunch length diagnostics will be located in and after the first stage bunch compressor.

**3.3.4.3.2 Positron Pre-Damping Ring** The pre-damping ring is roughly 230 m in circumference and has 10 dispersion-free straight sections for injection, extraction, rf, circumference correction chicanes, and damping wigglers; the latter have a total length of roughly 50 m. The ring has a radius of roughly 40 meters. It stores two bunch trains which are separated by more than 100 ns to allow for the rise and fall times of the injection and extraction kickers—these kickers must provide larger deflections than those in the main damping rings. To minimize rf transients during injection and extraction, a new bunch train will be injected one half turn after a train is extracted. In addition, the rf cavities are placed downstream of the injection kicker and upstream of the extraction kicker so that the injection/extraction process will not interrupt the beam current seen by the cavities.

The positron pre-damping ring is designed to damp the large emittance beam from the positron source to an emittance of less than  $\gamma\epsilon_{x,y} = 1.5 \times 10^{-4}$  m-rad; the parameters are

summarized in Table 3.24. The extracted positrons are then injected into the main damping ring where they are damped to the desired final emittances. The pre-damping ring allows the large aperture requirements for the incoming positron beams to be decoupled from the final emittance requirements of the linear collider.

The magnets and vacuum systems are designed to provide sufficient aperture to accept a 2-GeV beam with an edge emittance of  $\gamma\epsilon_{x,y}=0.03$  m-rad and momentum spread of  $|dp/p|=1.5\%$  plus betatron-action jitter of  $\Delta\gamma J_{x,y}=0.015$  m-rad for misalignments and missteering; this provides a substantial margin for injection and internal mismatches. In addition, the injector specifications allow significant overhead for injection losses into the pre-damping ring. The pre-damping ring is designed to operate with a maximum bunch charge that is roughly 20% greater than the maximum required at the IP.

Like the main damping rings, quadrupoles and sextupoles will have independent trim control, and magnet movers will be used to facilitate beam-based alignment as well as matching of the lattice functions, which is especially important in the pre-damping ring because of the limited aperture. BPMs will be located at every quadrupole and will have a resolution better than  $15\ \mu\text{m}$  for a single turn and  $5\ \mu\text{m}$  after averaging the stored orbit. In addition, a synchrotron radiation port will be used for bunch length and beam size measurements. There will be a beam size as well as energy and energy spread diagnostics located in the transfer line to the main damping ring.

### 3.3.4.4 Bunch Length Compressors

The bunch compressors must reduce the  $\sim 4$  mm rms length of the bunches extracted from the damping rings to the 90 to 150  $\mu\text{m}$  bunch length required for the main linacs and final focus systems. A two-stage compressor system has been designed in which the first stage follows the damping ring and the second stage is at the exit of the S-band pre-linac at a beam energy of 8 GeV. Electron and positron bunch compression systems are identical. The bunch compressor system has been designed to meet the following additional goals:

(1) Multibunch phase variations in the damping ring of up to  $\pm 5$  mm should not produce relative energy variations that are larger than  $\pm 0.1\%$  in the final focus systems. (2) The system should include a  $180^\circ$  turn-around arc to permit future main linac extensions and to allow beam abort and feedforward systems. (3) The transverse emittances must be preserved to within a reasonable budget with diagnostics and correction elements included in the design. (4) The compression systems should not depolarize the beams.

The two-stage system has a number of advantages over a single-stage compressor. In particular, it keeps the rms energy spread less than about 2% and the bunch length is more naturally matched to the acceleration rf frequency so that energy spread due to the longitudinal wakefields can be cancelled locally. The disadvantage of the two-stage design is that it is more complex and lengthy than a single-stage compressor. The first stage rotates the longitudinal phase by  $\frac{\pi}{2}$  while the second stage performs a  $2\pi$  rotation. In this manner, phase errors due to the beam loading in the damping rings and energy errors due to imperfect multibunch energy compensation in the 6 GeV S-band pre-linacs do not affect the beam phase at injection into the main linac.

Assuming an incoming rms energy spread of  $\sigma_\delta = 1 \times 10^{-3}$  and rms bunch length of  $\sigma_z=5$  mm, the first stage compresses the damping ring beam to a bunch length of about

0.6 mm. This stage consists of a 140 MV L-band (1.4 GHz) rf section followed by a long period wiggler which generates the momentum compaction needed for the bunch compression. The second bunch compression stage follows the 6 GeV pre-linac. The nominal configuration compresses the beam to a bunch length of 110  $\mu\text{m}$ . This compressor is a telescope in longitudinal phase space which rotates the phase space by  $2\pi$ . It consists of a  $180^\circ$  arc which is followed by a 600 MeV X-band (11.4 GHz) rf section and a chicane. Adjustments to either the low-energy or the high-energy compressors permit control of the final bunch length over the specified range of 150 to 90  $\mu\text{m}$ .

One of the rationales behind the compressor design has been to utilize naturally achromatic magnetic lattices wherever the beam energy spread is large. In particular, the optics is chosen so that quadrupoles are not placed in regions of large dispersion and strong sextupoles are not needed. This choice arises from experience with the second-order achromats in the SLC bunch compressors in which quadrupoles are located in dispersive regions and strong sextupoles are used to cancel the chromatic aberrations. Unfortunately, the SLC design was difficult to operate and tune because of large nonlinearities and sensitivity to multipole errors in the quadrupoles; over the years additional nonlinear elements were added (skew sextupoles and octupoles) to help cancel the residual aberrations but tuning remained problematic. To facilitate tuning, orthogonal tuning controls and diagnostics have been explicitly designed into the NLC system, which should make it relatively straightforward to operate. Details of the diagnostic equipment can be found in the optics decks.

Finally, although the tolerances on components in the bunch compressor systems are not nearly as tight as in the main linacs or the final focus systems, the same methods of beam-based alignment and tuning have been adopted. In particular, to ease the alignment procedures, all of the quadrupoles will be mounted on magnet movers and each quadrupole will contain a BPM with a resolution of  $< 2 \mu\text{m}$ . Similarly, all of the accelerator structures will be instrumented with rf BPMs to measure the induced dipole modes and each rf girder will be remotely movable for minimization of wakefields. There will be 4-wire parasitic emittance measurement sections and subsequent tune-up dumps after the first-stage bunch compressors, the 6 GeV pre-linacs, and the second-stage bunch compressors before injection into the main linac. There will also be synchrotron radiation-based bunch length and energy spread diagnostics in the first-stage wigglers, the second-stage arcs, and the second stage chicanes and there will be rf deflector-based bunch length monitors before injection into the main linac.

### 3.3.5 Beam Delivery

The beam delivery system (BDS) must both reduce the beams to the sizes required to produce luminosity and remove any particles that are far enough from the beam core to produce unacceptable detector backgrounds. In addition, the BDS must provide protection for the detector and beamline components against missteered beams emerging from the main linacs, and must safely transport the collided beams to water-cooled dumps which can absorb the high beam power density without damage. Finally, the BDS must provide instrumentation that can monitor the parameters of the collided beams, such as the energy spread and polarization after collision, which are required by the particle physics experiments.

Although the parameters of the JLC-X/NLC BDS are far beyond anything that has been achieved in a storage ring, the SLC demonstrated the viability of a fully integrated linear collider beam delivery system with millimeter-sized betatron functions and routine collision of beams with rms sizes of under  $1\ \mu\text{m}$ . The FFTB at SLAC was a single-beam demonstration of a linear collider beam delivery system with IP betatron functions comparable to those in the JLC-X/NLC. The BDS design is based upon experience from these two facilities. In addition, a vigorous R&D program on passive and active magnet position stabilization, ground motion, materials damage thresholds, and instabilities driven by collimators close to the beam have all yielded insights which have been incorporated into the design of the system.

The layout of the BDS components is shown in Figure 3.48. The six main subsystems of the beam delivery, from upstream to downstream, are: the emittance diagnostic and skew correction region, which provides parasitic measurement of the beam emittance and an orthogonal set of four skew quadrupoles to correct all sources of betatron coupling in the beam; the IR transport, which separates the beamlines to the low and high-energy IRs; the collimation system, which provides protection from errant beams and removes particles which might cause backgrounds; the final focus (FF), which focuses the beams down to the small spots; the IRs, which provides detector masking and specialized supports for the final doublet quadrupoles of the final focus; and the extraction line, which transports the spent beams to their respective dumps and provides the post-collision beam measurements. In addition, a high-power pulsed beam dump, which is not shown, is located in the energy collimation region to allow the full-power linac beam to be tuned before sending the beam through the final focus.

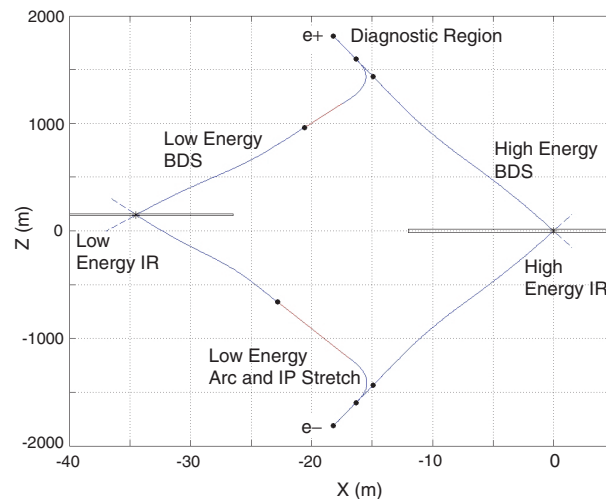


FIGURE 3.48. Beam delivery system layout with two interaction regions separated by 150 m longitudinally.

The beamline for the high energy IR is 1.8 km long. This distance includes a 1.4 km long collimation and final focus region, a 150 meter region where the beamlines for the low-energy IR diverge, and a 200 meter emittance diagnostic and skew correction section. The low-energy IR beamline splits off at the end of diagnostic region and includes arcs that bend the beam by about 25 mrad and a shorter 800 meter collimation region and final focus. The two IRs are separated by about 35 m transversely and 150 m longitudinally to provide vibration isolation and shielding so either IR hall may be accessed while the other is in operation.

### 3.3.5.1 Final Focus

The role of the final focus is to reduce the size of the beam at the IP sufficiently to provide the required luminosity. The small beam sizes are achieved using strong quadrupole magnets close to the IP to focus the low emittance beams and reducing  $\beta_{x,y}^*$  to  $8 \times 0.11$  mm. Unfortunately, the final quadrupoles also generate a huge chromaticity which, if uncorrected, would increase the spot sizes by one to two orders of magnitude.

Correcting the chromaticity of the final quadrupole doublet is the issue that drives much of the design. In the final focus systems used at the SLC and the FFTB, which were also the basis of the 1996 NLC ZDR final focus design, the chromaticity correction was accomplished in dedicated “chromaticity correction sections.” In these sections, a combination of bend magnets and sextupoles generated a chromaticity equal-and-opposite to that of the final doublet. Once the chromaticity of the final focus was corrected, the principal aberration to be cancelled was generated by the sextupoles that were required for chromaticity correction. This was accomplished by placing additional sextupoles in the beamline, with optical transformations between sextupoles which caused the geometric aberrations of the sextupoles to cancel while the chromatic aberrations remained.

In the SLC and FFTB, each of the sextupoles in a matched pair contributed 50% of the chromaticity correction. The combined effect of the chromaticities of the sextupoles, the quads between the sextupoles, the quads between the last sextupole and the final doublet, and the doublet chromaticity caused these designs to provide correct focusing to only a narrow range of particle energies. The 1997 JLC design by Oide ameliorated this limitation by generating as much of the chromaticity correction as possible in the sextupoles closest to the IP, rather than splitting it equally among the pairs of sextupoles in a given family.

The present NLC final focus design uses an extreme form of Oide’s asymmetric solution which places the chromaticity correction sextupoles in the final doublet itself. This configuration requires a horizontal dispersion through the final doublet, which is tuned to be exactly zero at the IP. The optics of the combined NLC final focus and the upstream collimations system are shown in Figure 3.49.

There are three clear advantages of the new final focus optics: first, the system requires many fewer magnets and is conceptually simpler. Second, it addresses a limitation of the earlier designs where the energy loss from synchrotron radiation between the last sextupole and the IP had to be minimized to avoid causing a breakdown of the chromaticity correction. Because of this requirement the bending magnets in the conventional final foci were weak, and the systems were correspondingly long. The present NLC configuration is much shorter than previous final-focus systems: less than 0.4 km is required for 750-GeV

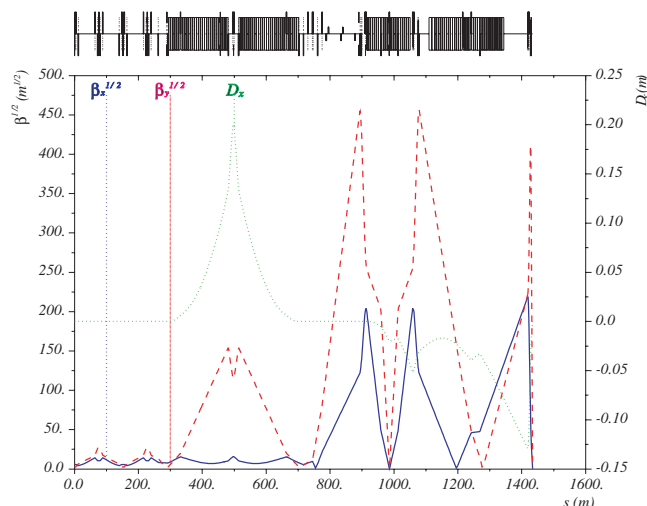


FIGURE 3.49. Optics of the NLC collimation and final focus systems.

beams as compared to 1.8 km in the NLC ZDR design and the present length of 0.7 km will handle 2500-GeV beams; the energy reach of the final focus is shown in Figure 3.50. Third, in the new design, off-energy particles tend to have small amplitudes in the final doublet magnet, whereas nonlinearities in the traditional final-focus systems tended to drive off-energy particles to very large amplitudes in the final doublet. The effect of the nonlinear amplitudes has not been considered in the past but the new design will simplify the beam collimation requirements significantly.

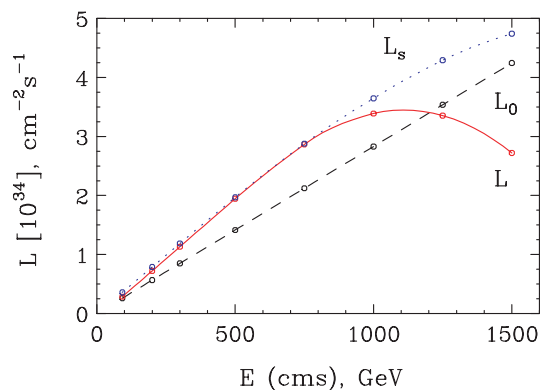


FIGURE 3.50. Energy reach of the NLC final focus where  $L_0$  is the luminosity without the pinch enhancement,  $L$  is the nominal luminosity, and  $L_s$  is the luminosity after scaling the bending magnets. By scaling the bending magnets in a manner to maintain the IP position the present system can accommodate beam energies well above 1500 GeV.

### 3.3.5.2 Collimation System

The collimation system must remove particles in the beam tails that can generate backgrounds in the detector and it must protect the final focus and detector from errant beams. As is well known, the population and distribution of the beam tails can be very hard to calculate and, because the backgrounds can severely limit the luminosity recorded by the detector, the collimation system must be designed quite conservatively. Beam collimation was one of the limiting factors in the SLC operation.

The collimation system must remove all primary beam particles which could be lost near the detector. However, tighter constraints arise due to the synchrotron radiation produced by the large amplitude particles in the final doublet focusing magnets. Because of the high beam energy, the photons emitted as the beam is focused in the final doublet have energies that are too high to be able to shield the detector with masking in the IR. Ray tracing shows that to prevent any synchrotron radiation photons from hitting in the IR, the angular divergence of the beam at the IP cannot exceed a rectangular aperture of  $570 \mu\text{rad}$  horizontally by  $1400 \mu\text{rad}$  vertically. This restriction on the beam tails is significantly tighter than that to prevent primary particles from hitting the vacuum apertures.

Another important consideration is the muons produced by the collimators when the high energy tails are removed. Simulation studies have shown that as many as  $10^9$  primary electrons or positrons per train can be removed by a collimation system located well upstream of the final focus without producing an unacceptable muon flux in the detector, although this number depends somewhat upon the exact configuration of the beamline. The number of primary particles that can be stopped within the final focus without unacceptable muon production is only  $10^4$ .

The most easily estimated source of beam tails in the linac is elastic scattering off the residual gas in the vacuum system; this process generates less than  $10^5$  large amplitude particles per bunch train. Transverse wakefields have little effect on a beam with a gaussian longitudinal profile unless the trajectory has huge oscillations that will also lead to unacceptably large ( $\sim 2000\%$ ) emittance dilutions. Unfortunately, the beam will not likely have a gaussian longitudinal distribution on exit from the damping rings and the bunch compressors, but it is difficult to estimate the exact form of the distribution until better estimates of the ring impedance and sources of nonlinearity in the bunch compressors are obtained. Generous estimates of these effects would still limit the number of particles in the beam tails to be less than  $10^6$  per train. Other possible sources of tails are parasitic rf buckets that are populated in the bunch compressors or the damping rings. Parasitic bunches with charges as high as a few percent of the primary beam were seen in the SLC damping rings. Because of the uncertainties and the importance of limiting the backgrounds, the NLC has been designed to remove  $10^9$  primary particles per bunch train which is a tail population that is 0.1% of the beam—this is the halo population that was observed during the last run of the SLC, which is thought to be a generous over-estimate of the possible load.

Because of the muon generation, the NLC collimation system is designed in four stages. First, there will be a transverse collimation section immediately after the damping rings at 1.98 GeV. This is desired because beam-gas and intrabeam scattering will generate beam tails that fill the damping ring vacuum aperture and it is pointless to accelerate all of these particles to high energy. This system has not yet been designed but is thought to be

straightforward. Second, after the pre-linacs at 8 GeV, the longitudinal phase space is collimated. This system removes many of the particles in the longitudinal tails, preventing them from being deflected into the transverse phase space by wakefields during the subsequent acceleration. Next, the primary collimation system is located at the end of the main linac. This system collimates both the transverse and longitudinal phase spaces with an efficiency of  $\sim 10^5$ —thus for  $10^9$  incident tail particles, only  $10^4$  will pass through the system. Finally, both the longitudinal and transverse phase spaces are collimated in the final focus itself. This is necessary to remove particles that escape the primary collimation system as well as additional particles scattered by the residual gas downstream of the collimation section; the latter is estimated to be less than  $10^3$  particles per bunch train.

All of these systems have dual purposes: they must collimate the beam tails and they form an integral part of the machine protection system (MPS). Because the particle beams have such high charge densities, a single bunch at the end of the linac or a few bunches at the linac entrance will damage almost any material unless the beam size is increased to very large values. Unfortunately, this requires an optics which is itself chromatic and can generate more halo particles. In practice, to limit the betatron functions in the collimation region, the collimation systems rely on thin spoilers (0.25–0.5 radiation length) which scrape the halo and which, if accidentally struck by the full power beam, will enlarge the spot size via multiple coulomb scattering. The scattered halo and enlarged beam are then stopped on thick (20 radiation length) absorbers. Although the damage threshold of the spoilers is considerably higher than that of the absorbers, the design outlined still requires an enlarged beam size at the spoiler location if the spoiler itself is to survive damage from an errant bunch train.

The betatron collimation system scrapes the beam halo and provides machine protection against infrequent orbit disruption of on-energy beams. Based on the SLC experience, very few of these events are expected to occur in each run. A lattice with relaxed tolerances has been designed that uses the concept of “consumable spoilers.” These are cylindrical spoilers or scrapers that can be rotated to present a clean surface to the beam if damaged by an errant pulse. Their circumference is such that approximately 1000 damaging pulses can be permitted before replacement is necessary. Tracking studies indicate that this system gives the 5 orders of magnitude of halo reduction required.

In contrast, the energy collimators are designed to be capable of surviving hits from a full bunch train because klystron trips causing off-energy beams may be relatively frequent events and can occur with only microseconds of warning. As seen in Figure 3.49, the system combines a large horizontal dispersion and a large vertical betatron function to ensure that the transverse size of beam pulses at the 0.5 radiation length spoilers is large enough that the charge density is below the damage threshold. Multiple coulomb scattering in the spoiler further increases the beam size before the spoiled bunch train is stopped in an absorber downstream.

Because of these difficulties, the collimation spoiler has been the subject of a substantial research program. There are three elements in the R&D program. The first is the fabrication of a prototype consumable spoiler from beryllium and copper to investigate the engineering challenge of providing accurately aligned surfaces in a piece of moving machinery that must operate under vacuum. A configuration in which each collimator jaw is a rotating wheel has been selected and a prototype has been constructed. This prototype

has pointed the way to minor design modifications and demonstrated that collimation devices of this type can be incorporated reliably into any final system design.

The second element of the collimator R&D effort is a series of beam damage experiments. Samples of various materials have been exposed to single shots of 30-GeV beam of  $3$  and  $20 \times 10^9$  electrons with rms transverse areas of  $50$ – $200 \mu\text{m}^2$  at the FFTB. The samples were then inspected to help understand the resulting damage. To date, thin samples of copper, nickel, titanium, and tungsten-rhenium alloy have been tested. The tests have indicated that, for targets which are less than 1 radiation length in thickness, the damage threshold which is naively calculated is a considerable underestimate of the instantaneous heating which the materials can tolerate. This is believed to be due to the fact that in thin targets the heated material is not fully constrained. Further tests of samples that more completely approximate an NLC spoiler are planned.

The third element of the collimation system R&D effort is a series of experiments to measure the collimator wakefields. The collimator gaps are on the order of  $500 \mu\text{m}$ . Wakefield effects due to the collimator shape, resistivity or smoothness may produce enough jitter amplification to adversely impact luminosity. A movable vacuum enclosure holding four collimator samples plus a standard large-diameter round beam pipe has been installed at the SLAC linac. Two sets of measurements have been performed: a set of tapered copper collimator jaws to study the geometric wakefields of such objects and a set of graphite collimates designed and built by the TESLA collaboration. Future tests will focus on additional resistive and geometric wakefields and on the surface roughness.

Finally, a recent development in the collimation system is the use of octupole doublets which permit the beam halo in one betatron phase to be reduced in amplitude, while leaving the beam core nearly unaffected. A pair of these doublets, located in the beta match section at the beginning of the final focus, has been shown to reduce the halo in the critical final doublet betatron phase by a factor of 4, which in turn would permit equivalently larger collimator apertures in that phase. This would also dramatically decrease the impact of collimator wakefields, as the wakefields are believed to scale with the inverse square of the gap size. There are plans to verify this concept in the FFTB or the LINX test facility at the SLC final focus.

### 3.3.6 Beam Dynamics and Luminosity Performance Studies

As described in Table 3.16 in Section 3.3.2, the JLC-X/NLC injectors are designed to produce 8 GeV bunch trains with normalized emittances of  $3.2 \mu\text{m}\cdot\text{rad}$  in the horizontal and  $0.022 \mu\text{m}\cdot\text{rad}$  in the vertical. The main linac and beam delivery regions must preserve these small emittances, and must collide beams with very small transverse sizes in order to achieve the luminosity goals. The main-linac and beam-delivery system designs must ensure that the dual goals of emittance preservation and colliding of ultra-small bunches are achievable. The emittance and jitter budgets for these subsystems are listed in Table 3.16.

Because of the relatively strong wakefields and tight tolerances, the topics of emittance preservation and jitter control have been studied extensively in the X-band designs. To ensure the collider will attain the performance goals, generous emittance and jitter budgets have been applied and multiple redundant emittance control solutions have been incorporated into the design. Furthermore, the diagnostic and controls required to preserve

the beam emittance have been explicitly designed into the facility and the required diagnostic performance has either been demonstrated or is a reasonable extrapolation from demonstrations in operating accelerators or test facilities. The performance of the systems has been studied extensively using simulation tools that were benchmarked with the SLC.

When discussing the luminosity performance, it is also important to separate the timescales. There are three regimes which are determined by the ability to feedback on the trajectory motion: beam jitter, which occurs at high frequencies  $f \gtrsim$  few Hz where the feedback systems have little impact and thus the beam overlap at the IP is degraded; emittance control, which occurs at low frequencies  $f \lesssim 0.01$  Hz where the trajectory errors increase the beam emittance and thereby the spot size at the IP; and the intermediate regime. Fortunately, the intermediate regime is not important in the JLC-X/NLC because the motion tends to be well correlated and beam-based feedbacks can easily damp any residual. The tolerances in these two regimes typically differ by two to three orders of magnitude. Furthermore, while the horizontal and vertical beam sizes at the IP are both quite small, the large IP aspect and emittance ratios (both approximately 100:1) imply that the challenges in the vertical plane will be 1–2 orders of magnitude more difficult than those in the horizontal.

An example of the vertical tolerances in the final focus can be seen in Figure 3.51 where the emittance control tolerances correspond to the “drift” tolerances. Without emittance correction and beam-based alignment techniques, the typical beam-to-quad *random* alignment tolerance throughout the JLC-X/NLC is between  $1 \mu\text{m}$  and  $10 \mu\text{m}$ , and the typical quadrupole *random* jitter tolerance is between 1 nm and 10 nm. These tolerances are very tight by the standards of today’s accelerators, however, when discussing tolerances, it is also important to consider the correlation of the motion and the response of the optics. In general, the beam is very insensitive to misalignments with wavelengths long compared to the betatron wavelength—this is  $\sim 100$  meters in the main linacs and beam delivery system. As an example, the luminosity impact of aligning the linear collider to follow the earth’s curvature is minimal although this implies a “misalignment” of roughly 10 meters at the IP. Fortunately, the micro-seismic ground motion tends to be highly correlated at low frequencies where its amplitude is large and tends to have small amplitudes at high frequencies where the correlation length is short. Similarly, both beam and mechanical alignment techniques tend to have good resolution over relatively short distances and much poorer accuracy over longer baselines.

In the following, we will first discuss the diagnostics and controls that are essential to the emittance preservation. Then, we will discuss the sources of beam jitter and, finally, we will cover the beam emittance control that is necessary for the luminosity.

### 3.3.6.1 Diagnostics and Controls

The JLC-X/NLC alignment tolerances can only be achieved through the use of beam-based diagnostics and corrections. For this reason, all subsystems in the accelerator have been designed to permit the use of beam-based techniques to measure the misalignments, and precision remotely controlled translation stages to position misaligned magnets. Use of beam-based techniques allows a tremendous improvement in the alignment precision over conventional survey methods. In the FFTB, for example, magnet alignment of  $50 \mu\text{m}$  was achieved by mechanical survey, but beam-based alignment achieved resolutions as small as

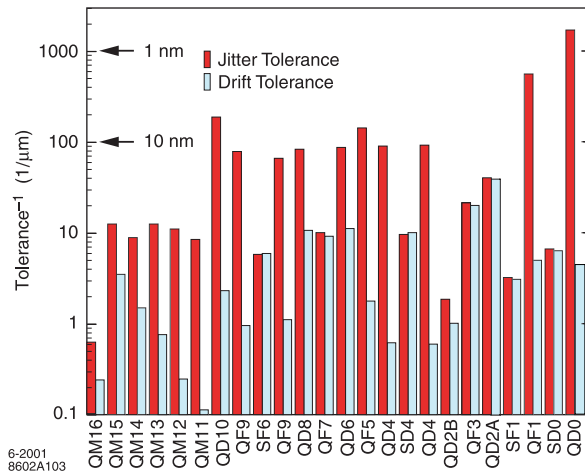


FIGURE 3.51. Magnet position jitter and drift (or alignment) tolerance of the NLC FFS calculated using the FFADA program. “Jitter” tolerance relates to the magnet’s capacity to steer beams out of collision at the IP, while “drift” refers to the magnet’s capacity to cause the beams at the IP to be too large. Reciprocal tolerances are shown, so in this case bigger is more difficult. Note the large jitter sensitivity of the final doublet magnets QF1 and QD0.

1  $\mu\text{m}$ ; independent techniques have been used to set an upper bound on the quadrupole misalignments of 7  $\mu\text{m}$ . These beam-based techniques are only possible with adequate diagnostic and control equipment. The diagnostic and correction devices needed to meet these tolerances are shown in Table 3.25. In general, the required capabilities are at most an incremental improvement upon existing hardware.

In addition to the devices listed in Table 3.25, the JLC-X/NLC will require a set of tuning algorithms that will convert the measurements of the diagnostics into new settings of the correction elements. Here again, the design will rely upon widely used and well-understood techniques in accelerator physics: quadrupole shunting, which has achieved beam-to-quad resolutions as small as 1  $\mu\text{m}$  in the FFTB; dispersion-free steering (DFS), which enabled both SLC and LEP to achieve record luminosities; and closed orbit bumps for global emittance tuning, which have been used routinely in the SLAC linac for many years. Because the JLC-X/NLC builds on the demonstrated success of existing colliders and test facilities, it is expected that modest advances in a few areas of the technology are all that will be required to achieve the performance goals.

### 3.3.6.2 Beam Jitter and Vibration

Beam jitter will arise from the motion of the quadrupole magnets along the beamline. This relatively high frequency motion of the beam has two effects: first, it causes the beams to be offset at the IP, directly reducing the luminosity, and, second, it degrades the performance of the beam position and beam size diagnostics. The direct impact of the beam jitter on the luminosity is straightforward to evaluate and is not the largest concern. Instead, the beam jitter will reduce the effectiveness of the beam-based alignment and tuning techniques without which it will not be possible to attain reasonable luminosity.

TABLE 3.25: Requirements for JLC-X/NLC diagnostic and correction devices, compared with achieved capabilities of existing equipment.

Item	Specification	Achieved	Improvement Needed
Quadrupole BPMs	0.3 $\mu\text{m}$ resolution	1 $\mu\text{m}$ resolution (FFTB striplines) 0.025 $\mu\text{m}$ resolution (FFTB cavities) 0.23 $\mu\text{m}$ resolution (NLC prototype cavity)	3 $\times$ None None
RF structure BPMs	5.0 $\mu\text{m}$ resolution	2 $\mu\text{m}$ resolution (DDS3 and RDDS1 structure prototypes)	None
Magnet movers	0.05 $\mu\text{m}$ step size	0.3 $\mu\text{m}$ step size (FFTB magnet movers)	6 $\times$
RF girder movers	1 $\mu\text{m}$ step size	0.3 $\mu\text{m}$ step size (FFTB magnet movers)	None
Laser profile monitor	1 $\mu\text{m}$ rms beam size	1 $\mu\text{m}$ rms beam size (SLC laser wire) 0.06 $\mu\text{m}$ rms beam size (FFTB laser interferometer profile monitor)	None None
Magnet/girder supports	< 3 nm vibration w.r.t. tunnel floor	$\sim$ 2 nm vibration w.r.t. tunnel floor (FFTB quadrupole supports)	None

## DESCRIPTIONS OF THE FOUR MACHINES AT 500 GEV C.M.

The motion of the magnets will be driven by natural ground motion, vibrations caused by accelerator equipment such as pumps and cooling water, and other human-made “cultural noise.” Other phenomena, such as the tendency of mechanical supports to amplify vibrations in some frequency band, can also make the problem significantly more difficult. The natural characteristics of the micro-seismic ground motion are that low-frequency motion, which typically accounts for hundreds of nanometers of rms motion, is highly coherent, while high-frequency motion, which is nearly incoherent, accounts for only a few nanometers of motion. Figure 3.52 shows a series of measurements of the power spectrum of micro-seismic motion, which have been taken at various sites around the world. Included are measurements taken in the SLAC tunnel at 2 AM during a period when the beam and rf structures were off but cooling water was flowing normally, data taken in the LEP, HERA and UNK tunnels, and data taken in the Hiidenvesi cave in Finland. All of the measurements indicate that the power density of natural micro-seismic motion is a strong function of frequency, with a characteristic  $1/\omega^4$  dependence. Although high frequencies are potentially the most deleterious from the point of view of beam-beam jitter, Figure 3.52 shows that natural ground motion contains very little power in frequencies above 1 Hz while the large amplitude peak at 0.15 Hz has a wavelength of  $\sim 10$  km. The JLC-X/NLC beam-beam jitter sensitivity favors a deep tunnel in relatively strong material at a location with minimal cultural noise, but these characteristics can be traded off against each other. A shallow tunnel site at a relatively deserted location can have noise characteristics comparable to a deep tunnel in a populated area. The most important lesson to be learned from the power spectral density measurements is that not all sites are equally viable for the JLC-X/NLC.

In order to minimize the “cultural noise” from the accelerator equipment vibrations and the impact of magnet supports, it will be necessary to subject every piece of hardware in the accelerator complex to carefully developed engineering criteria, in essence to establish a “vibration budget” for the equipment similar to the “impedance budget” of modern-day storage ring vacuum system. While achieving the vibration goals will require appropriate planning and design, as a proof-of-principle, magnets on the FFTB magnet supports were measured to have motions that were only 2 nm larger than that of the underlying ground. Comparable measurements have been made on NLC prototype quadrupoles which were also attached to rf structures. Other sources of cultural noise, for example the use of motor vehicles on site, will be addressed through appropriate selection of a site and of a tunnel depth. The LEP tunnel measurements in Figure 3.52 show that even a tunnel in a suburban area can be made relatively free of cultural noise sources. Thus, while many sources of accelerator component misalignment can be minimized or eliminated through engineering, the natural ground motion of the site is a potential source of misalignments that is not itself amenable to direct engineering.

When the influences of beam-based steering feedback, lattice response, and correlated motion are considered, it can be shown that quadrupole motion at frequencies below approximately 1 Hz will generally not contribute significantly to beam-beam jitter at the IP. For most of the quadrupoles in the JLC-X/NLC, considered as an ensemble, uncorrelated rms motion of 10 nm in the frequency range above 1 Hz will be acceptable. For example, Figure 3.51 shows that, with the exception of the final doublet, typical jitter tolerances in the final focus are on the order of 10 nm for incoherent motion of the magnets while the sensitivity of the luminosity to correlated motion is much smaller. If the SLAC

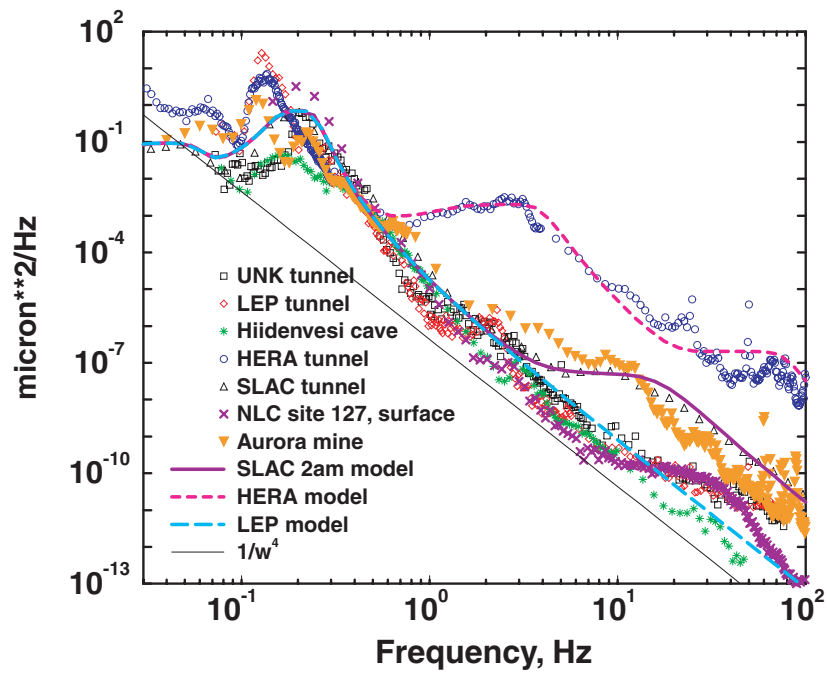


FIGURE 3.52. Power spectrum of ground motion, in units of  $\mu\text{m}^2/\text{Hz}$ , from several accelerator tunnels and a cave. The strong peak at 0.15 Hz in all spectra is from ocean waves. The shoulder at 4 Hz in the HERA data is most likely due to “cultural noise,” vibration sources within the accelerator complex and from the surrounding urban area.

## DESCRIPTIONS OF THE FOUR MACHINES AT 500 GEV C.M.

integrated ground motion and the FFTB quadrupole supports are used as a basis, then the rms quadrupole motion will be less than 4 nm in this frequency range. Thus, for a reasonable choice of site and magnet support technology, it will be possible to provide stability for most of the quadrupole magnets in an entirely passive manner.

In contrast, the jitter tolerances of the final doublet quadrupoles, QD0 and QF1, are roughly an order of magnitude tighter than those in the rest of the final focus. The final doublet quads are the only ones in the JLC-X/NLC that cannot meet their tolerances through passive stabilization alone. However, because the final doublets contain a small number of elements in a reasonably compact space, it is possible to contemplate solutions to the doublet motion problem that are too complex to be applied to a larger number of elements. Thus, jitter suppression for these magnets must include a combination of passive and active methods. Passive methods include locating the IR hall sufficiently far from cultural sources of vibration, minimizing potential vibration sources that can be controlled through proper engineering, and engineering to ensure that the detector, magnet technology, and doublet support girders are stable and do not amplify motion. Active vibration suppression techniques are based on feedback systems to control piezoelectric movers or other fast translation-stage technology which would allow constant position adjustment of the magnets at frequencies far above the beam repetition rate. Two different technologies for measuring the motion of the magnets with high resolution over a wide frequency band are under consideration: an optical anchor, which measures the positions of the final doublet magnets with respect to a fixed point on the detector floor; and inertial sensors which can measure the accelerations of the magnets directly. Both technologies would allow the additional vibrations of the detector to be suppressed, and would allow one doublet to be held fixed in position with respect to the other.

The measures described are expected to limit luminosity loss from beam-beam jitter to a few percent, which is acceptable. An additional measure, which can potentially provide further reduction, is a feedback at the interaction point that operates within a single bunch train. An intra-train collision feedback would use the beam-beam deflection to estimate the relative offset of the two bunch trains from the measured deflections of the first few bunches and would then be used to steer subsequent bunches back into collision. Such a feedback has been studied for the TESLA bunch train. The JLC-X/NLC implementation for such a feedback is made more complicated by the fact that both the bunch train and the intra-bunch spacing are much shorter than in TESLA. Nonetheless, a design of the system using available components has been developed and the system will be tested in the NLCTA.

### 3.3.6.3 Beam Emittance Control

The beam emittance dilutions primarily arise from misalignments of the beamline components. The BNS damping mechanism, a technique proven at the SLC, suppresses the Beam BreakUp instability (BBU) and eliminates emittance dilution from coherent (betatron) oscillations of the beam but requires a large energy spread of 0.7–1% which will make the beam more sensitive to incoherent misalignments of the quadrupole magnets. Similarly, incoherent rf-structure misalignments will lead to emittance dilution from short-range dipole wakefields, and construction errors in the structures can introduce substantial multibunch emittance dilution. The most serious sources of emittance dilution

are single-bunch effects due to misaligned magnets and rf structures. As discussed, the relevant scale in this case is about 1000 times larger than that for beam jitter and is microns. These misalignments are due to slow motion  $0.01 \text{ Hz} \gtrsim f \gtrsim \text{d.c.}$  and are referred to as static misalignments.

The alignment requirements are beyond what can be achieved by conventional survey techniques. Fortunately, it is possible to use beam-based alignment algorithms to achieve the most challenging tolerances in the main linac. Figure 3.53 shows the beamline hardware associated with beam-based alignment: remotely controlled translation stages for quadrupoles and rf girders, and high resolution BPMs in the quads and the rf structures. The equipment and instrumentation builds on the successful prototypes demonstrated at the FFTB and in ASSET as discussed in Section 3.3.6.1.

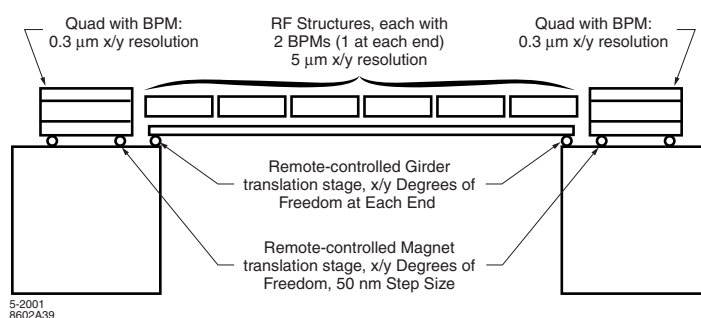


FIGURE 3.53. Beam-based alignment hardware in the NLC main linac.

There are several sources of multibunch emittance dilution in the main linac which cause the various bunches in a given bunch train to follow different trajectories down the beamline. Provided the BBU due to the long-range wakefield is kept small by the combination of detuning and damping, the jitter amplification will be negligible. In this case, the rf structure defects will generate a set of bunch-by-bunch deflections. The tolerances on the structure alignment to limit the multibunch dilutions are loose compared to those imposed by the single bunch effects; tolerances for 10% emittance dilution are shown in Figure 3.54. In addition, the multibunch dilutions will be nearly constant in time, and, as a result, they will be amenable to a feedback that corrects bunch positions within a train. Such a feedback is simultaneously fast (*i.e.*, its BPMs and correctors have a bandwidth of several-hundred MHz) and slow (*i.e.*, the system applies nearly the same set of corrections to each train). The linac design includes several subtrain feedback systems that utilize high-bandwidth BPMs and stripline kickers similar in many ways to the high-bandwidth transverse feedbacks of modern storage rings. Analytic estimates indicate that such systems can reduce the emittance dilution from multibunch sources by roughly a factor of 10, limited by the system bandwidth and the signal-to-noise performance of the BPMs.

Given that the emittance dilution is dominated by the single bunch effects, the primary issue is to attain and maintain the alignment of the quadrupoles and the rf girders. The following procedure is used to do this:

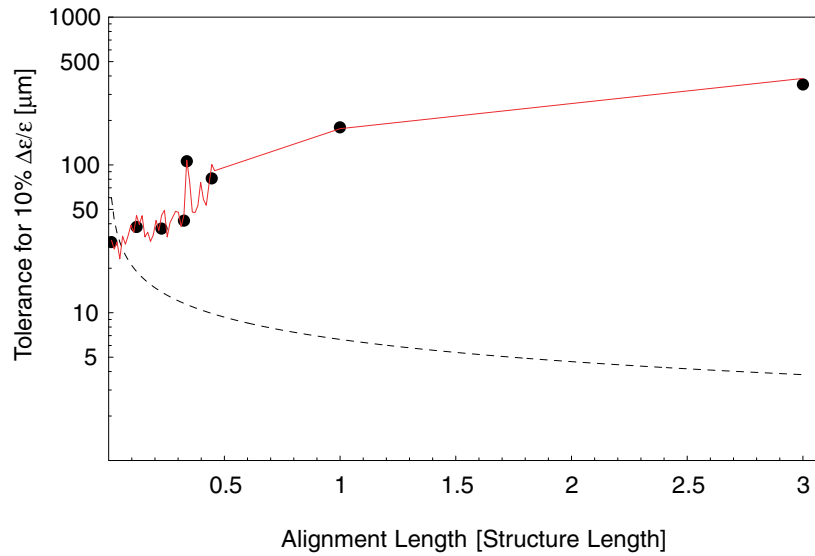


FIGURE 3.54. Misalignment amplitude leading to 10%  $\Delta\epsilon/\epsilon$  as a function of the accelerator structure length (90 cm) for the long-range (solid) and short-range transverse wakefields. An alignment length of one structure corresponds to random rigid misalignments of individual structures while lengths of less than one structure correspond to random piecewise misalignments of the structures. With the S-BPM and structure mover system, the JLC-X/NLC essentially eliminates the short-range wakefield tolerances.

1. Determine the “gold orbit” of the linac. This is the set of quadrupole BPM readings that corresponds to high luminosity. In the absence of BPM-to-quad offsets, the gold orbit would simply be zero on all BPMs.
2. Move the quadrupole magnets using the magnet movers until the gold orbit is achieved and then move the rf girders using the rf structure BPMs to align these to the beam trajectory.
3. Use a set of discrete steering feedback loops in the main linac to minimize the orbit drift due to component motion as a function of time. The steering feedback can operate quickly (at the level of 1 Hz or faster), and is entirely compatible with colliding for luminosity.
4. As diffusive ground motion moves the accelerator components, the luminosity will gradually decline. This is because the misalignments between the feedback correctors will become sufficiently large that the feedback can no longer maintain a reasonable approximation of the gold orbit. At this time, recover the gold orbit by returning to Step 2. This procedure should be compatible with colliding for luminosity if the magnet mover step sizes are small and the steering feedback loops are operating.
5. Over even longer time scales, the gold orbit will gradually cease to provide good luminosity. This is because the electrical centers of the Q-BPMs, the magnetic centers of the quadrupoles, and other parameters are subject to change over time. Once this has happened, return to step 1 and determine a new gold orbit using invasive procedures.

Determining the gold orbit is a crucial step in the algorithm as the quality of the gold orbit will determine the maximum luminosity performance of the collider. Ideally, the BPM-to-quad offsets can all be measured by the beam with sufficient accuracy by varying the focusing strength of each quadrupole and measuring the resulting deflection of the beam on downstream BPMs. This allows determination of the beam-to-quad offset, and the quad-to-BPM offset of the nearest BPM can then be deduced by subtraction. This procedure was demonstrated at the FFTB. For the main linac, a resolution of  $1\ \mu\text{m}$  would be straightforward to achieve for each quad, if the technique were not limited by systematic errors. The primary systematic error arises if the quadrupole center moves as the quadrupole strength is varied. Measurements of the quadrupole center motion, implies that electromagnetic quadrupoles could be aligned at the tolerance level of  $2\ \mu\text{m}$  while the alignment would be roughly 10 times worse with permanent magnets; permanent magnets have been considered for the main linac due to reliability and cost considerations.

Because the accurate determination of the BPM offsets will still provide the most local (hence most stable) correction of the emittance, the quad-varying technique remains the method of choice for determining the gold orbit. However, because of the sensitivity to quad-center variation, this technique may not be adequate by itself. An alternative technique for generating a gold orbit is Dispersion Free Steering (DFS), in which the dispersion is measured by varying the energy of the beam or beamline and measuring the change in the trajectory. This technique is less local than varying a single quadrupole at a time and measuring the resulting deflection, but it directly measures the dispersion. Furthermore, DFS relies only upon the BPM resolution to achieve an acceptable trajectory, and the BPMs will have a resolution that is much better than the knowledge of the BPM-to-quad offset under almost any imaginable circumstances. The emittance dilution after convergence is 20% with a  $0.3\ \mu\text{m}$  BPM resolution.

Additional improvement to the emittance can be achieved by applying closed-orbit bumps over a small region of the linac. These bumps generate dispersion or wakefields at a particular phase and in a particular location, which can cancel any existing dispersion at that phase and location. A simulation has been performed in which a set of dispersion bumps was applied to the main linac after DF steering. In the case where  $0.3\ \mu\text{m}$  BPM resolution was assumed for DFS, the final DFS + bumps emittance dilution is 5%.

As suggested in Step 5, the emittance obtained by repeatedly steering to the gold orbit in Step 2 will increase, as the BPM-to-quad offsets change with the passage of time. Once this has happened, it is necessary to repeat the procedure that was used to determine the gold orbit in the first place. The length of time between determinations of the gold orbit is difficult to estimate. Unfortunately, determining the gold orbit can be invasive and incompatible with colliding for luminosity. Measurements of the BPM centers in the FFTB stripline BPMs suggest that the gold orbit will not have to be re-measured more often than once a month and aggressive use of emittance bumps can further extend the life of a gold orbit.

As discussed in Step 3, another important technique for maintaining the luminosity is the use of steering feedback loops which stabilize the beam trajectory at frequencies up to  $\sim 1\ \text{Hz}$ . The main linac will use several discrete sets of fast, weak dipole correctors to provide steering feedback at 5 to 10 locations within the beamline. The main linac feedback provides partial reduction of the emittance dilution arising from diffusive ground motion. Figure 3.55 shows the emittance as a function of time at the end of the main linac due to

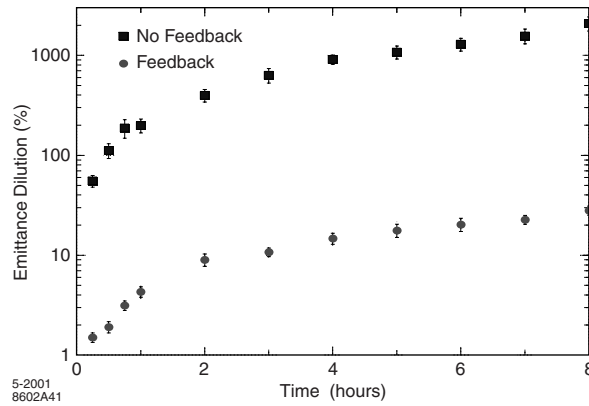


FIGURE 3.55. Emittance dilution (%) in the NLC main linacs due to diffusive ground motion, assuming an ATL coefficient comparable to that measured at SLAC. A case with no linac feedbacks (squares) and a case with the proposed NLC steering feedback architecture (circles) are both considered.

ATL motion, assuming a coefficient  $A$  of  $5 \times 10^{-7} \mu\text{m}^2/\text{m/s}$ , both with and without steering feedback in the main linac. Without feedback, the emittance dilution in the main linac would become unacceptable within minutes, while the addition of steering feedback preserves the emittance for hours. After this time period, it is necessary to recover the gold orbit throughout the linac by moving all of the quadrupoles on their magnet movers. The steering feedbacks also reduce the luminosity dilution that happens while the quadrupoles are being moved. Figure 3.55 suggests that the time-averaged luminosity loss from the slow completion of mover steering will be on the order of 2%.

Finally, Table 3.26 shows a tentative distribution of the main linac emittance budget amongst the various sources of dilution. Since the studies were performed with the 1 TeV c.m. configuration of the JLC-X/NLC, the lower-energy configurations, which have fewer rf structures and thus less challenging beam dynamics, should be substantially more tolerant. In addition, Table 3.26 assumes that DFS + bumps must be used for generation of a gold orbit, and that only a  $1.0 \mu\text{m}$  effective BPM resolution is achieved which is 3 times worse than the design specification.

The procedure described works well for the main linac. However, the beam dynamics in the final focus can be different from that in the main linac. The number of quadrupoles and the rms beam energy spread are both quite small, so phase mixing in the final focus is not a serious problem. This in turn implies that global knobs of various kinds will be more effective than in the linac. The final focus also contains horizontal bend magnets, so it is possible to adjust the dispersion with normal or skew quads at high-dispersion points rather than by varying the beam trajectory, as is done in the linac. On the other hand, the final focus contains many strong aberrations, such as chromaticity, sextupoles, and skew quadrupole effects, which typically are delicately balanced against one another. Therefore, the BDS has looser tolerances on the conditions that must be met before global corrections are applied than the main linac has, but the tolerances on stability over time are much tighter than in the main linac.

TABLE 3.26

Distribution of the main linac emittance budget and resulting engineering tolerances. Dilutions are applied to the vertical plane except where indicated. Beam-to-quad misalignment is an “effective misalignment” assuming DFS + bumps with  $1.0 \mu\text{m}$  effective BPM resolution. Multibunch sources assume factor of 10 suppression via subtrain feedback. Note that the tolerance on structure dipole frequencies is for the worst-case error mode (random cell-by-cell frequency errors which are reproduced in every structure), and all other distributions of frequency errors have considerably looser tolerances.

Effect	Tolerance	Resulting Emittance Dilution
Beam-to-quad misalignments	$2.0 \mu\text{m}$ (effective)	25%
Quad strength errors	0.1%	0.7% (x) / 0.5% (y)
Structure-to-girder misalignments	$30 \mu\text{m}$	8%
Structure-to-girder tilts	30 mrad	4%
Quadrupole rotations	200 mrad	4%
Structure BPM resolution	$5 \mu\text{m}$	3%
Mover steering interval	30 minutes	2%
Structure straightness (bow)	$50 \mu\text{m}$	1% (incl. feedback)
Cell-to-cell misalignments	$3.5 \mu\text{m}$	1% (incl. feedback)
Structure dipole frequencies	1 MHz	1%
Synchrotron radiation		3% (x)
Total		3.7% (x) / 50% (y)

Of course, the final focus of the JLC-X/NLC, like the main linacs, is designed with powerful diagnostic capabilities and robust correction devices. Every quadrupole and sextupole is on a remotely controlled magnet mover, similar to those in the main linac. Each quadrupole is paired with a BPM with submicron resolution, and in some critical locations ultra-high resolution cavity BPMs with resolutions better than 100 nm are also used. Laser-based beam-size monitors are installed at critical locations. All sextupoles, bends, and quads except for the final doublet are iron-dominated electromagnets, with high-precision power supplies. In addition, the final focus has two powerful diagnostics not available at other locations, the luminosity and the beam-beam deflection, each of which will be measured on every pulse in order to provide signals for feedback systems.

The tolerances for the final focus components are shown in Figure 3.51. Although these are small, it is important to note that these are so-called “bare” tolerances—tolerances in the absence of feedback systems or other non-invasive correction algorithms which can stabilize accelerator performance. Understanding the real performance of the final focus requires simulation studies that include the planned diagnostic and correction systems, and their algorithms. As an example, one of the most serious potential sources of emittance dilution is beamline magnet misalignments driven by diffusive ground motion. Figure 3.56 is the result of a simulation that misaligns the elements of the 1-TeV BDS configuration according to the ATL law with  $A = 5 \times 10^{-7} \mu\text{m}^2/\text{m}/\text{s}$ . The curves show that luminosity would degrade under ATL motion in approximately 2 minutes if only the beam-beam deflection collision stabilization feedback was present. If, in addition, orbit control feedback is allowed to steer the beam through the centers of critical quadrupole and sextupole magnets, then

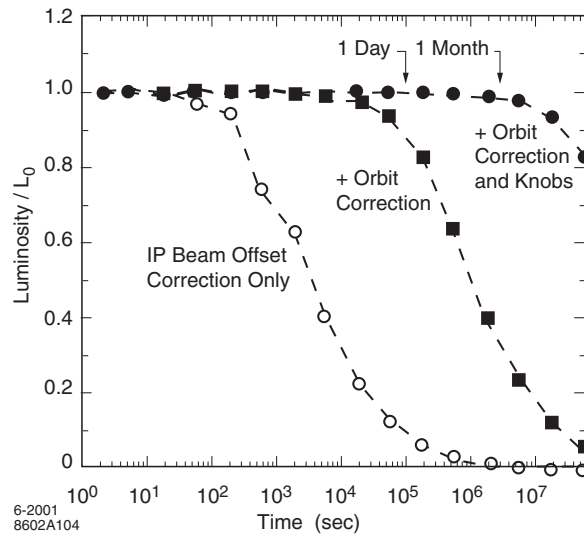


FIGURE 3.56. Degradation of alignment under ATL ground motion with IP beam-beam deflection based feedback only, with orbit feedback added, and with direct luminosity optimization added.

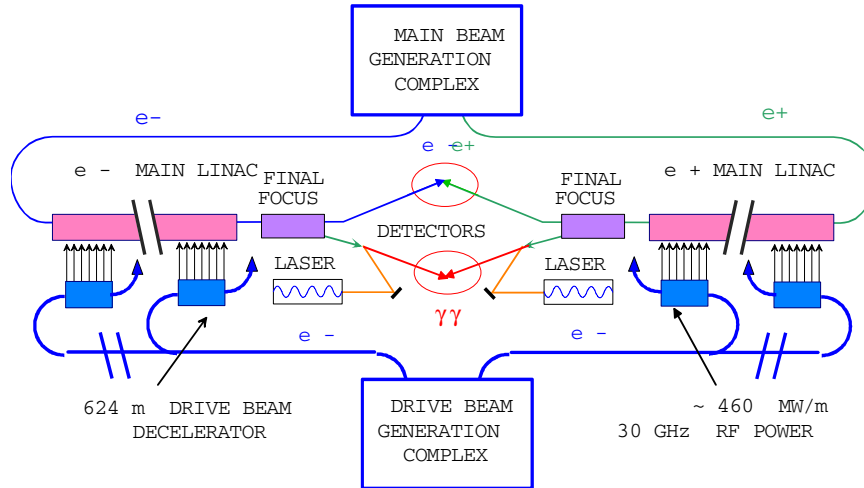
the time for luminosity degradation increases to approximately 1 day. Finally, if direct optimization of the main aberrations via global knobs is added to the system, then the luminosity lifetime increases to several months, after which a disruptive realignment procedure would be required.

## 3.4 CLIC

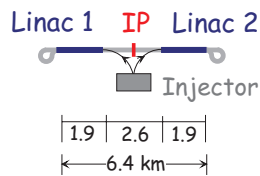
### 3.4.1 Introduction

#### 3.4.1.1 Overview of the Complex

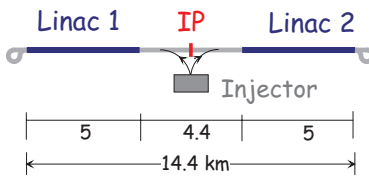
The CLIC (Compact Linear Collider) study aims at a multi-TeV, high luminosity  $e^+e^-$  linear collider design. Beam acceleration uses high frequency (30 GHz), normal conducting structures operating at high accelerating gradients (150 MV/m), in order to reduce the length and, as a consequence, the cost of the linac. The cost-effective rf power production scheme, based on the so-called Two-beam Acceleration method, enables electrons and positrons to be collided at energies ranging from about 0.1 TeV up to 5 TeV, in stages. Though the study has been optimized for a nominal center-of-mass (c.m.) energy of 3 TeV with a luminosity of  $10^{35} \text{ cm}^{-2}\text{s}^{-1}$  [7], the CLIC design is however such that its construction could be staged without major modifications (right side of Figure 3.57). The implementation of the lower energy phases for physics will depend on the existence or not of other accelerator facilities, but in a first stage it could cover, if required, the c.m. energies between  $\sim 0.1$  and 0.5 TeV with  $\mathcal{L}=10^{33}\text{--}10^{34} \text{ cm}^{-2}\text{s}^{-1}$ , where interesting physics and overlap with LHC (Large Hadron Collider) are expected. This stage could be extended to 1 TeV with  $\mathcal{L}$  above  $10^{34} \text{ cm}^{-2}\text{s}^{-1}$ . Next would come the desirable  $e^\pm$  collisions at 3 TeV which should break new physics ground, while the final stage might be 5 TeV.



**0.42 TeV Stage**



**1 TeV Stage**



**3 TeV Stage**

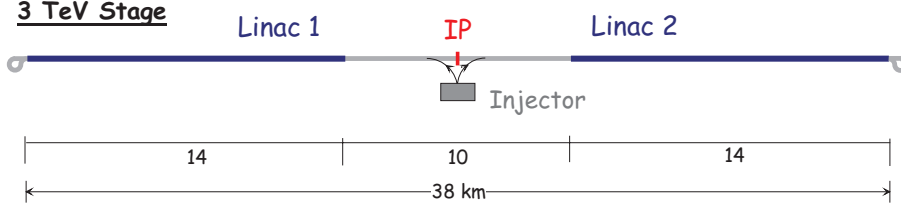


FIGURE 3.57. The top shows the overall layout of the CLIC complex and the bottom shows the tunnel lengths (km) for the linacs and the BDS (base-line design) on each side of the IP, at various cm energies.

## DESCRIPTIONS OF THE FOUR MACHINES AT 500 GeV C.M.

The left side of Figure 3.57 gives an overall layout of the complex which shows the linear decelerator units running parallel to the main beam [8]. Each unit is 625 m long and decelerates a low-energy high-intensity  $e^-$  beam (so-called drive-beam) which provides the rf power for each corresponding unit of the main linac through energy-extracting rf structures. Hence, there are no active elements in the main tunnel. With a gradient of 150 MV/m, the main beam is accelerated by  $\sim 70$  GeV in each unit. Consequently, the natural lowest-value and step-size of the colliding beam energy in the center-of-mass (c.m.) is  $\sim 140$  GeV, though both can be tuned by some adjustment of the drive-beam and decelerator. The minimum energy corresponds to 1 unit and the energy step to the addition of one unit, on either side of the interaction point (IP). The nominal energy of 3 TeV requires  $2 \times 22$  units (a total two-linac length of  $\sim 28$  km), each unit containing 500 power-extraction transfer structures (PETS) feeding 1000 accelerator structures. The 500 GeV c.m. energy needs  $2 \times 4$  units (a two-linac length of  $\sim 5$  km) and reaching exactly this energy implies to rearrange the decelerator and the linac so that a unit includes 455 PETS and 909 accelerator structures (gain of 62.5 GeV per unit instead of  $\sim 70$  GeV). It must be noted that this arbitrary choice of c.m. energy has no specific physics justification and that in practice an energy more natural for the CLIC scheme ( $\sim 560$  GeV with  $2 \times 4$  units) would be selected.

This modularity is facilitated by the fact that the complexes for the generation of all the beams and the Interaction Point (IP) are both in a central position, where all the power sources are concentrated. The main straight tunnel houses both linacs, the various beam transfer lines and, in its middle part, the two Beam Delivery Systems (BDS). The fact that there is such a single tunnel results in a simple and easily extendable arrangement. The right side of Figure 3.57 gives examples of estimated tunnel lengths for various energies in the center-of-mass.

The general description of the CLIC two-beam technology, of the main-beam complex and of the rf power source at 30 GHz is given in [7]. It also summarizes the main-beam (main-linac) and drive-beam (decelerator and accelerator) parameters at the nominal energy of 3 TeV as well as some possible main-beam parameters at various other energies. For the purpose of the present review however, the possible design of CLIC at 500 GeV has been studied more specifically than in the past and optimized to some extent. This work is still going on and the following description gives the status of this 500 GeV study with the corresponding parameters (see Megatables) and subsystem characteristics. Many of these systems are subjects of a continuing research and development program, in particular the high-gradient structures, the damping rings, the dynamic time-dependent effects, the vibration stabilization and the beam delivery system. In its present stage, the description of the 500 GeV design is therefore not totally self-consistent. In addition, the model of the main-linac accelerator structures and some consequent parameters used for beam-dynamics analysis do not exactly correspond to the structure design and to the rf power source associated with this design, as described in this report. Updating the simulations was however not considered urgent since the numerical model used gives pessimistic results. The CLIC nominal 3 TeV case will be described in the separate chapter on energy upgrade.

**3.4.1.1.1 Layout and Civil Engineering** Preliminary investigations on the engineering feasibility and impact of the large CLIC facility have been carried out using a possible site near CERN. For the civil-engineering arrangement, the guidelines retained are the following: to find out the right underground level for the main tunnel to be within favorable geological

conditions, to locate the IP on the CERN site, to minimize the environmental impact of the surface buildings of the injector-areas and shaft-areas, and to provide the lowest cost for the most suitable layout. A molasse of similar quality to that which was found for the SPS and LEP/LHC tunnels would give the most advantageous and cheapest conditions for CLIC. In these conditions, the maximum straight length available is about 40 km and this makes it possible to have a tunnel housing both the main linacs and the most conservative beam delivery systems ( $\sim 10$  km long base-line BDS, total) for a c.m. energy of 3 TeV. However, prospects also indicate that a straight length of approximately 52 km can be envisaged between two major faults. In addition, it is considered after further optimization that a total BDS length of  $\sim 5.2$  km is sufficient at both 500 GeV and 3 TeV c.m. A shaft for engineering work and maintenance should be planned at about every 3.2 km or 5 drive-beam units. Two return loops for the main linac beam with an average radius of 115 m are foreseen at each extremity of the tunnels. The injector complexes for both the main-beams and the drive-beams would require additional tunnel lengths of about 7 km and 5 km respectively (linacs and transfer lines). They remain the same at all cm energies and should be located in a central area, near the IP detector hall. In this way, the service buildings and the power sources (klystrons-modulators) could be concentrated in this central area.

The available data about the top of the molasse, the faults, the Piemont of the Jura and the water tables indicate that the 40 km long tunnel mentioned previously can be entirely positioned in the molasse if it lies at an average level of  $\sim 140$  m below ground level. The main tunnel could then be done by a tunnelling-boring machine. The excavation of the beam dump caverns, of the beam turn-around loops and of the IP experimental hall cavern would be carried out by a road-header (maybe by using explosives in the cavern). The minimum and maximum depths of the shafts would be about 80 m and 165 m respectively. The diameter of the main tunnel could be 3.8 m and that of the shafts 7 m (a total of 13 of them are required at 3 TeV and between 3 and 5 at 500 GeV). In the central area, it is possible to place the injectors (all the linacs of the injection complexes) close to the surface so as to make most of the injector tunnels by cut and cover method, hence reducing the cost and making the installation of the klystrons and modulators easier.

**3.4.1.1.2 Cooling and Ventilation System** The three main parts of the cooling system are related to the main tunnel, the injector complexes and the main beam dump area. In the main tunnel, the total power dissipated at 3 TeV by the quadrupoles and other systems ( $\sim 32$  MW), by the drive beam dumps located at the end of each 625 m long unit ( $\sim 29$  MW total) and by the accelerating and power-transfer structures ( $\sim 114$  MW) amounts to 175 MW, and approximately to 3 times less at 500 GeV. The cooling system there consists of primary water circuits which serve as a cold source for primary/secondary heat exchangers placed in the surface buildings. The primary circuit will probably consist of closed circuits with cooling water towers built around a limited number of tunnel access pits (*e.g.*, 2, 5, 9, and 11 at 3 TeV), in order to limit the environmental impact. The secondary circuit goes down the shafts to cool the tunnel equipment. The air quality is controlled by a main chilled water-cooled HVAC unit. For minimizing variations of temperature on the rf structures, air temperature gradient is reduced by using 32 intermediate HVAC units which cool the air through chilled water supplied from the surface.

The main-beam injector dissipates  $\sim 7$  MW (2 times more at 500 GeV because of a higher repetition rate) while the drive-beam generation system dissipates  $\sim 145$  MW at 3 TeV

(about 3 times less at 500 GeV). The cooling and ventilation of these subsystems located in the central area follows the same principle as for the main tunnel, with a closed primary circuit and a cooling water. The two main-beam dumps dissipate 14.7 MW each at 3 TeV ( $\sim 5$  MW at 500 GeV). In order to minimize shock-waves at each pulse, it is foreseen to cool these dumps with water at the set point of  $4^\circ\text{C}$  and to use a small temperature difference between inlet and outlet of  $0.4^\circ$ . Cooling towers provide cooling water to the chillers placed in an underground cooling plant. The chillers supply water to a pool used for the dumps in a closed circuit to reduce the water contamination.

**3.4.1.1.3 Power Distribution** A first study of a possible powering strategy has been carried out, assuming that CLIC and LHC would work simultaneously and that the central area is near the North-area of CERN. The power requirements cover, in decreasing order of importance, the rf system of the drive-beam generation, the main-beam injectors, the detectors, the magnets, the cooling and ventilation, and the general services. Considering the required power, the connection to the grid must be at 400 kV. The important power needs of the drive-beam rf require a separate primary system at 36 kV and a secondary system at 7.2 kV to adapt to the power converters of the klystrons. The main distribution voltage proposed for the central area would be 24 kV. For the long tunnel, major surface supply points are foreseen at each shaft, with an underground supply point and an additional underground supply point at 1280 m from the latter; a voltage of 24 kV is proposed for the system distribution. A major 24 kV substation would be needed in the central area. This major station might however be broken into smaller units, given the size of the central area. The main tunnel requires less power (about 1.5 MVA per km). Because of the distances, the distribution voltage level would be 24 kV, with underground supply points and 630 kVA transformers.

## 3.4.2 Main-Beam Subsystems

### 3.4.2.1 Injection System

**3.4.2.1.1 Basic Parameters** The bunch spacing in the main-beam train imposes an rf acceleration frequency of 1.5 GHz. The rf gun and the injector linacs run at L-band except the Booster Linac which runs at S-band. The particle production rate is  $0.9 \times 10^{14} e^\pm/\text{s}$ . A total incoherent energy spread of  $\Delta E/E = \pm 1\%$  corresponds to a maximum rms bunch length of  $\sigma_z = 3$  mm. The same bunch length is assumed from the rf gun, producing an  $e^-$  beam for  $e^+$  production, up to the first bunch compressor downstream to the  $e^+$  damping ring. For  $e^-$ , the bunch length of 3 mm is obtained after bunch compression upstream the  $e^-$  pre-injector linac. Two stages of bunch compression are foreseen. The first, at the damping ring exit, operates at 3 GHz while the second, at the entrance of the main linac, uses 30 GHz. The normalized transverse beam emittances at the I.P. are imposed by the required luminosity. The damping rings are designed in order to produce the necessary emittances taking into account the expected emittance growth in the main linac with the input emittances provided by the sources of the leptons. The maximum single bunch charge is 5 % higher than the charge at the IP to allow for beam losses in the injector complex and collimation at the entrance of the main linac. Table 3.27 summarizes the CLIC injector basic parameters.

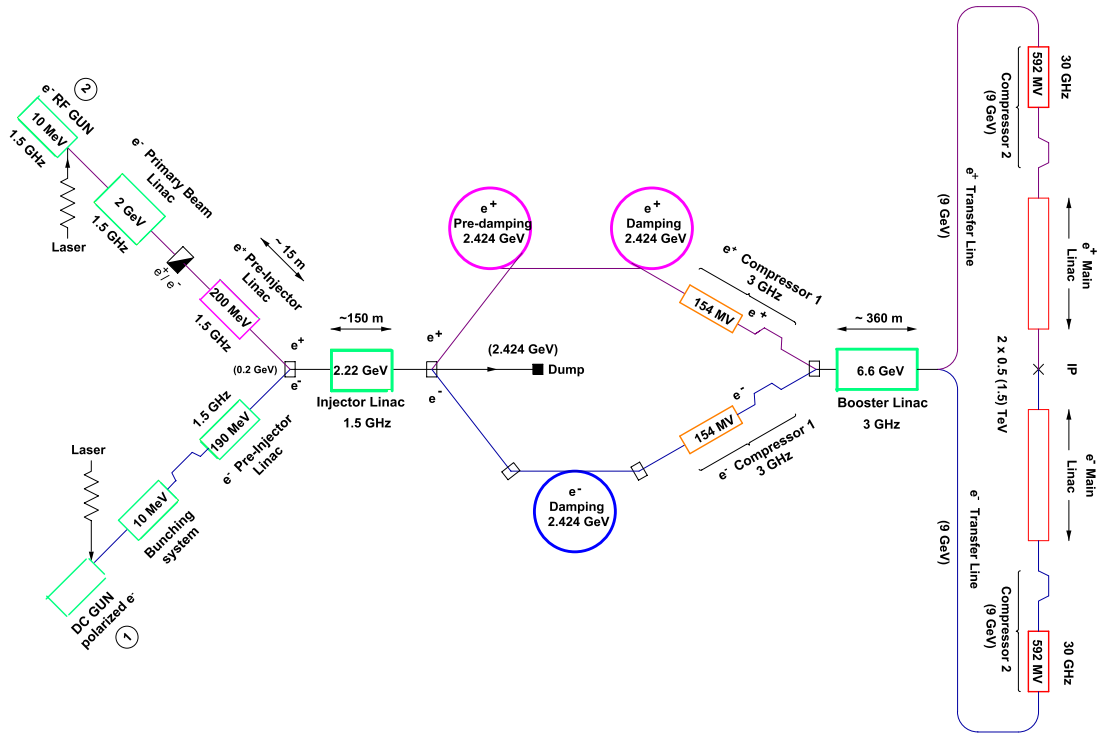
TABLE 3.27  
Basic target parameters at different stages of the injection.

General Parameters	Unit	Value
<b>At main linac injection</b>		
Energy	GeV	9
Nb particles per bunch	$10^{10} e^\pm$	0.42
Bunch length	$\mu\text{m}$	35
Energy spread	%	1.4
Transverse emittance ( $\gamma\epsilon_x$ )	$10^{-9}$ m·rad	1800
Transverse emittance ( $\gamma\epsilon_y$ )	$10^{-9}$ m·rad	5
<b>At damping ring exit</b>		
Energy	GeV	2.424
$N_b$ particles per bunch	$10^{10} e^\pm$	0.42
Bunch length	$\mu\text{m}$	1300
Energy spread	%	0.135
Transverse emittance ( $\gamma\epsilon_x$ )	$10^{-9}$ m·rad	1600
Transverse emittance ( $\gamma\epsilon_y$ )	$10^{-9}$ m·rad	3

**3.4.2.1.2 Injection Complex of the Main Beam** The general layout of the main-beam injection complex is given in Figure 3.58. This complex is composed of the two following systems:

- i. The system for the electron beam: The laser system and the photo-cathode DC electron gun, followed by an rf accelerating cavity, generate a 10 MeV, low charge beam. The pre-injector linac provides an energy gain of 190 MeV and an  $e^-$  beam energy at the exit of 200 MeV. The injector linac accelerates the beam by 2.224 GeV, giving a final energy of 2.424 GeV. This linac accelerates alternately the train of electrons and the train of positrons. A DC dipole magnet separates the  $e^-$  beam from the  $e^+$  beam. It also makes it possible to send the beam toward a dump where some beam instrumentation will be implemented. Then, there are successively, the damping ring for  $e^-$ , the first stage of the bunch compressor working at 3 GHz and 2.424 GeV, the booster linac accelerating alternately  $e^-$  and  $e^+$  beams up to 9 GeV, the transfer line and finally the second stage of the bunch compressor working at 30 GHz and 9 GeV at the entrance of the  $e^-$  main linac.
- ii. The system for the positron beam: The laser system and the photo-cathode rf electron gun generate a 10 MeV, high charge beam. The  $e^-$  Primary Beam Linac sends a 2 GeV beam onto the  $e^+$  target. Following the conventional positron source, which receives the high-intensity primary  $e^-$  beam, the  $e^+$  Pre-injector Linac accelerates  $e^+$  (and secondaries  $e^-$ ) up to 200 MeV. The injector linac (common to  $e^-$  and  $e^+$ ) provides a 2.224 GeV energy gain. Then the pre-damping ring and

DESCRIPTIONS OF THE FOUR MACHINES AT 500 GEV C.M.



CLIC INJECTOR COMPLEX FOR THE  $e^+$  and  $e^-$  MAIN BEAMS

FIGURE 3.58. CLIC injector complex for the  $e^+$  and  $e^-$  main beams.

the damping ring for  $e^+$  follow. The rest of the system consists of the same kind of compressors and transfer lines as for the  $e^-$  and includes the common booster linac.

**Electron Source for the Main Linac** The DC gun should produce 1 nC/bunch. The charge of  $0.62 \times 10^{10} e^-$  per bunch takes into account the transfer efficiency between the DC gun and the damping ring exit, at 2.424 GeV. A total charge of 150 nC is not an issue for the DC gun assuming that the bunch length and bunch spacing are adequate for the surface charge limit. The expected normalized edge emittances are  $10 \times 10^{-6}$  m-rad in both planes. It is required that the train-to-train charge jitter be below 0.5% (rms) and the bunch-to-bunch charge jitter (inside the train) be below 1% (rms). The transverse laser spot size on the photo-cathode should have a diameter variation smaller than 1%.

**Positron Source for the Main Linac** The rf gun works at 1.5 GHz with an electric field of 50 MV/m (on axis) and should deliver  $2 \times 10^{10} e^-$  per bunch. The expected normalized emittances are  $13 \times 10^{-6}$  m-rad (both planes) for the 2.2 nC per bunch needed to create the train for positrons production. The positron source for CLIC is a conventional one based on an electromagnetic shower created by electrons impinging on a high-Z material target. The source and its associated 2 GeV linac meet the specifications for the 500 GeV option. The

normalized yield is  $0.31 e^+/e^-$  per GeV at the exit of the  $e^+$  pre-injector linac. The charge per bunch for the primary electron beam is  $1.35 \times 10^{10} e^-$ . The incoming  $e^+$  emittance (edges) into the pre-damping ring is 0.09 m-rad for both planes. The longitudinal characteristics are 20 MeV energy spread (full width) and 50 ps bunch length (edge).

**The Linacs** Taking into account the necessary beam loading compensation, the  $e^+$  Pre-injector linac accelerates the particles up to 200 MeV with a loaded gradient of 24 MV/m. Therefore the final energy of the  $e^-$  beam at the end of the Pre-injector linac is the same as for the  $e^+$  beam. The energy gain in the  $e^-$  Primary Beam linac is a free parameter that will be adjusted for a good trade-off between cost and efficiency. The Injector linac (1.5 GHz) is based on a loaded gradient of 17 MV/m and is  $\sim 150$  m long in order to accelerate both beams to 2.424 GeV. The Booster linac (3 GHz) has a loaded gradient of 21 MV/m and is  $\sim 360$  m long in order to accelerate both beams up to 9 GeV. The rf pulse is 10  $\mu$ s long and accommodates two consecutive SLED pulses. The first is for  $e^+$  and the second for  $e^-$  acceleration respectively.

**3.4.2.1.3 Klystrons and Modulators** The main beams injector complex is required to deliver  $e^+$  and  $e^-$  beams at 9 GeV via the transfer lines to the CLIC main beam accelerator. The present injector design layout uses a series of linacs to accelerate the electron and positron beams. These L-band linacs (Figure 3.58), operating at a frequency of 1.5 GHz enable the energy of each beam to be increased to 2.424 GeV before injection into the damping rings. The klystron-modulators used in these linacs produce a 5  $\mu$ s rf pulse at peak powers up to 80 MW. Standard line-type modulators could be used for these pulsed rf sources except for the Injector Linac modulators where a configuration similar to the drive-beam modulators would be more appropriate because of the high average power per klystron. The S-band 3 GHz Booster Linac that follows the damping rings and the 3 GHz bunch compressors, will accelerate both electron and positron beams up to 9 GeV before injection into the 30 GHz compressors and the CLIC main linacs. The klystron-modulators in this linac are required to produce a long 10  $\mu$ s pulse with a peak rf power up to 80 MW. A high-duty cycle line-type modulator with the same configuration as for the drive-beam linac could also be used for this task as well again because of the high average power in each klystron. Table 3.28 gives a summary of the klystron and modulator requirements for the main-beam injector complex in the present 500 GeV CLIC scheme.

### 3.4.2.2 Damping Rings

The damping ring design (identical for  $e^+$  and  $e^-$ ) is based on the most demanding requirements at 3 TeV and some parameters are then adapted for the 500 GeV collision energy keeping the ring layout unchanged [9]. The need for very low emittances in the CLIC main linac implies a lattice with a small  $I_5$  synchrotron integral, which is obtained by using a TME (Theoretical Minimum Emittance) lattice, with compact arcs. The wiggler magnets needed in addition, as well as the injection and extraction insertions are located in dispersion-free regions. Making use in these regions of FODO-cells with zero dispersion, the average beta function  $\langle \beta_x \rangle$  through the wigglers can be kept reasonably small. In the limit of many wiggler poles and a short wiggler period  $\lambda$ , the damping and the quantum

TABLE 3.28: Main-beam klystron-modulator requirements. MDK= Modulator-Klystron system, SBK= Single-Beam Klystron, MBK= Multibeam Klystron.

MDK RF System	Number MDKs	Klystron Type	Repetition Rate [Hz]	Pulse Width [ $\mu$ s]	Frequency [MHz]	Peak Power [MW]	Average Power [kW]
$e^-/e^+$ pre-inj. linacs	4	SBK/MBK	200	5	1500	80	100
$e^-$ primary beam linac	24	SBK/MBK	200	5	1500	80	100
Injector linac	52	SBK/MBK	400	5	1500	40	100
Booster linac	52	SBK/MBK	200	10	3000	40	100

excitation only occur in the wiggler magnets and the final emittance without IBS (Intra Beam Scattering) does not depend on the unperturbed beam emittance in the arcs.

The ring circumference  $C$  is determined by the harmonic number  $h$ , the rf frequency, the number of bunch trains to be accommodated and the kicker rise-time or fall-time for injection and extraction. The ring energy is constrained by the IBS and by the spin tune selected to avoid integer spin resonances. In addition, avoiding instabilities implies keeping the momentum compaction  $\alpha_p$  relatively large. With these constraints, the optimum strengths of the arc dipoles and of the wigglers were then inferred from the minimum transverse emittance computed at extraction in the presence of IBS, for which the magnet fields were still considered reasonable.

Table 3.29 summarizes the main parameters required for the CLIC damping ring.

TABLE 3.29  
Target beam parameters for the damping ring at 500 GeV (3 TeV).

Parameter	Symbol	Value
Bunch population	$N_b$	$4.2 \times 10^9$
Number of bunches per train	$k_{bt}$	154
Repetition frequency	$f_r$	200 (100) Hz
Bunch spacing	$\tau_b$	0.2 m
Maximum kicker rise time	$\tau_k$	25 ns
Final transverse emittances	$\gamma\epsilon_{x,y}$	1600 (450), 3 nm·rad
Longitudinal emittance	$\gamma mc^2\epsilon_t$	$\leq 5000$ eV·m

The optics design proceeded by first solving the three differential equations describing the emittance time evolution in a smooth approximation, taking into account radiation damping and IBS parameterized by the Piwinski formalism, and by then constructing a MAD optics for the optimum parameters so determined. The energy for the damping ring is chosen as 2.424 GeV. The emittance is minimum if the horizontal phase advance  $\mu_x$  per TEM arc cell is  $284^\circ$ . This phase advance is far from ideal with regard to chromatic correction, and the horizontal and vertical phase advances per TME arc cell were adjusted to  $212^\circ/72^\circ$ . These values are close enough to the ones minimizing the emittance and allow good positioning of the sextupoles distributed in order to reduce both the non-linear chromaticity and the resonance driving terms. The damping ring accommodates two long straight wiggler-sections, in which the dispersion is almost negligible and the chromaticity is compensated by the arc sextupoles. The sextupole strengths are not as high as in previous designs while achieving a good correction of the nonlinear chromaticity, given the lattice characteristics summarized below. Preliminary results seem to indicate, however, that the resulting dynamic aperture is not yet sufficient and that a further optimization of the lattice and sextupole location is needed. Work on the damping ring optics is therefore actively pursued.

Starting from a generic TME layout, the CLIC arc lattice evolved toward a sequence of cells which comprise four quadrupoles and a combined function bending magnet. The cell optics

## DESCRIPTIONS OF THE FOUR MACHINES AT 500 GEV C.M.

is shown in Figure 3.59 (Left). Compared with a three-quadrupole cell, the four-quadrupole cell provides larger dispersion amplitudes at these quadrupoles ( $\sim 1.25$  cm and  $\sim 0.9$  cm at the QF and QD, respectively) where the sextupoles are located. The emittance detuning factor for this cell is  $\varepsilon_r = 1.71$ . The defocusing gradient in the bending magnet decreases the emittance by about 10–15% via the associated change of the damping partition  $J_x$ . The combined function magnet also facilitates the matching. The defocusing gradient retained is close to 150 kG/m.

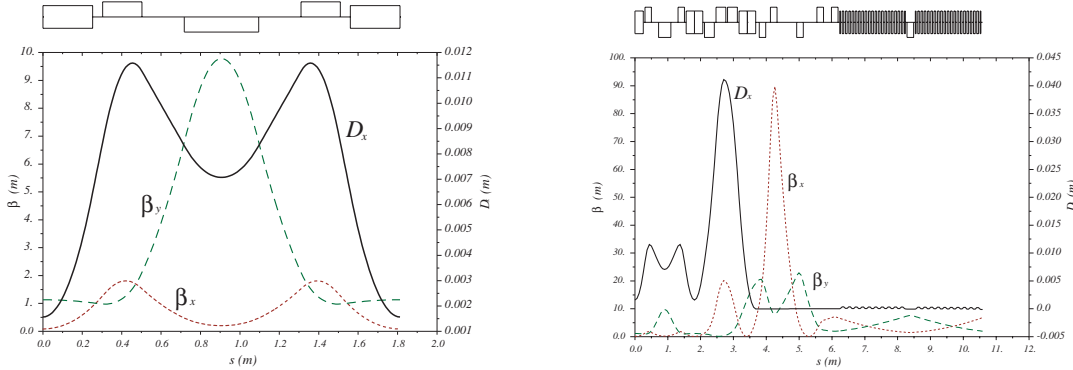


FIGURE 3.59. Left: Optical functions over the arc cell. Right: Optical functions from the end of the arc to the first wiggler FODO cell.

At the two edges of each of the two arcs, a dispersion suppressor is located which connects them to the dispersion-free straight sections that include rf cavities, FODO cells with wigglers, and injection/extraction sections, as is illustrated in Figure 3.59 (Right). In the straight sections, the phase advances of the FODO cells are  $90^\circ/70^\circ$  for the horizontal and vertical motion, respectively. The damping ring parameters for the design lattice are listed in Table 3.30. The rms bunch-length  $\sigma_z$  and energy-spread  $\sigma_\delta$  at extraction are compatible with the requirements for the subsequent bunch compressors. However, the obtained transverse emittances do not completely meet the target (nominal) values required (Table 3.29), in particular in the vertical plane. First an improvement of the damping ring design and then a revision of the overall emittance budget might resolve this inconsistency at 3 TeV. At 500 GeV, the conditions are relaxed and a larger horizontal emittance will likely allow the nominal vertical value to be reached. If it is not reached, then the luminosity would approximately go down with the square root of the ratio of the nominal to the actual emittances at the linac end, ratio which does not increase much when assuming that identical blow-ups add to the damping ring values (*e.g.*,  $\gamma\varepsilon_y$  at the DR extraction going from 3 to 5 nm implies an increase from 10 to 12 nm at the linac exit and a  $\sim 10\%$  luminosity loss). In any case, a reduction of  $\beta^*$  makes it possible to obtain a luminosity larger than  $10^{34}$   $\text{cm}^{-2}\text{s}^{-1}$  as aimed at, and thus to compensate for emittances somewhat larger than nominal. For the 200 Hz operation mode considered at 500 GeV, the store time of 45 ms is about equal to 20 transverse damping times, which assures that the beam at extraction is always in a steady state.

TABLE 3.30  
CLIC damping ring parameters (3 TeV present design).

Parameter	Symbol	Value
Nominal $e^+$ ring energy	$\gamma mc^2$	2.424 GeV
Number of bunch trains stored	$N_{\text{train}}$	9
Ring circumference	$C$	374.3 m
Number of cells	$N_{\text{cell}}$	100
Betatron coupling	$\varepsilon_y/\varepsilon_x$	2.1%
Extracted horizontal emittance	$\gamma\varepsilon_x$	619 nm·rad
Extracted vertical emittance	$\gamma\varepsilon_y$	7.5 nm·rad
Extracted longitudinal emittance	$\gamma mc^2\varepsilon_t$	4297 eV·m
Extracted energy spread	$\sigma_\delta$	$1.35 \times 10^{-3}$
Extracted bunch length	$\sigma_z$	1.31 mm
Damping time	$\tau_x$	2.676 msec
Damping time	$\tau_y$	2.735 msec
Damping time	$\tau_t$	1.383 msec
Horizontal tune	$Q_x$	69.21
Vertical tune	$Q_y$	29.63
Horizontal emittance without IBS	$\gamma\varepsilon_{x0}$	343 nm·rad
Field of bending magnet	$B_a$	10 kG
Field of wiggler	$B_w$	17.64 kG
Wiggler period	$\lambda_w$	20 cm
Length of bending magnet	$L$	0.506 m
Total length of wigglers	$L_w$	158 m
Energy loss per turn	$U_0$	2.213 MeV
RF voltage	$V_0$	3.0 MV
RF frequency	$f_{\text{rf}}$	1500 MHz
Harmonic number	$h$	1871
Momentum compaction	$\alpha_p$	$0.662 \times 10^{-4}$

## DESCRIPTIONS OF THE FOUR MACHINES AT 500 GEV C.M.

The strength of IBS increases with decreasing bunch dimensions. To achieve the low equilibrium emittances required at the highest energies, the damping times have to be considerably decreased using wigglers. The wiggler sections include a total of 76 units, each 2.1 m long and consisting of 21 pairs of magnetic poles.

### 3.4.2.3 Bunch Compressors and Transfer Lines

The damping ring is designed to deliver a beam at the energy of 2.424 GeV, bunched at the rf frequency of 3 GHz, of relative rms energy spread 0.135% and of rms length of 1.31 mm. The required bunch length in the main linac of 35  $\mu\text{m}$  results from a compromise between the reduction of the dilution effect of transverse wakefields on the vertical emittance and of the optimization of the energy-spread with a minimal phase-shift with respect to the rf voltage crest. The corresponding compression ratio is about 37.4 which cannot be obtained by a single compression stage because of the resulting energy spread which is too large for the following isochronous turn-around loop located at the entrance of each main linac. Thus two stages of compression are proposed one at 2.424 GeV and one at 9 GeV to benefit from a higher gradient and a larger rf frequency. A compromise has to be found between an acceptable rms energy spread at the exit of the first stage and the  $R_{56}$  required by the second stage. The compression factor of 4 of the first stage has been chosen because the rms energy spread at the exit is an acceptable value of 0.54% and the resulting  $R_{56}$  of the second stage is sufficiently small (-0.024 m) to prevent large CSR (Coherent Synchrotron Radiation) effects after optimization of the chicane design. In these conditions the compression ratio of the second stage is equal to 9.35 (rms bunch length shortened from 327.5  $\mu\text{m}$  to 35  $\mu\text{m}$ ) and the uncorrelated rms energy spread at the entrance of the main linacs is 1.36%. The rf voltages are 154 MV at 3 GHz and 592 MV at 30 GHz and the corresponding  $R_{56}$  amount to 0.235 m and 0.024 m, for the first and second compressor respectively. The second pseudo rotation in the longitudinal phase space is achieved by a magnetic chicane consisting of two parts one being the mirror image of the other. Each part is composed of two rectangular dipoles, of length  $L_m$  and bending angle  $\theta$ , separated by a drift space of length L. The chicanes have been optimized to reduce the maximum values of the  $\beta$  Twiss function. Their optical functions are shown in Figure 3.60 and their lengths (including the triplets making the matching to any FODO lattice possible) are equal to 68 and 79 m respectively.

Simulations indicate that the high-order magnetic effects of the chicane and of the wakefields are small, only slightly lengthening the bunch by one micron. The effect of the coherent radiation has not been investigated but a rough estimate suggests that it should be negligible. The 360° turn-round consists of 72 isochronous modules, each one made of three identical dipoles (1 m long) and of four quadrupoles. Symmetric triplets match the modules between them. The overall diameter of the turn-round is 231 m approximately, in order to limit to 45 nm-rad the horizontal emittance growth due to the incoherent synchrotron radiation.

### 3.4.2.4 Main Linac

**3.4.2.4.1 Lattice Description** The main linac of CLIC at a center-of-mass energy of 500 GeV is based on the one for 3 TeV cut at the point where the beam reaches

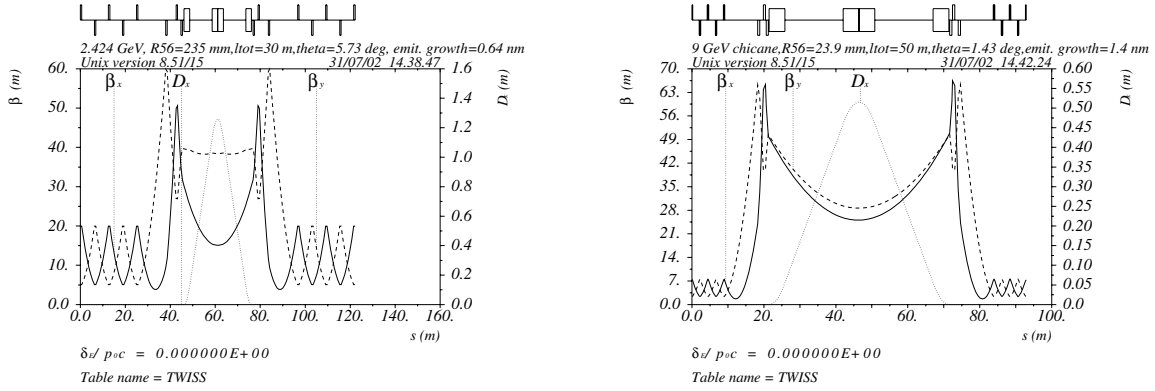


FIGURE 3.60. Left: Optical functions in the first chicane. Right: in the second chicane.

$E=250$  GeV. The rf phases have been readjusted but no further optimization has been performed. Note that the cavity parameters used in the quoted simulations correspond to those estimated for an accelerator structure of  $\pi/2$  phase-advance, introduced for solving the surface-field problem. Since this structure still suffers from pulse surface heating, another design addressing both problems is being studied, but it is not yet completed and therefore not presented here. Consequently, though not strictly consistent with the accelerator structure described in the next section, tracking results obtained with the  $\pi/2$  cavity have been kept since they are slightly pessimistic with respect to the ones corresponding to the description given.

In order to facilitate the geometrical matching of the drive beam decelerators and of the main linac, both are built of 2.23 m long modules. Each main linac module contains four 0.5 m long accelerator structures. Between one and four of these structures may be replaced by a quadrupole to provide the necessary focusing. A beam-position monitor (BPM) is placed at the head of each girder. The beam line of the whole linac consists of five sectors, each containing FODO cells of equal length and equal phase advance. In order to keep the cavity filling-factor and the BNS stability margin roughly constant along the linac, the target values of the focal length  $f$  and the quadrupole spacing  $L$  are scaled from the initial values  $f_0=1.5$  m and  $L_0=2.5$  m with the energy  $E$  as  $L(E) = L_0(E/E_0)^{1/2}$  and  $f(E) = f_0(E/E_0)^{1/2}$ . The actual values in each sector are adjusted to the hardware geometry. Figure 3.61 shows the vertical beta-function along the linac. The phase advance is about  $70^\circ$  per cell but varies slightly from sector to sector. This small value allows a better compromise between time-dependent and static misalignments. The optics matching between two sectors is achieved by adjusting the strengths of the last three quadrupoles of the previous sector and the first two of the following one. The cavity filling-factor is 73.5%.

The beam consists of a train of 154 bunches spaced by 20 cm with a charge of  $4 \times 10^9$  particles per bunch. The bunch length is  $\sigma_z=30$   $\mu\text{m}$ , and the initial, normalized, vertical and horizontal emittances are  $\gamma\epsilon_x=1800$  nm·rad and  $\gamma\epsilon_y=5$  nm·rad, respectively. The target for the increase of  $\gamma\epsilon_y$  is less than 5 nm·rad.

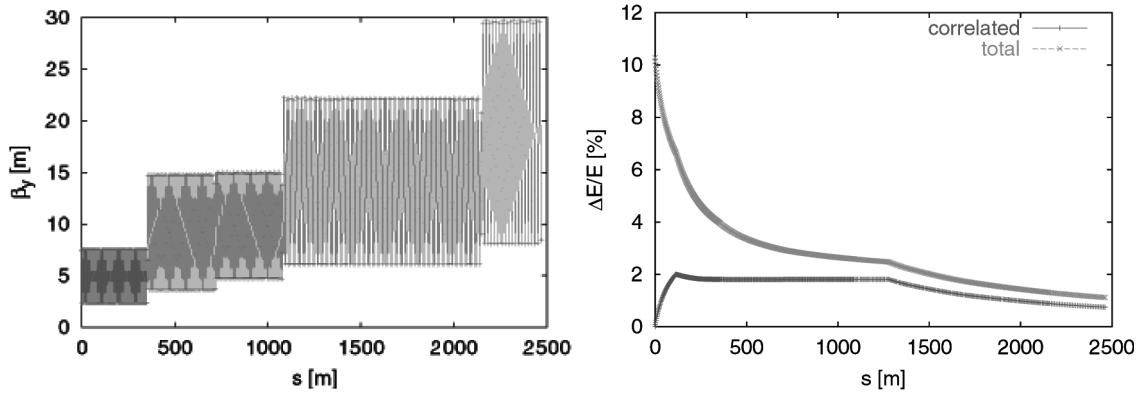


FIGURE 3.61. Left: The beta-function in the main linac lattice. Right: The full width energy spread along the linac. To estimate the total energy spread the uncorrelated incoming energy spread is cut at  $\pm 2.5\sigma_E$ .

In order to stabilize the beam, BNS damping is used. For energies between 9 and 20 GeV, the rf phase is set so as to create a relative energy spread in the bunch, which is then maintained in the main part of the linac by using another phase. In the last part, the rf phase is set in order to decrease the correlated energy spread to a full width of 0.75% so that the beam can pass the final focus system. The optimum phases will have to be determined experimentally in practice. In the presence of ground motion, a larger energy spread leads to better results if a few feedbacks are used to re-steer the beam, while a smaller energy spread is advantageous if a one-to-one correction is used for the same purpose. For the present simulations  $\Phi_{RF} = 4^\circ$  is retained in the main part of the linac, leading to the energy spread shown in Figure 3.61.

The control of the bunch-to-bunch energy spread requires the compensation of the beam loading in the main linac. It is proposed to achieve this compensation by generating a ramp in the rf power output of the Power Extraction and Transfer Structures (PETS). Simulations show that a full bunch-to-bunch energy spread of less than  $5 \times 10^{-4}$  can be obtained in the main beam with the rf voltage resulting from a delayed phase-switching technique.

**3.4.2.4.2 Static Correction** Before beam-based correction, the beam-line elements will be pre-aligned by means of a sophisticated system of wires. This system, which will also be used in the LHC, has been modelled to simulate 100 different cases of initial misalignments of the straight lines defined by the wires (resulting from the survey pre-alignment). The beamline components are randomly scattered around these straight lines. The r.m.s. amplitudes of their consequent misalignments are expected to be less than  $10 \mu\text{m}$ . While this accuracy is relevant for the beam-position monitors (BPMs) and for the accelerator structures pre-aligned on every girder with respect to the BPMs, it is not really critical for the quadrupoles which are re-aligned with the beam as explained here; for instance, an initial  $50 \mu\text{m}$  r.m.s. scattering is acceptable for quadrupoles. The relative misalignments of the girders are defined by those assumed for the BPMs.

This precision of  $10\ \mu\text{m}$  is not sufficient to keep the growth of the vertical emittance smaller than  $5\ \text{nm}\cdot\text{rad}$  in the main linac (corresponding to a relative growth of 100%). Therefore, beam-based alignment of the beam-line elements is necessary. In the so-called ballistic alignment method, first the BPMs and then the quadrupoles will be aligned. In the next step the accelerator structures need to be aligned on the beam trajectory. Finally emittance tuning bumps are used to minimize the remaining emittance growth.

In the ballistic alignment method the beam line is divided into a number of bins, containing 12 quadrupoles each, and the correction is applied successively in each bin. In the first step of the correction all the quadrupoles in the bin are switched off, except the first one. The beam is then steered into the last BPM of the bin. The other BPMs are moved onto the trajectory of the beam. It has been verified that the beam divergence does not generate a transverse beam-size larger than  $\sim 75\ \mu\text{m}$  r.m.s. over the length of a bin. The possible perturbing effect of weak remnant or earth magnetic fields can be reduced by either shielding, correcting or measuring and modelling them. In the second step of the correction, the quadrupoles are switched on again and a simple few-to-few correction is performed. This method allows all the BPMs in a bin to be aligned on a relatively straight line and thus to reduce the dispersion to a very small value. The remaining emittance growth is almost entirely due to the wakefields of the structures that are scattered around the beam trajectory. It therefore depends very little on the rf phases chosen.

In the simulations, all elements are assumed to be scattered around a common axis following a normal distribution with an r.m.s. of  $10\ \mu\text{m}$  for BPMs and structures and  $50\ \mu\text{m}$  for quadrupoles for the reasons explained previously. The BPM resolution is  $100\ \text{nm}$ .

Beam jitter during correction, remanent fields of the quadrupoles when switched off and the shift of the quadrupole center with field strength (from remanent to nominal field) are also possible error sources. In the simulation, a position jitter of the incoming beam of  $0.1\ \sigma$  is included. If the jitter is larger, then one can average over a number of pulses. The size of the remanent field is sampled from a constant distribution between 0% and 2% of the nominal quadrupole strength. The shift of the quadrupole center is assumed to follow a Gaussian distribution with an r.m.s. of  $10\ \mu\text{m}$ . The effect of these imperfections can be very large at the first correction step, but iterating the correction in a bin solves the problem almost completely. The emittance growth simulated with PLACET is about  $\Delta\epsilon_y/\epsilon_y=110\%$ , which is still larger than the goal set. This method of correction is robust and will be the basic static correction applied when starting the linac. Another method that is based on varying the strengths of the quadrupoles by a small amount ( $\sim 5\%$ ) and therefore avoiding switching them off could complement the ballistic alignment. This method, termed multistep lining-up correction, is based on the estimates of the quadrupole displacements from the measured trajectory difference. A fit through the BPM's readouts of one trajectory gives the steering angle required to recenter the beam in one bin. The quadrupoles and the BPMs can then be re-aligned.

A further reduction of the emittance growth after ballistic correction is necessary. A possible way to achieve this additional reduction consists of applying a number of local emittance-tuning bumps distributed along the linac. In the simulation case, these bumps are based on two groups of accelerator structures around two quadrupoles followed by a feedback system. The feedback system consists of two quadrupoles that are about  $\pi/2$  apart and serve to steer the beam onto the initial trajectory. Also a measurement station is necessary to measure the emittance. One could have one station after each bump inside the

linac or a single station at the end of the linac used for all the bumps. Having one station per bump is simpler in operation, but its integration inside the linac has to be studied. Having a single station at the end of the linac leads to slightly better performance and the design of the system could be simpler. However, the tuning procedure is less straightforward and an abnormal emittance growth localized in one part of the linac is more difficult to track down. To perform the tuning the two groups of accelerator structures are displaced and the feedback system is used in order to minimize the emittance at the measurement station. By inserting 2 bumps in the linac, the vertical emittance growth can be reduced to about 22% for  $\Phi_{RF} = 4^\circ$  (left side of Figure 3.62). Here, the results significantly depend on the rf phases because the emittance growth due to the dispersion is almost completely cancelled by the ballistic correction while the bumps prevent the emittance growth due to wakefields. The remaining blow-up corresponds to the cross talk between the dispersion and the wakefield effects. Using five bumps results in about 7% emittance growth after all the static corrections. For the machine with  $E_{cm}=3$  TeV, it has been shown that the multibunch results are very close to those for single bunches.

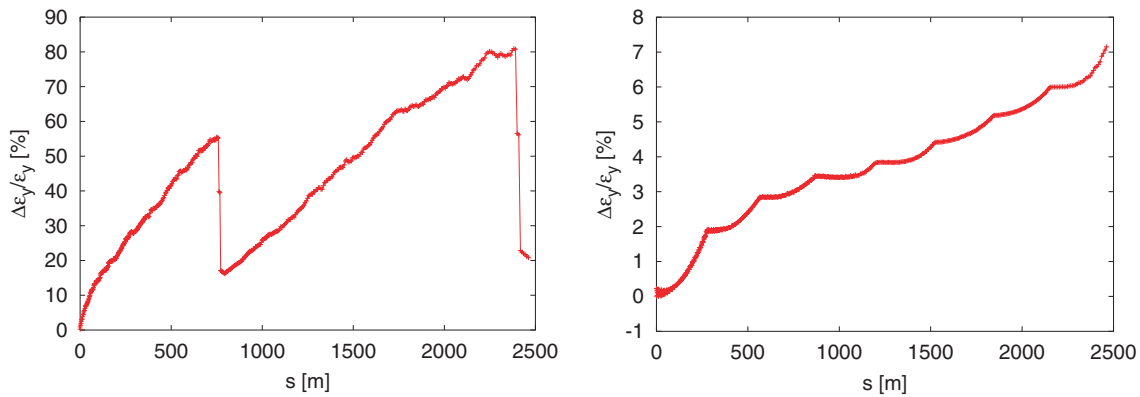


FIGURE 3.62. Left: The emittance growth in the linac after the ballistic alignment and optimization of the emittance tuning bumps. Right: The emittance growth after 1000 s of ground motion if seven feedbacks are used.

**3.4.2.4.3 Time Dependent Effects** Transverse position jitter of accelerator structures and quadrupoles can lead to an emittance growth. Here we define the emittance with respect to the average beam trajectory, *i.e.*, we integrate over a number of consecutive pulses. A 6% growth of the vertical emittance results from a position jitter of the quadrupoles with a r.m.s. of 3 nm or a pitch angle jitter of  $0.45 \mu\text{rad}$ , as well as from a structure position jitter of  $1.75 \mu\text{m}$  or a pitch angle jitter of  $0.75 \mu\text{rad}$ . It must be noted that the emittance growth due to an initial beam jitter is not significantly increased by the effects of the wakefields along the main linac.

Long-term, diffusive ground motion can also lead to emittance growth. We assume a simplified model following the ATL-law with  $A=0.5 \times 10^{-6} \mu\text{m}^2/(\text{m}\cdot\text{s})$ . Using seven feedbacks in the linac one finds  $\Delta\epsilon_y/\epsilon_y \approx 7\%$  after 1000 s (right side of Figure 3.62). Even

if one assumes that no information is transferred from one feedback to the next and that the beam has a transverse position jitter at injection of  $0.3 \sigma_y$  one can still choose a gain of 0.1. This ensures that the effects of ground motion during the response time of the feedbacks are kept to a small fraction of a percent.

### 3.4.2.5 Main Linac Accelerator Structures

The CLIC main linac accelerator structure, the TDS (Tapered Damped Structure) consists of 150 cells and is 500 mm long. It operates in the  $2\pi/3$  traveling wave mode. The design of the structure is driven by extreme performance requirements: accelerating gradients well in excess of 150 MV/m, power flows in excess of 200 MW, a  $10 \mu\text{m}$  structure straightness and alignment tolerance (to preserve single bunch emittance), long-range transverse wakefield suppression of over two orders of magnitude (to preserve train emittance) and ultimately a low mass production cost. The issues of gradient, power and tolerances are each in part addressed by ultra-high precision diamond turning the copper disks that make up the sections. This technique gives a  $1\text{--}2 \mu\text{m}$  dimensional tolerances and an optical quality surface finish. The  $10 \mu\text{m}$  tolerance of assembled sections is guaranteed by a specially developed hybrid brazing/diffusion bonding technique. Measured Q factors correspond to 98% of the theoretical value in (undamped) constant impedance structures. Constant impedance structures were tested in CTF1 to 125 MV/m (albeit with pulses that reached these peak levels for only a few nanoseconds). Long-range transverse wakefields are suppressed through a combination of strong damping and detuning. The damping is accomplished by coupling four individually terminated waveguides to each cell of the structure. The damping waveguides have a rectangular cross-section of 4.5 mm by 1.9 mm, thus a cutoff frequency of 33.3 GHz, which is above the fundamental but below all higher order modes. In this way higher-order mode energy propagates out of the cells via the damping waveguides but the fundamental mode energy does not. This results in a Q of approximately 16 for the lowest, and most dangerous, dipole passband. A taper in the iris diameter from 4.5 mm at the head of the structure to 3.5 mm at the tail provides a detuning frequency spread of 2 GHz (5.4%). The layout of the structure cells can be seen in Figure 3.63.

Cell dimensions and some of the fundamental mode characteristics of the beginning, middle and end cells are given in Table 3.31. Using these calculated fundamental mode characteristics, the power flow, the accelerating gradient (left side of Figure 3.64) and other quantities along the structure have been obtained. The nominal average gradient of 150 MV/m is obtained with 250 MW input power.

A number of methods have been developed to calculate the transverse wakefield of the TDS (right side of Figure 3.64). These include an uncoupled circuit model, a semi-coupled time domain model, a complex wave number model and a double band circuit model. The validity of the long-range wakefield analysis and of the TDS design has been directly demonstrated by the measurement of a 15 GHz structure at the ASSET facility at SLAC (left side of Figure 3.65).

DESCRIPTIONS OF THE FOUR MACHINES AT 500 GEV C.M.

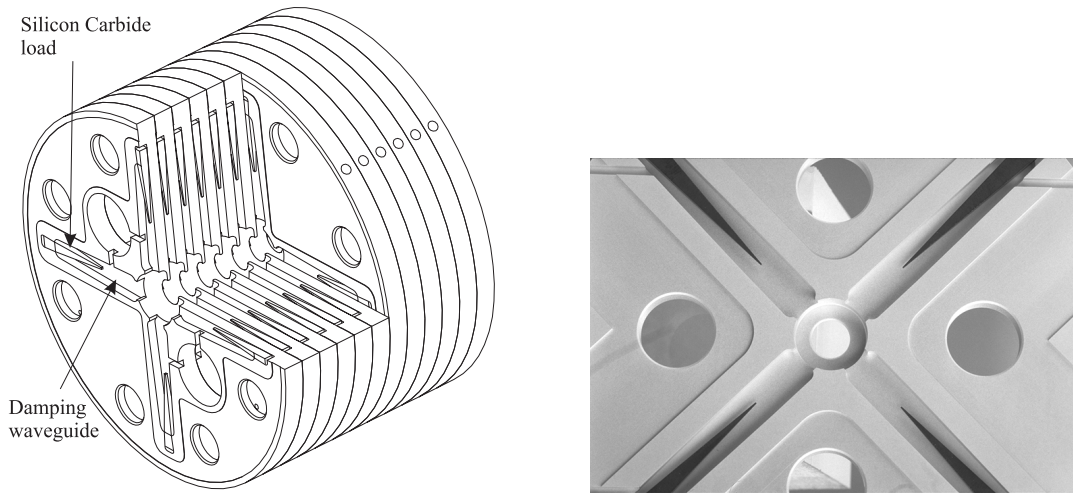


FIGURE 3.63. Left: Cross-sectional view of the TDS geometry. Right: Photograph of a TDS cell with damping waveguides and SiC loads.

TABLE 3.31  
Fundamental mode parameters of the TDS as calculated using HFSS.

Cell Radius [mm]	Iris Radius [mm]	Q	R'/Q [k $\Omega$ /m]	$v_g/c$
4.255	2.250	3628	20.2	10.4
4.111	2.000	3615	23.0	7.5
3.984	1.750	3621	27.1	5.2

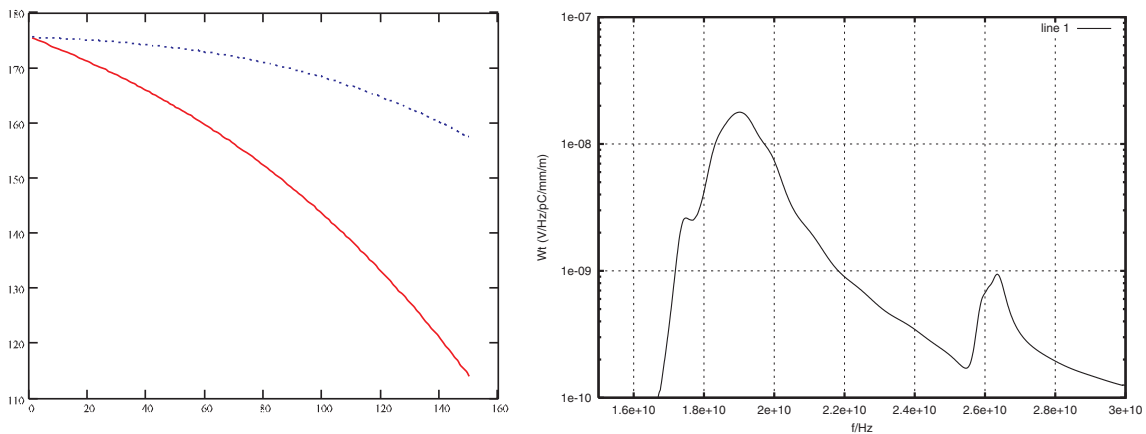


FIGURE 3.64. Left: Accelerating gradient in MV/m as a function of cell number. The solid line is with beam and the dotted one without. Right: Transverse wake spectrum in V/Hz/pC/mm/m between 16 and 30 GHz.

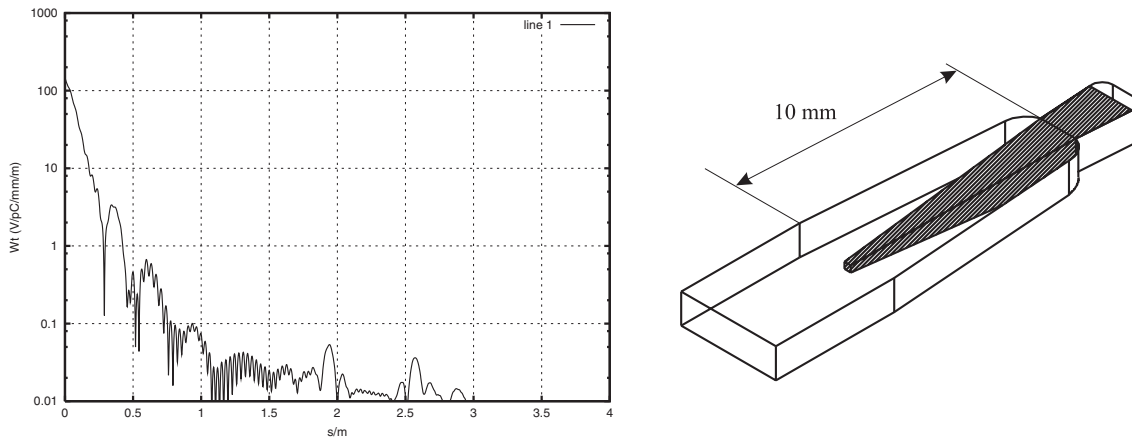


FIGURE 3.65. Left: Transverse wake of the TDS with the 10 mm load, as computed by the double-band circuit model (n.b. the computation has been made for a 15 GHz structure). Right: Detail of the TDS load. The load is 2 mm wide at its base and  $0.2 \text{ mm}^2$  at the tip.

The damping waveguide load must simultaneously be well matched down to near the waveguide cut-off frequency, compact, vacuum compatible, and compatible with assembly by brazing of the accelerator structure. A low reflection coefficient is obtained by using a taper of Silicon Carbide (right side of Figure 3.65). The performance of the load near the cut-off is improved by tapering *inward* the damping waveguide at the point at which the load begins. In this way the impedance change caused by the SiC is partially compensated by the impedance change of the narrowing waveguide. The current load design has been optimized using HFSS and has an overall length of 10 mm.

Operation of this structure with the nominal average accelerating gradient of 150 MV/m has not yet been demonstrated. The feasibility of such a gradient has been established with a small-aperture (6 mm) copper X-band structure which has been conditioned to an accelerating gradient of 154 MV/m with 150 ns pulses without any damage. Damage has however been observed in the copper input couplers of 30 GHz accelerator structures tested in CTF2. The surface field where the damage occurred was about 260 MV/m limiting the accelerating gradient to 60 MV/m. Two main approaches are being pursued to raise the achievable accelerating gradient and to avoid damage: changes to the rf design and new materials. In a recent test, a 30 cell structure with a reduced surface field geometry and irises made from molybdenum reached a peak accelerating gradient of 193 MV/m with a pulse length of 15 ns. No damage was observed.

It has to be noted that, during the process of modifying the structure design in view of solving the problems due to surface fields, an accelerator structure of  $\pi/2$  phase advance was considered. This explains why simulations of the main beam dynamics have been done with such a designed structure, although this solution will likely not be retained for reasons mentioned elsewhere. Further developments presently focus on  $2\pi/3$  structures of aperture smaller than the one described in this section with optimized geometry and rf-coupler.

### 3.4.2.6 Beam Delivery System

The beam delivery system (BDS) comprises energy and betatron collimation, a beta-matching section, and the final focus. The system described here was designed for 3 TeV and then scaled back for 500 GeV keeping the same overall length of 2.6 km, significantly smaller than the one of the base-line design [7]. The most recent BDS design [10] is indeed based on a short collimation system made of one module instead of two for the energy collimation and a compact final focus as proposed at SLAC, which features a nonzero dispersion across the final doublet and chromaticity sextupoles located next to the final quadrupoles. In front of these quadrupoles is a 200 m long bending section, which produces the dispersion. Upstream sextupoles correct the geometric aberrations. The free length between the final quadrupole and the IP is as large as  $l^* = 4.3$  m. This might be a major advantage of the compact final focus for the final quadrupole remains outside of the detector solenoid and its fringe. The length of the compact Final Focus system is 550 m.

The 3 TeV collimation optics upstream of the compact final focus is based on the collimation lattice developed for the NLC. Starting from this lattice, the length of the energy collimation was scaled by a factor of 5 and the bending angles by a factor of 1/12. The  $I_5$  radiation integral at this high energy amounts to  $1.9 \times 10^{-19}$  m, which corresponds to an emittance growth of  $\Delta(\gamma\epsilon_x) \approx 0.09 \mu\text{m}$ , near the tolerable limit. At 500 GeV, the bending angles as well as the dispersion are increased, but only by 20%, and the emittance growth from synchrotron radiation is of course much smaller. Accepting the quoted emittance blow-up at 3 TeV and a possible reduction of the collimation efficiency still to be estimated, the total length of the collimation system now proposed amounts to slightly more than 2 km.

Both energy-collimations and betatron-collimations are included in this system. The transverse beam halo must indeed be collimated in order to ensure acceptable background in the detector. The transverse collimation depth is set by the requirement that the synchrotron-radiation fan generated in the final quadrupoles does not hit any aperture upstream of the collision point. Leaving a margin of  $2\sigma_x$  and  $3\sigma_y$ , respectively, the betatron collimation should be set at 3 TeV to  $\pm 12\sigma_x$  and  $\pm 80\sigma_y$ . The same collimation depths are assumed for 500 GeV, where the aperture of the final quadrupoles can be largely increased. The situation is different for the energy collimation. Here, the requirements are imposed by failure modes in the linac. According to a detailed study energy collimation at about  $\pm 1.5\%$  will protect the downstream parts of the beam delivery system against all the linac failures considered, including the associated betatron oscillations. Main-beam energy errors, due to failures in the drive-beam sector, are not always accompanied by large emittance growth, and thus call for a reliable energy collimation (by contrast, pure betatron oscillations in the linac rapidly filament and give rise to largely increased emittances). The tight energy collimation planned will however ensure that a beam perturbed in energy is intercepted at the energy spoiler without hitting downstream betatron collimators. Hence the energy collimation depth is determined by the effect of failure modes and, collimator survival is not required for the betatron spoilers at the nominal emittances.

In the final focus, a high field in the last quadrupole doublet reduces the chromaticity generated by this doublet and consequently reduces the high-order aberrations of the final-focus. Given the limited space and the tight requirements on the mechanical stability, a permanent magnet is the most adequate solution. It uses  $\text{Sm}_2\text{Co}_{17}$  material for its

thermal stability and radiation hardness. The beam-pipe radius in the last quadrupole is 3.8 mm in order to produce a gradient of 388 T/m as required by the optics at 3 TeV, while the corresponding values for the preceding quadrupole of the doublet are  $\sim 10$  mm and  $\sim 135$  T/m respectively. Much weaker magnets are needed at 500 GeV. It is assumed that the permanent-magnet field cannot be varied and that fine tuning of the IP beta functions is done using upstream quadrupoles, as it has been done at the SLC. The bending angles and the dispersion function in the final focus are 4.25 times larger at 500 GeV than at 3 TeV and the sextupole fields are correspondingly reduced (decreasing the high-order aberrations). Since the Oide effect is much weaker at 500 GeV, the  $\beta$  functions at the IP can be squeezed down to values as small as  $\beta_x^*=3$  mm, and  $\beta_y^*=50$   $\mu\text{m}$ . Note that the IP distribution then becomes distinctly non-Gaussian and the rms beam size is no longer a good indication of the luminosity. Tracking shows that, for constant emittances at the entrance of the final focus, the geometric luminosity without pinch increases from  $L=1.02\times 10^{34}$   $\text{cm}^{-2}\text{s}^{-1}$  for  $\beta_y^*=150$   $\mu\text{m}$ ,  $\beta_x^*=10$  mm, to  $L=1.85\times 10^{34}$   $\text{cm}^{-2}\text{s}^{-1}$  for  $\beta_y^*=50$   $\mu\text{m}$ ,  $\beta_x^*=3$  mm (at 200 Hz with  $\gamma\epsilon_y=10$  nm,  $\gamma\epsilon_x=2$   $\mu\text{m}$ ). This is almost twice the desired  $L$  target value. The luminosity with pinch is inferred from integrated simulations, which show that reducing only  $\beta_y^*$  and leaving  $\beta_x^*$  at 10 mm preserves the quality of the luminosity spectrum. With the assumed emittances, the effective rms spot sizes  $\sigma_{x,y}$  are 178 nm and 4.07 nm respectively. The optical functions at 500 GeV are displayed in Figure 3.66. The bandwidth of this optics in the presence of synchrotron radiation exceeds a relative momentum full width of 1%. At 500 GeV the inner radius of the final quadrupole must be increased, by about a factor of 2, in order to provide a beam stay clear of  $6\text{--}10$   $\sigma_x$ . A study covering optics layout, muon background, collimator survival, and wakefield effects is being carried out, but all these aspects will be relaxed at 500 GeV compared to 3 TeV.

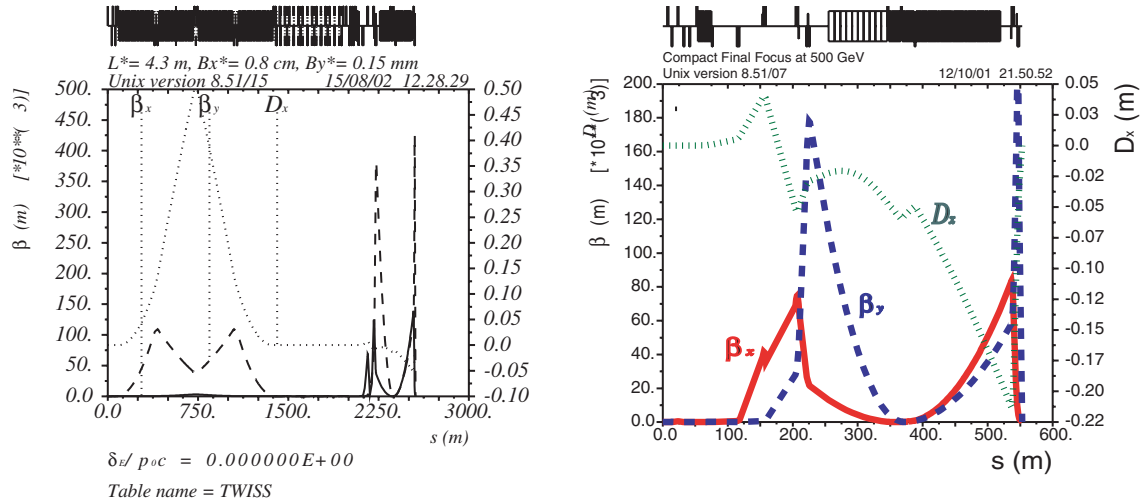


FIGURE 3.66. 500-GeV optics for the compact beam delivery (left) and final focus (right) systems.

## DESCRIPTIONS OF THE FOUR MACHINES AT 500 GEV C.M.

Extraction of the disrupted beam from the interaction point necessitates collisions with a crossing angle. The crossing angle is set to 20 mrad, in view of various constraints. Specifically, the multibunch kink instability and beamstrahlung photons impose a minimum value for the crossing angle, while synchrotron radiation and dispersion in the solenoid field give rise to an upper bound. A crab cavity with about 1 MV maximum voltage at 30 GHz will avoid luminosity loss due to the crossing angle. The relative phase error between the two crab cavities on either side of the collision point should remain within  $0.1^\circ$ . The voltage increases and the phase tolerance decreases with rf wavelength. Schematics of the CLIC IP region are displayed in Figure 3.67.

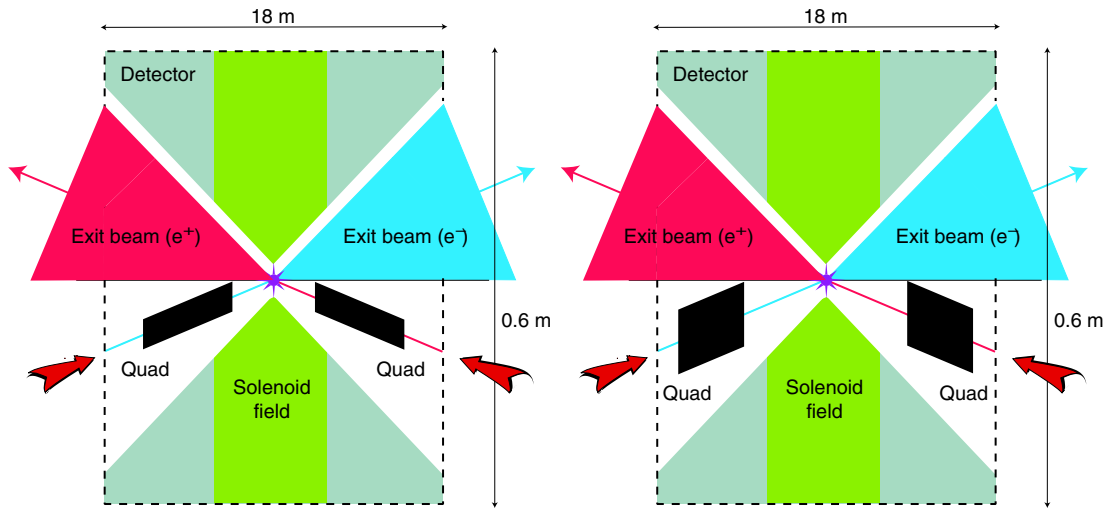


FIGURE 3.67. Top view of the CLIC IP region with the detector, the colliding beams, and the final quadrupoles for the base-line (left) and the compact final-focus optics (right) at 3 TeV. Scales are indicated. The transverse size of the detector is about 17 m.

A related critical issue is the collision of beams with nanometer size. The vertical rms beam size is about 1 nm at 3 TeV and 4 nm at 500 GeV. The final quadrupoles need to be stabilized to a fraction of this value, *i.e.*, stabilization levels of about 0.2 nm at 3 TeV and 0.8 nm at 500 GeV are required for frequencies above several Hz. In order to assess the feasibility, a stability project was launched and preliminary results have been obtained. The acoustic waves generated by beam impact at collimators or beam dump and their potential effects were studied. The integrated motion of the ground above 4 Hz was found to be not larger than a few nm in sites like the LEP or SLAC tunnels. However, the motion of quadrupoles in a realistic accelerator environment, such as the CLIC Test Facility 2 (CTF2), was measured to be about 10 nm. It is therefore planned to explore the improvements attainable by an active stabilization system. The magnet motion measured under different conditions will then serve as an input to simulation studies of the time-dependent luminosity performance. Preliminary results indicate that actively stabilized supports built by industry succeeded to damp the floor vibration in a test-stand installation by a factor of 20. Rms motion of a CLIC prototype quadrupole placed on a stabilized table was measured to be  $0.9 \pm 0.1$  nm vertically above 4 Hz with a nominal flow

of cooling water. Horizontally and longitudinally, without cooling water, the measured numbers are  $0.4 \pm 0.1$  nm and  $3.2 \pm 0.4$  nm.

Tuning and feedback strategies are essential for reaching the design performance. A fast feedback at the collision point, acting over a few pulses, will be supplemented by an ultra-fast intra-train feedback, the potential performance of which has been investigated by simulations. In addition, tight local orbit control in the beam delivery system, and automated optical tuning loops optimizing luminosity-related signals will likely prove indispensable for maintaining the desired spot size. The extraction and disposal of the spent beam as well as diagnostics for the disrupted beam and the beamstrahlung photons are important topics for further studies.

Depolarization during the collision is significant at 3 TeV. An effective decrease of the polarization due to the collisions of about 7% and a total depolarization through the whole complex of 23% are predicted. Though it may be less critical at 500 GeV, a polarimeter on either side of the collision point will be beneficial even for the lower energy.

### 3.4.2.7 Machine-Detector Interface and Beam-Beam Interaction

The machine-detector interface has been investigated for a center-of-mass energy of  $E_{cm}=3$  TeV. At lower energies it will be simpler.

In the interaction point, the electro-magnetic forces of the two colliding beams focus each other. This enhances the luminosity but also leads to the emission of beamstrahlung. In CLIC with center-of-mass energies of up to 1 TeV the critical energy of this radiation is below the beam energy, but this is not the case at  $E_{cm}=3$  TeV. The resulting luminosity and luminosity spectrum have been simulated using GUINEA-PIG. At 3 TeV, the beamstrahlung has a total power of about  $P=4.6$  MW, but it is emitted into small cones in the forward direction and does not produce direct backgrounds. However, protection of the magnets in the spent beam line is an issue which has not yet been investigated. Secondary particles—especially neutrons—are also a concern.

In addition, the beam-beam interaction will generate background via coherent and incoherent pair creation. In the coherent process, a hard beamstrahlung photon turns into an electron-positron pair in the strong field of the oncoming bunch. GUINEA-PIG simulations show that about  $6.8 \times 10^8$  pairs are produced per bunch crossing; a number comparable to the number of beam particles. Thus these particles influence the beam-beam interaction significantly. Initially they have small angles but they can be deflected by the beams. The number of particles produced via the incoherent process is much smaller than the number of particles in the bunch (about  $4.5 \times 10^5$ ), but they can have significant inherent angles.

A simplified detector geometry has been simulated using GEANT to evaluate the background. It consists of the beam pipe, a vertex detector, a central tracker, and the calorimetry. Around the quadrupoles, which are inside of the detector, tungsten masks are placed to shield the main part of the detector from backscattered particles.

The full crossing angle between the two beams is  $\theta_c=20$  mrad. A first design of the final quadrupole has an outer radius of  $r=20$  mm. The exit hole for the spent beam can thus be large enough to extract the bulk of the coherent pairs. Also the effect of the multibunch

## DESCRIPTIONS OF THE FOUR MACHINES AT 500 GEV C.M.

kink instability is small for this crossing angle. The blow-up of the spot size due to the coupling of the beam to the detector solenoid field  $B_z=4$  T is still acceptable.

A preliminary design of the mask has been developed (Figure 3.68). Its inner opening angle is chosen such that all particles from coherent pair creation and the bulk of the particles from incoherent pair creation should enter the mask. Assuming a distance of the mask opening to the IP of 1 m, this angle must be larger than 60 mrad for  $B_z=4$  T. To allow for some contingency, a value of  $\theta_i=80$  mrad is chosen. The outer angle is then defined by the required thickness of the mask. Studies for TESLA indicated that a mask thickness of 5 to 7.5 cm is sufficient. The outer angle has therefore been set to 120 mrad, which leads to a mask thickness of 8 cm. It should be possible to increase the thickness of the mask by adding material on the inside, an option that was excluded in TESLA because of the space requirement of the cryostat around the quadrupole.

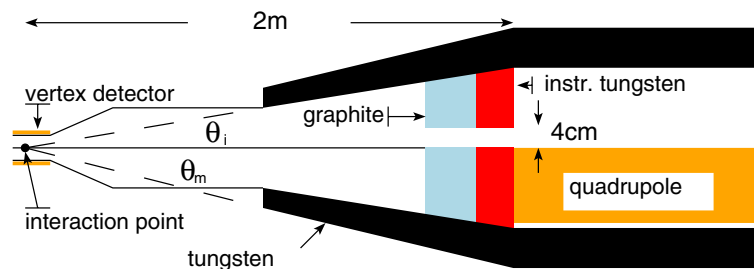


FIGURE 3.68. View from above on the adopted mask design. The sketch is stretched in the vertical direction. Care has to be taken that no particles are backscattered through the hole in the mask.

Inside the mask described, a second mask is placed which consists of tungsten covered on the IP side by a low-Z material. This is necessary to reduce to a negligible level the rate of particles that are scattered back from the quadrupoles into the vertex detector. This mask is instrumented to allow a fast luminosity measurement and the tagging of low angle particles. The lowest angle for this tagging is likely to be  $\theta_0=40$  mrad. At smaller angles one expects a large energy flow from the pair background. The inner mask needs one hole for the incoming beam and another one for the outgoing beam. The one for the spent beam has a radius of  $r=2$  cm to keep the number of coherent pair particles lost inside of the detector small. The simulation predicts a total energy deposition in the inner mask of 250 TeV per side and per bunch crossing. The hole for the spent beam is small enough so that the inner mask can still shield the vertex detector from neutrons coming from the tunnel. Simulations have verified that backscattering of charged particles is almost completely suppressed, reducing the hit density in the vertex detector by an order of magnitude. However it has to be ensured that no charged particles are scattered back through this hole, since they could hit the vertex detector.

The vertex detector will be directly hit by a number of particles from the incoherent pair production that have large initial angles and transverse momenta. Assuming that it covers

an angle of  $|\cos\theta| \leq 0.98$ , the minimum inner radius to ensure less than 1 hit per  $\text{mm}^2$  and bunch train is  $r=30$  mm in a magnetic field of  $B_z=4$  T.

The number of hadronic background events per bunch crossing is high, about 2.3 events with a center-of-mass energy above 5 GeV. These events have been simulated in the detector using GUINEA-PIG, PYTHIA and GEANT. Most of the energy goes into very small angles, so it is lost inside of the masks. The hadrons significantly contribute to the total density of charged hits in the vertex detector with a highest density of  $\rho=0.25$   $\text{mm}^{-2}$  per bunch train. Also the secondary neutron flux due to the hadronic showers in the detector (including masks and low angle taggers) have been simulated. The neutron flux found at a radius of  $r=0.3$  m is  $3 \times 10^9$   $\text{cm}^{-2}$  per year. It reaches a maximum around the masks and is lower at the IP.

### 3.4.3 Power-Source Subsystems

#### 3.4.3.1 The RF Power Source—General Principles

CLIC requires short rf pulses of high peak power at 30 GHz (130 ns long, with 230 MW per accelerator structure). Since no conventional rf source at 30 GHz can provide such pulses, the two-beam acceleration technique is used, in which an electron beam (the drive beam) is accelerated using standard, low-frequency rf sources and then decelerated to produce rf power at high frequency.

In linear collider projects based on conventional rf sources (klystrons), pulse compression or delayed distribution techniques are used in order to obtain the needed high peak power and short pulse length. Similar techniques are used in the CLIC two-beam accelerator. In this case, however, the compression and distribution are done with electron beams. The main advantage of electron beam manipulation, with respect to manipulation of rf pulses, consists of the very low losses that can be obtained while transporting the beam pulses over long distances and compressing them to very high ratios. A further advantage is the possibility of pulse compression, achieved by interleaving bunched beams by means of transverse rf deflectors. The pulse length is given by the filling requirement of the accelerator structures and by the number of bunches in the main beam. The 30 GHz frequency is effectively obtained through the short bunch length and a distance between the bunches in the train being a small multiple of the nominal rf period. The net result of the whole process is so-called frequency multiplication (from 0.937 GHz to 30 GHz). In the following we will describe the CLIC rf power source complex used to generate all the rf power needed for one of the two main linacs (electron or positron). Possibilities to combine some elements of both the  $e^+$  and  $e^-$  complexes are under study. A schematic layout of one complex is shown in Figure 3.69.

The CLIC rf power source essentially combines and transforms several long, low-frequency rf pulses into many short, high-power pulses at high frequency. During the process, the energy is stored in a relativistic electron beam, which is manipulated in order to obtain the desired time structure and then transported to the place where the energy is needed. The energy is extracted from the electron beam in resonant decelerating structures (the Power Extraction and Transfer Structures—PETS), which are located parallel to the main accelerator. The key points of the system are an efficient acceleration of the drive beam in conventional structures, the introduction of transverse rf deflectors to compress the drive

## DESCRIPTIONS OF THE FOUR MACHINES AT 500 GEV C.M.

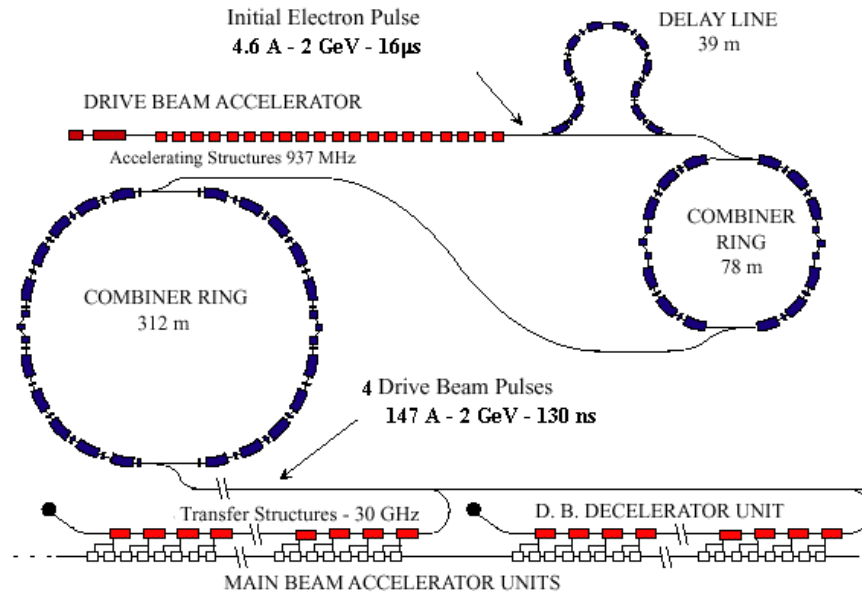


FIGURE 3.69. Schematic layout of the CLIC rf power source. Two such complexes (one for each of the main linacs) will be needed to provide the power for 500 GeV c.m. CLIC operation. Only two of the 4 decelerator/accelerator units composing a linac are shown.

beam, and the use of several drive-beam pulses in a counter-flow distribution system, each one powering a different section of the main linac. The method discussed here seems relatively inexpensive, very flexible and can be applied in various linear colliders over the entire frequency and energy range.

The drive-beam generation complex is located at the center of the linear collider complex, near the final-focus system. For 500 GeV c.m. operations, two times 4 decelerator units, each 625 m long, are required to power the two main linacs which each accelerate the colliding beams up to 250 GeV. In this case, the energy for the rf production is initially stored in a  $16.7 \mu\text{s}$  long electron beam pulse (corresponding to twice the length of one main linac) which is accelerated to about 2 GeV by a normal-conducting, low-frequency (937 MHz) traveling wave linac. The linac is powered by conventional long-pulse klystrons. A high-energy transfer efficiency is paramount in this stage. The drive beam is accelerated in relatively short structures (4.5 m long), so that the rf losses in the copper are minimized. Furthermore, the structures are fully beam-loaded, *i.e.*, the accelerating gradient is nearly zero at the downstream end of each structure and negligible rf power flows out to a load. In this way, about 97% of the rf energy can be transferred to the beam.

The beam pulse is composed of  $32 \times 4$  subpulses, each one 130 ns long. In each subpulse the electron bunches occupy alternately even and odd buckets of the drive-beam accelerator fundamental frequency (937 MHz). Such a time structure is produced after the thermionic gun in a subharmonic buncher, whose phase is rapidly switched by  $180^\circ$  every 130 ns. This provides us with a means to separate the subpulses after acceleration, while keeping a constant current in the accelerator and avoiding transient beam-loading.

As the long pulse leaves the drive-beam accelerator, it passes through a delay-line combiner where “odd” and “even” subpulses are separated by a transverse rf deflector at the frequency of 468.5 MHz. Each “even” bunch train is delayed with respect to the following “odd” one by 130 ns. The subpulses are recombined two-by-two by interleaving the electron bunches in a second rf deflector at the same frequency. The net effect is to convert the long pulse to a periodic sequence of drive-beam pulses with gaps in between. After recombination, the pulse is composed of  $16 \times 4$  subpulses (or trains) whose spacing is equal to the train length. The peak current and the bunch frequency (of 937 MHz) are doubled.

The same principle of electron-bunch pulse combination is then used to combine the trains four-by-four in a first combiner ring, with a 78 m long circumference. Two 937 MHz rf deflectors create a time-dependent local deformation of the equilibrium orbit in the ring. This bump is used for injection of a first train in the ring (all its bunches being deflected by the second rf deflector onto the equilibrium orbit). The ring perimeter is equal to the spacing between trains plus  $\lambda/4$ , where  $\lambda$  is the spacing between bunches, equal to the wavelength of the rf deflectors. Thus, for each revolution period, the rf phase seen by the bunches circulating in the ring increases by  $90^\circ$ , and when the second train is injected, the first one does not see any deflection and its bunches are interleaved with the ones which are injected (at a  $\lambda/4$  distance). This is repeated twice, then the four interleaved trains are extracted from the ring by an ejection kicker half a turn later, and the same cycle starts again. After the first combiner ring the whole pulse is composed of  $4 \times 4$  trains. The trains are combined again, using the same mechanism, in a second combiner ring, with a 312 m long circumference, yielding another factor of 4 in frequency multiplication, and obtaining the final 4 trains required for each main linac. At this point, each final train is 39 m long and consists of 1952 bunches with a charge of 9.8 nC/bunch and an energy of 2 GeV.

Such drive-beam pulses are distributed down the main linac via a common transport line, in a direction opposite to the direction of the main beam. The periodic distance between trains is now 1248 m, corresponding to twice the length of the linac section which they will power, so that they will arrive at the appropriate time to accelerate a high-energy beam traveling in the opposite direction.

Pulsed magnets deflect each beam at the appropriate time into a turn-around. After the turn-around each pulse is decelerated in a 624 m long sequence of low-impedance PETS (which is by definition one drive-beam decelerator unit) down to a minimum energy close to 0.2 GeV. The resulting output power is transferred to the structures which accelerate the high-energy beam in the main linac. As the main beam travels along, a new drive-beam train periodically joins it and runs in parallel but ahead of it to produce the necessary power for a 624 m long linac unit. At the end of a unit the remaining energy in the drive beam is dumped while a new one takes over the job of accelerating the main beam. The main characteristics of the CLIC rf Power Source are given in Table 3.32.

## DESCRIPTIONS OF THE FOUR MACHINES AT 500 GEV C.M.

TABLE 3.32  
Power source basic parameters.

Parameter	Symbol	Value
<b>Drive-beam pulse</b>		
Energy (initial)	$E_{in,dec}$	2 GeV
Energy (final, minimum)	$E_{fin,dec}$	200 MeV
Average current in a pulse	$I_{dec}$	147 A
Train duration (FWHH)	$\tau_{train}$	130 ns
Number bunches/train	$N_{b,dec}$	1952
Bunch charge	$Q_{b,dec}$	9.8 nC
Bunch separation	$\Delta_{b,dec}$	0.067 ns
Bunch length, r.m.s.	$\sigma_{z,dec}$	0.4 mm
Normalized emittance, r.m.s. (injection)	$\gamma\epsilon_{dec}$	150 $\mu\text{m}\cdot\text{rad}$
<b>Decelerator unit</b>		
Repetition rate	$f_{rep}$	200 Hz
Unit length (total)	$L_{unit,tot}$	624 m
Unit length (active)	$L_{unit,act}$	400 m
Number of PETS/unit	$N_{PETS,unit}$	500
Power extracted/metre	$P_{out}$	458 MW
Main beam energy gain/unit	$\Delta E_{main}$	62.5 GeV

### 3.4.3.2 Drive Beam Generation Complex

**3.4.3.2.1 Overview of the System** Each drive beam injector is composed of 5 subsystems:

1. A thermionic gun.
2. A bunching system providing a bunched beam at 10 MeV.
3. An injector linac accelerating the beam up to 50 MeV.
4. A spectrometer line with beam diagnostic and collimation.
5. A matching section to the Drive Beam Accelerator. Figure 3.70 gives a schematic layout of one injector.

The total pulse, at the injector exit, is 16.7  $\mu\text{s}$  and is composed of  $32 \times 4$  subpulses. The time structure is produced after the thermionic gun in a subharmonic buncher, in such a way that the electron bunches of each subpulse occupy alternatively even and odd buckets (Figure 3.71).

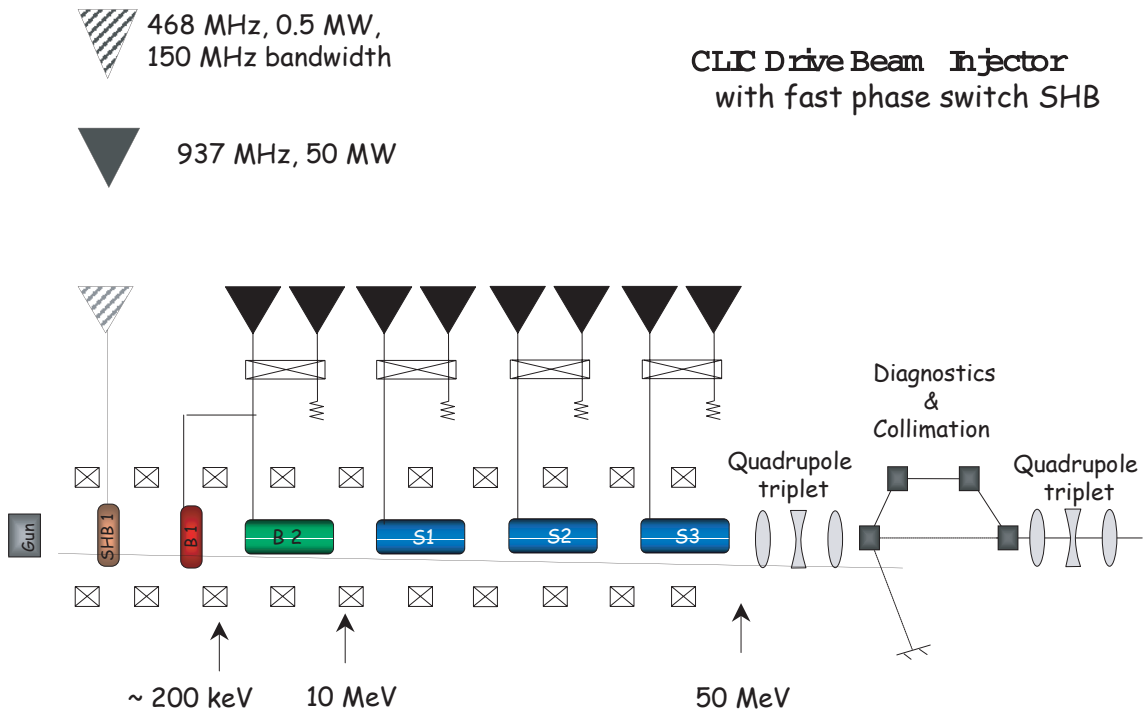


FIGURE 3.70. Layout of the CLIC Drive Beam Injector.

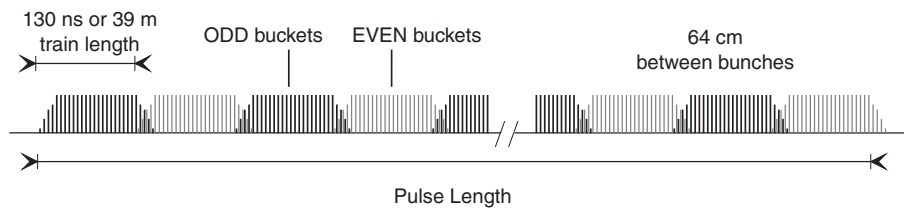


FIGURE 3.71. Combined pulses at the drive-beam injector linac entrance.

**3.4.3.2.2 Injector Characteristics** The bunching system of the drive-beam injector is made of one subharmonic buncher (468.5 MHz), powered by one klystron of 1 MW, and of one buncher (937 MHz) powered by two 50 MW-klystrons. The rest of the injector consists of three accelerator structures (937 MHz), identical to those of the drive-beam accelerator, each powered by two 50 MW-klystrons.

At the injector exit, the beam reaches the energy of 50 MeV and fulfills the following necessary conditions:

- i. The total number of bunches has to be a multiple of 32 (frequency multiplication factor).
- ii. The pulse for the PETS requires bunches of lower intensity for the pre-fill of the structures and bunches of constant charge for the power generation. The energy spread at the exit of the injector linac is partly correlated due to the beamloading. The uncorrelated energy spread is 0.75% and the total energy spread is less than 1%. Such value is obtained with a beam collimation at  $\pm 3 \sigma_E$  before the injection in the accelerating linac. The rms value for the single bunch length is 4 mm at the injector exit. Since a large beam size would cause losses in the decelerating structures, it is crucial to obtain a beam at 2 GeV with an emittance as small as possible. Assuming an emittance blow-up of 50% between the injector and the decelerator, a normalized emittance of 100  $\mu\text{m}\cdot\text{rad}$  is an upper value at 50 MeV. Table 3.33 summarizes the beam characteristics at the injector exit for 500 GeV. Figure 3.71 shows the composition of the bunch train at the linac entrance.

TABLE 3.33  
Beam characteristics at the drive-beam injector exit.

Parameter	Unit	Value
Beam energy	MeV	50
Pulse length (Total train)	$\mu\text{s}$	16.7
Beam current per pulse	A	5
Charge per pulse	$\mu\text{C}$	80
Number of bunches per pulse		7808
Bunch length (FWHH)	ps	32
Bunch length (r.m.s.)	mm	4
Normalized emittance (r.m.s.)	mm-rad	$\leq 100$
Energy spread	%	$\leq 1$
Repetition frequency	Hz	200

**3.4.3.2.3 A Photoinjector Option** The possibility to use an rf photoinjector as the drive beam source is under investigation. A CW laser working at 468.5 MHz provides a

continuous train. During  $17 \mu\text{s}$  the necessary power is generated in order to create the charge of  $80 \mu\text{C}$  on the photo-cathode. The laser beam illuminates the photo-cathode of an rf gun powered by a klystron at 937 MHz. It generates an electron beam with a momentum of several MeV at the exit of the photoinjector. The requested sequence of pulses can be directly injected into the injector linac. However several issues remain to be addressed and an R & D program has been set up to try to overcome these issues.

**3.4.3.2.4 Accelerator Lattice and Dynamics** The drive beam accelerator consists of 108 accelerator structures (each powered by two 50 MW klystrons). The initial beam energy is 50 MeV, the final one 2 GeV, and the average beam current is 4.59 A. Each structure is  $\sim 4.5$  m long and has a loaded gradient of about 4 MV/m. Simulations were however carried out with a slightly higher beam power corresponding to a final energy of 2.1 GeV and a beam current of 4.88 A, for these values corresponded to the  $\pi/2$  phase-advance main-linac structure studied at the time of the tracking in an attempt to resolve the surface-field question. The results obtained in this case should be rather pessimistic.

Simulations for CTF3 showed that the best compromise between wakefield and dispersive effects can be achieved by using a triplet lattice. Two structures are placed between the triplets and the total length per cell is 14 m. The relative strength of outer and inner quadrupoles is chosen to achieve a round beam in the structures (left side of Figure 3.72). The transverse wakefields were derived by scaling the ones calculated for CTF3 with respect to the frequency. To evaluate the beam stability, a beam with an initial offset has been tracked through the perfectly aligned linac using PLACET. The transverse  $Q$ -factors in the simulation were 50% larger than calculated to allow for imperfect SiC loads. As can be seen in the right side of Figure 3.72, the initial jitter of the beam is amplified. However this amplification seems acceptable. The bunches coming after the phase switch which generates the odd and even bucket subpulses are more strongly kicked than the other ones. If the transition is done more gradually, as it will be in practice, then the kick will be much smaller.

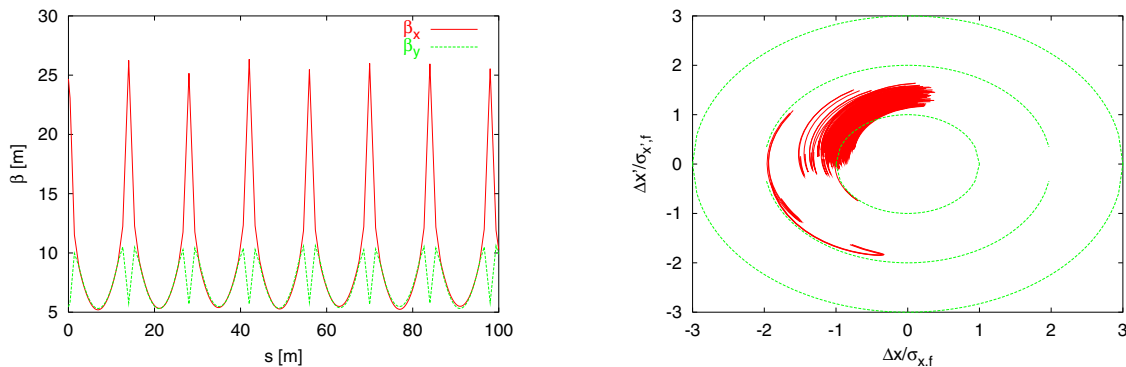


FIGURE 3.72. Left: The beta functions in the drive beam accelerator. Right: The final offset of a beam entering the structure with an offset of one rms bunch size  $\sigma$ . The value is normalized to the final beam size.

### 3.4.3.3 Accelerator Structures, Design, HOM Damping

The accelerator structures common to the drive-beam accelerator (DBA) and drive-beam injector of CLIC each consist of 42 cells adding to the length of  $\sim 4.5$  m indicated previously (mechanically a little more). It will operate in  $2\pi/3$  mode, fully beam loaded by a beam current of 4.59 A. It has a moderate accelerating gradient and a nominal unloaded gradient of 7.2 MV/m.

Two types of structures have been studied. The first type considered is the “Tapered Damped Structure” (TDS) originally designed for the CLIC main accelerator and downscaled by a factor of 32. Dipole mode damping in TDS is obtained by coupling SiC loads through 4 waveguides to the accelerating cavities. The cut-off frequency of these waveguides is chosen above the operating frequency, but below the higher order mode frequencies. It thus serves as a high-pass filter between the cavity and the dampers. A TDS scaled to 937 MHz would however be very large (outer diameter 1.4 m). The impractical size of the TDS was one of the reasons to study in detail a second and novel type of structure, called SICA for “Slotted Iris—Constant Aperture.” It has 4 radial slots in each iris, which virtually do not perturb the fundamental mode field. Dipole mode currents however are intercepted by the slots. The slots are radially extended into ridged waveguides which contain tapered SiC loads. These are designed as to drastically reduce the Q of the dipole modes (to values typically below 20). As opposed to the TDS, where the higher order modes are separated by a filter from the accelerating mode, mode separation in the SICA uses the geometric differences and special symmetries of the mode patterns. SICA structures were successfully built and tested at 3 GHz and are being implemented as DBA structures for CTF3. At 937 MHz, SICA structures would have an outer diameter of approximately 250 mm. The left side of Figure 3.73 shows an artist’s conception of the accelerator structure and its right side shows a photograph of a machined disc for the 3 GHz prototype.

Cell dimensions and some of the fundamental mode characteristics of the beginning, middle and end SICA cells are given in Table 3.34, for both the 3 GHz structure built for CTF3 and the scaled 937 MHz version envisaged for the CLIC drive beam accelerator.

Another feature of the SICA structures is the constant iris aperture which reduces the short range wakes. The detuning is obtained by introducing nose cones with varying depths. These nose cones lead to a larger ratio of surface field to accelerating gradient in the downstream cells (ratio of up to 3.4), but this is acceptable since the overall accelerating gradient is moderate. Issues which were addressed in the design were i) the field enhancement at the slot edges and ii) the presence of low frequency “slot modes” and their potential impact on the performance. The field enhancement is reduced to an acceptable 40% by a modest rounding of the edges (rounding radius of approximately half the slot width). This additional field enhancement will lead to a maximum surface field of 33 MV/m at the slot edges in the last cell. The slot modes, which occur at frequencies of about  $2/3$  of the operating frequency, have the electric field across the slots and are strongly damped ( $Q \leq 6$ ) if the cut-off frequency of the ridged waveguide is chosen low enough. The kick factor of the slot mode is found to be at an acceptable 5% of that of the lowest dipole mode. The parameters of the CTF3 and CLIC drive beam accelerator structures are summarized in Table 3.34.

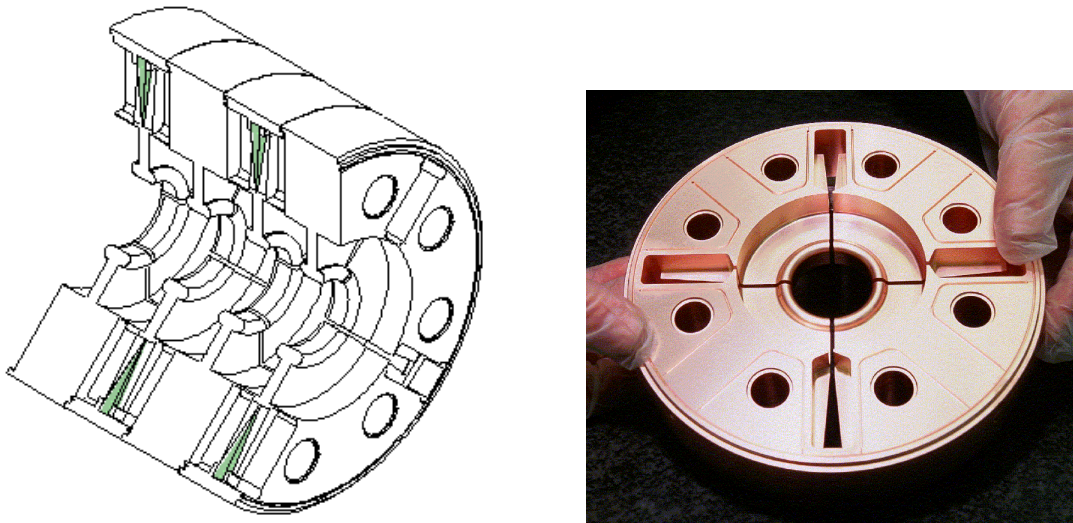


FIGURE 3.73. Left: Conceptual view of the SICA accelerator structure. Right: Machined disc of the 3 GHz version of the SICA structure.

TABLE 3.34: Parameters of the SICA drive-beam accelerator structures.

	3 GHz SICA (CTF3)			937 MHz SICA (CLIC)			Unit
Operating frequency	2998.55	937.05		MHz			
Beam current	3.5	4.88		A			
Cavity diameter	79.00	center cell	last cell	center cell	last cell	238.05	
Nose cone size	2.53	4.66		mm			
Iris thickness	6.00			mm			
Iris diameter	34.00			mm			
Phase advance/cell	120°			mm			
$r'/Q$ (Linac $\Omega$ )	3292	3165		$\Omega/m$			
Group velocity	3.49	2.36		% c			
Q accelerating mode	12771	10950					
Frequency 1 <sup>st</sup> dipole	4147	4097		MHz			
Kick factor 1 <sup>st</sup> dipole	555	843		V/pC/m <sup>2</sup>			
Q 1 <sup>st</sup> dipole mode	17.5	6.2					
Frequency 2 <sup>nd</sup> dipole	4243	4379		MHz			
Kick factor 2 <sup>nd</sup> dipole	206	197		V/pC/m <sup>2</sup>			
Q 2 <sup>nd</sup> dipole mode	3.4	17.3					
Cell length	33.32	24.4		mm			
Number of cells/structure	32						
Structure length	1.22			m			
Fill time, $\tau$	98			ns			
Input power	30			MW			
Acceler. voltage unloaded	13.3			MV			
Acceler. voltage loaded	7.9			MV			
Beam loading, $\kappa$	97.4			%			
Efficiency, $\eta$	92.5			%			
Number of structures (injector + accelerator)	2 + 16						
Total energy gain	127			MeV			

### 3.4.3.4 Klystrons and Modulators

The drive-beam complex requires high-power klystrons working in the L-band range of frequencies (468 and 937 MHz) for subharmonic bunching, the  $\times 2$  delay line combiner, the first  $\times 4$  combiner ring and for drive-beam acceleration. Higher frequency klystrons operating at 3750 MHz are also required for rf deflection systems in the second  $\times 4$  combiner ring. The klystron-modulators used in the drive-beam systems are shown in Figure 3.74.

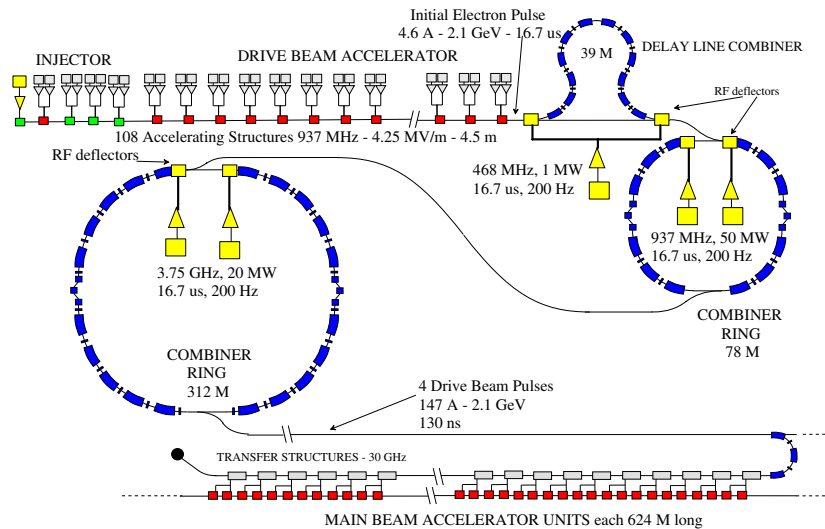


FIGURE 3.74. Drive-beam klystron-modulators for one generation complex.

Most of the very high power klystron-modulators are in the drive-beam accelerators (224 in each accelerator). For this application a multibeam klystron (MBK) having 6 internal beams is being designed. The long-term, targeted peak power for this MBK is 50 MW and 500 kW average for a 3 TeV machine. At the present time, a design study and current experience by manufacturers indicate a possible maximum of 40 MW for a klystron having a good lifetime and reliability. For the 500 GeV mode of operation the CLIC drive-beam can be powered by the layout in Figure 3.75 with each klystron also working at 50 MW in the extreme case, for the repetition rate is twice as high but the pulse length six times shorter than for the 3 TeV mode. In normal operation with two MBK per SICA structure, each klystron must provide a nominal power of  $\sim 44$  MW (Table 3.34, input power). However, reliability constraints require that in case of structure failure the gradient of the functioning structures be possibly increased by up to 5%, which means an increase of 10% in power. This implies that the klystrons be able to deliver a power close to the 50 MW considered. It must be noted that if the actual maximum power of the klystrons appears to be lower than 50 MW, then it is always possible to adjust the structure-length and

## DESCRIPTIONS OF THE FOUR MACHINES AT 500 GEV C.M.

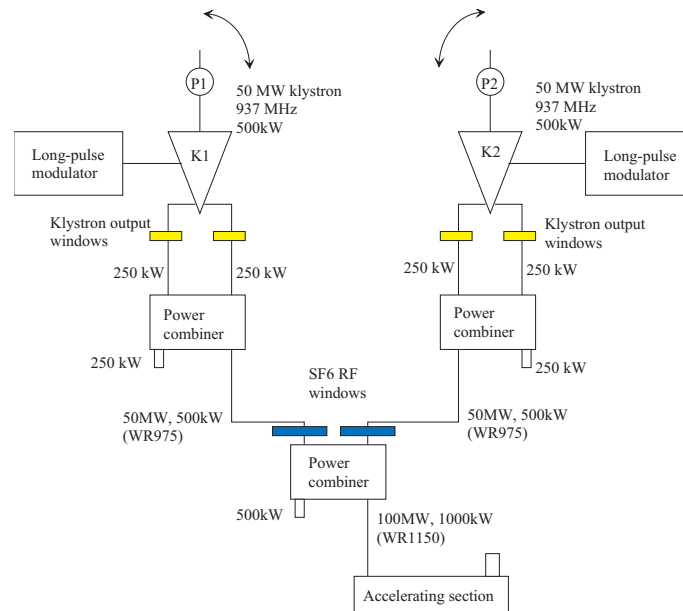


FIGURE 3.75. 50 MW MBK rf module layout.

linac-length in order to accommodate the two MBK per structure layout to this constraint, while keeping the reliability margin. The MBK data for 50 MW peak are given in Table 3.35.

In the drive-beam accelerator each MBK has its own high-power modulator and pairs of these klystron-modulators are connected as modules (Figure 3.75) to provide the rf power for a single structure.

A conventional line-type modulator has been studied that could power a single 50 MW multibeam klystron. This uses a double pulse forming network (PFN) and two thyatron switches that discharge the stored energy into the MBK via a step-up pulse transformer. A similar modulator design could be used for all drive-beam klystrons requiring wide voltage pulses at specific repetition rates. Alternative modulator designs using solid-state switching are to be investigated as a future replacement for the thyratrons. The requirements for very high power conversion efficiency together with high system reliability are important design issues. Table 3.36 gives a summary of the klystron and modulator (MDK) minimum power requirements for the drive-beam in the 500 GeV CLIC scheme, as well as the respective numbers of MDK needed for the accelerators, injectors and rf deflectors.

### 3.4.3.5 Combiner Rings

The main issue in the pulse compression system (delay line plus combiner rings) is the preservation of the length and longitudinal phase-space distribution of the bunches and the control of bunch-to-bunch phase variations. The rings, the delay line and the transfer lines must therefore be isochronous. The final bunch length must be short ( $\sigma_z$  of 0.4 mm, for a 9.8 nC charge per bunch) in order to maximize the 30 GHz rf power production efficiency in the drive-beam decelerator. High-charge, short bunches can radiate Coherent Synchrotron

TABLE 3.35: Multibeam klystron data

Parameter	Target Design	Present Design	500 GeV Design	Units
RF frequency	937.5	937.5	937.5	MHz
Repetition frequency	100	100	200	Hz
RF pulse width	100	100	16.7	$\mu$ s
Microperveance	0.5	0.5	0.5	$I/V^{3/2}$
Number of beams	7	6	6	$n_b$
$J_{max}$	6	6	6	A/cm <sup>2</sup>
Efficiency	65 to 70	65 to 70	65 to 70	%
Gain at saturation	$\geq 47$	$\geq 43$	$\geq 43$	dB
Klystron beam voltage	212	211	189	kV
Klystron beam current	342	293	245	A
Peak rf output power	50	40	50	MW

TABLE 3.36: Drive-beam klystron-modulator requirements.

MDK RF System	Number MDKs	Klystron Type	Repetition Rate [Hz]	Pulse Width [ $\mu$ s]	Frequency [MHz]	Peak Power [MW]	Average Power [kW]
Drive-beam accelerator	432	MBK	200	16.7	937	50	100
Drive-beam injector	16	MBK	200	16.7	937	50	100
Drive-beam injector	2	SBK	200	16.7	468	1	3.4
		150 MHz BW					
RF deflectors	4	SBK	200	16.7	3750	20	67
RF deflectors	4	MBK	200	16.7	937	50	100
RF deflectors	2	SBK	200	16.7	468	1	3.4

## DESCRIPTIONS OF THE FOUR MACHINES AT 500 GEV C.M.

Radiation (CSR), leading to both an energy loss and an intra-bunch energy spread. The energy loss and spread must be kept small, in particular because the bunches belonging to different trains make a different number of turns in the rings (from  $1/2$  to  $7/2$ ) and will develop different energy distributions. This will cause relative phase errors between bunches and some bunch lengthening. These intense and short bunches will also interact with any small discontinuity of the beam chamber. It is therefore highly desirable to manipulate relatively long bunches in the pulse compression system, and to reduce their length just before the injection into the drive-beam decelerator sections.

The upper limit to the bunch length is given by the variation of the rf deflector kick strength along the bunches, due to their phase extension. This variation reduces the clearance from the septum of the circulating bunches for a given kick amplitude and induces a single-bunch emittance growth for the injected ones. These effects are critical in the second combiner ring, where the deflector frequency (3.75 GHz) is the highest. The maximum acceptable bunch length in this location is 2 mm r.m.s. approximately. The correlated energy spread ( $\sim 1\%$  r.m.s.) suitable for the final bunch compression is obtained in the drive beam accelerator by the combined effect of the rf curvature and longitudinal wakefields. The need to preserve the correlation all along the compression system means that all the distortions of the longitudinal phase space must be kept small. In particular, attention must be given to the higher orders of the momentum compaction. A numerical analysis has shown that second-order effects would be unacceptable and must be corrected by using sextupoles.

Another concern is the beam loading in the rf deflectors. Again, this is particularly important just before the extraction from the second combiner ring, where the average current in the train and the deflector frequency are the highest. In order to overcome this problem, a traveling-wave iris-loaded structure with a short filling time with respect to the train duration has been chosen. A steady-state condition is then reached with minimum transient effects, although at the expense of a loss in the deflection efficiency. Numerical simulations have shown that a proper choice of the ring tune can minimize the effect.

The extraction system of both rings is also a critical item, the two main issues being the high repetition rate of the extraction kick ( $\sim 1$  MHz in the first ring and 250 kHz in the second ring, which correspond to 4 and 16 times  $2 \times 130$  ns, respectively) and the interaction of the system with the high-current beam (particularly in the second ring—147 A). A possible solution is based on the use of pairs of traveling TEM wave transmission-lines.

A preliminary design of the lattices for the delay line and the combiner rings was made in 1999. Since then, the CLIC rf pulse length has been reduced from 143 ns to 130 ns. The drive beam energy and bunch charge have also been modified to 2 GeV and 9.8 nC, respectively. Such parameter changes imply a reduction of the delay introduced in the delay-line as well as a reduction of the circumference and of the magnetic field strength in the combiner rings. The existing lattice design could in principle be modified to fit the new parameters. Another possibility would be to use the design of the isochronous cells retained for CTF3. Such a design is based on the use of three bending magnets per module or cell instead of four. Being more compact, it would be better adapted to smaller rings and transfer lines.

The delay-line geometry was chosen to minimize both CSR emission and overall dimensions and is still based on the same type of isochronous arc design as in the combiner rings. In order to avoid distortions in the longitudinal phase space, all the arcs must be made

isochronous up to the second order by the use of sextupoles placed in the high-dispersion regions where there are no dipoles. The use of different families of sextupoles makes it possible to correct the third order as well.

One 3-bend magnetic chicane is located in the delay line and two in each ring. They are used for fine path-length tuning ( 0.5 mm tuning range), in order to adjust the relative phase of the bunches and compensate for orbit variations. Each chicane works around an average bending angle of  $\theta_0 \sim 150$  mrad. The tuning range is obtained with a bending angle variation of  $\Delta\theta=1.5$  mrad; such a small value of  $\Delta\theta/\theta_0$  does not perturb the optics. The small finite  $R_{56}$  generated by the chicane is compensated in the two adjacent cells, slightly detuned away from their isochronous point.

The ring injection is similar to a conventional fast injection scheme based on a septum and a fast kicker, where the kicker is, however, replaced by an rf deflector. Another deflector is placed upstream of the septum (with a phase advance difference of  $-\pi$ ), and provides the pre-compensation of the kick given by the injection deflector to the circulating bunches. A  $\pi/2$  phase advance FODO lattice is used in the injection straight section, with the septum and deflectors close to the focusing quadrupoles, so that the angular kick from the deflector corresponds to a maximum displacement in the septum (left side of Figure 3.76).

All the rf deflectors are short traveling-wave iris-loaded structures, in which the resonant mode is a deflecting hybrid mode with a  $2\pi/3$  phase advance per cell and a negative group velocity. The design is basically the same for all the deflectors, with the cell dimensions linearly scaled with frequency. The extraction kickers consist of pairs of TEM traveling-wave transmission-lines, powered in anti-phase, with the wave moving against the beam. The design of the extraction region lattice is based on a triplet placed between the kicker and the extraction septum (right side of Figure 3.76). The phase advance between the kicker and the septum is equal to  $\sim \pi/2$ . The use of a triplet allows a rather constant  $\beta$ -amplitude along the kicker.

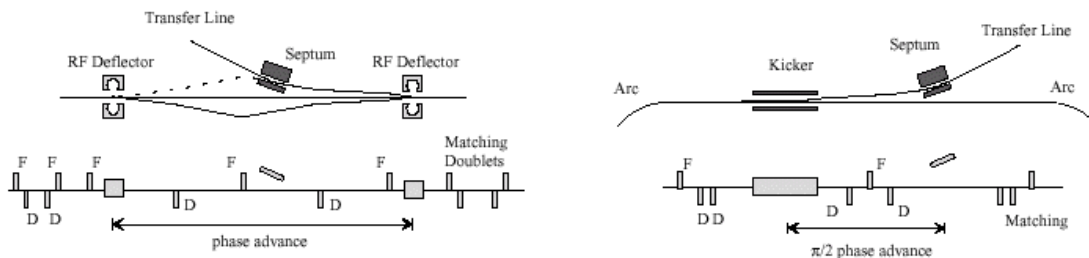


FIGURE 3.76. Schematic layout of the injection insertion with rf deflectors (left) and of the extraction insertion (right). At injection, the circulating bunches will travel on the central or inner orbit, while the injected bunches are kicked by the 2<sup>nd</sup> deflector onto the equilibrium orbit. The train of combined bunches is ejected before the next pulse reaches the deflecting phase represented by the dotted line trajectory (intercepting the septum).

### 3.4.3.6 Drive-Beam Decelerator

Each drive beam decelerator has to feed 1000 main linac accelerator structures. It contains 500 Power Extraction and Transfer Structures (PETS). All beam line elements are mounted on girders which have the same length as the ones of the main linac, in order to facilitate the geometrical matching of the two lattices. Each girder supports two quadrupoles and two PETSs. A BPM is located in front of each quadrupole.

If the single bunch effects could be neglected, then the optimum frequency of the PETS would exactly be the same as the one of the main linac accelerator structures. Since one cannot neglect the single bunch effect, the case for optimum efficiency is obtained by using PETS with a frequency slightly different from the main linac frequency. Depending on their longitudinal position, the particles in the bunch are indeed decelerated differently. The maximum of the deceleration energy defines the minimum initial energy of the beam, which is required for the beam to pass through a given number of structures and which is directly related to the overall efficiency. For the given bunch length of  $\sigma_z=400 \mu\text{m}$ , the optimum frequency is  $f_{PETS} \approx 30.45 \text{ GHz}$  (left side of Figure 3.77). It should be noted that the maximum output power, obtained by adjusting the beam current, is reached for a much smaller detuning. However the maximum deceleration is also decreasing. A bunch charge of  $N=6.13 \times 10^{10}$  produces an output power of 512 MW per PETS structure when the losses in the structures are neglected. After subtracting the losses this provides the required power of 231 MW per main linac structure. The initial beam energy has to be  $E_0=1.994 \text{ GeV}$ . The lowest final energy in the beam is then  $\tilde{E}_f=0.1994 \text{ GeV}$ . The final beam energy distribution is shown in the right side Figure 3.77. The energy spread in the beam is very large and the ratio of the lowest to the highest energy is 10. The decelerator lattice must accommodate a very large energy spread. This can be easily achieved by using a FODO lattice. The length of the FODO cells is kept constant along the decelerator and the quadrupole strength is adjusted so that the phase advance per cell is constant for the particle that is decelerated most. Particles that are decelerated less are automatically focused to smaller amplitudes.

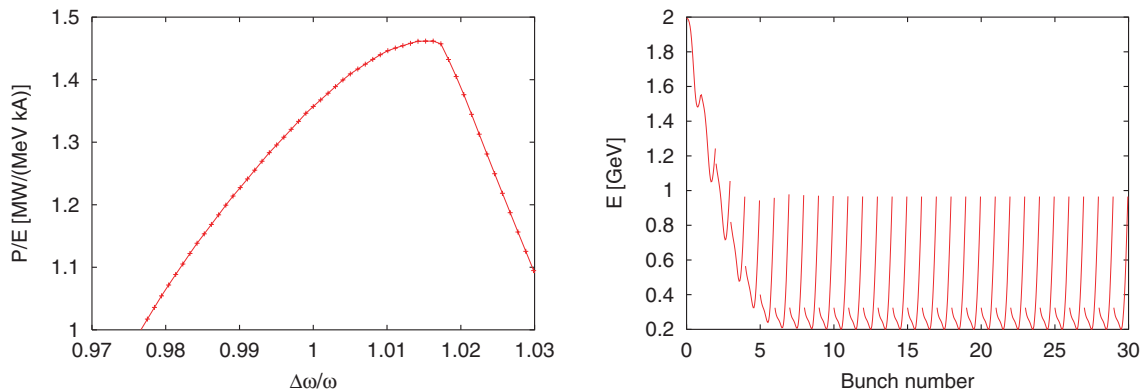


FIGURE 3.77. Left: The ratio between output power and maximum decelerating field as a function of the fundamental frequency of the PETS. Right: The final energy distribution in the various bunches of the drive-beam train.

To evaluate the beam stability in the decelerator, the envelope of a  $3\text{-}\sigma$  beam with an initial offset  $\Delta y = \sigma_y$  has been simulated using PLACET. In the program, the longitudinal and transverse wakefields are modelled using a single mode for each. The different group velocities, which are high, are taken into account and the beam is tracked through the structures in several steps using the proper field profiles. The deviation of the particle velocity from the speed of light is also accounted for. The left side of Figure 3.78 shows the result together with the envelope of a nominal  $4\text{-}\sigma$  beam without offset. The wakefield effects are small. The ballistic method is foreseen to correct the initial misalignments of the quadrupoles and of the BPMs. For the simulation, we assumed an initial r.m.s. position error of  $100\ \mu\text{m}$  for all the elements. The envelope that embraces the  $3\sigma$ -envelopes of the 100 cases simulated is shown in the right side of Figure 3.78 together with three particular cases (three different seeds).

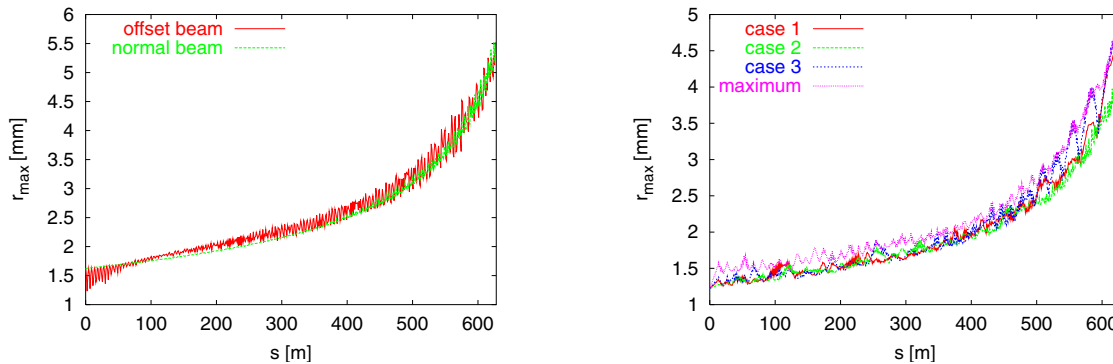


FIGURE 3.78. Left: The  $3\sigma$ -envelope of a beam with initial offsets of  $\Delta x = \sigma_x$  and  $\Delta y = \sigma_y$ . For comparison the  $4\sigma$ -envelope of a beam with no offset is also shown. Right: the  $3\sigma$ -envelopes in a decelerator after beam-based alignment. Three examples are shown together with the envelope that contains all of 100 simulated cases.

### 3.4.3.7 Power Extraction and Transfer Structures

**3.4.3.7.1 Definition and Functions of the PETS** The Power Extraction and Transfer Structure (PETS) is a passive microwave device in which the bunches of the drive beam interact with the impedance of the periodically corrugated waveguide and excite preferentially the synchronous TM01 mode at 30 GHz. In the process, the beam kinetic energy is converted into electromagnetic energy at the mode frequency, which travels along the structure with the mode group velocity. The rf power produced is collected at the downstream end of the structure by means of the Power Extractor and conveyed to the main linac structure by means of rectangular waveguides. The circularly symmetric structure (C-PETS) concept with distributed damping was eventually adopted, for it satisfies the requirements and ensures the azimuthal uniformity of the longitudinal electric field. In its configuration, the C-PETS is a circular waveguide with a shallow sinus-type

## DESCRIPTIONS OF THE FOUR MACHINES AT 500 GEV C.M.

corrugation with damping slots and rf loads as displayed in Figure 3.79, which shows the C-PETS with beam chamber diameter 25 mm.

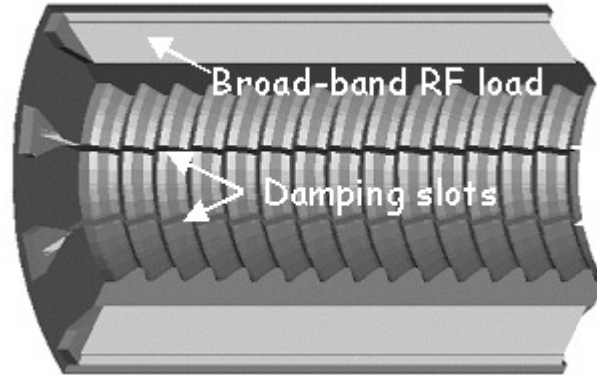


FIGURE 3.79. A quarter geometry of the C-PETS with 12 damping slots and SiC loads.

**3.4.3.7.2 Structure Parameters** Table 3.37 gives the main geometric and rf parameters of the C-PETS (with a 25 mm beam chamber aperture) which has been chosen as the power extracting structure for the drive-beam accelerator.

**3.4.3.7.3 RF Power Extraction** The quasi-optical approach was used for the rf power extraction from the regular part of C-PETS. This choice was done for high efficiency, large bandwidth and mode purity. The power extractor consists of (Figure 3.80) the mode launcher, which converts the  $TM_{01}$  mode of the circular waveguide (WG) to the TEM mode of the oversized coaxial WG and of the diffractor, which modifies the TEM mode into the  $TE_{10}$  modes of the following 8 rectangular WG's, that are then combined into two output WG's. The simulated rf power extraction efficiency is about 99% at 30 GHz, with a mode purity better than -30db, for both the reflected and transmitted ones.

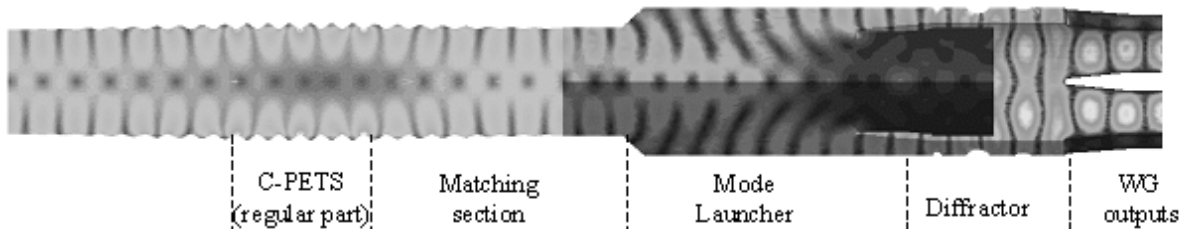


FIGURE 3.80. The electric field pattern of the rf power extractor for the C-PETS.

TABLE 3.37  
Parameters of the C-PETS.

Parameter	Value	Units
Beam chamber diameter	25	mm
Synch. mode frequency	29.9855	GHz
Synch. mode $v_g/c$	0.85	
Synch. mode $R'/Q$	244	$\Omega/m$
Synch. mode Q-factor	12000	
Number of damping slots (1.0 mm width)	8	
Transverse mode $v_g/c$	0.793	
First dipole mode kick-factor	0.58	V/pC/m/mm
Transverse mode Q-factor	< 50	
Structure length	0.8	m
Nominal output rf power	512	MW

**3.4.3.7.4 Transverse Mode Damping** A new concept of distributed damping of the transverse modes in a circularly symmetric structure has been developed. It is best explained in terms of array antennas. The damping is provided by thin longitudinal slots running all along the length of the structure. Every period of the slot-loaded structure acts like a single source in an array antenna, radiating through the slots to the outside. The radial component of the radiation (damping) is a function of the phase advances between two cells. The smaller the phase advance, the stronger the damping. Broadband rf loads terminate the slots. In the design of a 20 mm beam aperture C-PETS, the damping is provided by 12 equally spaced radial slots of 0.5 mm, as shown in Figure 3.79. Each of the 12 loads consists of a long SiC rod with a triangular cross-section, which is matched to the slot. The slot depth and load geometry are chosen to minimize the external Q-factor of the first dipole mode around 30 GHz. To verify the damping ability, a full-scale simulation of C-PETS (100 cells) was done with the special EM computer code GDFIDL. The loaded Q-factor was calculated to be about 35. This value is very close to the one calculated with HFSS during the design stage.

The long-range transverse wakes and transverse impedances are shown in Figure 3.81. The second big spike in the wake distribution for the undamped case (left side of Figure 3.81) results from a partial (about 30%) reflection from the ends of the structure. In the presence of damping the reflection is not seen because of the strong attenuation of the reflected wave. A comparison of the transverse impedances with and without damping (right side of Figure 3.81) shows that low-frequency trapped modes are significantly suppressed with this distributed damping technique. Comparing time domain simulations (see above) with wakefield reconstruction from the frequency domain data (HFSS) for a bunch length of 600  $\mu\text{m}$  established that the influence of the first dipole mode is dominant (more than 90%). Furthermore, the single-mode concept was considered for the beam dynamics simulations both for the short-range and long-range wakefield effects. On the basis of beam dynamic simulations with optimized efficiency and beam stability, a 25 mm

DESCRIPTIONS OF THE FOUR MACHINES AT 500 GEV C.M.

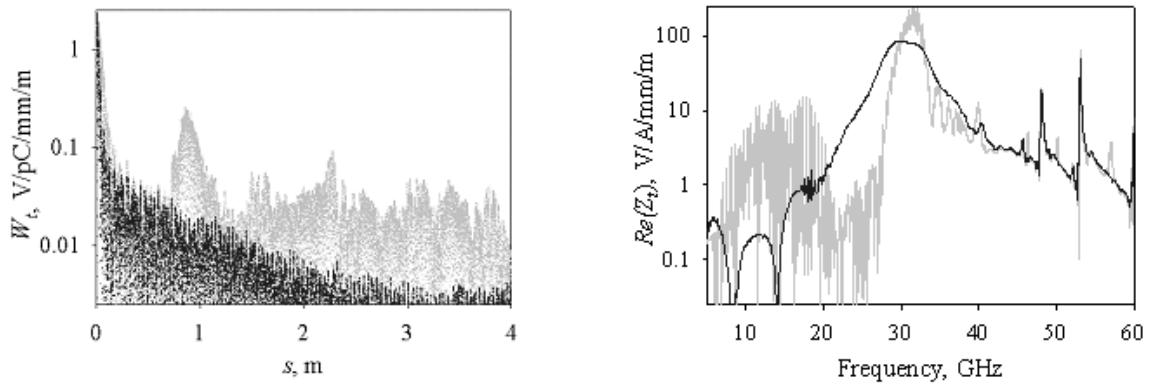


FIGURE 3.81. Left: The long-range wakes in the C-PETS. Right: The transverse impedance in the C-PETS.(grey: without damping, dark: with damping.)

beam aperture C-PETS with 8 damping slots, each 1.0 mm wide, is now proposed (parameters of Table 3.37). The peak electric field on the surface of the structure with the nominal rf power output was calculated to be about 90 MV/m. Due to the damping slots it is further enhanced by 20%—up to 110 MV/m. This field level is within the acceptable range for the 30 GHz structures.

# BIBLIOGRAPHY for CHAPTER 3

- [1] R. Brinkmann, *et al.* (eds.), TESLA Technical Design Report Part-II, DESY-2001-011, March 2001.
- [2] R. Brinkmann, *et al.* (eds.), Conceptual Design of a 500 GeV Linear Collider with Integrated X-ray Laser Facility, Vol. I, DESY-1997-048, May 1997.
- [3] N. Toge, ed. [JLC Design Study Group], “JLC design study,” KEK-REPORT-97-1 (1997).
- [4] T.O. Raubenheimer, ed. [NLC ZDR Design Group], “Zeroth order design report for the Next Linear Collider,” SLAC-R-0474 (1996).
- [5] C. Adolphsen *et al.* [International Study Group Collaboration], “International study group progress report on linear collider development,” SLAC-R-559 (2000).
- [6] N. Phinney, ed. [NLC Collaboration], “2001 report on the Next Linear Collider: A report submitted to Snowmass ’01,” SLAC-R-571 (2001).
- [7] The CLIC Study Team, Ed. G.Guignard, A 3 TeV  $e^+e^-$  Linear Collider Based on CLIC Technology, Report CERN 2000-008 (July 2000).  
<http://cern.web.cern.ch/CERN/Divisions/PS/CLIC/General.html>
- [8] H.H. Braun, R. Corsini (Ed.), T. D’Amico, J.P. Delahaye, G. Guignard, C.D. Johnson, A. Millich, P. Pearce, L. Rinolfi, A.J. Riche, R.D. Ruth, D. Schulte, L. Thorndahl, M. Valentini, I. Wilson, W. Wuensch, The CLIC RF Power Source - A Novel Scheme of Two-Beam Acceleration for Electron-Positron Linear Colliders, CERN 99-06 (1999).
- [9] M. Korotsolev, F. Zimmermann, “CLIC damping ring design study,” presented at the 8th European Part. Acc. Conf. (EPAC02), Paris, June 2002.
- [10] F. Zimmermann, *et al.*, “Design Status of the CLIC Beam Delivery System,” presented at the 8th European Part. Acc. Conf. (EPAC02), Paris, June 2002.

